

# DISSERTATION

## **Engineering Gate Stacks for Field-Effect Transistors**

ausgeführt zum Zwecke der Erlangung des akademischen Grades  
eines Doktors der technischen Wissenschaften

eingereicht an der Technischen Universität Wien  
Fakultät für Elektrotechnik und Informationstechnik  
von

THOMAS WINDBACHER

Dietrichgasse 12b/1  
2700 Wr. Neustadt, Österreich

Matr. Nr. 9925579  
geboren am 24. November 1979 in Mödling

---

# Kurzfassung

---

DER FELDEFFEKT-TRANSISTOR hat sich seit seinen Anfängen als bescheidenes gerade so funktionierendes Bauteil im Jahre 1947 zu einem unverzichtbaren Basisbaustein unserer modernen Technologie entwickelt. Nach fünf Jahrzehnten konstanter Weiterentwicklung und Verkleinerung mit unzähligen neuen Transistortypen und Anwendungen sind erstmals die physikalischen Grenzen in die nahe Zukunft gerückt. Dennoch ist das Gebiet der Feldeffekt-Transistoren noch immer nicht ausgereizt, jede neue Transistorgeneration weist verbesserte Eigenschaften auf und viele aufregende Möglichkeiten des Feldeffekt-Konzeptes sind noch immer unerforscht.

Das äußerst vielfältig einsetzbare Feldeffekt-Konzept eröffnet ein weites Feld an möglichen Einsatzgebieten. In dieser Arbeit werden vier vielversprechende und interessante Aspekte der Gate-Stack-Modellierung aufgegriffen und genau erläutert. Zu Beginn erfolgt die Beschreibung der Materialien, welche eine hohe Dielektrizitätskonstante aufweisen (high-k), wie sie in modernen CPUs zum Beispiel von Intel oder IBM Anwendung finden. Das Augenmerk liegt dabei auf Gate-Stack-Strukturen, wie sie für Schalttransistoren und in nicht flüchtigen Speicherzellen Anwendung finden. Dabei wird im Speziellen das Flash-Gate-Stack mit möglichen alternativen Gate-Stack-Strukturen verglichen, die weitere Transistorgenerationen ermöglichen. Danach erfolgt ein Überblick über die wichtigsten Technologien, die es erlauben die Ladungsträgerbeweglichkeit trotz kleinerer Transistorabmessungen zu erhöhen, indem sie den Kanal des Transistors mechanisch verspannen. Weiters folgt die Beschreibung des ferroelektrischen Gate-Stacks als vielversprechende Alternative zu dem weit verbreiteten Flash-Gate-Stack und eine kurze Einführung in elektrolytische Grenzflächen und den darauf basierenden biologisch sensitiven Feldeffekt-Transistoren.

Anschließend wird zuerst auf die mathematische Beschreibung von mechanischer Verspannung und Verformung im Allgemeinen und danach auf Halbleiterstrukturen und Quantisierungseffekte in Dünnschicht-Feldeffekt-Transistoren im Speziellen eingegangen. Dies erfolgt mit Hilfe der  $\mathbf{k}\cdot\mathbf{p}$  Methode und der Annahme eines einschränkenden Potentialtopfs. Das daraus resultierende Modell ermöglicht eine sehr gute Beschreibung der Bandstruktur für verspanntes Silizium bis etwa 0.5 eV und ist in der Lage, Vorhersagen für die effektiven Massen der  $\Delta$  und  $\Delta'$  Subbänder zu treffen. Der wesentliche Vorteil gegenüber vergleichbaren Methoden besteht darin, dass das verwendete Modell numerisch wesentlich weniger aufwändig ist.

Zum Abschluss wird das sich noch in den Anfängen befindende Gebiet der biologisch sensitiven Feldeffekt-Transistoren (BioFETs) vorgestellt. Diese erlauben die Messung von biochemischen Vorgängen auf durchgehend elektronischem Wege. Die wichtigsten Ionentransporteffekte in Elektrolyten und ihre mathematische Beschreibung werden erläutert, gefolgt von Beispielen von Simulationen zu verschiedenen Anwendungsgebieten mit jeweils zugehörigen mathematischen Modellen.

---

# Abstract

---

THE FIELD-EFFECT TRANSISTOR has evolved since its advent in 1947 from a humble barely working proof of concept device to an innumerable and indispensable basis for modern technology. After five decades of constant improvement and miniaturization, enabling new devices and applications, one can see the physical limits in the near future. However, the field-effect devices are still improving every generation cycle and many exciting possibilities of the field-effect concept are still uncharted.

The very powerful field-effect concept enables a vast area of possible applications. In this work four promising and interesting aspects of gate stack modeling are presented and described in detail. First with high-k materials utilized by modern CPU manufactures like Intel or IBM are reviewed. Special emphasis is layed on the description of the gate stacks for switching transistors and for non-volatile memory applications. Thereby, flash gate stacks are compared with alternative gate stack structures, which are able to facilitate the next technology node. Then an overview of different commonly employed strain techniques which enable one of the major mobility boosts in state of the art devices, is given. The discussion of ferroelectric gate stacks for non-volatile memory applications follows as a promising candidate for a flash gate stack replacement. Thereafter, a short introduction to electrolytic interfaces and the biologically sensitive field-effect transistor (BioFET) is presented.

Starting with the concept of stress and strain in general, a focus on the mathematical description of strain in semiconductors and thereafter on quantization effects in ultra-thin body FETs follows. This is realized by a two-band  $\mathbf{k}\cdot\mathbf{p}$  model and the assumption of a confinement potential. The resulting model is able to predict the band structure in strained silicon up to about 0.5 eV quite well and delivers effective masses for the primed and unprimed subbands. The big advantage of the employed model compared to other available methods lies in the reduced computational effort.

Finally, the still young field of biologically sensitive field-effect transistors (BioFETs) is presented. These devices enable the sensing of biochemical processes from start to finish via electronic means. At first all the major effects of ionic transport in electrolytes and their mathematical modeling, is given, followed by examples of simulations for various applications, and their corresponding mathematical models.

---

# Acknowledgment

---

FIRST I WANT TO thank my advisor *Prof. Siegfried Selberherr* for giving me the opportunity to join his research group and to work in the vast and amazing field of microelectronics. He took care for excellent working conditions, a calm working environment, and last but not least encouraged me to attend several high class scientific conferences.

I am also indepted to *Viktor Sverdlov* for his scientific guidance, his sometimes hard, but appreciated, comments on my work, and his ability in fixing problems. He introduced me to the  $\mathbf{k}\cdot\mathbf{p}$  method and the physics of strained semiconductors.

*Prof. Erasmus Langer*, the head of the Institute for Microelectronics, eased long working days with his sarcastic comments and took care of all the bureaucracy.

I also thank *Prof. Johann Summhammer* for serving on my examination committee.

*Dr. Clemens Heitzinger* introduced me to the commencing field of biological applications in microelectronics and the mathematicians' way of thinking. *Prof. Hans Kosina* is always a reliable source regarding various physical questions. *Prof. Tibor Grassler* is often hard to catch, but always open for questions and a really smart guy.

I was blessed with easygoing and genial colleagues. *Martin Vasicek* and I met first at our physics studies and soon became friends. He suggested to join him at the Institute of Microelectronics and it is always fun to chat with him. *Hajdin Ceric* introduced me at the institute and taught me the finite element method, which I like pretty much. *Otmar Ertl* was initially one of my room mates, has always an open ear for questions, and shares with me the love for open source and technical gadgets. *Roberto Orio de Lacerda* introduced me to the Brasillian culture and showed always a positive and relaxed attitude. *Goran Milovanovic* is also one of my friends from my studies and I enjoy discussing with him various themes. *Paul-Jürgen Wagner* proofed as an incredible solver of L<sup>A</sup>T<sub>E</sub>X problems and always had the right package/command up his sleeve. *Franz Schanovsky* was really helpful regarding to various questions and problems related to SGFramework. *Johann Cervenka* is the guy to ask, if you have a software problem and you need a quick fix and do not know how to tackle it. *Philipp Hehenberger* reignited my love for soya products and supported my addiction with tofu on a regular basis. *Oliver Triebel* helped as one of the MINIMOS-NT experts at the institute. *Oskar Baumgartner* shares with me the vice of coffee addiction and is an interesting discussion partner. *Wofgang Gös* impressed me with

## ACKNOWLEDGMENT

---

his *ironman* degree, something I will probably never be capable of. *Karl Rupp* served as the mathematician at hand and suffered under my spontaneous meetings and questions. *Stanislav Tyaginov* surprised me with his sensitive hobby of breeding bulb flowers. I did not know how colorful they can be.

During my work at the institute I had the pleasure to collaborate on different levels with many other colleagues I have a high regard for: *Markus Bina*, *Lado Filipovic*, *Abel Garcia-Barrientos*, *René Heinzl*, *Alexander Makarov*, *Mihail Nedjalkov*, *Neophytos Neophytou*, *Vassil Palankovski*, *Mahdi Pourfath*, *Philipp Schwaha*, *Zlatan Stanojevic*, *Ivan Starkov*, *Franz Stimpfl*, *Stanislav Vitanov*, and *Josef Weinbub* as well as those I apologize not to mention here.

I want to thank the proofreaders of this thesis, who greatly improved this work by their numerous suggestions.

*Manfred Katterbauer*, *Ewald* and *Christoph Haslinger*, and *Renate Winkler* took care of the administrative work and ensured the continuity at our institute. Special thank goes to all former members of the Institute for Microelectronics for leaving a precious heritage for all coming generations and to all other colleagues for their assistance and the stimulating working atmosphere they created.

This work was supported in part by the Austrian Science Fund FWF, Project P19997-N14.

Last but not least, I want to thank my family. My parents made possible all of my studies by their continuous support. They have taught me how to work hard and bring out the best of myself.

My wife, *Cornelia*, detached me from the computer from time to time in order to enjoy our family and free my mind from work. She also supported me in many other ways and provided me with love and understanding for endless working days. Only she knows how much I owe her. And of course there are my daughters *Lea* and *Yana* who make my world complete.

---

# Contents

---

<b>Kurzfassung</b>	<b>i</b>
<b>Abstract</b>	<b>iii</b>
<b>Acknowledgment</b>	<b>iv</b>
<b>Contents</b>	<b>vi</b>
<b>List of Symbols</b>	<b>x</b>
Notation . . . . .	x
Physical Quantities . . . . .	x
Constants . . . . .	xii
<b>List of Figures</b>	<b>xiii</b>
<b>List of Tables</b>	<b>xviii</b>
<b>1 Introduction</b>	<b>1</b>
<b>2 Gate Stack Overview</b>	<b>2</b>
2.1 High-k Gate Stacks . . . . .	3
2.1.1 Flash Memory . . . . .	5
2.1.1.1 Working Principle . . . . .	6
2.1.1.2 NOR . . . . .	7

2.1.1.3	NAND . . . . .	7
2.1.2	Comparison Between Floating Gate and SONOS . . . . .	8
2.1.3	Scaling of Floating Gate and SONOS . . . . .	9
2.2	Strained Interfaces . . . . .	11
2.2.1	Global Strain . . . . .	11
2.2.2	Local Strain . . . . .	13
2.2.2.1	Contact Etch Stop Liner - Gate Stacks . . . . .	13
2.2.2.2	Stress Memorization Gate Stack . . . . .	14
2.2.2.3	Selective Epitaxial Growth . . . . .	14
2.2.2.4	Shallow Trench Isolation . . . . .	14
2.2.2.5	Strain Technologies in High Volume Production . . . . .	15
2.3	Ferroelectric Gate Stacks . . . . .	16
2.3.1	Ferroelectric Materials . . . . .	16
2.3.2	Applications . . . . .	17
2.3.2.1	Ferroelectric Thin-Films in FRAM . . . . .	17
2.3.2.2	Ferroelectric Field-Effect Transistors (FeFETs) . . . . .	18
2.4	Electrolytic Interfaces . . . . .	20
2.5	Working Principle of a BioFET . . . . .	21
<b>3</b>	<b>Strain and Semiconductor Properties</b>	<b>23</b>
3.1	Strain . . . . .	23
3.2	Stress . . . . .	25
3.3	Stress-Strain Relation . . . . .	26
3.4	Miller Index Notation . . . . .	27
3.5	Strain and Bulk Band Structure . . . . .	27
3.5.1	Deformation Potential Theory . . . . .	28
3.5.1.1	Strain Induced Conduction Band Splitting . . . . .	28
3.5.1.2	Strain Induced Degeneracy Lifting at the <i>X</i> Point . . . . .	29
3.5.1.3	Strain Induced Valence Band Splitting . . . . .	32
3.5.2	The <b>k·p</b> Method . . . . .	32
3.5.2.1	Effective Electron Mass in Unstrained Silicon . . . . .	33
3.5.2.2	The Silicon Conduction Band Minimum's Dependence on Strain	35

3.5.2.3	The Conduction Band Minimum of Silicon and its Energy Dispersion under Strain . . . . .	36
<b>4</b>	<b>Quantum Confinement and UTB</b>	<b>39</b>
4.1	Unprimed Subbands . . . . .	39
4.1.1	Scaled Energy Dispersion Relation . . . . .	46
4.1.2	Small Strain Values . . . . .	46
4.1.3	High Values of $\zeta$ . . . . .	47
4.2	Effective Mass of Unprimed Subbands . . . . .	49
4.3	Primed Subbands . . . . .	51
4.4	Effective Mass of Primed Subbands . . . . .	53
<b>5</b>	<b>Modeling of Electrolytic Interfaces</b>	<b>54</b>
5.1	Electrochemistry of Ionic Solutions . . . . .	54
5.2	Charge Transport in Electrolytes . . . . .	56
5.2.1	Bulk Transport . . . . .	56
5.2.2	Interface Transport . . . . .	57
5.3	Double Layer . . . . .	58
5.4	Stern Modification . . . . .	59
5.5	Ionic Activity . . . . .	61
5.6	Site-Binding Model . . . . .	61
5.7	Potential of an ISFET Gate Stack . . . . .	64
5.8	The ISFET as a Sensor . . . . .	69
5.8.1	Sensing pH with an ISFET . . . . .	69
5.8.2	Sensing via Catalysts . . . . .	70
5.8.3	Examples for ISFETs as pH Sensor . . . . .	71
<b>6</b>	<b>Generalization of the ISFET Concept</b>	<b>74</b>
6.1	Sensing via the Long-Range Field-Effect . . . . .	74
6.2	Modeling BioFETs . . . . .	75
6.2.1	Poisson-Boltzmann Model . . . . .	76
6.2.2	Poisson-Boltzmann Model with Sheet Charge . . . . .	77
6.2.3	Poisson-Boltzmann Model with Homogenized Interface Conditions . . . . .	77

## CONTENTS

---

6.2.4	Extended Poisson-Boltzmann Model . . . . .	78
6.2.5	Debye-Hückel Model . . . . .	78
6.2.6	Buffers and Ionic Strength . . . . .	80
6.2.6.1	Temperature Effects on Buffers . . . . .	80
6.2.6.2	Debye-Hückel Relationship . . . . .	81
6.2.6.3	Henderson-Hasselbach Equation . . . . .	81
6.2.6.4	PBS as an Example . . . . .	82
6.3	Analytical Comparison between the Poisson-Boltzmann, the Extended Poisson-Boltzmann, and the Debye-Hückel Model . . . . .	84
6.4	BioFET Examples . . . . .	87
6.4.1	DNAFET . . . . .	87
6.4.1.1	DNA Structure . . . . .	87
6.4.2	DNA Hybridization Sensors . . . . .	87
6.4.2.1	Studying the Angular Dependence of DNA in Relation to the Surface on the Device Characteristics . . . . .	87
6.4.2.2	Studying different Models for DNA Sensing with Low Concentrated Buffers in SGFETs . . . . .	91
6.4.3	Protein-FET - Streptavidin-Biotin-FET . . . . .	95
<b>7</b>	<b>Summary and Outlook</b>	<b>101</b>
	<b>Appendix</b>	<b>103</b>
A.	Re-expressing $X_1$ as a Function of $X_2$ . . . . .	103
B.	Expressing the Equations (4.18) and (4.19) . . . . .	104
C.	Estimating Diffusive Layer Charge . . . . .	106
D.	Relation Between Charge Density and Potential Drop . . . . .	107
E.	Flatband Potential and MOSFET Properties . . . . .	108
	<b>Bibliography</b>	<b>112</b>
	<b>Own Publications</b>	<b>132</b>
	<b>Curriculum Vitae</b>	<b>135</b>

---

# List of Symbols

---

## Notation

$x$	...	Scalar
$\vec{x}$	...	Vector
$\bar{X}$	...	Tensor

## Physical Quantities

Symbol	Unit	Description
$V_t$	V	threshold voltage
$\mu_{\text{eff}}$	$\text{cm}^2 \text{V}^{-1} \text{s}^{-1}$	effective mobility
$\vec{R}$	m	displacement vector
$\bar{\epsilon}$	1	displacement tensor
$\bar{\epsilon}$	1	strain tensor
$\epsilon_{ij}$	1	displacement tensor component
$\varepsilon_{ij}$	1	strain tensor component
$\vec{\sigma}$	$\text{Nm}^{-2}$	stress vector
$\bar{\sigma}$	$\text{Nm}^{-2}$	stress tensor
$C_{ijkl}$	$\text{Nm}^{-2}$	elastic stiffness tensor
$S_{ijkl}$	$\text{N}^{-1} \text{m}^2$	elastic compliance tensor
$m_l$	kg	longitudinal electron mass
$m_t$	kg	transversal electron mass
$\mathcal{H}$	eV	Hamiltonian
$\mathcal{H}(\bar{\epsilon})$	eV	strain dependent Hamiltonian
$\mathcal{D}^{\alpha\beta}$	eV	deformation potential for strain components $\alpha\beta$
$E$	eV	energy
$\delta E_0^{v_i}$	eV	energy shifts of the conduction band edge for vleys along $\langle 100 \rangle$ and $\langle 111 \rangle$ direction
$\Xi_d^v$	eV	dilatation deformation potential for a valley of type $v = \Delta, L$

LIST OF SYMBOLS

---

$\Xi_u^v$	eV	uniaxial deformation potential for a valley of type $v = \Delta, L$
$\Xi_{u'}$	eV	shear strain deformation potential
$\vec{r}$	$m^D$	space vector for $D$ dimensions
$\Psi_n$	$m^{-D/2}$	wave function in the eigenstate $n$ and $D$ dimensions
$E_n$	eV	eigenenergy of the eigenstate $n$
$\vec{k}$	$m^{-D}$	wave vector for $D$ dimensions
$u_{n\vec{k}}(\vec{r})$	$m^{-D/2}$	Bloch function for $D$ dimensions
$\Omega$	$m^D$	volume of the first Brillouin zone
$m_{ij}^*$	kg	effective mass tensor
$m_l$	kg	longitudinal effective mass
$m_t$	kg	transversal effective mass
$[X]$	mol/l	concentration of molecule/atom $X$
$\Lambda_\infty$	$l\Omega^{-1}\text{mol}^{-1}$	molar conductivity of an electrolyte in infinite dilution
$\Lambda$	$l\Omega^{-1}\text{mol}^{-1}$	effective conductivity of an electrolyte
$\Lambda^\pm$	$l\Omega^{-1}\text{mol}^{-1}$	molar conductivities for positive and negative ions
$\nu^\pm$	1	valences for positive and negative ions
$\mu^\pm$	$\text{cm}^2\text{V}^{-1}\text{s}^{-1}$	ionic mobility for positive and negative ions
$K$	$\Omega\text{mol}^{3/2}l^{-3/2}$	Kohlrausch coefficient
$V_o$	V	overpotential (applied potential minus built in potential)
$V_a$	V	externally applied potential
$\tilde{u}_X$	V	electrochemical potential for material $X$
$u_X$	V	chemical potential for material $X$
$\Phi_X$	V	inner potential of material $X$
$E_{\text{ref}}$	V	reference electrode potential
$\chi_X$	V	electron affinity $X$
$V_{\text{FB}}$	V	flatband voltage
$\psi$	V	potential
$\epsilon_{\text{sol}}$	1	relative permittivity of the solute
$c_0$	mol/l	bulk concentration
$\sigma_0$	$\text{As cm}^{-2}$	charge density of the electrolytic double layer
$K_a$	mol/l	reaction equilibrium constant for positive charging
$K_b$	mol/l	reaction equilibrium constant for negative charging
$\sigma_{\text{Ox}}$	$\text{As cm}^{-2}$	surface charge density
$N_s$	$\text{cm}^{-3}$	total binding site density
$\sigma_s$	$\text{As cm}^{-2}$	charge density of the semiconductor
$\xi$	1	valency of the corresponding ion
$c_\xi^\infty$	mol/l	bulk concentration for the ion with valency $\xi$
$\psi_\mu$	V	chemical potential
$\rho_{\text{Space}}$	$\text{As cm}^{-3}$	space charge density
$\sigma_{\text{Sheet}}$	$\text{As cm}^{-2}$	sheet charge density
$\lambda_D$	m	Debye length
$I$	mol/l	ionic strength

## LIST OF SYMBOLS

---

$\varphi$	1	scaled potential
$\mathcal{E}$	$\text{m}^{-1}$	electric field
$\mathcal{E}$	1	scaled energy
$\mu_n$	$\text{cm}^2 \text{V}^{-1} \text{s}^{-1}$	electron mobility
$\mu_p$	$\text{cm}^2 \text{V}^{-1} \text{s}^{-1}$	hole mobility

## Constants

$h$	...	<i>Planck's</i> constant	$6.6260755 \times 10^{-34} \text{ Js}$
$\hbar$	...	reduced <i>Planck's</i> constant	$h/(2\pi)$
$k_B$	...	<i>Boltzmann's</i> constant	$1.380662 \times 10^{-23} \text{ JK}^{-1}$
$q$	...	elementary charge	$1.6021892 \times 10^{-19} \text{ C}$
$m_0$	...	electron rest mass	$9.1093897 \times 10^{-31} \text{ kg}$
$n_A$	...	Avogadro's constant	$6.022\,141\,79 \times 10^{23} \text{ mol}^{-1}$
$K_{\text{eq}}$	...	equilibrium constant for water dissociation (at $25^\circ\text{C}$ )	$1.8 \times 10^{-16} \text{ mol/l}$
$K_w$	...	equilibrium constant for water dissociation (at $25^\circ\text{C}$ )	$1. \times 10^{-14} \text{ mol}^2/\text{l}^2$
$\varepsilon_0$	...	vacuum permittivity	$8.8541878 \times 10^{-12} \text{ As V}^{-1}\text{m}^{-1}$

---

# List of Figures

---

2.1	Scheme of a high-k gate stack. By exchanging the $SiO_2$ gate-dielectric with $HfO_2$ the critical oxide thickness of $\approx 2$ nm for tunneling can be met while keeping control over the channel. . . . .	4
2.2	Basic scheme of a flash memory cell. Depending on the charge stored in the floating gate one bit SLC or multiple bits MLC can be saved. . . . .	6
2.3	Schemes of the basic circuits for NAND and NOR flash memory devices. . . . .	6
2.4	Scheme of a SONOS gate stack. . . . .	8
2.5	Overview of common strain techniques. . . . .	11
2.6	Scheme for different global strain techniques: 1.) strained silicon layer on $SiGe$ on bulk wafer; 2.) strained silicon layer directly on insulator (SDGOI); 3.) strained silicon layer on $SiGe$ substrate on insulator (SSGOI). . . . .	12
2.7	Combining selective epitaxial growth in source and drain regions and a stress liner to introduce tensile uniaxial stress for n-channel MOSFETs and compressive uniaxial stress for p-channel MOSFETs. . . . .	15
2.8	Schematic views for the different FeFET designs. . . . .	19
2.9	The working principal of a BioFET. If charged, sample molecules attach to the receptors at the biofunctionalized surface and the potential within the semiconductor changes. This causes a change in the resistance of the field-effect transistors channel. . . . .	21
3.1	Scheme of stress components and how they act on an infinitesimal cube. . . . .	25

3.2	Energy dispersion of the conduction bands $\Delta_1$ and $\Delta_2$ near the zone boundary $X$ point along $[001]$ . For $\varepsilon_{xy} = 0\%$ the conduction bands are degenerate at the zone boundary. Introduction of shear strain $\varepsilon_{xy} \neq 0$ lifts this degeneracy and opens up a gap. The energy separation $2\delta E_1$ between the bands becomes larger with increasing strain $\varepsilon_{xy}$ . At the same time the two minima of the lower conduction band $\Delta_1$ move closer to the zone boundary with rising strain $\varepsilon_{xy}$ , until they merge at the zone boundary and stay there for further increasing strain. . . . .	30
3.3	Energy dispersion of the two lowest conduction bands at the zone boundaries $X = \frac{2\pi}{a_0}(1, 0, 0)$ and $\frac{2\pi}{a_0}(0, 1, 0)$ . The band separation of unstrained $Si$ at the conduction band edge $\vec{k}_{\min} = \frac{2\pi}{a_0}(0, 0, 0.85)$ is denoted by $\Delta$ . Contrary to the conduction bands along $[001]$ the conduction bands along $[100]$ and $[010]$ are not affected by shear strain $\varepsilon_{xy}$ . . . . .	31
4.1	Potential in an ultra-thin SOI film of a single-gate MOSFET (left) and a corresponding model square well potential with infinite walls. . . . .	40
4.2	Conduction band profile close to the X-point for $\eta = 0$ (solid lines, $\eta = 0.5$ (dashed lines), and $\eta = 4$ (dashed-dotted line). . . . .	41
4.3	The right hand side of (4.16) and (4.17) plotted close to the point $\sqrt{\zeta^2 + X^2} = 0$ . It is clearly seen that the sign of the square root must be alternated at this point. . . . .	43
4.4	Subband quantization energies $E_n$ (normalized to the ground subband energy) for a film thickness of 3.3 nm. The valley splitting appears for non-zero shear strain $\zeta$ . . . . .	44
4.5	The same as in Fig. 4.4 for a film thickness 6.5 nm. The valley splitting depends strongly on the film thickness. The valley splitting is maximal at high strain values. . . . .	44
4.6	Difference of the subband quantization energies $\Delta E_n$ (normalized to the ground subband energy) from (4.18) and (4.19) for a film thickness of 3.3 nm. The valley splitting appears for non-zero shear strain $\zeta$ . . . . .	45
4.7	$\Delta E_n(\zeta)$ for a film thickness of 6.5 nm. The splitting depends strongly on the film thickness. . . . .	45
4.8	Splitting induced by shear strain for several film thicknesses. As can be seen for ultra-thin films the splitting is already larger than $k_B T$ for moderate stress levels. . . . .	48
4.9	Ultra-thin films exhibit different effective masses for the two ground subbands even without stress. The thinner the film the more pronounced is the difference in effective masses. . . . .	48
4.10	The dependence of the effective masses on the film thickness for the lowest two subbands. . . . .	50
4.11	The two ground subbands as contour plots. . . . .	50

LIST OF FIGURES

---

5.1 Most biological and chemical experiments are carried out in an ionic solution. Polar solutions (like water) can break up strong ionic bonds and ease chemical reactions. Each ion (red and dark blue) is surrounded by an aggregate of water molecules. The non-vanishing dipole moment of the water molecules weakens the electric field binding the ions together. . . . . 55

5.2 The different surface effects. The (*non-*) *specific adsorption*, due to (partial) release of the solvation shell and conjoint closer approach to the interface, the so called IHP, is depicted with blue circles. The effect of *surface complexation*, due to the high affinity of attracting counter ions, is shown by the green circle. The Stern layer ends at the OHP, the zone without counter ions exhibiting their full water shell (depicted with red circles, surrounded by small light blue circles), and is continued by the Gouy-Chapman layer. . . . . 60

5.3 The insulator surface exhibits open binding sites due to the lack of insulator bonding partners at the surface. These binding sites can be either negatively/positively charged or neutral, depending on the properties of the liquid covering the surface. The surface charge density depends on the surface potential  $\psi_0$ , material properties, and the local hydrogen concentration  $[H^+]_b$ . . . . . 62

5.4 As illustrated in the panels a.) to d.), the higher the surface site density  $N_s$  is the bigger the maximal surface charge density  $\sigma_0$  will be. All curves show two distinct steps in the relation between surface charge density  $\sigma_0$  and surface potential  $\psi_0$ . The larger the difference between the forward positively charging reaction rate  $K_a$  and the negatively charging reaction rate  $K_b$  the more pronounced and steeper are these steps. . . . . 65

5.5 Potential profile in an ISFET structure for a cut along the z-axis.  
 1.) The potential drop at the electrode-electrolyte interface, caused by the Gouy-Chapman-Stern double layer ( $E_{ref} + \chi_{sol} - \chi_M$ ).  
 2.) The Gouy-Chapman-Stern double layer at the electrolyte-insulator interface ( $\psi_0$ ).  
 3.) The potential drop in the insulator ( $\psi_{ox}$ ).  
 4.) The potential drop due to the depletion charges in the semiconductor ( $\psi_s$ ). . . . . 66

5.6 Introducing a membrane into the ISFET hinders unwanted ion-species to diffuse to the insulator interface. Thus, only the selected ion species can approach the gate insulator, and the selectivity of the ISFET is ensured. . . . . 71

5.7 Potential profile for a cut perpendicular to the surface of the ISFET (beginning at the left border: semiconductor, dielectric, and solute). The simulations were carried out for a.) 100 mMol, b.) 10 mMol, and c.) 1 mMol phosphate buffered saline (PBS).  $Si_3N_4$  was utilized as gate dielectric at different pH values. Simulation results with the parameter set by Harame et al. [1], fit excellent the experimental values. With decreasing buffer concentration the screening is reduced and the saturation starts at higher pH values. The reduced screening is also reflected in the prolonged decay of the potential in the liquid. . . . . 73

6.1 Sensing a macromolecule via the long-range field-effect. . . . . 75

LIST OF FIGURES

---

6.2	BioFET: different simulation zones. . . . .	77
6.3	The dependence of the Debye length on ion concentration for a 1 : 1 electrolytic solution. Higher salt concentration reduces the repulsion between complementary DNA strands, and thus accelerates the hybridization events, but, at the same time, decreases the Debye length $\lambda_D$ and therefore the device signal. . . . .	79
6.4	The dependence of the concentrations for different ionic components and the ionic strength on the local pH. . . . .	83
6.5	Illustrating the different screening characteristics for the Poisson-Boltzmann, the extended Poisson-Boltzmann, and the Debye-Hückel model. In the limit of $a \rightarrow 0$ the extended Poisson-Boltzmann model rejoins the Poisson-Boltzmann model, while for increasing closest possible ion distance $a$ , which corresponds to a decreasing salt concentration, the screening is reduced and resembles for $a = 0.275$ the Debye-Hückel model. . . . .	86
6.6	a.) The unbound single-stranded DNA at the surface of the dielectric. b.) Single-stranded DNA on the oxide surface. Two iso-surfaces for plus and minus $0.2 \frac{k_B T}{qA^2}$ are shown. . . . .	88
6.7	a.) Potential profile in the whole device for double-stranded DNA perpendicular to surface. b.) Potential profile at the interface (from left to right: semiconductor, oxide, solute). . . . .	89
6.8	a.) Output characteristics before hybridization for a mean distance $\lambda = 10nm$ and $\lambda = 15nm$ without dipole moment. b.) Output characteristics after hybridization for a mean distance $\lambda = 10nm$ and $\lambda = 15nm$ without dipole moment. . . . .	89
6.9	a.) Output characteristics after hybridization for a mean distance $\lambda = 15nm$ : without dipole moment, with $0^\circ$ , and $90^\circ$ . b.) Potential profile from semiconductor to oxide (left to right). . . . .	90
6.10	a.) Transfer characteristics of a SGFET for Poisson-Boltzmann model and DNA charge modeled via space charge density. b.) Transfer characteristics of a SGFET for Poisson-Boltzmann model and DNA charge modeled via sheet charge density. c.) Transfer characteristics of a SGFET for Debye-Hückel model and DNA charge modeled via space charge density. . . . .	93
6.11	Potential for the Poisson-Boltzmann model with space charge, starting from the semiconductor (left) and ending in the analyte (right). It can be seen that doubling the charge does not lead to twice the potential shift due to nonlinear screening. . . . .	94
6.12	Potential for the Poisson-Boltzmann model with sheet charge, starting from the semiconductor (left) and ending in the analyte (right). Here the shift is a bit increased but far away from the values from the measurement. However, also here doubling the charge does not lead to twice the potential shift due to nonlinear screening. . . . .	94

## LIST OF FIGURES

---

6.13	Potential for the Debye-Hückel model with space charge, starting from the semiconductor (left) and ending in the analyte (right). It can be seen that doubling the charge leads to twice the potential shift due to the weaker linear screening. . . . .	94
6.14	Scheme of the tetrameric protein streptavidin and biotin. . . . .	95
6.15	Biotin-streptavidin complex [2] on the oxide surface. Two iso-surfaces for plus and minus $0.03 k_B T / q \text{Å}^2$ are shown. . . . .	96
6.16	Output curve for $\text{SiO}_2$ for unprepared, prepared but unbound, and bound state at $\lambda = 10\text{nm}$ and $\lambda = 15\text{nm}$ , respectively. . . . .	98
6.17	Output curve for $\text{Al}_2\text{O}_3$ for unprepared, prepared but unbound, and bound state at $\lambda = 10\text{nm}$ and $\lambda = 15\text{nm}$ , respectively. . . . .	98
6.18	Output curve for $\text{Ta}_2\text{O}_5$ for unprepared, prepared but unbound, and bound state at $\lambda = 10\text{nm}$ and $\lambda = 15\text{nm}$ , respectively. . . . .	98
6.19	Output curves for $\text{SiO}_2$ , $\text{Al}_2\text{O}_3$ , and $\text{Ta}_2\text{O}_5$ for calculation without dipole moment, $0^\circ$ (perpendicular to surface), and $90^\circ$ (parallel to surface). . . . .	99
6.20	Small signal resistance for $\text{SiO}_2$ , $\text{Al}_2\text{O}_3$ , and $\text{Ta}_2\text{O}_5$ for calculation without dipole moment, $0^\circ$ (perpendicular to surface), and $90^\circ$ (parallel to surface) at biotin only. . . . .	100
6.21	Small signal resistance for $\text{SiO}_2$ , $\text{Al}_2\text{O}_3$ , and $\text{Ta}_2\text{O}_5$ for calculation without dipole moment, $0^\circ$ (perpendicular to surface), and $90^\circ$ (parallel to surface) at bound state (biotin-streptavidin). . . . .	100

---

# List of Tables

---

4.1	Comparison between the effective masses for the lowest ground subband obtained with fullband calculations [3], calculations from [4], and the two-band $\mathbf{k}\cdot\mathbf{p}$ model. Excellent agreement with the fullband calculations is achieved. . . . .	53
5.1	Parameters for the site-binding model commonly used for sensing ( $pK_i = -\log_{10}(K_i)$ analog to the definition of $pH = -\log_{10}([H^+])$ ). . . . .	64
5.2	Sensitivity of ISFET devices for different gate dielectrics. . . . .	70
6.1	Parameters for the chosen phosphate buffer saline (PBS) [5]. . . . .	83

# Chapter 1

---

## Introduction

---

THE International Roadmap for Semiconductors (ITRS) [6] is an indicator, where the industry is now and where it should go to keep up in the race for technological progress. Now, after four decades of constant improvement, predicted by the ITRS, we are at the introduction of the 32 nm node [7, 8]. The development for the following 22nm node has started and will be even more demanding than the nodes before [6, 9].

Depending on the gate stack of the field-effect transistor many different applications can be realized, for instance, the well known transducer which amplifies electrical signals (starting with silicon dioxide as gate oxide due to its excellent interface properties [10] and shifting now to high-k dielectric materials due to scaling issues [8, 11]). However, today's probably most important application as a switch enables incredible complex digital devices like modern CPUs [12, 13], PDAs, mobile phones, mp3-players, cameras etc. By storing charge in the gate stack one is able to facilitate cheap, robust, high density, commodity storage like memory cards (CF<sup>TM</sup>, SD<sup>TM</sup>, Memory Stick<sup>TM</sup>, XD<sup>TM</sup> etc.) or solid-state disk for all kinds of portable devices, thus, enabling application areas and designs which were impossible some years ago. Even though the concept of flash memory is very popular today, in future due to scaling limits alternative concepts will be needed (FeRAM, MRAM, PCRAM, RRAM [14, 15]). There are new applications emerging, extending the field of established electrical engineering. Exchanging the polysilicon/metal gate structure with a biofunctionalized gate oxide surface, the realization of various biochemical sensors is feasible, starting with a simple pH sensor [16] for a native gate oxide, spanning over to detecting DNA snippets with DNAFETs [17].

In this work I study some selected gate stacks with emphasis on the engineering and modeling point of view. In Chapter 2 there is a general overview regarding the different types of gate stacks in use. Also the working principle and the most important properties of these devices are examined. Chapter 3 reviews strain-influenced gate stacks and how they can be exploited to change the band structure in order to boost the transport. The  $\mathbf{k}\cdot\mathbf{p}$  method is used for this purpose. Chapter 4 specializes on the electrolytic gate stacks and their mathematical description combined with simulation results. Chapter 5 provides a summary and a conclusion.

## Chapter 2

---

# Gate Stack Overview

---

**T**HERE ARE NUMEROUS gate stack types currently in use. Their classification can either be done by their application (e.g. digital switch, RAM, amplifier, BioFET, DNAFET) or by their material properties (ferroelectric, magnetic, electrolytic).

In the following there will be four selected gate stack types treated, namely, high-k, strained interface, ferroelectric, and electrolytic gate stacks. At first an introduction into high-k gate stacks for amplification and switching purposes will be given. Then, gate stack architectures for storage devices are described. Due to their rising importance over the last years flash-type FETs will be explained in more detail, followed by an examination of techniques able to introduce strain into the device architecture in order to boost the device performance. Afterwards, an introduction into ferroelectric materials and their properties is shown and last electrolytic interfaces and their exploitation in BioFETs will be taken care of.

## 2.1 High-k Gate Stacks

MOORE [18] PREDICTED THE NUMBER of transistors to double on a chip every two years. To be able to keep that exponential growth the components on the chip have to shrink accordingly every chip generation. However, it is not sufficient to reduce only the gate length and width. It also involves a reduction of all other dimensions including the gate/source and gate/drain alignment, the oxide thickness, and the depletion layer widths. Scaling of the depletion layer width also demands a corresponding adjustment of the substrate doping concentration [19].

At the 45nm node the so called *geometric scaling* or *classic scaling* is strongly impeded. For instance, the gate oxide thickness in 2009 was 7.5 Å according to the ITRS [20]. At this thickness the scaling of about  $\sim 0.7$  per generation is hindered due to the few atom layers of  $SiO_2$  left and the gate leakage caused by tunneling. So instead of scaling the oxide thickness down, the material has to be exchanged. Therefore, the oxide thickness is exchanged by the Equivalent Oxide Thickness (EOT) with respect to  $SiO_2$ . The material is actually thicker than silicon dioxide requires, but exhibits at the same time a much higher k-value. Thus, the gate leakage can be suppressed, while maintaining control over the channel.

The switch to high-k + metal gate states one of the major cuts since the advent of CMOS technology. Over 40 years  $SiO_2$  was the material of choice as gate insulator. The first high-k + metal gate transistors in a high volume manufacturing process were reported in [21]. They showed a working 153 Mb SRAM array with good process yield, performance, and reliability. The transistors were manufactured with a hafnium-oxide gate dielectric (EOT 1.0 nm), dual workfunction metal gate electrodes, enhanced channel strain, ultra shallow junctions, and nickel silicide.

Mistry et al. [21] employed a high-k first and metal gate last process. The processing until the salicidation is analog to their 90 nm and 65 nm node [22, 23], with the exception of atomic layer deposited hafnium-based high-k dielectric instead of  $SiO_2$ . After the interlayer dielectric deposition, the poly dummy gates are opened by polishing and subsequently removed, followed by deposition of PMOS workfunction metal and a patterning process removing the PMOS metal from NMOS areas and deposition of the NMOS workfunction metal. The gate ranches are filled with aluminum for low gate resistance and planarized by a metal polishing step. Finally, the contact etch stop layers are deposited. The resulting 45 nm high-k + metal gate transistors incorporate third generation strained silicon and feature a  $25\times$  reduction for NMOS and  $1000\times$  reduction of gate leakage for PMOS as well as an average drive current improvement of 32 % at the same voltage and  $I_{off}$  compared to the 65 nm node.

Recently Jan et al. [11] presented a 32 nm System-On-Chip (SOC) platform technology with a second generation high-k + metal gate and three transistor architectures. This technology is the successor of the previously presented 45 nm technology by Jan et al. [8]. In order to meet the requirements for the different functional circuit blocks of SOC applications the three transistor types offer a logic (High Performance (HP) or Standard Performance/Power (SP)), an ultra Low Power (LP), and a high voltage I/O design, which can be employed simultaneously but optimized independently. The short time ago expensive to implement triple gate architecture has become feasible due to the extremely low gate leakage of the high-k dielectric, allowing a much simpler gate implementation by sharing the same high-k dielectric layers for the logic

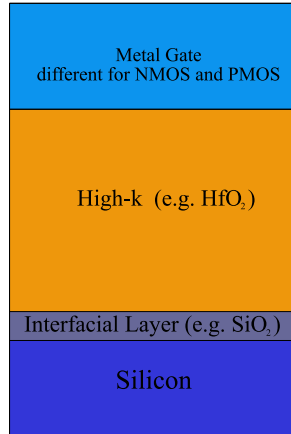


**Figure 2.1:** Scheme of a high-k gate stack. By exchanging the  $SiO_2$  gate-dielectric with  $HfO_2$  the critical oxide thickness of  $\approx 2$  nm for tunneling can be met while keeping control over the channel.

and the low power transistors. The I/O transistors feature an additional pre-patterned thermal oxide layer underneath the high-k layer to improve the stress tolerance related to high voltage. Furthermore, strained silicon technologies have been employed in the form of tensile contact strain, compressive metal gate fill for NMOS, embedded high  $Ge$   $SiGe$ , and reduced proximity raised source/drain. Overall, this architecture features logic transistors with extremely high drive currents and low leakage in a single chip.

Packan et al. [24] showed a high performance 32 nm logic technology featuring also 2<sup>nd</sup> generation high-k/metal gate and 4<sup>th</sup> generation strained silicon transistors. He reported a 28%/19% improvement in  $I_{dsat}$  and a 35%/20% enhancement in  $I_{dlin}$  over the 45 nm technology for PMOS/NMOS, respectively. The utilized replacement metal gate flow allows to place stress enhancement techniques before the poly gate is removed and has been shown to further increase strain. Furthermore, the variation of the employed 32 nm devices is equivalent to the previous 45 nm technology, which is an important criterion for the required minimum operating voltage for Static Random Access Memory (SRAM) and register file circuits. Good  $V_{ccmin}$  and the highest reported SRAM density for 32 nm or 28 nm technology were reported. Fully functional 32 nm processors exploiting this technology were demonstrated in January 2009 and are now in volume production.

Further scaling demands an even smaller EOT (32 nm  $\rightarrow$  8 Å and 22 nm  $\rightarrow$  6 Å). One possible solution to this problem is to switch from  $HfO_2$  with  $k_{HfO_2} \approx 25$  to oxides with higher dielectric constants. Frank et al. [25] studied two different metal gate/high-k gate stacks with gate first integration schemes. The first scheme employs a highly nitrated bottom interfacial layer Fig. 2.1 below the hafnium-based dielectric, thus increasing its overall dielectric constant, while the other scheme replaced the hafnium-based dielectric with “higher-k” titanium dioxide ( $k_{TiO_2} \approx 30 - 170$  depending on the crystal structure and orientation) and optional barrier layers to impede undesirable oxygen migration [26, 27, 28]. Good results for the  $Si_3N_4$  interfacial layer

were reported. Amazingly, no adverse effects like reduced mobility or a negative threshold voltage shift due to positive fixed charges were observed. Frank et al. found an EOT of  $\sim 6.2\text{\AA}$ , which is suitable for the 22nm technology node and renders highly nitrided bottom interlayers attractive for scaling hafnium-based gate stacks. The titanium dioxide approach experienced some difficulties in preventing the diffusion of oxygen from  $TiO_2$  to the high-k/channel interface. Some of the problems were growth of  $SiO_2$  and up-diffusion of oxygen to the poly- $Si/TiN$  interface, forming  $SiO_2$  and creating an additional path for degradation and disintegration. The down diffusion of oxygen can be decreased, but not suppressed, by a combination of  $HfO_2$  and  $Si_3N_4$  as bottom barrier layer. Furthermore an aluminum oxide bottom and top barriers are only insufficiently blocking oxygen migration [29]. Therefore, in order to allow further scaling more suitable barrier layers and/or metal electrodes which are less susceptible to oxygen in-diffusion are needed.

Another important parameter is the threshold voltage  $V_t$ . There are three ways to tune  $V_t$ : channel engineering, choosing the right metals (near band edge for high performance applications or slightly off band edge for low standby power applications), and using capping layers in the dielectric. Tseng et al. [30] studied the last method and showed the relevance of the interfacial layer. The threshold voltage is controlled via a dipole induced shift in the effective workfunction. The dipole is formed at the interface between the high-k oxide and the  $SiO_2$  interfacial layer [31, 32, 33]. Tseng et al. proposed that the  $V_t$  tuning is due to the net dipole moment of the  $Hf-O$  and  $RE-O$  (rare earth) bonds at the high-k/ $SiO_2$  interface. This is supported by the correlation between dopant electronegativity, ionic radius, and  $V_t$ .

While the above mentioned gate stacks are for use in a switching device in e.g. SRAM (volatile Random Access Memory (RAM)), there is also a huge demand for Non-Volatile Random Access Memory (NVRAM). The most common NVRAM type today is NAND flash memory. Over the last few years the Silicon-Oxide-Nitride-Oxide-Silicon (SONOS) gate stack attracted interest, as a possible candidate for flash devices. Therefore I will review both device types and compare them subsequently.

### 2.1.1 Flash Memory

Flash memory was invented by Dr. Fujio Masuoka [34] in 1980 at Toshiba. Flash memory can be divided into NOR- and NAND-based memory<sup>1</sup> [35]. NOR-based flash memory provides high read performance and enables full address and data bus access: Thus, it supports eXecution In Place (XIP), which allows applications to run directly from the flash memory instead of reading the program into the system RAM first. The disadvantages are extremely slow write-and-erase cycles and a bigger cell size compared to NAND-based flash memory, which makes it cost effective in low-capacity data storage which rarely needs to be updated, like in computer BIOS or the firmware of set-top boxes. NAND flash memory has about half the cell size of NOR flash memory and is an ideal solution for high-capacity data storage. It offers fast read and write performance, but lacks the easy memory access of NOR flash memory. Data must be read serially in blocks. Typically block sizes range from hundreds to thousands of bits. This feature disables the use of NAND flash memory as a drop-in replacement for program Read Only Memorys (ROMs), because most microcontrollers and microprocessors need byte-level access. Therefore, NAND flash memory is used in the category of other secondary storage devices like

---

<sup>1</sup>due to their operation as logic NAND and NOR

hard disks or optical media (e.g. CD, DVD). It is utilized as mass storage such as memory cards and USB flash drives. Due to the extremely high packing density it was possible to release a new generation of memory card formats exhibiting extremely small feature size. For instance, the microSD™ card has an area of about 1.5 cm<sup>2</sup>, with a thickness of less than 1 mm and offers presently up to 16 GB [36] of storage capacity at the same time.

### 2.1.1.1 Working Principle

Flash memory is made out of memory cells which are placed in an array. Every memory cell contains one floating gate transistor allowing to store at least one bit (Fig. 2.2). Single-Level Cells (SLCs), are able to store one bit of information, while Multi-Level Cells (MLCs) allow to store more than one bit per cell, by choosing between multiple levels of electrical charge in the floating gate of a cell.

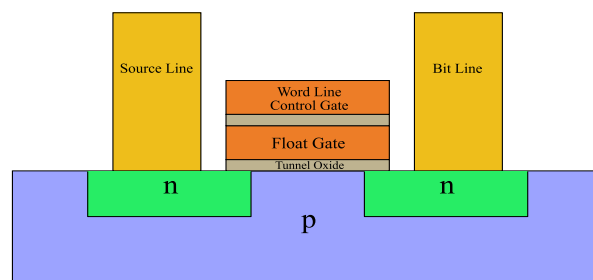


**Figure 2.2:** Basic scheme of a flash memory cell. Depending on the charge stored in the floating gate one bit SLC or multiple bits MLC can be saved.

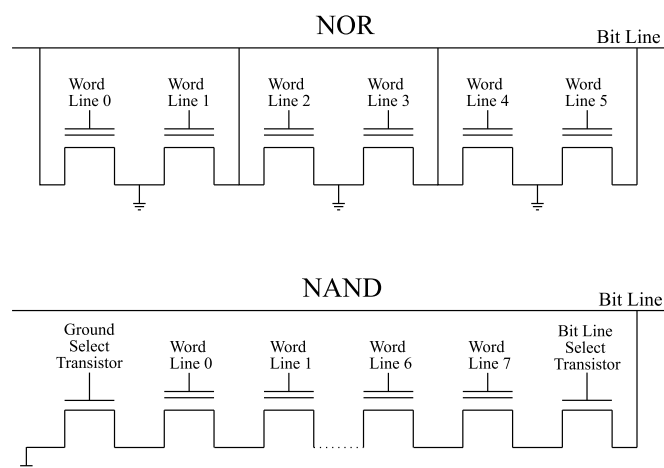


**Figure 2.3:** Schemes of the basic circuits for NAND and NOR flash memory devices.

### 2.1.1.2 NOR

In NOR gate flash memory each cell consists of a standard MOSFET with two gates instead of one. The top gate is the so called Control Gate (CG), which is used like a normal MOSFET gate. The second gate below is called Floating Gate (FG) Fig. 2.2. The FG is insulated by a surrounding oxide. Electrons in the FG are trapped and will retain in there for many years, if there is no manipulation from outside. A charge stored in the FG will (partially) screen the electric field from the CG. Thus the threshold voltage  $V_t$  of the cell is modified. During the read-out, a voltage, sufficiently low to preserve the amount of charge in the FG, but high enough to distinguish between a charged and uncharged FG is applied to the CG. Depending on the amount of charge in the FG the MOSFET will stay insulating or become conducting at the chosen CG voltage. The current through the channel is sensed as binary information and represents in combination with the other cells the stored data. In cells which are able to store more than one bit, instead of just sensing if there is current, the amount of current is mapped to a corresponding bit pattern.

This flash type is called "NOR flash", because it behaves like a NOR gate Fig. 2.3. If one of the word lines is brought high, the related floating gate transistor pulls the output bit line low. SLC NOR flash cells are in their default state logically equivalent to binary "1", because by applying a moderate voltage to the control gate current will flow.

The following steps are needed to write or program a NOR flash cell to "0":

- applying an elevated voltage to control gate (typically above 5 V)
- assuming an NMOS transistor, the channel is now turned on so electrons can flow from the source to the drain
- if the source to drain current is sufficiently high, there will be some high energy electrons able to jump from the channel through the insulating layer into the floating gate. This process is called hot-electron injection.
- now there is charge trapped in the floating gate and thus the threshold voltage  $V_t$  is shifted due to the partial cancelation of the electric field from the control gate.

Erasing a NOR flash cell, setting it to logically "1", works as follows:

- a large voltage of the opposite polarity is applied between gate and source
- the generated large electrical field pulls the electrons out of the floating gate via quantum-mechanical tunneling.

Up-to-date NOR flash chips split their memory into erase segments (also known as blocks or sectors). Erasing can only be performed on a block-wise basis, while the write procedure can be performed on a single byte or word at a time basis.

### 2.1.1.3 NAND

In a NAND flash memory the transistors are connected in series (Fig. 2.3). Only if all word lines are pulled high (above the transistors  $V_t$ ), the bit line is pulled low. This resembles a NAND

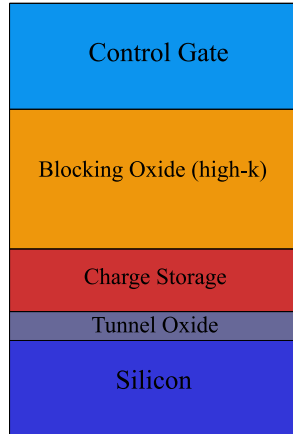


**Figure 2.4:** Scheme of a SONOS gate stack.

gate. These groups are connected via some additional transistors to a NOR-style bit line array. For reading, all word lines except the one to read, are set to a voltage above  $V_t$  of a programmed bit, while the bit line for reading is set just over the  $V_t$  of an erased bit. The series group will conduct only (and pull the bit line low), if the selected bit has not been programmed. Regardless of the additional transistors, NAND flash allows a denser layout, due to the reduced bit lines and ground wires. Additionally, NAND flash is usually allowed to exhibit a certain number of faults, while NOR flash is expected to be fault free (e.g. for use in a BIOS ROM).

NAND flash writing operates with tunnel injection and tunnel release for erasing.

### 2.1.2 Comparison Between Floating Gate and SONOS

While flash memory cells store their charge in a polysilicon layer sandwiched between two oxide layers (ONO), SONOS devices store the charge in a non-conductive nitride layer with a high density of deep charge trapping sites, which are able to hold an electrostatic charge (Fig. 2.4). In theory this approach has several advantages. The gate stack is thinner (up to  $\sim 50\%$ ), because the floating gate polysilicon must be fairly thick to provide an acceptable coupling ratio between the floating gate and the control gate, which does not apply to SONOS gate stacks. Thus, step coverage is alleviated and the number of necessary masks and processing steps can be reduced in comparison to floating gate cells. Another limiting factor for floating gate cells is the height of the ONO gate stack (reduction of the tunnel oxide leads to an increased leakage from the polysilicon). The estimated scaling limit for floating gate cells is at the 30 nm technology node, due to electrical interference between adjacent cells, caused by the electric field of the electrons stored in the polysilicon layer [37].

SONOS gate stacks offer a higher quality charge storage due to the smooth homogeneity of the nitride film compared to the polycrystalline film of floating gate stacks and are less prone to oxide defects. Because of the insulating nature of the nitride film, an occurring leakage path is locally

confined and only able to empty a few traps. Therefore, Stress Induced Leakage Current (SILC) should not be a big issue, (i.e. the generation of traps within the oxide’s band gap, enabling trap-assisted tunneling and leading to a discharge of the floating gate. [38]). In comparison to floating gate technology, SONOS is not susceptible to drain turn-on and floating gate interference and also insensitive to SILC, when the bottom oxide layer is thinner than in the floating gate technology, thus, enabling faster programming and lower write/erase voltages. However, there are also disadvantages: The trap related reliability issues are not fully understood and there is an erase saturation which can lead to a permanent logic ”1“ state, rendering the cell useless.

### 2.1.3 Scaling of Floating Gate and SONOS

In the present floating gate technology node, the control gate wraps around the floating gate, which serves as the necessary electrical coupling for the operation of the device. Applying an external voltage at the CG induces a voltage drop between the tunnel dielectric and the *Si* substrate. Depending on the amount of the applied voltage, the charge stored in the FG can be sensed (read out) or electrons can tunnel through the dielectric (program/erase) at higher voltages.

Further scaling of the feature size will lead to a modification of the device structure due to the lack of physical space between neighboring cells. This will cause a planarization of the device and a degradation of the coupling factor. To compensate the loss of the coupling capacitance of the sidewalls two approaches are considered. Firstly, by exchanging the Inter Poly Dielectric (IPD) with a high-k material the gate coupling factor is increased and secondly, by replacing the flash ONO gate stack by a SONOS charge trapping gate stack, facilitates a thinner gate stack. For charge trapping devices also high-k materials are needed as Blocking Oxides (BOs) between the trap layer and the control gate (Fig. 2.4). Both applications require high-k materials with large band gaps and band offsets, limiting the materials to choose and restricting the k-values in the moderate range from  $\sim 9$  to 20 [39]. Due to the charge retention specifications for flash-based memory ( $\sim 15$  years) very low leakage through IPD or the BO is needed. Therefore, the trap density of the high-k dielectric should be as low as possible.

$Al_2O_3$  with ( $k \sim 9$ ) is a possible candidate for replacing *SiO<sub>2</sub>* as IPD and BO in the near future. A substantial improvement in device characteristics for crystalline  $Al_2O_3$  compared to amorphous  $Al_2O_3$  has been reported [40]. At  $\sim 850^\circ C$   $Al_2O_3$  crystallizes into the  $\gamma-Al_2O_3$  phase, increasing its band gap and band offsets, and localizing its defects in a horizontal band between 1.7 eV and 2.0 eV. However, the properties of the  $Al_2O_3$  films (crystallization, texture, and microstructure) have been found to depend strongly on the deposition technique and parameters.

While for the next technology node  $Al_2O_3$  with a *TiN* metal control gate may be sufficient, future generations demand higher even  $k$ -values. Therefore, several dielectrics with higher  $k$ -values (12 – 30) are under investigation. The improvement in  $k$ -values must not be at the expense of a reduced band gap or increased trap density. Promising candidates are aluminates and scandates. For instance, the rare earth scandates *DyScO* and *GdScO* feature higher  $k$ -values compared to *Sc<sub>2</sub>O<sub>3</sub>*, while maintaining at the same time the band gap (6 eV) and band offset ( $\sim 2$  eV with respect to *Si*) over a wide range of compositions. Aluminates such as *HfAlO* and rare earth aluminates *REAlO* (e.g. *LaAlO*) inherit a band gap of  $\sim 6$  eV for their amorphous phase, and are close to amorphous  $Al_2O_3$  for a wide compositional range, but exhibit a lower than crystalline  $Al_2O_3$ . Also their band offsets remain independent over a wide

compositional range and stay close to amorphous  $Al_2O_3$ . Additionally, the permittivities of amorphous  $HfAlO$  and  $LaAlO$  vary approximately linearly with composition ( $\sim 14$  for  $LaAlO$ , and  $\sim 16$  for  $HfAlO$  at an 1 : 1 ratio) [39].

However, also for floating gate devices the interfacial properties are of great importance. Govoreanu et al. [41] investigated various top gate materials ( $TiN$ ,  $TaN$ , and  $n^+$ -poly- $Si$ ) and different processing procedures and found for the used  $SiO_2$ - $HfAlO$  IPD (1 nm and 12 nm respectively) the  $SiO_2$  layer as a limiting element for the achievable program window, due to shallow traps and their interaction with the  $HfAlO$  as parasitic Variable Oxide Thickness (VARIOT) gate stack.

Potentially better suited to build ultra-scaled devices are approaches like storing the information in a silicon nanocrystal layer instead of a nitride layer [42, 43]. Silicon nanocrystal memories show no erase saturation for small tunnel oxide thickness, deeper electron storage traps ( $\sim 3$  eV), extra local field effects as well as Coulomb blockade (essential to superior Fowler-Nordheim erase characteristics compared to SONOS). The device variability due to the variation of crystal size and distance is not critical due to partial selfordering [44]. Ohba [45] demonstrated a 10 nm bulk-planar SONOS type memory with a double tunnel junction, exhibiting good scalability while offering low write/erase voltages and excellent charge retention characteristics at the same time. There are additionally FinFET architectures in SONOS and nanocrystal devices, indicating a promising path way [46], and investigations for quantum dot materials different to silicon [47].

## 2.2 Strained Interfaces

The end of scaling has often been predicted [48], but until now, always been proven wrong. For instance, end of scaling at  $\sim 400$  nm due to the limit of spatial resolution by lithography [49, 50] and at 3 nm oxide thickness as a result of increasing gate leakage current [51, 52] has been predicted, but by brilliant engineers circumvented. Presently the physical scaling of the  $Si$  gate oxide thickness has been halted [48] and the improvement through material properties became state of the art. As a result of the higher vertical fields (constant voltage scaling), in down scaled MOSFET devices, the mobility tends to lower values. Hence, at the 90 nm technology node strain techniques have been introduced [53, 54].

First investigations of strain on the intrinsic mobility took place in the 1950's [55, 56]. In the 1990's the concept of enhancing mobility with strain gained interest again [57]. Welser et al. [58, 59] found a 70% higher effective mobility  $\mu_{\text{eff}}$  compared to the value in unstrained substrate's. In the following years many different technologies to introduce strain into the channel of a MOSFET have been developed.

Strain techniques can be classified into two main categories. There are *global* strain techniques, where strain is introduced across the entire substrate, and *local* strain techniques, which insert strain locally at certain places. An overview of widespread strain technologies is depicted in Fig. 2.5. In the following chapter several common strain technologies are reviewed.

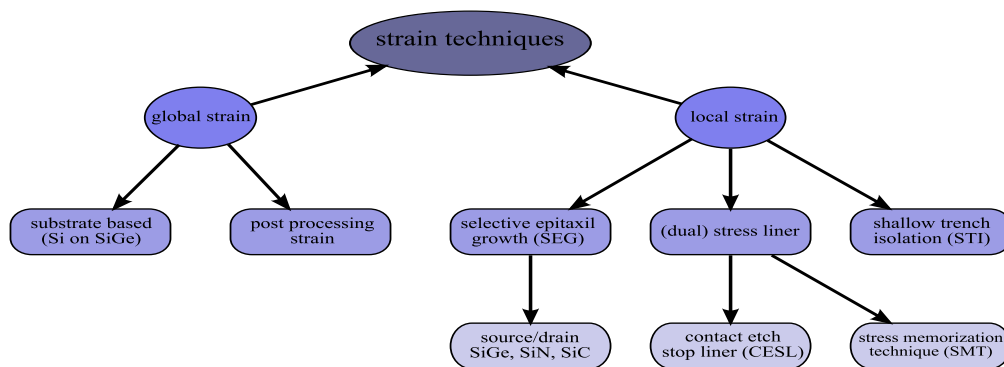
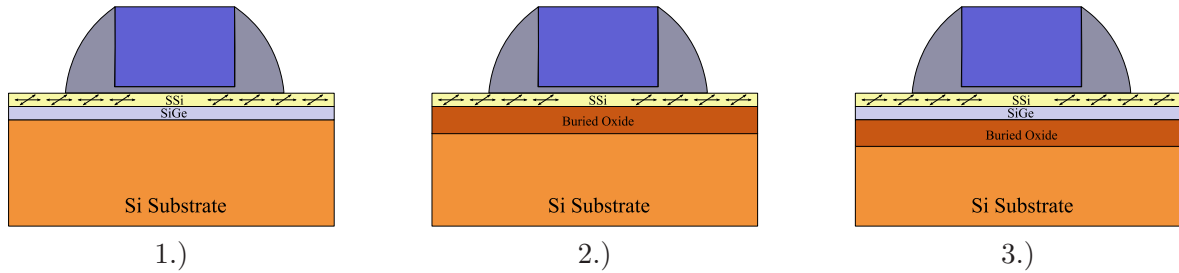


Figure 2.5: Overview of common strain techniques.

### 2.2.1 Global Strain

Mechanically compressing and/or stretching of the  $Si$  crystal lattice introduces strain and can be realized by various means (c.f. Fig. 2.6). In the beginning research was concentrated on biaxial global strain accomplished by a thin epitaxially grown  $Si$  layer on a relaxed  $SiGe$  virtual substrate [58, 59]. Due to the lattice mismatch between  $Si$  and  $SiGe$ , the  $Si$  lattice is biaxially



**Figure 2.6:** Scheme for different global strain techniques: 1.) strained silicon layer on *SiGe* on bulk wafer; 2.) strained silicon layer directly on insulator (SDGOI); 3.) strained silicon layer on *SiGe* substrate on insulator (SSGOI).

tensile strained along the interface plane. For instance, Rim et al. [53] showed a mobility enhancement of 110% for electrons and 45% for holes in the strained silicon layer for {001} oriented substrates on < 100 nm strained *Si* MOSFETs.

Layer transfer and wafer bonding techniques allow integration of global strain on SOI substrates. Comparable to wafers without insulating layer electron and hole mobility enhancement has been demonstrated for ultra-thin Strained silicon layer on Silicon-Germanium On Insulator (SSGOI) [60, 61, 62, 63] and Strained Silicon layer Directly On Insulator (SSDOI) [64, 65].

Ultra thin SSGOI is of special interest, due to the removal of the *SiGe* layer before transistor fabrication. Thus, process-integration problems caused by the *SiGe* layer can be overcome. Some of these problems are:

- Ge up-diffusion from the *SiGe* layer reduces the thermal budget window for *SiGe* on insulator [60].
- A high density of defects is inserted into the neighboring Si layer by *SiGe* strain relaxation [57].
- *SiGe* exhibits an enhanced dopant diffusion rate (e.g. B, As) [66].
- SSGOI devices possess lower thermal conductivity, induced by the *SiGe* layer, and therefore suffer significant device self-heating [67].

Alternatively, the strain can be introduced after the wafer has completely been processed [68, 69]. This is realized by thinning the wafer to less than 10  $\mu\text{m}$  and transferring it to a polymere film. After this, mechanically straining the Si membrane allows uniaxial and biaxial strain parallel to the substrate surface without inducing defects, e.g. interstitials or vacancies, in the Si layer. The mechanically strained wafer can be bonded to a final substrate safely, as long as the strain level stays within the elastic limit. At ultra-low strain levels ( $\sim 0.052\%$ ), mobility  $\mu_{\text{eff}}$  improvement of 18.4% and in saturation current of 18.05% was found for n-channel MOSFETs, and 14.35% (14.56% at saturation current) for p-channel MOSFETs (at 0.031%) [68]. Despite its cost effectiveness there are also yield and reliability issues which hinder the full-scale IC manufacturing application [70].

The major disadvantage of global strain techniques is that they facilitate only one type of strain. Due to the fact that the effective mobility  $\mu_{\text{eff}}$  behaves differently for electrons and holes at compressive/tensile strain only one of the mobilities can benefit, while the other is degraded (e.g. compressive biaxial strain can raise the mobility for p-channel MOSFETS, while degrading the mobility of n-channel MOSFETs). This obstacle can be circumvented by local strain techniques which enable different strain types for n-channel and p-channel MOSFETs.

### 2.2.2 Local Strain

There are manifold processes that can be utilized to generate strain in the transistor channel (Fig. 2.5). The subsequently described techniques induce strain in the MOSFET channel locally and therefore are often addressed as *local* strain techniques.

Beginning in the late 1990's the influence of local stress induced by various process steps on the MOSFET performance was studied. The following process steps were identified to introduce stress into the transistor channel:

- Shallow Trench Isolation (STI) [71, 72]
- silicidation at the source/drain region [73]
- nitride Contact Etch Stop Liner (CESL) [74, 75]

In spite of initially lower strain levels compared to global strain techniques, local strain techniques feature three main advantages:

- strain can be individually customized to the needs of n-channel and p-channel MOSFETs at the same time
- local stress techniques are compatible and cheaper with standard CMOS technology [76]
- the threshold voltage shift is smaller in uniaxially stressed MOSFETs [77]

A key issue is the optimization of process modules towards maximization of beneficial effects from stressors while minimizing negative side effects. A downside of process-induced strain techniques is their less predictable behavior at scaling due to their strong device geometry dependence [78].

The following chapters are devoted to four relevant stress-transfer techniques: CESL, Stress Memorization Technique (SMT), Selective Epitaxial Growth (SEG) of source and drain regions (SEG), and STI.

#### 2.2.2.1 Contact Etch Stop Liner - Gate Stacks

The contact etch stop liner technique (CESL) is realized after wafer silicidation by uniformly depositing a highly stressed liner on top of the gate stack. Dependent on the thickness and material properties of the liner different stress conditions are realized [74]. Yang et al. [79] showed an 11 % enhancement of the saturated drive current of n-channel and 20 % for p-channel

MOSFETs. Applying one single liner limits to one type of stress for n-channel and p-channel MOSFETs. Accordingly, only the mobility of one transistor type is enhanced, while the other eventually is deteriorated, similar to global strain techniques. As a consequence, two types of stress liners have to be introduced, in order to improve the performance of n-channel and p-channel MOSFETs. This is implemented by a Dual Stress Liner (DSL) process with a highly tensile nitride deposited on top of the n-channel MOSFET gate stack, while a highly compressive nitride is deposited on top of the p-channel MOSFETs gate stack [79, 80].

More than 2.0 GPa tensile and 2.5 GPa compressive stress have been shown for  $Si_3N_4$  layers. This correlates to a stress level of more than 1 GPa in the MOSFET channel [81] and competes in magnitude with the stress induced by selective epitaxial growth (2.2.2.3).

### 2.2.2.2 Stress Memorization Gate Stack

For this technique, first a tensile stressor capping layer is deposited and then a spike anneal for dopant activation is performed [76, 82, 83, 84]. Regardless of removing the stressor nitride layer before the silicide process, the stress is transferred from the nitride to the channel during annealing. The stress memorization takes place via re-crystallization of source, drain, and the poly gate amorphized layer. Up to 15% on-current enhancement for n-channel MOSFETs is achieved by this technique [85].

### 2.2.2.3 Selective Epitaxial Growth

Selective growth of a local epitaxial film in the source and drain regions of a transistor is able to introduce uniaxial strain in the channel. Arising from the mismatch in lattice constants between source/drain regions and the channel region, one is able to generate large uniaxial stress. This is accomplished by etching the source and drain regions and forming recess areas. Then, these pockets are filled with epitaxy.

However, it is also possible to grow the epitaxial film directly on top of source and drain without etching these regions in advance [86]. Depending on the lattice constant mismatch and epitaxial layer thickness the induced stress varies. For instance, in order to create uniaxial compressive stress in p-channel MOSFETs epitaxially grown  $SiGe$  is used [78, 87, 88], while tensile stress in n-channel MOSFETs can be achieved via  $Si_{1-x}C_x$  stressors with a molefraction of  $\sim 1\%$  [89]. Chui et al. [90] showed a drive-current improvement of up to 50% at a gate length of 50 nm for n-channel MOSFETs with  $Si_{0.987}C_{0.013}$  incorporated in the source and drain regions.

### 2.2.2.4 Shallow Trench Isolation

Mechanical stress induced from Shallow Trench Isolation (STI) can not be neglected in the sub-micron regime at small active areas [91]. STI is able to generate large stress parallel to the channel (lateral) and in the direction along the width of the transistor (transversal). Reducing the transistor width boosts the compressive stress in the channel by the shallow trench effect and has been found to enlarge the hole mobility [92].

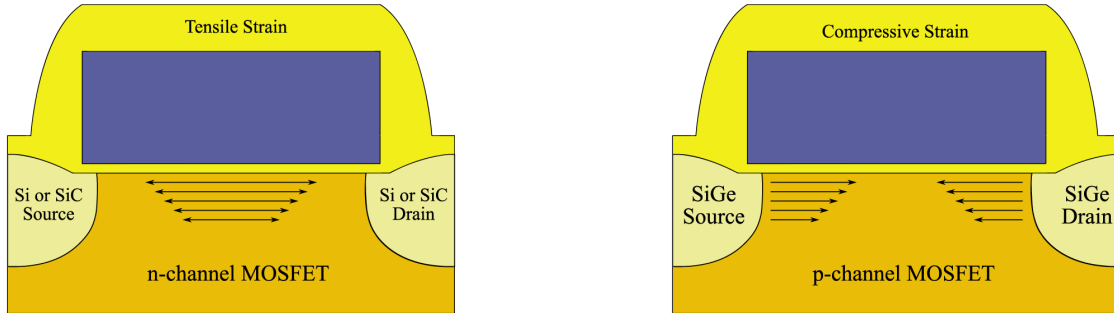


**Figure 2.7:** Combining selective epitaxial growth in source and drain regions and a stress liner to introduce tensile uniaxial stress for n-channel MOSFETs and compressive uniaxial stress for p-channel MOSFETs.

### 2.2.2.5 Strain Technologies in High Volume Production

The local strain approach proved to be more appropriate for industrial exploit. Therefore, the first strain technologies in high volume production evolved on the basis of uniaxial process-induced strain. Intel [87], IBM [88], Freescale [93], and Texas Instruments [86], integrate selective epitaxially growth techniques at their 90 nm technology node.

Stress levels in the range from 500 – 900 MPa are achieved, depending on the Ge content of the *SiGe* compound and the distance to the channel [94], enabling a saturation drain current increase up to 20% – 25% for p-channel MOSFETs [87,93] and up to 10% for tensile uniaxially stressed n-channel MOSFETs [87]. AMD and IBM developed in a joined effort a less complex technique [79]. Together with epitaxial films in the source and drain regions tensile and compressive capping layers on top of the transistors are used as local stressors [95,80].

$Si_3N_4$  is able to exhibit compressive or tensile strain depending on the deposition conditions. First, a highly tensile Si nitride layer is deposited via thermal Chemical Vapor Deposition (CVD) over the whole wafer. Afterwards the layer is etched away selectively for the p-MOS active areas. Then, a compressive  $Si_3N_4$  layer is deposited via plasma assisted CVD. Afterwards the compressive nitride layer is etched away at the n-channel MOSFET active areas, yielding n-channel transistors under tensile and p-channel transistors under compressive uniaxial strain. Drive current enhancements of 11%/20% for n/p-channel MOSFETs have been shown for this dual stress liner technique [79]. Today, strain techniques are mandatory to sustain the pace in scaling. Joining two or more strain techniques in one device (Fig. 2.7) is a logical consequence when increasing strain levels even further. For instance, n-channel MOSFEETs uniaxial tensile strained via cap films and p-channel MOSFETs with selective epitaxially grown films, providing compressive stress, have been demonstrated by [96]. Horstmann et al. [84] showed a nice example of how to combine different strain techniques on SOI CMOS. They demonstrated an optimized stress integration scheme, combining an embedded *SiGe* process and a compressively stressed liner film for p-channel MOSFETs, while a stress memorization process and a tensile stressed liner film are used for n-channel MOSFETs. After optimization, p/n-channel saturation drive current enhancements of 53%/32% were obtained, demonstrating the process compatibility and strain additvness of the manufacturing approach.

## 2.3 Ferroelectric Gate Stacks

Ferroelectric materials are vital for a huge field of applications. In form of thin-films, ferroelectrics, or in a more general sense polar materials, have been exploited in RF devices, non-volatile memories, various sensors and actuators, and for tunable microwave devices [97]. The development of ferroelectric films dates back to the late 1960s and early 1970s triggered by progress in integrated silicon devices and thin film processing techniques raising interest in ferroelectric thin films for non-volatile memories [98, 99, 100].

### 2.3.1 Ferroelectric Materials

Ferroelectricity is the effect of spontaneous electric polarization of a material, which can be reversed by application of an electric field [101, 102]. The term ferroelectric has been chosen in analogy to the permanent magnetic moment exhibited by ferroelectric materials. Valasek [103, 104] discovered the first ferroelectric material, namely Rochelle salt, in 1920. At this time ferromagnetism was already known and therefore the prefix iron relates to ferromagnetism and not to actually iron, thus resolving the contradiction caused by the missing iron atoms in most ferroelectric lattices. Unfortunately, the industrial exploitation is rather limited, since Rochelle salt is only ferroelectric for a certain composition and slight variations already lead to a loss of ferroelectricity. Therefore, for several decades it remained as an interesting physical effect, until 1945, when ferroelectric behavior was found for BaTiO<sub>3</sub> [102].

BaTiO<sub>3</sub> material belongs to the stable perovskite type, which represents one of the fundamental crystal lattice structures. This discovery initiated investigations of perovskite type materials. Soon other perovskites with ferroelectric properties were discovered, thus opening the path to industrial application. Perovskites are still the most important ferroelectric materials.

Initially Lead Zirconate Titanate (PZT) was the material of choice for Ferroelectric Random Access Memory (FRAM) applications. The properties of PZT depend strongly on the composition of the alloy. Currently *Ti/Zr* ratios of 60/40 and 70/30 are employed, offering clearly defined switching and high switchable polarization.

Strontium Bismuth Tantalate (SBT) (*SrBi<sub>2</sub>Ta<sub>2</sub>O<sub>9</sub>*) is another ferroelectric material of layered perovskite type. It possesses a smaller remanent and switchable polarization compared to PZT, but does not show polarization fatigue like PZT due to repeated switching with platinum electrodes. Furthermore, it exhibits two more processing disadvantages: due to the biaxial nature of the polarization vector the occurring crystal growth direction can lead to ferroelectric films with unwanted switching directions regarding to the externally applied field. The processing temperatures for high quality SBT films are higher (100 – 250°C) than for PZT.

While for the polarization fatigue feasible solutions exist [105], the time and temperature depend development of preferred polarization orientations, also known as *imprint*, concerns all of the thin film ferroelectric materials [106, 107, 108].

Park et al. [109] presented an alternative material based on Bi<sub>4</sub>Ti<sub>3</sub>O<sub>12</sub> in 1999. They substituted lanthanum and neodymium into the *A* site of bismuth titanate, resulting in materials known as Bismuth Lanthanum Titanate (BLT) and Bismuth Neodymium Titanate (BNT). These materials exhibit larger remanent polarization and lower processing temperatures compared to SBT

in conjunction with an increased coercive field.

Commonly ferroelectric materials are integrated as polycrystalline films, but also ferroelectrics epitaxially grown on silicon show good results [110].

### 2.3.2 Applications

Due to the dedication of this work to gate stacks for field-effect transistors, I will concentrate on the applications of ferroelectric gate stacks for non-volatile RAM applications. There are several design concepts taking advantage of these materials. The initially developed FRAM exhibits a similar design concept as Dynamic Random Access Memory (DRAM), and therefore is exploited as an analogy to a capacitor and not as a gate stack material. The Ferroelectric Field-Effect Transistor (FeFET) utilizes the polarization of the ferroelectric material within the gate stack.

#### 2.3.2.1 Ferroelectric Thin-Films in FRAM

Non-volatile FRAM is based on the polarization reversal by an externally applied electric field of metal-ferroelectric-metal capacitors [111, 112]. The logic states of 1 and 0 are mapped to the positive and negative remanent polarization state, respectively. The destructive readout procedure is realized by the displacement current. FRAM is appealing due to its write and read cycle times in the sub-100 ns regime and low power consumption, in comparison to other non-volatile memory technologies. Ferroelectric memory integrated in silicon CMOS was shown in 1987. The chip contained only 256 bits, and each bit contained two PZT capacitors forming a non-volatile shadow RAM. Although the cell size was large and the density low, it initiated further higher density test chips and ferroelectric random access memory products [113, 114]. Despite the quite successful demonstration of ferroelectric memories utilizing PZT, difficulties to reach read/write cycles above  $10^{12}$  started the investigation of other ferroelectric thin-film materials [115]. Relevant alternative materials are  $SrBi_2Ta_2O_9$  (SBT) [116],  $(BiLa)_4Ti_3O_{12}$  [117],  $BaMgF_4$ ,  $Bi_4Ti_3O_{12}$  [118], and  $Pb_5Ge_3O_{11}$  [119]. The target of these investigations was to find a ferroelectric material exhibiting little or no degradation of the switchable ferroelectric polarization caused by typical read and write operations. Among the alternative ferroelectric materials, *Bi*-based compounds showed the biggest improvement in read-write cycle endurance, but only SBT has reached the market in FRAM products [120].

Another approach in order to increase the read-write endurance is to utilize Non-Destructive Readout (NDRO) for the ferroelectric capacitor polarization state [118]. Since many memory applications demand more read than write operations, a NDRO will reduce the wear of the ferroelectric capacitor. Unfortunately, all proposed NDRO ferroelectric memories seem to exhibit a common data disturb problem raised by partial back switching of the remanent polarization state during the each read cycle, resulting in a long term degradation of the read signal margin (loss of data state retention) [121].

Since the advent of FRAM, efforts on PZT capacitor process development and Destructive Readout (DRO) design for reliability yielded FRAM products with almost unlimited read-write endurance ( $> 10^{15}$ ) and 10 years of data retention for industrial temperature range specifications of  $-40$  to  $85^\circ C$  [122, 123]. Several commercial FRAM devices feature a Two Transistors Two Capacitors (2T2C) cell with  $0.5 \mu m$  minimum Complementary Metal Oxide Semiconductor

(CMOS) gate length [124]. The ferroelectric capacitors of these devices are built on top of a field oxide in a way that the accompanying transistors are neighboring and each component of the cell exhibits a uniquely defined area. This so called Capacitor Over Field Oxide (COFO) architecture requires a relatively large cell size ( $60 F^2$ ,  $F$  denotes the metal half-pitch) for the employed 2T2C devices. In order to increase the memory density also significantly smaller cell sizes ( $33 F^2$ ) incorporating One Transistor One Capacitor (1T1C) designs have been developed [125]. Applications for these FRAM devices span from electrical power meters, printer configuration memories, and data loggers to video games and toy watches. Due to the success of FRAM mass production at  $0.5 \mu\text{m}$  and  $0.35 \mu\text{m}$  and the appealing application for various stand-alone and embedded applications, several companies have strengthened their efforts on continued scaling for FRAM to benefit from higher capacity and higher density [126, 127, 128, 129, 130]. Further scaling efforts led to a change in the FRAM cell design, reducing the cell size to  $18 F^2$ . This is realized by building the ferroelectric capacitor on top of a plug that connects it to the underlying access transistor. The Capacitor On Plug (COP) architecture has been demonstrated for 4 and 64 Mbyte memories [131, 132].

### 2.3.2.2 Ferroelectric Field-Effect Transistors (FeFETs)

Despite the successful application of FRAM in commercial products, the need for ever increasing packing densities, due to scaling, demands more space efficient designs. A FeFET represents a 1T cell and consists of a Metal Oxide Semiconductor Field-Effect Transistor (MOSFET) whose gate dielectric has been replaced by a ferroelectric. Additionally to the smaller cell size, the read operation is non-destructive. Unfortunately, these devices exhibit only short retention times as non-volatile memory [133, 134, 135]. The concept of the FeFET was presented by Ross in the form of a patent [136]. Despite the huge research efforts on FeFETs including diverse material combinations and layouts, FeFETs were not able to reach maturity for a commercial product. Nevertheless, the brilliant concept of the FeFET is still quite appealing and its advantages and disadvantages will be discussed in the sequel.

At first, one has to note that the CMOS integration issues for a FeFET are a bit different to the FRAM case. A FRAM capacitor is about 100 nm or more afar from the MOSFET, so both devices are physically independent. For an ideal FeFET, the ferroelectric is in direct contact with the drain to source channel of the transistor (see Fig. 2.8(a)). Therefore, the ferroelectric is an active part of the transistor and the performance is hugely affected by its interface properties. This is also one of the most serious problems for FeFETs. The localized states and impurities at the interface strongly influence the transistor properties like threshold voltage, saturation voltage, and the C-V curve of the gate stack. Another potential problem of FeFETs is the inter-diffusion between the ferroelectric and the *Si*. This is analog to the interface problems for native *SiO<sub>2</sub>* and high-k dielectrics in high performance MOSFETs (q.v. Section 2.1). The basic challenges for FeFETs are found in the enhancement of the retention time and the suppression of parasitic effects like the charge traps at the *Si*-ferroelectric interface.

A possible solution in order to circumvent the problematic interface is to employ an insulating buffer layer between the *Si* and the ferroelectric as shown in Fig. 2.8(b) resulting in a Metal Ferroelectric Insulator Semiconductor (MFIS) structure [135, 134]. Various buffer layers such as *SiO<sub>2</sub>*, *CeO<sub>x</sub>*, and *Si<sub>3</sub>N<sub>4</sub>* have been studied. *HfO<sub>2</sub>* and *HfAlO* show auspicious results. For a gate stack built from *Pt/SBT/HfO<sub>2</sub>/Si* layers a retention time of 30 days has been

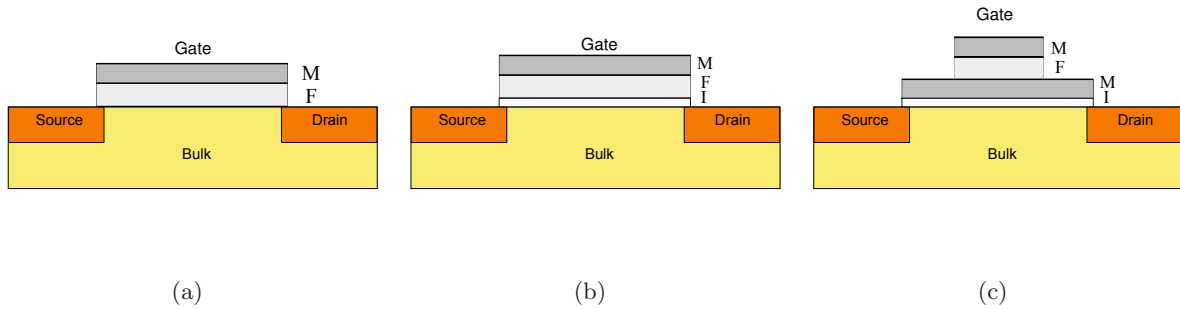


**Figure 2.8:** Schematic views for the different FeFET designs.

shown [135, 137].

Additionally to a low density of interface states the band offset between silicon and the ferroelectric or the buffer must be large enough to impede electron injection during programming. For instance, despite the quasi perfect growth of the high- $k$   $SrTiO_3$  on  $Si$  by Molecular Beam Epitaxy (MBE), the small band offset of  $SrTiO_3$  on  $Si$  causes strong current injection and a compensation of the ferroelectric boundary charge by electrons [138, 139, 140]. Also more complex gate stacks have been studied such as the Metal Ferroelectric Metal Insulator Semiconductor (MF MIS) gate structure (as depicted in Fig. 2.8(c)) [133, 135]. The benefit of these gate stacks lies in the already available optimized metal-ferroelectric-metal process from FRAMs. Furthermore, it is possible to match the charge between the ferroelectric and the buffer layer by adjusting the area ratio. A smaller area of the MFM structure in comparison to the IS structure below results in a lower field strength in the buffer. The maximum charge density of  $SiO_2$  is  $3.5 \mu C/cm^2$  and relates to an electric field of 10 MV/cm, which is pretty close to the breakdown field of  $SiO_2$ . Typical complex oxide ferroelectrics possess more than ten times higher polarization densities. Therefore, often subloops are utilized to avoid electrical breakdown of the buffer [135].

Ferroelectricity is not restricted to complex oxides and can be found in several material classes. For instance, Polyvinylidene Fluoride (PVDF) copolymers possess ferroelectric properties [141]. The incorporation of ferroelectric polymers as gate oxides is an interesting approach. It has the advantage of negligible inter-diffusion due to its processing at room temperature and the probably superfluous buffer layer. Successful research has been carried out on  $Si$  substrates [142, 143, 144] as well as on entire field-effect transistors [145, 146, 147]. This opens up the prospect of cheap and flexible non-volatile memory. One has to note that the experienced switching times are significantly lower than those for oxide FRAMs, and thus the field of application will be different.

## 2.4 Electrolytic Interfaces

A typical workflow for detecting a certain Deoxyribonucleic Acid (DNA) complex is like this: At first the concentration of the DNA sample has to be increased either by Reverse TRanscription (RT) or Polymerase Chain Reaction (PCR). Then there would be a step to mark the DNA with a so called label, enabling the detection of the DNA via radiation or light, followed by applying the sample to a microarray. Microarraies contain an array of spots. Every single spot exhibits a different chemical reaction and is therefore able to detect a different type of molecule. After the reaction took place the array is read by an expensive microarray reader.

State of the art technologies to detect pathogens, antigen-antibody complexes, and tumor markers are timeconsuming, complex and expensive [148, 149].

Thus, the field-effect transistor comes into play. By replacing the optical sensing mechanism with an electrical signal detection several benefits arise. Firstly, the expensive readout device becomes superfluous. Additionally, using field-effect transistors allows to integrate analyzing and amplifying circuits on the same chip, enabling a further cost reduction due to cheaper equipment. The exceptional development of semiconductor process industry enables mass production of such devices in conjunction with reducing the price per device dramatically. Reams of reaction pairs are attainable and studied: for instance, detecting DNA [17, 150, 151], cancer markers [152], proteins like biotin-streptavidin [153, 154, 155, 156], albumin [157], and transferrin [158]. These papers show the diversity of device types and materials which where investigated. Even though much promising research has been carried out about BioFETs, they are still in their commencement and many unresolved questions remain.

The BioFET concept is extremely powerful. Literally, every molecule which exhibits a charge within the solute and can be bound to the surface layer of a BioFET can be detected. The devices become smaller, cheaper, and easier to use, so it could enable a family doctor to screen for diseases on his own and decide faster which treatment is the best for a patient, choosing the medication that offers the best results depending on the patients genetic profile. This is one aspect of the so called Point Of Care (POC) applications, which aim to offer help right there where it is needed without much effort. A typically POC application, which is commonly used today, is the blood sugar measurement. The devices are affordable, small, easy to use, and can be applied by the patient. A tiny drop of blood is enough to check the blood sugar level and enables the patient to decide how to proceed. There is also the vision to control the spread of diseases within a population or monitor environmental pollution with such devices.

The effort to integrate a BioFET into a chip environment is not very high. Either by isolating the surrounding areas by a thick oxide or polymere or by putting a microfluidic channel above the functionalized gate of the BioFET the chip can be turned into a mini-laboratory also known as Lab On Chip (LOC). This concept improves the control over environmental parameters like local pH or detecting the amount of a special protein, and it facilitates local measurements (e.g. how a cell reacts to stimulus), thus offering a complete LOC. However, there are still many obstacles to circumvent and a lot more of research is needed.

Park et al. [159] presented a CMOS compatible albumin FET-type sensor for diagnosing nephritis. Nephritis is the inflammation of a kidney and caused by an infection or an autoimmune process. Due to the infection the microscopic filters in a kidney are damaged or closed. This leads to an extraction of important proteins from the blood. Therefore, the characteristic symp-

toms of a nephritis are called proteinuria. Albumin was identified as a potential candidate to diagnose nephritis. The regular device represents a differential setup and consists of a BioFET able to detect albumin and a reference transistor measuring the background noise. The channel region measured  $100\ \mu\text{m}$  in length and  $20\ \mu\text{m}$  in width. In human urine an albumin concentration of  $< 10\ \text{mg/l}$  is considered as normal, while a concentration above  $30\ \text{mg/l}$  in urine is an indicator of nephritis. The device shows a linear response from  $30\ \text{mg/l}$  to  $100\ \text{mg/l}$ . This competes with the established method (urinary stripes), which detects albumin above  $100\ \text{mg/l}$  really good.

Fritz et al. [150] showed a DNAFET with a Poly-L-Lysine (PLL) immobilization layer able to distinct a single mismatch in a 12-mer oligonucleotide. An oligonucleotide is a short nucleic acid polymer, typically with twenty or fewer bases. They used a differential setup with two sensors in parallel to suppress thermal fluctuations, drift, and non-specific binding. Each sensor exhibited a  $50 \times 50 - \mu\text{m}^2$  sensing area and was prepared with a different type of oligonucleotide (A and B differ with one mismatch). Injecting complementary to A (cA) into the system only the FET functionalized with oligonucleotide A was able to hybridize and become more negatively charged compared to the FET with oligonucleotide B which could not hybridize. Then complementary to B (cB) was injected and only the FET with B was able to bind the oligonucleotides. Thus, the difference in surface charge vanished again and the differential signal faded out.

## 2.5 Working Principle of a BioFET

A BioFET contains the following parts: a semiconductor transducer, a dielectric layer, a biofunctionalized surface, the analyte, and a reference electrode (the gate in FET terms) as shown in Fig. 2.9. The semiconductor transducer is realized by a conventional field-effect transistor. The dielectric layer is an oxide (e.g.  $\text{SiO}_2$ ) and has two tasks the first is to isolate the channel

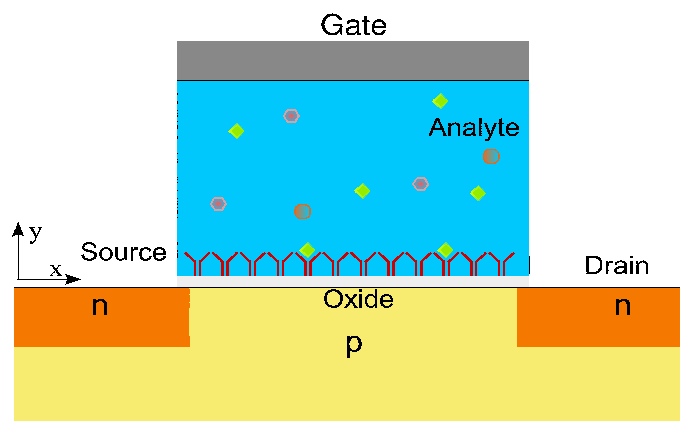


**Figure 2.9:** The working principal of a BioFET. If charged, sample molecules attach to the receptors at the biofunctionalized surface and the potential within the semiconductor changes. This causes a change in the resistance of the field-effect transistors channel.

of the FET from the liquid and the second is to electrostatically couple the surface layer charge into the channel. On top of the dielectric is a biofunctionalized layer which exhibits immobilized biomolecule receptors able to bind the desired molecule. The analyte is a solution which contains the dissolved sample molecules. The reference electrode allows to adjust the device so its sensitivity will be maximized (the optimum lies around moderate inversion [160]). If the target molecules bind to the receptors, a change in the surface charge density occurs. This change alters the potential in the semiconductor and thus the conductivity in the channel of the field-effect transducer. The chemical reaction of the sample and receptor molecules takes place at the Angstrom length scale, while the BioFET is in the micrometer length scale. This points out the importance of a proper mathematical description of the solution/semiconductor interface.

---

# Physical Influence of Strain on the Semiconductor Properties

---

**A**FTER AN OVERVIEW of the process side of strain in manufacturing an introduction into the physical description of strain in semiconductors will be given in the following chapter. At first, a general description of the strain and stress tensors in semiconductors is derived. Then, there will be a small introduction to crystal structures and band structures, due to the important properties which can be derived from the band structure, followed by an overview of methods to calculate the band structure. Finally a more detailed view on the  $\mathbf{k}\cdot\mathbf{p}$  method is given.

### 3.1 Strain

First a basic set of expressions to describe strain in semiconductors is introduced [161, 162, 163]. The orthonormal vector set  $\vec{x}$ ,  $\vec{y}$ , and  $\vec{z}$  is the basis of the unstrained solid.  $\vec{x}'$ ,  $\vec{y}'$ , and  $\vec{z}'$  represent the distorted vectors under a uniform deformation,

$$\begin{aligned}\vec{x}' &= (1 + \epsilon_{xx})\vec{x} + \epsilon_{xy}\vec{y} + \epsilon_{xz}\vec{z}, \\ \vec{y}' &= \epsilon_{yx}\vec{x} + (1 + \epsilon_{yy})\vec{y} + \epsilon_{yz}\vec{z}, \\ \vec{z}' &= \epsilon_{zx}\vec{x} + \epsilon_{zy}\vec{y} + (1 + \epsilon_{zz})\vec{z},\end{aligned}\tag{3.1}$$

where  $\epsilon_{ij}$  are the deformation coefficients of the system.

Assuming a uniform deformation, a point located at  $\vec{r} = x\vec{x} + y\vec{y} + z\vec{z}$  will be shifted to  $\vec{r}' = x\vec{x}' + y\vec{y}' + z\vec{z}'$ , which leads to the displacement  $\vec{R}$  defined as

$$\begin{aligned}
\vec{R} &\equiv \vec{r}' - \vec{r} = x(\vec{x}' - \vec{x}) + y(\vec{y}' - \vec{y}) + z(\vec{z}' - \vec{z}) \\
&= (\epsilon_{xx}x + \epsilon_{yx}y + \epsilon_{zx}z)\vec{x} + \\
&\quad (\epsilon_{xy}x + \epsilon_{yy}y + \epsilon_{zy}z)\vec{y} + \\
&\quad (\epsilon_{zx}x + \epsilon_{zy}y + \epsilon_{zz}z)\vec{z} \quad .
\end{aligned} \tag{3.2}$$

Further generalization leads to a description for non-uniform deformation, introducing a position dependent vector function  $\vec{u}(\vec{r})$ ,

$$\vec{R}(\vec{r}) = u_x(\vec{r})\vec{x} + u_y(\vec{r})\vec{y} + u_z(\vec{r})\vec{z} \tag{3.3}$$

Restricting to small displacements from  $\vec{r}$ , the displacement function  $\vec{u}(\vec{r})$  can be developed into a Taylor series and truncated after the linear term at  $\vec{R}(\vec{0}) = \vec{0}$ , leading to a relation between the local displacement tensor and the displacement function,

$$\begin{aligned}
\epsilon_{xx} &= \frac{\partial u_x}{\partial x} & \epsilon_{yx} &= \frac{\partial u_x}{\partial y} & \epsilon_{zx} &= \frac{\partial u_x}{\partial z} \\
\epsilon_{xy} &= \frac{\partial u_y}{\partial x} & \epsilon_{yy} &= \frac{\partial u_y}{\partial y} & \epsilon_{zy} &= \frac{\partial u_y}{\partial z} \\
\epsilon_{xz} &= \frac{\partial u_z}{\partial x} & \epsilon_{yz} &= \frac{\partial u_z}{\partial y} & \epsilon_{zz} &= \frac{\partial u_z}{\partial z}
\end{aligned} \quad .$$

Therefore, the displacement can be expressed as  $\varepsilon_{ij} = \frac{\partial u_j}{\partial r_i}$ . Frequently, the displacements  $\varepsilon_{ij}$  are expressed via the strain tensor  $\epsilon_{ij}$  to describe the deformation of a body in three dimensions. In the limit of small deformations, the strain tensor is known as the Green tensor or Cauchy's infinitesimal strain tensor,

$$\varepsilon_{ij} = \frac{\epsilon_{ij} + \epsilon_{ji}}{2} \quad . \tag{3.4}$$

The relative length change in the  $\vec{x}_i$  direction is described by the diagonal coefficients  $\varepsilon_{ii}$ , while the off-diagonal elements  $\varepsilon_{ij}$  ( $i \neq j$ ) denote the angular distortions by shear strains.

Also very common are the engineering strains  $e_{ij}$ , which are linked with the strain tensor as follows:

$$\begin{pmatrix} e_{xx} & e_{xy} & e_{xz} \\ e_{yx} & e_{yy} & e_{yz} \\ e_{zx} & e_{zy} & e_{zz} \end{pmatrix} = \begin{pmatrix} \varepsilon_{xx} & 2\varepsilon_{xy} & 2\varepsilon_{xz} \\ 2\varepsilon_{yx} & \varepsilon_{yy} & 2\varepsilon_{yz} \\ 2\varepsilon_{zx} & 2\varepsilon_{zy} & \varepsilon_{zz} \end{pmatrix} \quad . \tag{3.5}$$

The Voigt notation uses the six independent components of the strain tensor in a more compact vector form

$$(\varepsilon_{xx}, \varepsilon_{yy}, \varepsilon_{zz}, \gamma_{yz}, \gamma_{xz}, \gamma_{xy}) = (e_1, e_2, e_3, e_4, e_5, e_6) \quad . \tag{3.6}$$

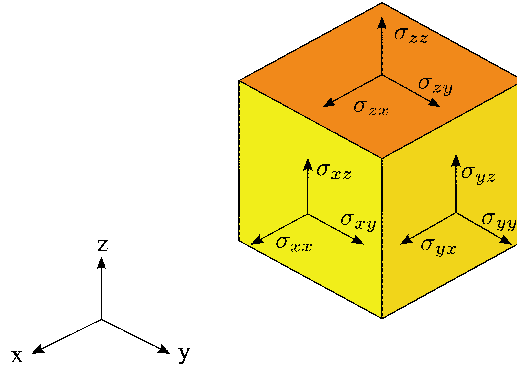


**Figure 3.1:** Scheme of stress components and how they act on an infinitesimal cube.

## 3.2 Stress

In mechanical equilibrium, all forces acting on a body must sum up to zero. In a more general and sophisticated formulation, within a body forces which an enclosed volume imposes on the remainder of the body, must be in equilibrium with the forces upon it from the remainder of the body. Cauchy was the first that formulated this principle and enabled a way to calculate stress. Considering a small element of the body enclosed by the area  $\Delta A$  and looking at the forces  $\Delta \vec{F}$ , which act on this element, the stress at this point can be determined. The stress vector  $\vec{\sigma}$  is then defined as the limit of the following expression for an infinitesimal small area:

$$\vec{\sigma} = \lim_{\Delta A \rightarrow 0} \frac{\Delta \vec{F}}{\Delta A} = \frac{d\vec{F}}{dA} . \quad (3.7)$$

Therefore, for a given plane the stress vector can be decomposed in a force perpendicular to the plane and two orthogonal in-plane vectors. The force normal to the surface is called normal component and the forces that act in-plane are the shear components. These three forces in combination with the three main planes ( $x$ ,  $y$ , and  $z$ ) form the nine components of the stress tensor Fig. 3.1:

$$\vec{\sigma} = \begin{pmatrix} \sigma_{xx} & \sigma_{xy} & \sigma_{xz} \\ \sigma_{yx} & \sigma_{yy} & \sigma_{yz} \\ \sigma_{zx} & \sigma_{zy} & \sigma_{zz} \end{pmatrix} . \quad (3.8)$$

Due to the moment equilibrium for every plane, the shear stress components across the diagonal are identical

$$\sigma_{xy} = \sigma_{yx}, \quad \sigma_{yz} = \sigma_{zy}, \quad \sigma_{xz} = \sigma_{zx} . \quad (3.9)$$

### 3.3 Stress-Strain Relation

Within the elastic limit of a material Hooke's law is a good approximation for relating stress and strain. The generalization of Hooke's law for three-dimensional elastic bodies leads to

$$\sigma_{ij} = C_{ijkl} \varepsilon_{kl} . \quad (3.10)$$

The elastic stiffness tensor  $C_{ijkl}$  is of fourth order and contains 81 ( $3^4$ ) elements. Introducing additional symmetry considerations, the number of needed components can be reduced [162]. Cubic semiconductors like *Si*, *Ge* or *GaAs* are characterized by only three constants ( $c_{11}$ ,  $c_{12}$ , and  $c_{44}$ ).

$$\begin{pmatrix} \sigma_{xx} \\ \sigma_{yy} \\ \sigma_{zz} \\ \sigma_{yz} \\ \sigma_{xz} \\ \sigma_{xy} \end{pmatrix} = \begin{pmatrix} c_{11} & c_{12} & c_{12} & 0 & 0 & 0 \\ c_{12} & c_{11} & c_{12} & 0 & 0 & 0 \\ c_{12} & c_{12} & c_{11} & 0 & 0 & 0 \\ 0 & 0 & 0 & c_{44} & 0 & 0 \\ 0 & 0 & 0 & 0 & c_{44} & 0 \\ 0 & 0 & 0 & 0 & 0 & c_{44} \end{pmatrix} \cdot \begin{pmatrix} \varepsilon_{xx} \\ \varepsilon_{yy} \\ \varepsilon_{zz} \\ \gamma_{yz} \\ \gamma_{xz} \\ \gamma_{xy} \end{pmatrix} \quad (3.11)$$

If the strain, instead of stress, is the quantity of interest, it can be calculated by inversion of the elastic stiffness tensor (3.10)

$$\varepsilon_{ij} = S_{ijkl} \sigma_{kl} , \quad (3.12)$$

or in matrix form

$$\begin{pmatrix} \varepsilon_{xx} \\ \varepsilon_{yy} \\ \varepsilon_{zz} \\ \gamma_{yz} \\ \gamma_{xz} \\ \gamma_{xy} \end{pmatrix} = \begin{pmatrix} s_{11} & s_{12} & s_{12} & 0 & 0 & 0 \\ s_{12} & s_{11} & s_{12} & 0 & 0 & 0 \\ s_{12} & s_{12} & s_{11} & 0 & 0 & 0 \\ 0 & 0 & 0 & s_{44} & 0 & 0 \\ 0 & 0 & 0 & 0 & s_{44} & 0 \\ 0 & 0 & 0 & 0 & 0 & s_{44} \end{pmatrix} \cdot \begin{pmatrix} \sigma_{xx} \\ \sigma_{yy} \\ \sigma_{zz} \\ \sigma_{yz} \\ \sigma_{xz} \\ \sigma_{xy} \end{pmatrix} \quad (3.13)$$

The stiffness constants are normally denoted as  $c_{ij}$ , while the compliance constants are named as  $s_{ij}$ . The compliance constants can be calculated from the stiffness constants with the following relations:

$$\begin{aligned} s_{11} &= \frac{c_{11} + c_{12}}{c_{11}^2 + c_{11}c_{12} - 2c_{12}^2} , \\ s_{12} &= \frac{-c_{12}}{c_{11}^2 + c_{11}c_{12} - 2c_{12}^2} , \text{ and} \\ s_{44} &= \frac{1}{c_{44}} . \end{aligned} \quad (3.14)$$

### 3.4 Miller Index Notation

The position of a crystal plane is determined by three independent non-collinear points. If these points reside on independent crystal axes, the plane can be characterized in units of the axes. However, it is more convenient to describe the planes location via Miller indices [164, 162]. The Miller indices are a triplet of integer values  $(hkl)$ , which denote the ratio between the points that intercept the plane and the chosen crystal axes. The Miller indices can be found as follows:

- Define three lattice vectors  $\vec{a}_1, \vec{a}_2,$  and  $\vec{a}_3$ . In the case of a cubic crystal, the lattice vectors are chosen along the edges of the crystallographic unit cell (unit cube).
- Identify the intercepting points  $\vec{a}_1, \vec{a}_2,$  and  $\vec{a}_3$  between the plane and the lattice vectors, and express them in units of the lattice vectors  $\vec{a}_1, \vec{a}_2,$  and  $\vec{a}_3$ .
- Calculate the reciprocal of the  $\vec{a}_1, \vec{a}_2,$  and  $\vec{a}_3$  and choose the smallest three integer values  $(hkl)$  that have a greatest common divisor of one.

Negative indices are denoted by a bar above their value  $\bar{3}$  or  $\bar{h}$ . If there is no interception between an axis and the plane, the Miller index is 0 (they intercept in infinity). Depending on the brackets used, their meaning can be further distinguished:

- $(hkl) \dots$  round brackets denote a certain plane or the vector perpendicular to the plane
- $\{hkl\} \dots$  curly braces stand for all planes that are equivalent to  $(hkl)$  due to the symmetry of the crystal.
- $[hkl] \dots$  these brackets mean a given direction in the crystal.
- $\langle hkl \rangle \dots$  angle brackets describe all directions that are equivalent to the direction  $[hkl]$ .

$(210)$  means that the plane intersects the axis vectors at  $\frac{1}{2}\vec{a}_1$  and at  $\vec{a}_2$ . Additionally, the direction vector  $[hkl]$  is always perpendicular to the plane  $(hkl)$ , for cubic crystal structures.

### 3.5 The Influence of Strain on the Bulk Band Structure

The band structure expresses the allowed energy states in the crystal momentum space for electrons and holes. Many important electronic and optical properties are destined by the band structure.

The energy surfaces of the six conduction band valleys in unstrained silicon have a prolate ellipsoidal shape. Their semi-axes represent the longitudinal  $m_l$  and the transversal electron mass  $m_t$ . There are three valley pairs with coinciding minima along the three equivalent directions  $\langle 100 \rangle$ .

### 3.5.1 Deformation Potential Theory

Bardeen and Shockley [165] originally developed the deformation potential theory. Herring and Vogt [166] generalized this theory. Bir and Pikus [161] studied various semiconductors via group theory and showed how to calculate strain effects on the band structure with deformation potentials. A short introduction into the deformation potential theory is given subsequently.

The deformation potential theory introduces an additional Hamiltonian  $\mathcal{H}(\bar{\varepsilon})$ , that is attributed to strain and its effects on the band structure. This Hamiltonian is based on first order perturbation theory and its matrix elements are defined by

$$\{\mathcal{H}(\bar{\varepsilon})\}_{ij} = \sum_{\alpha,\beta=1}^3 \mathcal{D}_{ij}^{\alpha\beta} \varepsilon_{\alpha\beta} , \quad (3.15)$$

$\mathcal{D}^{\alpha\beta}$  denotes the deformation potential operator which transforms under symmetry operations as second rank tensor [167] and  $\varepsilon_{\alpha\beta}$  describes the  $(\alpha\beta)$  strain tensor component. The subscripts  $(ij)$  in  $\mathcal{D}_{ij}^{\alpha\beta}$  denote the matrix element of the operator  $\mathcal{D}^{\alpha\beta}$ . Due to the symmetry of the strain tensor with respect to  $\alpha$  and  $\beta$ , also the deformation potential operator has to obey this symmetry  $\mathcal{D}^{\alpha\beta} = \mathcal{D}^{\beta\alpha}$  and thus limits the number of independent deformation potential operators to six.

In the case of cubic semiconductors the edges of the conduction band and the valence band are located on symmetry lines. These symmetries are reproduced in the energy band structure and in the basis states. Furthermore, the symmetry of the basis states allows to describe the deformation potential operator of a particular band via two or three deformation potential constants [166].

Although, theoretically the deformation potential constants can be calculated via the empirical pseudo potential method or by ab initio methods, it is more convenient to fit the deformation potentials to experimental results obtained by electrical, optical, microwave techniques, or by analyzing stress induced absorption edges. Even though, theoretical predictions and measurements match quite well, deformation potentials in literature and found by different methods deviate from each other [168].

#### 3.5.1.1 Strain Induced Conduction Band Splitting

Cubic crystals exhibit a strain induced energy shift for the non-degenerate energy levels of the conduction band. Along the  $\Delta$  symmetry line it is sufficient to describe the deformation potential operators  $\mathcal{D}^{\alpha\beta}$  as scalars by one or two independent constants. The energy shifts of the conduction band edge of valleys along the  $\langle 111 \rangle$  and  $\langle 100 \rangle$  directions is determined by two independent deformation potential constants <sup>1</sup> [169]:

$$\delta E_0^{v_i} = \Xi_{\text{d}}^v \text{Tr}(\bar{\varepsilon}) + \Xi_{\text{u}}^v \vec{a}_i^T \bar{\varepsilon} \vec{a}_i . \quad (3.16)$$

$\Xi_{\text{u}}^v$  describes the uniaxial- and  $\Xi_{\text{d}}^{\text{d}}$  the dilatation deformation potential constants for valleys of the type  $v = L, \Delta$ .  $\vec{a}_i$  denotes the unit vector parallel to the  $\vec{k}$  vector of valley  $i$ . The  $\Gamma_2'$

<sup>1</sup>neglecting strain induced splitting of the degenerate conduction bands  $\Delta_1$  and  $\Delta_2'$  at the  $X$  point

conduction band minimum valley shift can be determined from a single deformation potential constant

$$\delta E_0^\Gamma = \Xi_u^\Gamma \text{Tr}(\bar{\varepsilon}) . \quad (3.17)$$

Via the two relations from above the valley splitting from uniaxial stress along arbitrary directions can be calculated.

### 3.5.1.2 Strain Induced Degeneracy Lifting at the $X$ Point

Additionally to strain induced energy shifts of energy levels of the conduction band edges, there can also be a partially or complete lifting of degeneracy for degenerate bands, caused by the reduction of symmetry. Due to the special symmetry of the diamond structure (three glide reflection planes at  $x = a_0/8$ ,  $y = a_0/8$  and  $z = a_0/8$ ), the lowest two conduction bands  $\Delta_1$  and  $\Delta_{2'}$  touch at the zone boundary  $X$ . Shear strain  $\varepsilon_{xy}$  due to stress along  $[110]$  reduces the symmetry of the diamond crystal structure and produces an orthorhombic crystal. The glide reflection plane  $z = a_0/8$  is removed by the shear strain component and thus the degeneracy of the two lowest conduction bands  $\Delta_1$  and  $\Delta_{2'}$  at the symmetry points  $X = \frac{2\pi}{a_0}(0, 0, \pm 1)$  is lifted [161, 170]. It should be mentioned that in biaxially strained  $Si$  layers grown on  $\{001\}$   $Si_{1-x}Ge_x$  substrates and for uniaxially strained/stressed  $Si$  along a fourfold rotation axis  $\langle 100 \rangle$  the glide reflection symmetry is preserved.

Bir and Pikus found from  $\mathbf{k}\cdot\mathbf{p}$  theory, that when the degeneracy at the zone boundary  $X$  is lifted, a relatively large change in the energy dispersion of the conduction band minimum located close to this  $X$  point arises [161]. This effect was experimentally proved for  $Si$  by Hensel and Hasegawa [170], who measured the change in effective mass for stress along  $\langle 110 \rangle$ , and by Laude [171], who showed the effect via the indirect exciton spectrum.

Therefore, in order to take the lifting of the degeneracy of the two lowest conduction bands  $\Delta_1$  and  $\Delta_{2'}$  at the  $X$  points  $\frac{2\pi}{a_0}(0, 0, \pm 1)$  into account, (3.16) has to be adapted [170]

$$\begin{pmatrix} \delta E_0 & \delta E_1 \\ \delta E_1 & \delta E_0 \end{pmatrix} \begin{pmatrix} \xi \\ \hat{\xi} \end{pmatrix} = \delta E \begin{pmatrix} \xi \\ \hat{\xi} \end{pmatrix} , \quad (3.18)$$

where  $\Xi_{u'}$  denotes a new deformation potential,

$$\delta E_0 = \Xi_d^\Delta \text{Tr}(\bar{\varepsilon}) + \Xi_u^\Delta \varepsilon_{zz} , \quad (3.19)$$

$$\delta E_1 = \Xi_{u'} e_{xy} = 2\Xi_{u'} \varepsilon_{xy} . \quad (3.20)$$

The solutions of the eigenvalue problem look like:

$$\delta E = \delta E_0 \pm \delta E_1 \quad \text{for} \quad \hat{\xi} = \pm \xi , \quad (3.21)$$

which shows that at the  $X$  points  $\frac{2\pi}{a_0}(0, 0, \pm 1)$  the band shifts by an amount of  $\delta E_0$  (like before in (3.16)) plus an additional splitting of  $2\delta E_1$ , which lifts the degeneracy. (3.20) shows the proportional dependence on shear strain  $\varepsilon_{xy}$  for the splitting

$$(E_{\Delta_1} - E_{\Delta_{2'}}) \Big|_{X_{[001]}} = 2\delta E_1 = 4\Xi_{u'} \varepsilon_{xy} . \quad (3.22)$$

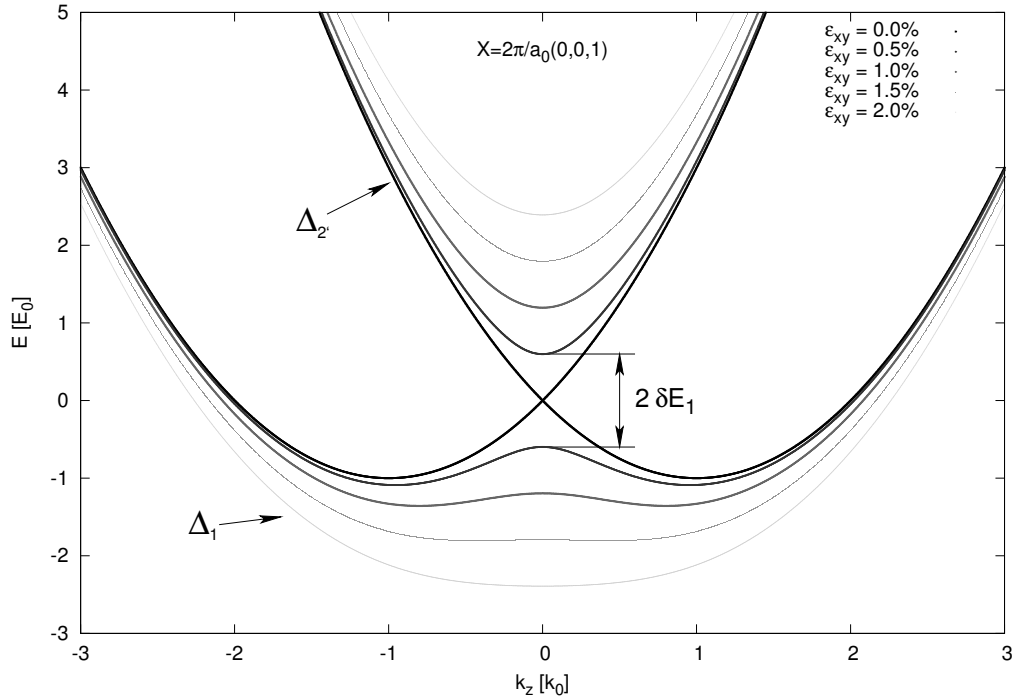


**Figure 3.2:** Energy dispersion of the conduction bands  $\Delta_1$  and  $\Delta_{2'}$  near the zone boundary  $X$  point along  $[001]$ . For  $\varepsilon_{xy} = 0\%$  the conduction bands are degenerate at the zone boundary. Introduction of shear strain  $\varepsilon_{xy} \neq 0$  lifts this degeneracy and opens up a gap. The energy separation  $2\delta E_1$  between the bands becomes larger with increasing strain  $\varepsilon_{xy}$ . At the same time the two minima of the lower conduction band  $\Delta_1$  move closer to the zone boundary with rising strain  $\varepsilon_{xy}$ , until they merge at the zone boundary and stay there for further increasing strain.

A value of  $5.7 \pm 1$  eV has been predicted by Hensel for the shear deformation potential  $\Xi_{u'}$  [170]. Laude [171] confirmed this value by his measurement of  $7.5 \pm 2$  eV via the indirect exciton spectrum of  $Si$ .

The splitting is already strongly pronounced for shear strain  $< 1\%$ . Due to the lifting of the degeneracy the  $\Delta_1$  conduction band is deformed close to the symmetry points  $X = \frac{2\pi}{a_0}(0, 0, \pm 1)$  (Fig. 3.2).

A non-vanishing shear strain component  $\varepsilon_{xy}$  has the following effects on the energy dispersion of the lowest conduction band:

- The band edge energy of the valley pair along  $[001]$  direction shifts down with respect to the other four valleys along  $[100]$  and  $[010]$ .
- The effective mass of the valley pair along  $[001]$  changes with increasing  $\varepsilon_{xy}$ .
- The conduction band minima along  $[001]$  move to the zone boundary  $X$  points at  $\frac{2\pi}{a_0}(0, 0, \pm 1)$  with increasing  $\varepsilon_{xy}$ .

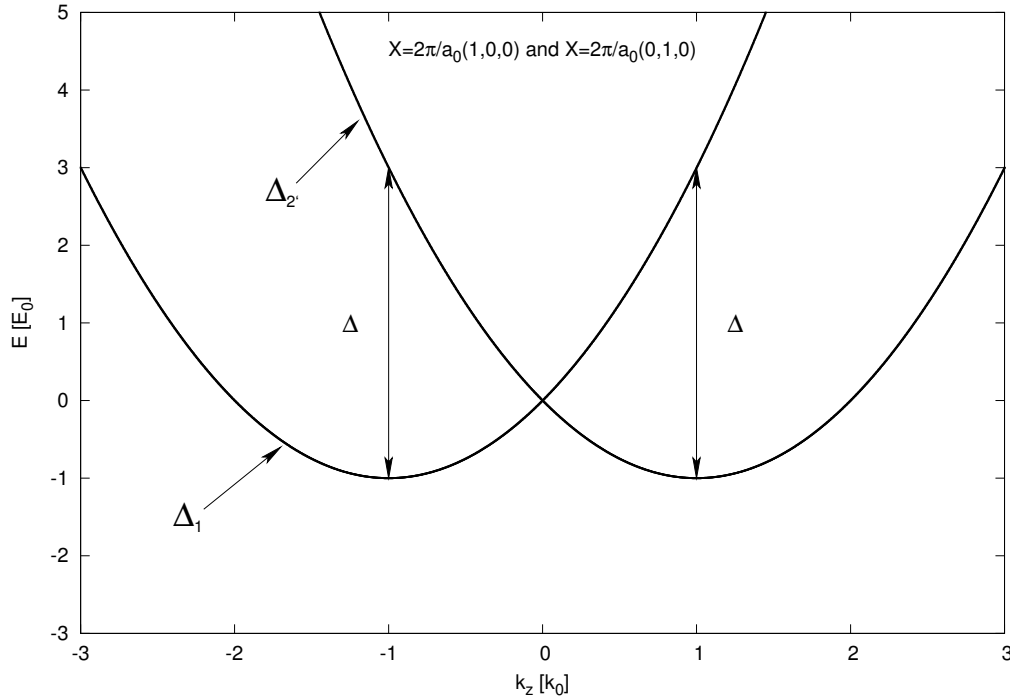


**Figure 3.3:** Energy dispersion of the two lowest conduction bands at the zone boundaries  $X = \frac{2\pi}{a_0}(1, 0, 0)$  and  $\frac{2\pi}{a_0}(0, 1, 0)$ . The band separation of unstrained  $Si$  at the conduction band edge  $\vec{k}_{\min} = \frac{2\pi}{a_0}(0, 0, 0.85)$  is denoted by  $\Delta$ . Contrary to the conduction bands along  $[001]$  the conduction bands along  $[100]$  and  $[010]$  are not affected by shear strain  $\varepsilon_{xy}$ .

For differing strains ( $\varepsilon_{xy} \neq \varepsilon_{xz} \neq \varepsilon_{yz}$ ), the conduction band minima along the  $\langle 001 \rangle$  axes are different in their energies, causing a repopulation between the six conduction band valleys. This kind of effect is not covered with (3.16), due to the negligence of possible degeneracy liftings by shear strain and by ignoring a possible repopulation of energy states.

The model presented shows no change in the conduction bands near the zone boundaries  $X = \frac{2\pi}{a_0}(\pm 1, 0, 0)$  and  $X = \frac{2\pi}{a_0}(0, \pm 1, 0)$  for a shear component  $\varepsilon_{xy}$  (Fig. 3.3). However, shear components like  $\varepsilon_{xz}$  or  $\varepsilon_{yz}$  lift the degeneracy at  $X = \frac{2\pi}{a_0}(\pm 1, 0, 0)$  or  $X = \frac{2\pi}{a_0}(0, \pm 1, 0)$ .

Applying a degenerate  $\mathbf{k}\cdot\mathbf{p}$  theory at the zone boundary  $X$  point [161,170] enables an analytical description for the valley shift along the  $\Delta$  direction. Shear strain  $\varepsilon_{xy}$  causes an energy shift between the conduction band valleys along  $[100]/[010]$  and the valleys along  $[001]$ . This shift is described by

$$\delta E_{\text{shear}} = \begin{cases} -\frac{\Delta}{4}\kappa^2\varepsilon_{xy}^2 & , \quad |\varepsilon_{xy}| < 1/\kappa \\ -\frac{\Delta}{4}(2\kappa|\varepsilon_{xy}| - 1) & , \quad |\varepsilon_{xy}| > 1/\kappa \end{cases} \quad (3.23)$$

$\kappa = (4E_{u'})/\Delta$  is a dimensionless parameter and  $\Delta$  denotes the band separation between the lowest two conduction bands at the conduction band edge

$$\Delta = (E_{\Delta_2'} - E_{\Delta_1}) \Big|_{\vec{k}=\vec{k}_{\min}}. \quad (3.24)$$

$\vec{k}_{\min} = \frac{2\pi}{a_0} (0, 0, 0.85)$  denotes the position of the band edge in the unstrained lattice.

### 3.5.1.3 Strain Induced Valence Band Splitting

Caused by the degeneracy at the maximum of the valence bands the deformation potential is different than that of the conduction bands. The deformation potential operators  $\mathcal{D}^{\alpha\beta}$  are no longer scalars and have to be expressed as  $3 \times 3$  matrices. Using symmetries the six independent operators can be described via three independent entries, commonly named  $l, m, n$  or  $a, b, d$ , related to the applied set of eigenfunctions [172]. For the basis  $|x, s\rangle, |y, s\rangle, |z, s\rangle$ , with  $s = \uparrow, \downarrow$  denoting the spin state, the perturbation Hamiltonian takes the following form:

$$\bar{H}_{strain} = \begin{pmatrix} \bar{H} & \bar{0}_{3 \times 3} \\ \bar{0}_{3 \times 3} & \bar{H} \end{pmatrix} \begin{pmatrix} |\uparrow\rangle \\ |\downarrow\rangle \end{pmatrix}, \quad (3.25)$$

$\bar{H}$  denotes the  $3 \times 3$  matrix

$$\bar{H} = \begin{pmatrix} l\varepsilon_{xx} + m(\varepsilon_{yy} + \varepsilon_{zz}) & n\varepsilon_{xy} & n\varepsilon_{zx} \\ n\varepsilon_{xy} & l\varepsilon_{yy} + m(\varepsilon_{zz} + \varepsilon_{xx}) & n\varepsilon_{yx} \\ n\varepsilon_{zx} & n\varepsilon_{yz} & l\varepsilon_{zz} + m(\varepsilon_{xx} + \varepsilon_{yy}) \end{pmatrix} \begin{pmatrix} |x\rangle \\ |y\rangle \\ |z\rangle \end{pmatrix}. \quad (3.26)$$

In the case of the valence band the description of the strain induced shifts of the heavy-hole, light-hole, and the split-off band are more complex [169].

## 3.5.2 The $\mathbf{k}\cdot\mathbf{p}$ Method

The  $\mathbf{k}\cdot\mathbf{p}$  method allows to derive analytical expressions for the energy dispersion and the effective masses [161]. It enables the extrapolation of the band structure over the entire Brillouin zone from the energy gaps and matrix elements at the zone center. In addition to the common use of the  $\mathbf{k}\cdot\mathbf{p}$  method to model the valence band of semiconductors, it is also well suited to describe the influence of strain on the conduction band minimum.

The  $\mathbf{k}\cdot\mathbf{p}$  method can be derived from the one-electron Schrödinger equation as follows:

$$\mathcal{H}\Psi_n(\vec{r}) = \left( \frac{\vec{p}^2}{2m} + V(\vec{r}) \right) \Psi_n(\vec{r}) = E_n \Psi_n(\vec{r}) \quad (3.27)$$

$V(\vec{r})$  denotes the periodic lattice potential and  $\mathcal{H}$  the one-electron Hamilton operator.  $\Psi_n$  describes the one-electron wave function in an eigenstate  $n$  and  $E_n$  the eigenenergy for the eigenstate  $n$ . Due to the periodicity of the lattice potential (3.27) the Bloch theorem is applicable and the solution can be written in the form of:

$$\Psi_{n\vec{k}}(\vec{r}) = e^{i\vec{k}\cdot\vec{r}} u_{n\vec{k}}(\vec{r}), \quad (3.28)$$

The wave function  $\Psi_{n\vec{k}}(\vec{r})$  can be expressed as the product of a plane wave and the function  $e^{i\vec{k}_0\cdot\vec{r}} u_{n\vec{k}}(\vec{r})$ , which reflects the periodicity of the lattice.  $n$  denotes the band index and  $\vec{k}$  represents a wave vector. If the given potential  $V(\vec{r})$  only depends on one spatial coordinate (also called *local*), (3.28) can be substituted in (3.27).

Luttinger [173] showed that it is possible to use the eigenfunctions of the ground states as a complete set of eigenfunctions and that the wave function can be expanded by

$$\chi_{n\vec{k}} = e^{i\Delta\vec{k}} \Psi_{n\vec{k}_0} = e^{i(\vec{k}_0 + \Delta\vec{k})} u_{n\vec{k}_0} \quad (3.29)$$

for  $k_0 \neq 0$ . Inserting (3.29) into (3.27) yields:

$$\begin{aligned} \left( \frac{(\hbar \Delta\vec{k} + \vec{p})^2}{2m} + V(\vec{r}) \right) \Psi_{n\vec{k}_0}(\vec{r}) &= E_{n\vec{k}} \Psi_{n\vec{k}_0}(\vec{r}) \\ \left( \frac{\vec{p}^2}{2m} + V(\vec{r}) + \frac{\hbar(\vec{k}_0 + \Delta\vec{k}) \cdot \vec{p}}{m} \right) u_{n\vec{k}}(\vec{r}) &= \left( E_{n\vec{k}} - \frac{\hbar^2(\vec{k}_0 + \Delta\vec{k})^2}{2m} \right) u_{n\vec{k}}(\vec{r}) . \end{aligned} \quad (3.30)$$

This way, for any fixed wave vector  $\vec{k} = \vec{k}_0$ , (3.30) for the unperturbed system, delivers a complete set of eigenfunctions  $u_{n\vec{k}_0}$ , which completely cover the space of the lattice periodic functions in real space. Therefore, the wave function  $\Psi_{n\vec{k}}(\vec{r})$  at  $\vec{k}$ , for the full system, can be expressed via  $u_{n\vec{k}_0}$

$$\Psi_{n\vec{k}}(\vec{r}) = \sum_{n'} C_{n,n'}(\vec{k}, \vec{k}_0) e^{i(\vec{k}_0 + \Delta\vec{k}) \cdot \vec{r}} u_{n'\vec{k}_0} . \quad (3.31)$$

As soon as the eigenenergy  $E_{n\vec{k}_0}$  and the  $u_{n\vec{k}_0}$  of the unperturbed system are determined, the eigenfunctions  $\Psi_{n\vec{k}}(\vec{r})$  and eigenenergies  $E_{n\vec{k}}$  can be calculated for any  $\vec{k} = \vec{k}_0 + \Delta\vec{k}$  in the vicinity of  $\vec{k}_0$  by accounting the  $\frac{\hbar\vec{k} \cdot \vec{p}}{m}$  term in (3.30) as a perturbation. This method has been introduced by Seitz [174] and extended by [172, 173, 175] to study the band structure of semiconductors.

Due to the  $\frac{\hbar\vec{k} \cdot \vec{p}}{m}$  term in (3.30) this method is also known as the **k·p** method. Provided that the energies at  $\vec{k}_0$  and that the matrix elements of  $\vec{p}$  between the wave functions, or the wave functions themselves, are known, the band structure for small  $\Delta\vec{k}$ 's around  $\vec{k}_0$  can be calculated. The entire first Brillouin zone can be calculated by diagonalizing (3.30) numerically, provided a sufficiently large set of  $u_{n\vec{k}_0}$  to approximate the complete set of basis functions is used [172].

The following subsections will explain the effective masses for the non-degenerate conduction band of silicon and the energy dispersion utilizing a non-degenerate **k·p** theory. In order to analyze the effects of shear strain on the two lowest conduction bands  $\Delta_1$  and  $\Delta_2'$ , the **k·p** method is adapted to enable degeneracy, due to the coincidence of the  $\Delta_1$  and  $\Delta_2'$  bands at the  $X$  point.

### 3.5.2.1 Effective Electron Mass in Unstrained Silicon

The conduction band minima of silicon reside on the  $\langle 001 \rangle$  axes at a distance of  $0.15 \frac{2\pi}{a_0}$  from the  $X$  symmetry points. By means of non-degenerate perturbation theory and the knowledge of the eigenenergies  $E_{n\vec{k}_0}$  and the wave functions  $u_{n\vec{k}_0}$  at the conduction band minima  $\vec{k}_0$ , the

eigenvalues  $E_{n\vec{k}}$  at neighboring points  $\vec{k}$  can be expanded to second order terms in  $k_i$ .

$$E_{n\vec{k}} = E_{n\vec{k}_0} + \frac{\hbar^2}{2m_0} \sum_{i,j} k_i \delta_{ij} k_j + \frac{\hbar^2}{m_0^2} \sum_{ij} \sum_{n' \neq n} k_i \frac{\langle u_{n\vec{k}_0} | p_i | u_{n'\vec{k}_0} \rangle \langle u_{n'\vec{k}_0} | p_j | u_{n\vec{k}_0} \rangle}{E_{n\vec{k}_0} - E_{n'\vec{k}_0}} k_j . \quad (3.32)$$

Scalar products  $\vec{k} \cdot \vec{p}$  are expressed via index notation  $\sum_i k_i p_i$  and the matrix elements with Dirac's notation

$$\langle u_{n\vec{k}_0} | p_j | u_{n'\vec{k}_0} \rangle = \frac{1}{\Omega} \int_{\Omega} u_{n\vec{k}_0} \frac{\hbar}{i} \frac{\partial}{\partial x_j} u_{n'\vec{k}_0} d\vec{r} . \quad (3.33)$$

The linear terms in  $k_i$  can be set to zero under the assumption that  $E_{n,\vec{k}_0}$  is a minimum. The expression for the effective mass tensor  $m_{n,i}^*$  can be derived from the dispersion relation (3.32)

$$\frac{1}{m_{n,i}^*} = \frac{1}{m_0} + \frac{2}{m_0^2} \sum_{n' \neq n} \frac{\langle u_{n\vec{k}_0} | p_i | u_{n'\vec{k}_0} \rangle \langle u_{n'\vec{k}_0} | p_j | u_{n\vec{k}_0} \rangle}{E_{n\vec{k}_0} - E_{n'\vec{k}_0}} . \quad (3.34)$$

The effective mass tensor for the lowest conduction band  $\Delta_1$  in diamond crystal structures is characterized by two masses. In the principal coordinate system for the [001] valley the effective masses can be written as

$$\frac{1}{m_l} = \frac{1}{m_0} + \frac{2}{m_0^2} \sum_{n' \neq \Delta_1} \frac{|\langle u_{\Delta_1\vec{k}_0} | p_z | u_{n'\vec{k}_0} \rangle|^2}{E_{\Delta_1\vec{k}_0} - E_{n'\vec{k}_0}} \quad (3.35)$$

and

$$\frac{1}{m_t} = \frac{1}{m_0} + \frac{2}{m_0^2} \sum_{n' \neq \Delta_1} \frac{|\langle u_{\Delta_1\vec{k}_0} | p_x | u_{n'\vec{k}_0} \rangle|^2}{E_{\Delta_1\vec{k}_0} - E_{n'\vec{k}_0}} . \quad (3.36)$$

$\Delta_1$  denotes the band index  $n$  of the lowest conduction band. Therefore, the energy dispersion can be formulated as:

$$E(\vec{k}) = \frac{\hbar^2 (k_z - k_0)^2}{2m_l} + \frac{\hbar^2 (k_x^2 + k_y^2)}{2m_t} . \quad (3.37)$$

From the derived equations follows that due to the coupling between electronic states in different bands (via  $\mathbf{k} \cdot \mathbf{p}$  term), an electron in a solid has a different mass than a free electron. The coupling terms are related to the following criteria:

- The bigger the energetic gap between two bands, the smaller is the effect on the effective mass. The relative importance of a band  $n'$  to the effective mass of band  $n$  is controlled by the energy gap between the two bands.
- All bands  $n'$  with non-zero matrix elements  $\langle u_{n\vec{k}_0} | \vec{k} \cdot \vec{p} | u_{n'\vec{k}_0} \rangle$  can be found via the matrix element theorem [176] by group theoretical considerations checking all possible symmetries for  $u_{n'\vec{k}_0}$ .

It is possible to calculate numerically all matrix elements and subsequently the effective masses from (3.34) via the empirical pseudo potential method [177].

### 3.5.2.2 The Silicon Conduction Band Minimum's Dependence on Strain

(3.58) only requires the direction of the  $\vec{k}$  vector, indicating the location of the valley, to describe the shift of the valley minima. Hence, the valley shift is independent of the exact value of the wave vector  $\vec{k}$  and all  $\vec{k}$  points belonging to a particular valley experience the same shift. Since the effective mass is given by the second derivative of the energy dispersion  $\frac{1}{m_{ij}^*} = \frac{1}{\hbar^2} \frac{\partial^2 E}{\partial k_i \partial k_j}$  and (3.16) does not change the curvature of the energy band, the formula predicts no change in the effective electron mass due to strain.

However, there is a clear experimental proof that shear strain changes the effective masses of electrons in the lowest conduction band [170] and the exciton spectrum of silicon [171]. In order to explain this behavior one has to take the splitting of the lowest two conduction bands at the  $X$  symmetry point by shear strain into account. The lifting of the degeneracy can be calculated with the deformation potential constant  $\Xi_{u'}$  via (3.21). (3.21) is only valid at the  $X$  symmetry point and cannot be used to predict the effect of strain on the valley minima  $\vec{k}_{\min}$ . In order to circumvent this obstacle a degenerate  $\mathbf{k} \cdot \mathbf{p}$  theory has to be applied around the  $X$  symmetry point.

A different approach was adapted in [161]. The Hamiltonian at the  $X = \frac{2\pi}{a_0} (0, 0, \pm 1)$  points can be described via the theory of invariants:

$$\mathcal{H}(\vec{\varepsilon}, \vec{k}) = \lambda \mathbb{1} + \sigma_x (A_3 k_x k_y + D_3 \varepsilon_{xy}) + A_4 \sigma_z k_z . \quad (3.38)$$

where,

$$\lambda = A_1 k_z^2 + A_2 (k_x^2 + k_y^2) + D_1 \varepsilon_{zz} + D_2 (\varepsilon_{xx} + \varepsilon_{yy}) , \quad (3.39)$$

$\sigma_x$  and  $\sigma_z$  are the Pauli's matrices and  $A_1$  and  $A_2$  denote scalar constants

$$\sigma_x = \begin{pmatrix} 0 & 1 \\ 1 & 0 \end{pmatrix} \quad \text{and} \quad \sigma_z = \begin{pmatrix} 1 & 0 \\ 0 & -1 \end{pmatrix} \quad (3.40)$$

The scalar constants  $D_1$ ,  $D_2$ , and  $D_3$  are connected to the deformation potential constants  $\Xi_u$ ,  $\Xi_d$ , and  $\Xi_{u'}$  through

$$D_1 = \Xi_u + \Xi_d , \quad (3.41)$$

$$D_2 = \Xi_d , \quad (3.42)$$

$$D_3 = 2 \Xi_{u'} . \quad (3.43)$$

From (3.38) eigenvalues can be calculated which represent the energy dispersion for the first and second conduction band

$$E_{\pm}(\vec{\varepsilon}, \vec{k}) = \lambda \pm \sqrt{A_4^2 k_z^2 + (2 \Xi_{u'} \varepsilon_{xy} + A_3 k_x k_y)^2} , \quad (3.44)$$

where  $E_-$  denotes the energy dispersion of  $\Delta_1$  and  $E_+$  that of  $\Delta_2'$ . Under the assumption that this description is valid around the  $X$  point up to the minimum of the lowest conduction band at  $\vec{k}_{\min} = \frac{2\pi}{a_0} (0, 0, \pm 0.85)$ ,  $A_4$  and  $A_1$  can be related to each other via

$$\left. \frac{\partial E_- (\vec{\varepsilon} = 0, \vec{k})}{\partial k_z} \right|_{\vec{k}_{\min}} = 2 A_1 k_0 + \frac{A_4^2 k_0}{\sqrt{A_4^2 k_0^2}} = 0 . \quad (3.45)$$

$\vec{k}_0 = 0.15 \frac{2\pi}{a_0}$  describes the distance of the conduction band minimum of unstrained silicon to the  $X$  point.  $A_4$  can be determined from (3.45)

$$|A_4| = 2 A_1 k_0 . \quad (3.46)$$

The effect of shear strain on the shape of the lowest conduction band is examined in the following section.

### 3.5.2.3 The Conduction Band Minimum of Silicon and its Energy Dispersion under Strain

Up to now it has been assumed that the conduction band minima are located at  $\vec{k}_{\min} = \frac{2\pi}{a_0} (0, 0, \pm 0.85)$ . This is only valid for small shear strain. The minimum of the conduction band moves towards the  $X$  point in conjunction with an increasing splitting between the conduction bands, when the shear strain rises (as can be seen in Fig. 3.2). This causes a change in the shape of the conduction bands and the assumption that the minima lie fixed at  $\vec{k}_{\min} = \frac{2\pi}{a_0} (0, 0, \pm 0.85)$  does not hold anymore.

Therefore, a model which is able to cover the effects of shear strain on the effective masses has to take the movement of the conduction band as a function of strain into account. In the following a model will be derived that takes this movement of  $\vec{k}_{\min}(\varepsilon_{xy})$  into account.

Starting with (3.44) and setting  $k_x = k_y = 0$  the minimum can be found from the dispersion relation

$$E_- = \frac{\hbar^2 k_z^2}{2m_1} - \sqrt{\frac{\hbar^4 k_0^2 k_z^2}{m_1} + 4\Xi_{u'}^2 \varepsilon_{xy}^2} . \quad (3.47)$$

The constants  $A_1$  and  $A_4$  are replaced with the relations (3.46) and (3.37), and  $\vec{k}_0 = 0.15 \frac{2\pi}{a_0}$  describes the position of the conduction band minimum measured from the zone boundary  $X$ . Setting the first derivative of (3.47) to zero,  $\frac{\partial E_-}{\partial k_z} = 0$ , and solving for  $k_z$  results in the desired relation between  $\vec{k}_{z,\min}$  and shear strain.

$$k_{z,\min} = \begin{cases} k_0 \sqrt{1 - \kappa^2 \varepsilon_{xy}^2} & , |\varepsilon_{xy}| < 1/\kappa \\ 0 & , |\varepsilon_{xy}| > 1/\kappa \end{cases} . \quad (3.48)$$

Here  $\kappa = \frac{4\Xi_{u'}}{\Delta} = \frac{2\Xi_{u'} m_1}{\hbar^2 k_0^2}$  is introduced and represents the ratio between the shear deformation potential  $\Xi_{u'}$  and the band separation between the two lowest conduction bands  $\Delta$  at zero shear strain (Fig. 3.3). (3.48) shows that for strain smaller than  $1/\kappa$ , the minimum position shifts towards the  $X$  point. At  $|\varepsilon_{xy}| = 1/\kappa$ , the minimum is located at the  $X$  point ( $k_{z,\min}$ ). Increasing shear strain above  $\varepsilon_{xy} > 1/\kappa$  does not shift  $k_{z,\min}$  anymore. The change of shape of the two lowest conduction bands  $\Delta_1$  and  $\Delta_2$  and accordingly the position change of the minimum with increasing shear strain can be seen in Fig. 3.2.

The strain dependent longitudinal mass  $m_1(\varepsilon_{xy})$  can be calculated from (3.47) with

$$\frac{1}{m_1(\varepsilon_{xy})} = \frac{1}{\hbar^2} \left. \frac{\partial^2 E_-}{\partial k_z^2} \right|_{\vec{k}=(0,0,k_{z,\min})} . \quad (3.49)$$

After some algebraic manipulations the strain dependent mass  $m_l(\varepsilon_{xy})$  can be expressed as

$$m_l(\varepsilon_{xy}) = \begin{cases} m_l (1 - \kappa^2 \varepsilon_{xy}^2)^{-1} & , |\varepsilon_{xy}| < 1/\kappa \\ m_l \left(1 - \frac{1}{\kappa|\varepsilon_{xy}|}\right)^{-1} & , |\varepsilon_{xy}| > 1/\kappa \end{cases} . \quad (3.50)$$

Accordingly to (3.48) the dependence of the longitudinal masses is different for a strain level above or below  $1/\kappa$ . For the derivation of the transversal masses we rotate the principal coordinate system by  $45^\circ$  around the  $z$ -axis with the following transformation:

$$k_{x'} = \frac{k_x + k_y}{\sqrt{2}} \quad k_{y'} = \frac{k_x - k_y}{\sqrt{2}} \quad k_{z'} = k_z . \quad (3.51)$$

The energy dispersion in the rotated coordinate system is

$$E_{\pm}(\hat{\varepsilon}, \vec{k}) = \lambda \pm \sqrt{A_4^2 k_z^2 + \left(2\Xi_{u'} \varepsilon_{xy} + \frac{A_3}{2} (k_x^2 - k_y^2)\right)^2} . \quad (3.52)$$

The effective mass in the  $[110]$  and  $[1\bar{1}0]$  directions is defined by

$$\frac{1}{m_{t,x'}(\varepsilon_{xy})} = \frac{1}{\hbar^2} \left. \frac{\partial^2 E_{-}}{\partial k_{x'}^2} \right|_{\vec{k}=(0,0,k_{z,\min})} , \quad (3.53)$$

and

$$\frac{1}{m_{t,y'}(\varepsilon_{xy})} = \frac{1}{\hbar^2} \left. \frac{\partial^2 E_{-}}{\partial k_{y'}^2} \right|_{\vec{k}=(0,0,k_{z,\min})} . \quad (3.54)$$

Applying (3.53) and (3.54) to (3.52) gives for the  $[110]$  direction

$$m_{t,x'}(\varepsilon_{xy}) = \begin{cases} \frac{m_t}{1+\eta\kappa\varepsilon_{xy}} & , |\varepsilon_{xy}| < 1/\kappa \\ \frac{m_t}{1+\eta\text{sgn}(\varepsilon_{xy})} & , |\varepsilon_{xy}| > 1/\kappa \end{cases} , \quad (3.55)$$

and

$$m_{t,y'}(\varepsilon_{xy}) = \begin{cases} \frac{m_t}{1-\eta\kappa\varepsilon_{xy}} & , |\varepsilon_{xy}| < 1/\kappa \\ \frac{m_t}{1-\eta\text{sgn}(\varepsilon_{xy})} & , |\varepsilon_{xy}| > 1/\kappa \end{cases} , \quad (3.56)$$

for the  $[1\bar{1}0]$  direction with the parameter  $\eta = \frac{m_t}{2m'}$  and  $m'$  is defined by

$$\frac{1}{m'} = \frac{2}{m_0^2} \sum_{n \neq \Delta_1} \frac{\langle \Delta_1 | p_x | n \rangle \langle n | p_y | \Delta_2' \rangle}{E_n - E_{\Delta_1}} . \quad (3.57)$$

As can be seen along the  $[110]$  direction the effective mass is reduced (mobility is enhanced) for  $\varepsilon_{xy} > 0$ , while for the  $[1\bar{1}0]$  direction the effective mass is increased (the mobility is reduced) for increasing shear strain ( $\varepsilon_{xy} < a/\kappa$ ). For shear strain above  $\varepsilon_{xy} > 1/\kappa$  the effective mass is a constant which depends on the sign of the strain.

The analytical valley shift induced by shear strain  $\varepsilon_{xy}$  (given in (3.23)) can now be calculated. Substituting the expression for  $k_{z,\min}$  from (3.48) into equation (3.47) delivers the equation for

shear strain. The shift between the valley pair along [001] and the valley pairs [100] or [010] due to  $\varepsilon_{xy}$  can be obtained in the form of

$$\delta E_{\text{shear}} = E(\varepsilon_{xy}, \vec{k}_{\text{min}}) - E(0, \vec{k}_{\text{min}}) = \begin{cases} -\frac{\Delta}{4} \kappa^2 \varepsilon_{xy}^2 & , |\varepsilon_{xy}| < 1/\kappa \\ -\frac{\Delta}{4} (2 \kappa |\varepsilon_{xy}| - 1) & , |\varepsilon_{xy}| > 1/\kappa \end{cases} . \quad (3.58)$$

---

# Quantum Confinement in UTB Films

---

**M**ULTI-GATE FinFETs and Ultra Thin Body Silicon On Insulator (UTBSOI) FETs are considered as perfect candidates for the 22 nm technology node and beyond. Strong size quantization leads to a formation of quasi-two-dimensional subbands in carrier systems in thin silicon films. For analytical hole subband structure calculations a six-band  $\mathbf{k}\cdot\mathbf{p}$  Hamiltonian is commonly employed. The electron subband structure consists of six equivalent minima located close to the X-points in the Brillouin zone. Close to the minimum the energy dispersion is usually described by a parabolic approximation with the transversal masses  $m_t$  and the longitudinal mass  $m_l$ . Isotropic non-parabolicity takes into account deviations in the density of states at higher energies. A more general description is, however, needed in ultra-thin silicon films, especially in the presence of shear strain [178]. The two-band  $\mathbf{k}\cdot\mathbf{p}$  Hamiltonian accurately describes the bulk structure up to energies of 0.5 – 0.8 eV [179]. It includes a shear strain component which is neglected in the parabolic approximation [161, 170, 179]. Shear strain is responsible for effective mass modification and is, therefore, an important source of the electron mobility enhancement in ultra-thin silicon films [180, 178].

### 4.1 Quantization in UTB Films for Unprimed Subbands

In the following I will concentrate on the analytical analysis of the problem, allowing computationally cheap results, while offering an already detailed characterization of the subband structure in the Ultra Thin Body (UTB) silicon films behavior under uniaxially strain. However, the used assumption of a square well potential with infinite walls is only valid as long as the ground subband energy is much higher than the amplitude of the potential profile in the film. As soon as this assumption breaks down, a generalized numerical treatment of the  $\mathbf{k}\cdot\mathbf{p}$  Schrödinger and Poisson equations is required.

The two-band  $\mathbf{k}\cdot\mathbf{p}$  Hamiltonian of a [001] valley in the vicinity of the X-point of the Brillouin zone in Si must be in the form [161]:

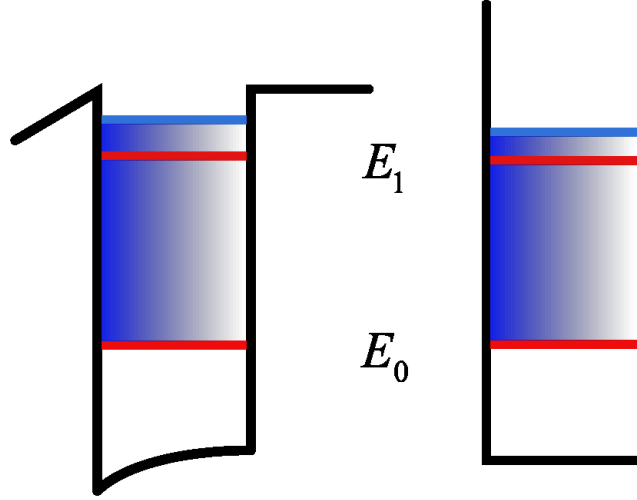


**Figure 4.1:** Potential in an ultra-thin SOI film of a single-gate MOSFET (left) and a corresponding model square well potential with infinite walls.

$$\mathcal{H} = \left( \frac{\hbar^2 k_z^2}{2m_l} + \frac{\hbar^2(k_x^2 + k_y^2)}{2m_t} + U(z) \right) \mathbb{1} + \left( 2\Xi_{u'} \varepsilon_{xy} - \frac{\hbar^2 k_x k_y}{M} \right) \sigma_x + \frac{\hbar^2 k_z k_0}{m_l} \sigma_z , \quad (4.1)$$

where  $\sigma_{x,z}$  are the Pauli matrices,  $\mathbb{1}$  is the  $2 \times 2$  unity matrix,  $k_0 = 0.15 \times 2\pi/a_0$  is the position of the valley minimum relative to the X-point in unstrained Si,  $k_i$  with  $i \in \{x, y, z\}$  is the wave vector,  $\varepsilon_{xy}$  denotes the shear strain component in physics notations,  $M^{-1} = m_t^{-1} - m_0^{-1}$ , and  $\Xi_{u'} = 7 \text{ eV}$  is the shear strain deformation potential [161, 170, 179, 180].

For a square well potential the wave function is set to zero at the boundaries, which allows an analytical analysis of the subband structure.

In the two-band model the wave function is a spinor with two components. Therefore, we use the following ansatz,

$$\Psi = \begin{pmatrix} a(\vec{k}) \\ b(\vec{k}) \end{pmatrix} e^{i\vec{k} \cdot \vec{r}} , \quad (4.2)$$

where  $a(\vec{k})$  and  $b(\vec{k})$  are constants depending on the wave vector  $\vec{k}$ . Substituting this ansatz into the equation system (4.1) delivers the following eigenvalue problem:

$$(\mathcal{H} - E) \begin{pmatrix} a(\vec{k}) \\ b(\vec{k}) \end{pmatrix} e^{i\vec{k} \cdot \vec{r}} = 0 . \quad (4.3)$$

Taking the determinant of (4.3) and setting it to zero results in the energy dispersion relation

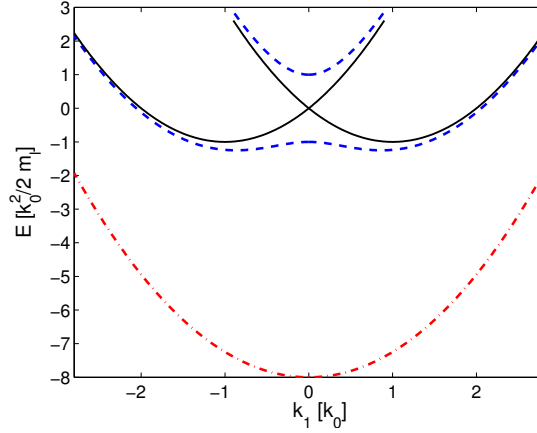


**Figure 4.2:** Conduction band profile close to the X-point for  $\eta = 0$  (solid lines),  $\eta = 0.5$  (dashed lines), and  $\eta = 4$  (dashed-dotted line).

of the system.

$$E(\vec{k}) = \frac{\hbar^2 k_z^2}{2m_l} + \frac{\hbar^2(k_x^2 + k_y^2)}{2m_t} \pm \sqrt{\delta^2 + \left(\frac{\hbar^2 k_z k_0}{m_l}\right)^2} \quad (4.4)$$

with

$$\delta = \left(2\Xi_{u'}\varepsilon_{xy} - \frac{\hbar^2 k_x k_y}{M}\right) \quad (4.5)$$

For each energy  $E$  there are four solutions for  $k_z$ . Fig. 4.2 shows that  $E(\vec{k})$  is even with respect to  $k = 0$ . Therefore, there are always two independent values  $k_z = k_1$  and  $k_z = k_2$  for the wave vector, which are complemented to four values by alternating their signs. For energies in the gap the two values are imaginary. The wave function is then a superposition of the solutions with the four eigenvectors:

$$\Psi(z) = \begin{pmatrix} a(k_1) \\ b(k_1) \end{pmatrix} e^{ik_1 \cdot z} + \begin{pmatrix} a(-k_1) \\ b(-k_1) \end{pmatrix} e^{-ik_1 \cdot z} + \begin{pmatrix} a(k_2) \\ b(k_2) \end{pmatrix} e^{ik_2 \cdot z} + \begin{pmatrix} a(-k_2) \\ b(-k_2) \end{pmatrix} e^{-ik_2 \cdot z} \quad (4.6)$$

We introduce  $c(k)$  as the ratio between  $b(k)$  and  $a(k)$ .  $c(k)$  is an odd function with respect to  $k_z$ :

$$c(k_z) = \frac{b(k_z)}{a(k_z)} = -\frac{\frac{\hbar^2 k_z k_0}{m_l}}{\frac{\hbar^2 k_z^2}{2m_l} + \frac{\hbar^2(k_x^2 + k_y^2)}{2m_l} + \delta - E(k_z)} \quad (4.7)$$

Additionally, fulfilling the boundary conditions  $\Psi(z = \pm t/2) = 0$ , demands that  $a(-k_z) = \pm a(k_z)$  is satisfied. Thus resulting in

$$\begin{aligned} \Psi(z) = & a(k_1) \left( \begin{pmatrix} 1 \\ c(k_1) \end{pmatrix} e^{ik_1 \cdot z} \pm \begin{pmatrix} 1 \\ -c(k_1) \end{pmatrix} e^{-ik_1 \cdot z} \right) + \\ & + a(k_2) \left( \begin{pmatrix} 1 \\ c(k_2) \end{pmatrix} e^{ik_2 \cdot z} \pm \begin{pmatrix} 1 \\ -c(k_2) \end{pmatrix} e^{-ik_2 \cdot z} \right) . \end{aligned} \quad (4.8)$$

After some simplifications the two pairs of independent equations

$$a(k_1) \cos(k_1 t/2) + a(k_2) \cos(k_2 t/2) = 0 , \quad (4.9)$$

$$a(k_1)c(k_1) \sin(k_1 t/2) + a(k_2)c(k_2) \sin(k_2 t/2) = 0 , \quad (4.10)$$

and

$$a(k_1) \sin(k_1 t/2) + a(k_2) \sin(k_2 t/2) = 0 , \quad (4.11)$$

$$a(k_1)c(k_1) \cos(k_1 t/2) + a(k_2)c(k_2) \cos(k_2 t/2) = 0 , \quad (4.12)$$

are obtained.

Expressing  $a(k_1)$  with (4.9) and (4.11) and putting them into (4.10) and (4.12) leads to these two conditions:

$$\tan(k_1 t/2) = \frac{c(k_2)}{c(k_1)} \tan(k_2 t/2) , \quad (4.13)$$

$$\cot(k_1 t/2) = \frac{c(k_2)}{c(k_1)} \cot(k_2 t/2) . \quad (4.14)$$

After transforming the equations into dimensionless form

$$X_{1,2} = \frac{k_{1,2}}{k_0} , E_0 = \frac{\hbar^2 k_0^2}{m_l} , \mathcal{E} = \frac{E}{E_0} , \zeta = \frac{\delta}{E_0} , \quad (4.15)$$

and a few calculation steps found in the Appendix A., the equations can be written in the form:

$$\tan(X_1 k_0 t/2) = \frac{X_2}{X_1} \frac{\zeta \pm \sqrt{\zeta^2 + X_1^2}}{\zeta \pm \sqrt{\zeta^2 + X_2^2}} \tan(X_2 k_0 t/2) , \quad (4.16)$$

$$\cot(X_1 k_0 t/2) = \frac{X_2}{X_1} \frac{\zeta \pm \sqrt{\zeta^2 + X_1^2}}{\zeta \pm \sqrt{\zeta^2 + X_2^2}} \cot(X_2 k_0 t/2) . \quad (4.17)$$

For the numerical solution it is convenient to reformulate the equations as:

$$\sin(X_1 k_0 t/2) \cos(X_2 k_0 t/2) = \frac{X_2}{X_1} \frac{\zeta \pm \sqrt{\zeta^2 + X_1^2}}{\zeta \pm \sqrt{\zeta^2 + X_2^2}} \cdot \sin(X_2 k_0 t/2) \cos(X_1 k_0 t/2) , \quad (4.18)$$

$$\cos(X_1 k_0 t/2) \sin(X_2 k_0 t/2) = \frac{X_2}{X_1} \frac{\zeta \pm \sqrt{\zeta^2 + X_1^2}}{\zeta \pm \sqrt{\zeta^2 + X_2^2}} \cdot \cos(X_2 k_0 t/2) \sin(X_1 k_0 t/2) . \quad (4.19)$$

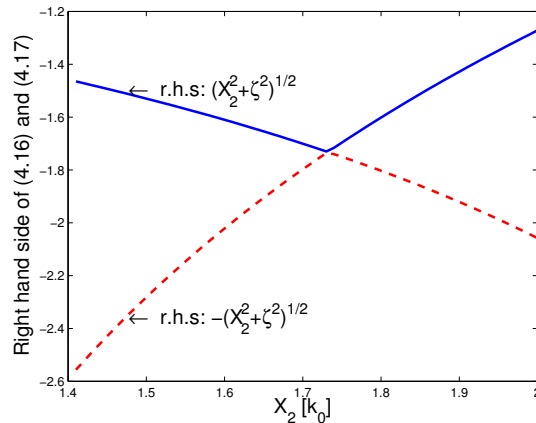


**Figure 4.3:** The right hand side of (4.16) and (4.17) plotted close to the point  $\sqrt{\zeta^2 + X^2} = 0$ . It is clearly seen that the sign of the square root must be alternated at this point.

$X_1$  and  $X_2$  coexist in the equations. Therefore, we need an extra relation to re-express  $X_1$  as a function of  $X_2$  or vice versa, the derivation of which can be found in the Appendix A.:

$$X_1^2 = X_2^2 + 4 + 4\sqrt{X_2^2 + \zeta^2}, \quad (4.20)$$

$$X_2^2 = X_1^2 + 4 - 4\sqrt{X_1^2 + \zeta^2}. \quad (4.21)$$

Eliminating one of the two  $X$ 's with (4.20) or (4.21) in (4.18) and (4.19) allows to calculate  $X$  as a function of strain  $\zeta$ . Then one can calculate the energy as a function of strain  $\zeta$  by using (4.4).

Interestingly, (4.16) and (4.17) coincide with the dispersion relations obtained from an auxiliary tight-binding consideration [181]. For  $\zeta = 0$  (4.16) and (4.17) become equivalent. For higher strain values (4.18) and (4.19) must be solved numerically. The value  $X_2 = \sqrt{X_1^2 + 4 - 4\sqrt{\zeta^2 + X_1^2}}$  becomes imaginary at high strain values. In this case the trigonometric functions in (4.16)/(4.17) or (4.18)/(4.19) are replaced by the hyperbolic ones. Special care must be taken to choose the correct branch of  $\sqrt{X_2^2 + \zeta^2}$  in (4.16)/(4.17) or alternatively (4.18)/(4.19). The sign of  $\sqrt{X_2^2 + \zeta^2}$  must be alternated after it becomes zero, as it is displayed in Fig. 4.3.

Fig. 4.4 and Fig. 4.5 show the energies of the subbands as a function of shear strain for two different film thicknesses. Shear strain opens the gap between the two conduction bands at the X-point making the energy dispersion non-parabolic [179], which removes the subband degeneracy and introduces the valley splitting. Fig. 4.6 and Fig. 4.7 show the energy difference between two unprimed subbands  $\Delta E_n$  as a function of strain for the same quantum number  $n$ .

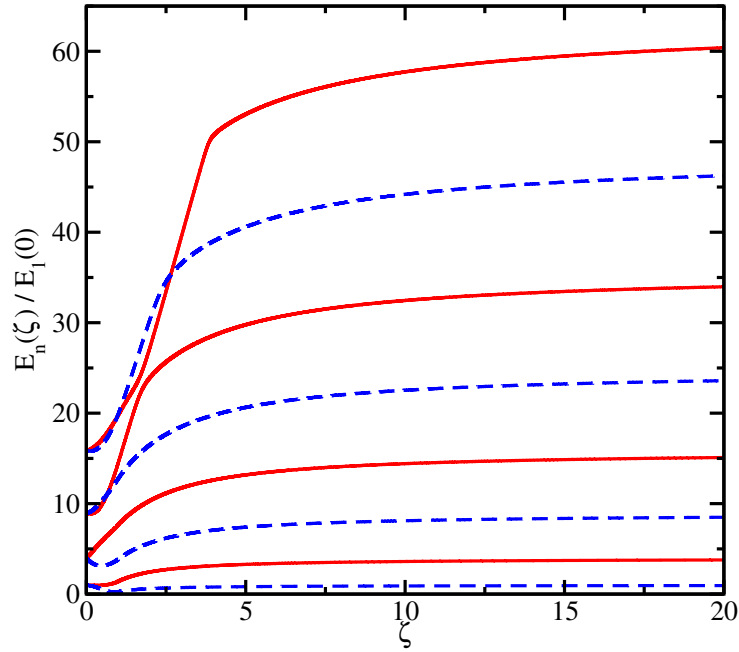


**Figure 4.4:** Subband quantization energies  $E_n$  (normalized to the ground subband energy) for a film thickness of 3.3 nm. The valley splitting appears for non-zero shear strain  $\zeta$ .

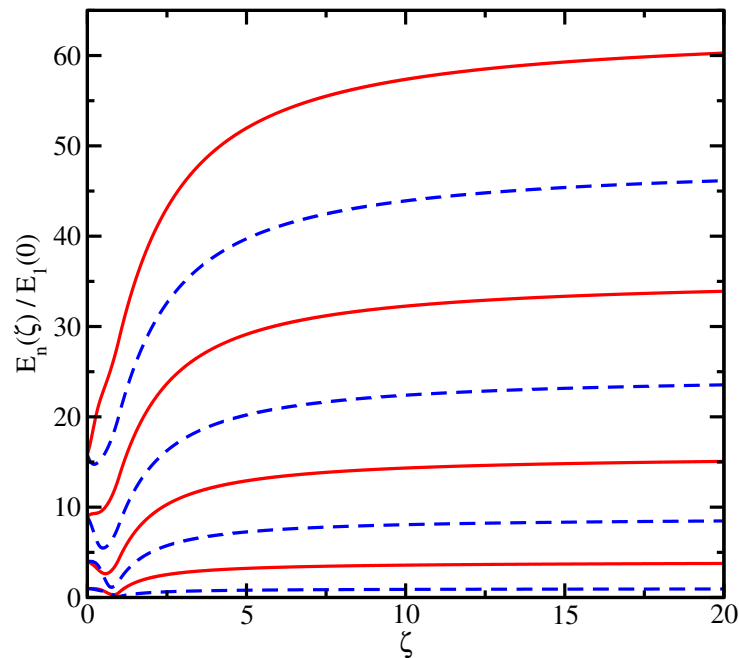


**Figure 4.5:** The same as in Fig. 4.4 for a film thickness 6.5 nm. The valley splitting depends strongly on the film thickness. The valley splitting is maximal at high strain values.

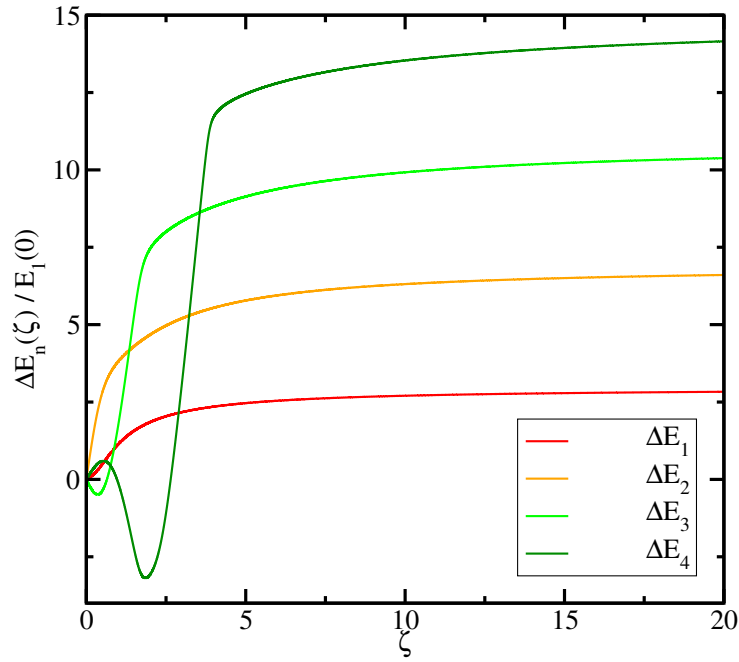


**Figure 4.6:** Difference of the subband quantization energies  $\Delta E_n$  (normalized to the ground subband energy) from (4.18) and (4.19) for a film thickness of 3.3 nm. The valley splitting appears for non-zero shear strain  $\zeta$ .

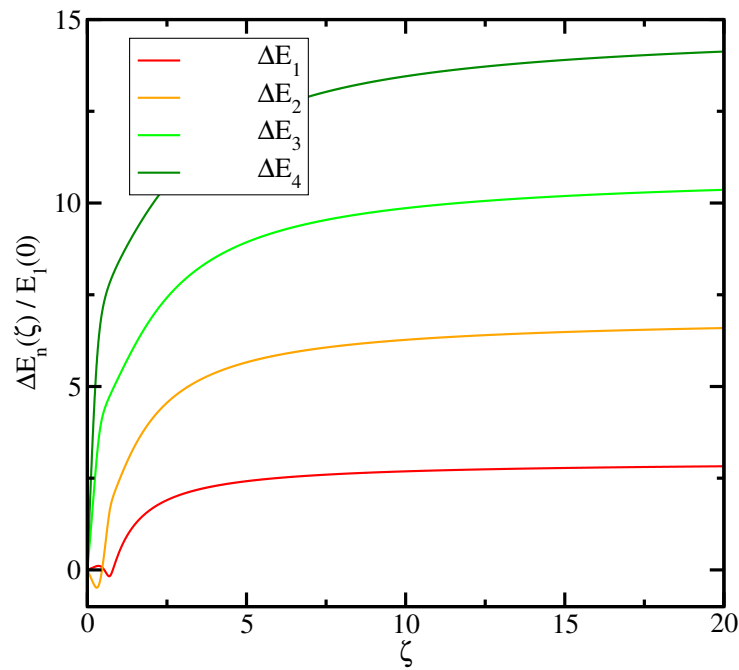


**Figure 4.7:**  $\Delta E_n(\zeta)$  for a film thickness of 6.5 nm. The splitting depends strongly on the film thickness.

### 4.1.1 Scaled Energy Dispersion Relation

For the sake of completeness the energy dispersion relation (q.v. (4.4) and (3.58)) after transformation to dimensionless units is given below:

$$\mathcal{E}(X) = \begin{cases} \frac{X^2}{2} - \sqrt{X^2 + \zeta^2} + \frac{\zeta^2}{2} + \frac{1}{2} & \text{for } \zeta < 1 \text{ ,} \\ \frac{X^2}{2} - \sqrt{X^2 + \zeta^2} + \zeta & \text{for } \zeta > 1 \text{ .} \end{cases} \quad (4.22)$$

### 4.1.2 Small Strain Values

The valley splitting was shown to be linear in strain for small shear strain values and to depend strongly on the film thickness [181]. To support these findings we reformulated (4.18) and (4.19) for the sum and the difference of  $X_1$  and  $X_2$ . First we introduce the transformation rules for  $y_n$  and  $\bar{y}_n$  as,

$$y_n = \frac{X_1 - X_2}{2} \quad \text{and} \quad \bar{y}_n = \frac{X_1 + X_2}{2} \quad (4.23)$$

or

$$(y_n + \bar{y}_n)^2 = X_1^2 \quad \text{and} \quad (y_n - \bar{y}_n)^2 = X_2^2 \text{ .} \quad (4.24)$$

We only show the derivation for (4.18), due to the similarity with (4.19). Using the above given transformation and rewriting (4.18) to separate  $y_n$  and  $\bar{y}_n$  leads to the following expression.

$$\sin(y_n k_0 t) + \sin(\bar{y}_n k_0 t) = \frac{c(X_2)}{c(X_1)} \cdot (-\sin(y_n k_0 t) + \sin(\bar{y}_n k_0 t)) \quad (4.25)$$

Further simplification steps result in:

$$\sin(y_n k_0 t) = \frac{c(X_2) - c(X_1)}{c(X_2) + c(X_1)} \sin(\bar{y}_n k_0 t) \quad (4.26)$$

Now we re-express  $\bar{y}_n$  as function of  $y_n$  (Appendix B.) resulting in

$$\bar{y}_n^2 = \frac{1 - y_n^2 - \zeta^2}{1 - y_n^2} \text{ .} \quad (4.27)$$

The derivation of the fraction containing  $c(X_1)$  and  $c(X_2)$  can be found in Appendix B..

$$\sin(y_n k_0 t) = \pm \frac{\zeta y_n \sin\left(\sqrt{\frac{1 - y_n^2 - \zeta^2}{1 - y_n^2}} k_0 t\right)}{\sqrt{(1 - y_n^2)(1 - \zeta^2 - y_n^2)}} \quad (4.28)$$

For zero stress the ratio on the right hand side of (4.28) is equal to zero, and the standard quantization condition  $q_n = \pi n/k_0 t$  is recovered. Due to the plus/minus sign in the right-hand side of (4.28), the equation splits into two non-equivalent branches for  $\zeta \neq 0$  and non-parabolic

bands. (4.28) is nonlinear and can be solved only numerically. However, for small  $\zeta$  the solution can be thought in the form  $y_n = q_n \pm \zeta$ , where  $\zeta$  is small. Substituting  $y_n = q_n$  into the right-hand side of (4.28) and solving the equation with respect to  $\zeta$ , we obtain for the valley splitting:

$$\Delta E_n = 4 \left( \frac{\pi n}{k_0 t} \right)^2 \frac{\Xi_{uv} \varepsilon_{xy}}{k_0 t} \frac{\sin(k_0 t)}{|1 - q_n^2|} \quad (4.29)$$

In accordance with earlier publications [182, 183, 184, 185], the valley splitting is inversely proportional to the third power of  $k_0$  and the third power of the film thickness  $t$ . The value of the valley splitting oscillates with film thickness, in accordance with [183, 184, 185]. In contrast to previous works, the subband splitting is proportional to the gap  $\delta$  at the X-point, and not at the  $\Gamma$ -point. Since the parameter  $\zeta$ , which determines non-parabolicity, depends strongly on shear strain, the application of uniaxial [110] stress to [001] ultra-thin Si film generates a valley splitting proportional to strain.

### 4.1.3 High Values of $\zeta$

For high strain values the dispersion relations (4.4) of the lowest conduction band become parabolic again (shown in Fig. 4.2) and the quantization levels in a square well potential with a parabolic band must be recovered in this limit. We note that in the limit  $\delta \gg E_0$   $X_2 = 2\sqrt{-\zeta}$  and equations (4.16) and (4.17) take the form [181]:

$$\tan(X_1 k_0 t / 2) \approx \frac{b(X_1)}{a(X_1)} \frac{1}{\sqrt{\zeta}}, \quad (4.30)$$

$$\cot(X_1 k_0 t / 2) \approx \frac{b(X_1)}{a(X_1)} \frac{1}{\sqrt{\zeta}}. \quad (4.31)$$

For large  $\zeta$  (4.30) has the solution  $X_1 = \pi(2n - 1)/k_0 t$ , while (4.31) gives  $X_1 = 2\pi n/k_0 t$ , which results in the well-known quantization result  $X_1 = \pi n/k_0 t, n = 1, 2, 3, \dots$  for subbands in an infinite potential square well with a single parabolic band. For the difference in energy  $\Delta E_n$  between the two subbands we get  $\Delta E_n = E_1(4n - 1)$  in the limit of large  $\zeta$ , which is perfectly consistent with the results shown in Fig. 4.6 and Fig. 4.7.

Fig. 4.8 shows for several film thicknesses that the unprimed subbands split for non-zero shear strain. In ultra-thin films already at moderate stress levels the splitting energy is larger than  $k_B T$ . In this case the higher subband becomes de-populated, indicating a mobility enhancement in (001) ultra-thin films strained along [110] direction. For small strain values the splitting is linear in strain. For large strain the quantization relations in an infinite square well potential with a single parabolic band are recovered resulting in the largest subband splitting. Uniaxial stress is currently used to enhance performance of modern MOSFETs, where it is introduced in a controllable way. Therefore, the valley splitting can be controlled by adjusting strain and thickness  $t$ .

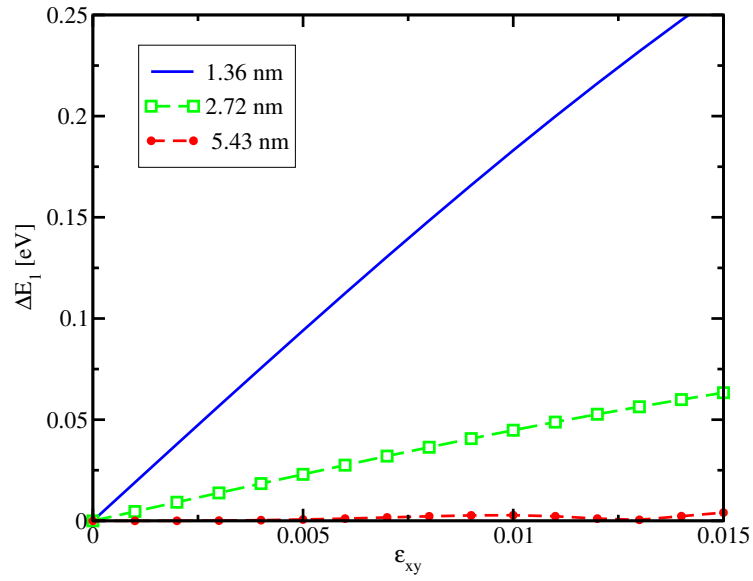


**Figure 4.8:** Splitting induced by shear strain for several film thicknesses. As can be seen for ultra-thin films the splitting is already larger than  $k_B T$  for moderate stress levels.

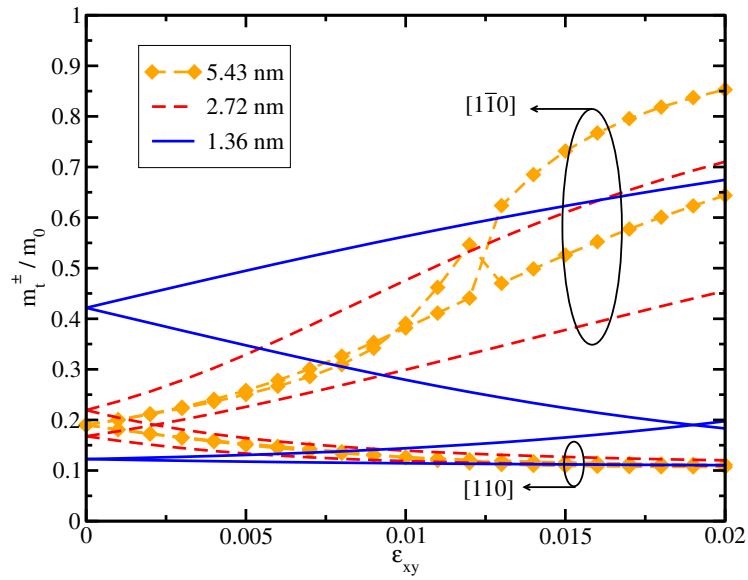


**Figure 4.9:** Ultra-thin films exhibit different effective masses for the two ground subbands even without stress. The thinner the film the more pronounced is the difference in effective masses.

## 4.2 Effective Mass of Unprimed Subbands

Fig. 4.9 shows that the effective masses along  $[110]$  and  $[1\bar{1}0]$  become different for decreasing film thickness. The dependence of the effective masses of the two ground subbands without strain on film thickness is shown in Fig. 4.10. However, due to symmetry restrictions their subband energy dispersion relations are not parabolic as demonstrated in Fig. 4.11. For a given  $k_x$  and  $k_y$  there is a subband with a lower energy in the form of the unification of two equi-energy ellipses with the effective masses  $m_1$  and  $m_2$  and a subband which is higher in energy given by the intersection of the same ellipses. The difference between the bulk description and the numerically obtained thickness dependent result is caused by the growing value of the right-hand side in (4.28), which cannot be neglected for thin films. The coupling between the two conduction bands in (4.1) is described via the right-hand side of (4.28) and therefore of great importance for thin films. The two bands exhibit minima at  $k_z = \pm k_0$  with respect to the corresponding  $X$ -point. One can think of the coupling between the bands as interaction between the valleys. This interaction is caused by the term  $\zeta \neq 0$  and is also responsible for the non-parabolicity of the bulk bands.

Substituting  $y_n^0 = q_n = \frac{\pi n}{k_0 t}$ <sup>1</sup> into (4.28) and solving for small strain  $\zeta$  the dispersion relation for the unprimed subbands  $n$  can be obtained:

$$E_n^\pm = \frac{\hbar^2}{2m_l} \left( \frac{\pi n}{t} \right)^2 + \frac{(k_x^2 + k_y^2)}{2m_t} \pm \left( \frac{\pi n}{k_0 t} \right)^2 \frac{\left| D\varepsilon_{xy} - \frac{\hbar^2 k_x k_y}{M} \right|}{k_0 t \left| 1 - \left( \frac{\pi n}{k_0 t} \right)^2 \right|} \sin(k_0 t) . \quad (4.32)$$

(4.32) illustrates that the subband degeneracy is preserved only in the absence of shear strain and either  $k_x = 0$  or  $k_y = 0$ . (4.32) shows that the unprimed subbands for thin films are not equivalent, even without shear strain. Deriving the expression for the effective masses from (4.32) also reveals two independent effective masses in  $[110]$  direction for the unprimed subbands with the same quantum number  $n$  without strain:

$$m_{(1,2)} = \left( \frac{1}{m_t} \pm \frac{1}{M} \left( \frac{\pi n}{k_0 t} \right)^2 \frac{\sin(k_0 t)}{k_0 t \left| 1 - \left( \frac{\pi n}{k_0 t} \right)^2 \right|} \right)^{-1} . \quad (4.33)$$

This behavior is in agreement with the numerically found effective masses for the two ground subbands in relaxed thin films shown in Fig. 4.10.

---

<sup>1</sup>for small  $\zeta$  the right-hand side can be of (4.28) ignored and  $y_n^0$  be found

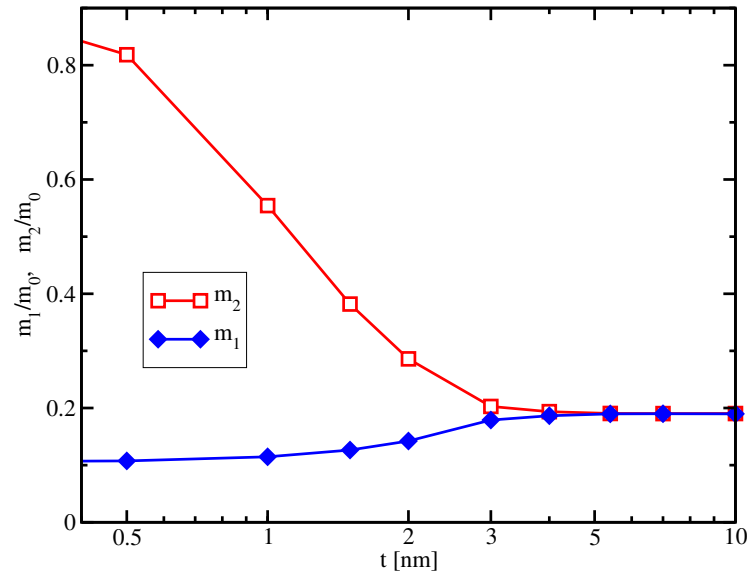


**Figure 4.10:** The dependence of the effective masses on the film thickness for the lowest two subbands.

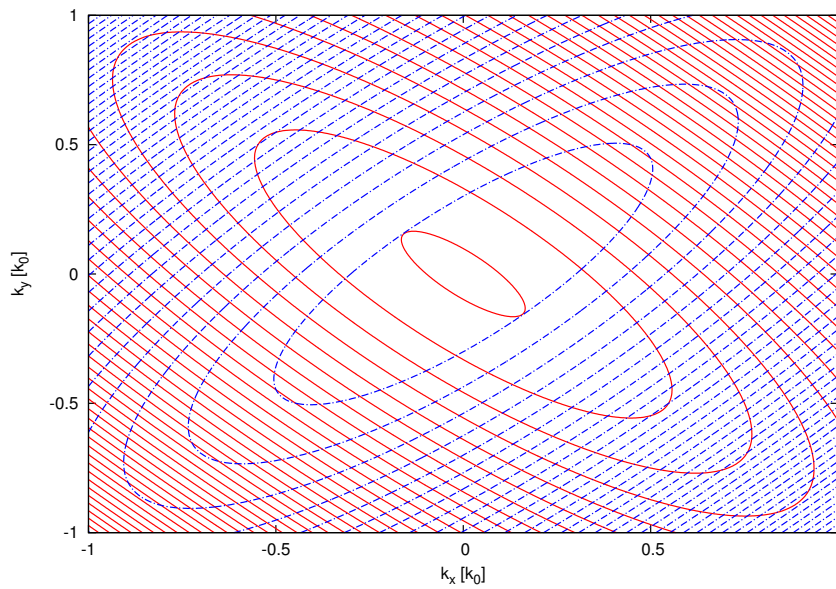


**Figure 4.11:** The two ground subbands as contour plots.

### 4.3 Quantization in UTB Films for Primed Subbands

As pointed out before a shear strain component in the [110] direction does not affect the primed valleys along [100] and [010] direction, except for a small shift of the minimum [186]. However, *the linear combination of bulk bands* method gained with the empirical pseudo-potential calculations [4] and calculations of the primed subbands based on the density functional theory (DFT) [3] uncover the relationship of the transport effective masses on the silicon film thickness  $t$ . Here we analyze the dependence of the primed subbands effective mass via the two-band  $\mathbf{k}\cdot\mathbf{p}$  Hamiltonian utilized before (4.1). At first we have to derive analogously to the unprimed subbands an analytical expression for  $k_1$  as a function of  $k_2$  and vice versa:

$$\mathcal{H} = \begin{pmatrix} \frac{\hbar^2 k_z^2}{2m_l} + \frac{\hbar^2 k_x^2}{2m_t} + \frac{\hbar^2 k_y^2}{2m_t} - \frac{\hbar^2}{M} k_x k_y & \frac{\hbar^2 k_z k_0}{m_l} \\ \frac{\hbar^2 k_z k_0}{m_l} & \frac{\hbar^2 k_z^2}{2m_l} + \frac{\hbar^2 k_x^2}{2m_t} + \frac{\hbar^2 k_y^2}{2m_t} + \frac{\hbar^2}{M} k_x k_y \end{pmatrix}. \quad (4.34)$$

Starting with the transformation to dimensionless form according to:

$$X = \frac{k_x}{k_0}, \quad Y = \frac{k_y}{k_0}, \quad Z = \frac{k_z}{k_0}, \quad E_0 = \frac{\hbar^2 k_0^2}{m_t}, \quad (4.35)$$

and some further rearrangements

$$\mathcal{E} = \frac{E}{E_0} - \frac{m_t}{m_l} Z^2/2 - Y^2/2, \quad \nu = \frac{m_t}{m_l} Z, \quad (4.36)$$

the eigenvalue problem takes the following form:

$$\begin{pmatrix} \frac{X^2}{2} - \frac{m_t}{M} XY - \mathcal{E} & \nu \\ \nu & \frac{X^2}{2} + \frac{m_t}{M} XY - \mathcal{E} \end{pmatrix}. \quad (4.37)$$

Setting the determinant of (4.37) to zero allows to obtain  $X$  as a function of  $\mathcal{E}$

$$\left( \frac{X^2}{2} - \mathcal{E} - \frac{m_t}{M} XY \right) \left( \frac{X^2}{2} - \mathcal{E} + \frac{m_t}{M} XY \right) - \nu^2 = 0 \quad (4.38)$$

$$\left( \frac{X^2}{2} - \mathcal{E} \right)^2 - \frac{m_t^2}{M^2} X^2 Y^2 - \nu^2 = 0 \quad (4.39)$$

Like before for the unprimed subbands, the obtained fourth order equation,

$$X^4 - 4 \left( \mathcal{E} + \frac{m_t^2}{M^2} Y^2 \right) X^2 + 4 (\mathcal{E}^2 - \nu^2) = 0, \quad (4.40)$$

can be reformulated into two second order equations:

$$\begin{aligned} X_{1,2}^2 &= 2 \left( \mathcal{E} + \frac{m_t^2}{M^2} Y^2 \right) \pm \sqrt{4 \left( \mathcal{E} + \frac{m_t^2}{M^2} Y^2 \right)^2 - 4 (\mathcal{E}^2 - \nu^2)}, \\ &= 2 \left( \mathcal{E} + \frac{m_t^2}{M^2} Y^2 \pm \left| \frac{m_t}{M} Y \right| \sqrt{2\mathcal{E} + \frac{m_t^2}{M^2} Y^2 + \frac{\nu^2 M^2}{m_t^2 Y^2}} \right), \\ &= \left( \frac{m_t}{M} |Y| \pm \sqrt{2\mathcal{E} + \frac{m_t^2}{M^2} Y^2 + \frac{\nu^2 M^2}{m_t^2 Y^2}} \right)^2 - \frac{\nu^2 M^2}{m_t^2 Y^2}. \end{aligned} \quad (4.41)$$

The identities

$$\frac{X_1^2 + X_2^2}{2} = 2 \left( \mathcal{E} + \frac{m_t^2}{M^2} |Y| \right) , \quad (4.42)$$

$$\frac{X_1^2 - X_2^2}{2} = 2 \frac{m_t}{M} |Y| \sqrt{2\mathcal{E} + \frac{m_t^2}{M^2} Y^2 + \frac{\nu^2 M^2}{m_t^2} Y^2} , \quad (4.43)$$

allow to introduce a  $X_1, X_2$  dependence in (4.41) and formulate the problem as  $X_1(X_2)$  and vice versa

$$\begin{aligned} X_{1,2}^2 &= \left( \frac{m_t}{M} |Y| \pm \frac{X_1^2 - X_2^2}{4} \left( \frac{m_t}{M} |Y| \right)^{-1} \right)^2 - \frac{\nu^2 M^2}{m_t^2 Y^2} , \\ X_{1,2}^2 &= \left( \frac{m_t^2}{M^2} Y^2 \pm \frac{(X_1^2 - X_2^2)}{2} + \frac{M^2}{m_t^2 Y^2} \left( \frac{X_1^2 - X_2^2}{4} \right)^2 \right) - \frac{\nu^2 M^2}{m_t^2 Y^2} . \end{aligned} \quad (4.44)$$

So  $X_1$  as a function of  $X_2$  is described by the following equation:

$$X_1^2 = \left( \frac{m_t^2}{M^2} Y^2 + \frac{(X_1^2 - X_2^2)}{2} + \frac{M^2}{m_t^2 Y^2} \left( \frac{X_1^2 - X_2^2}{4} \right)^2 \right) - \frac{\nu^2 M^2}{m_t^2 Y^2} . \quad (4.45)$$

Substituting  $\Upsilon = \frac{m_t^2}{M^2} Y^2$  into (4.45) results in:

$$0 = X_1^4 - 2(4\Upsilon + X_2^2) X_1^2 + (16(\Upsilon^2 - \nu^2) - 8\Upsilon X_2^2 + X_2^4) , \quad (4.46)$$

and enables the derivation of  $X_1$  as a function of  $X_2$

$$X_1^2 = X_2^2 + 4\Upsilon + 4\sqrt{\Upsilon X_2^2 + \nu^2} \quad \text{or} \quad (4.47)$$

$$X_1^2 = X_2^2 + 4\frac{m_t^2}{M^2} Y^2 + 4\sqrt{\frac{m_t^2}{M^2} Y^2 X_2^2 + \frac{m_t^2}{m_l^2} Z^2} . \quad (4.48)$$

In order to obtain  $X_2(X_1)$  the minus branch of (4.44) is used:

$$X_2^2 = \left( \frac{m_t^2}{M^2} Y^2 - \frac{(X_1^2 - X_2^2)}{2} + \frac{M^2}{m_t^2 Y^2} \left( \frac{X_1^2 - X_2^2}{4} \right)^2 \right) - \frac{\nu^2 M^2}{m_t^2 Y^2} . \quad (4.49)$$

After analogous treatment of (4.49) the relation of  $X_2$  as a function of  $X_1$  is derived:

$$X_2^2 = X_1^2 + 4\Upsilon - 4\sqrt{\Upsilon X_1^2 + \nu^2} \quad \text{or} \quad (4.50)$$

$$X_2^2 = X_1^2 + 4\frac{m_t^2}{M^2} Y^2 - 4\sqrt{\frac{m_t^2}{M^2} Y^2 X_1^2 + \frac{m_t^2}{m_l^2} Z^2} . \quad (4.51)$$

The corresponding scaled energy dispersion relation is given by:

$$\tilde{\mathcal{E}}(X, Y, Z) = \frac{X^2}{2} + \frac{Y^2}{2} + \frac{m_t^2}{m_l^2} Z^2 \pm \sqrt{\frac{m_t^2}{M^2} Y^2 X^2 + \frac{m_t^2}{m_l^2} Z^2} . \quad (4.52)$$

**Table 4.1:** Comparison between the effective masses for the lowest ground subband obtained with fullband calculations [3], calculations from [4], and the two-band  $\mathbf{k}\cdot\mathbf{p}$  model. Excellent agreement with the fullband calculations is achieved.

$t[\text{nm}]$	$\frac{m_t(t)}{m_t}$		
	$\mathbf{k}\cdot\mathbf{p}$	[3]	[4]
1.201	2.404		1.547
1.496	2.212		1.418
1.791	2.065		1.330
1.965	1.974	1.871	
2.028	1.950		1.272
2.323	1.830		1.228
2.618	1.718		1.194
2.978	1.608	1.578	
3.917	1.406		1.111
3.972	1.400	1.399	
4.982	1.283	1.289	
5.276	1.258		1.075
6.693	1.169		1.058
6.984	1.163	1.174	
7.992	1.126		1.048
9.350	1.096		1.040
9.993	1.082	1.100	

#### 4.4 Effective Mass of Primed Subbands

Applying the same numerical procedure for the derived relations for the primed as for the unprimed subbands yields the energy dispersion and the effective masses in the primed subbands. The results of these calculations are shown in Table 4.1 and exhibit excellent agreement with the results of the *linear combination of bulk bands* method with a potential barrier of 3 eV at the film interface [4]. The results are also consistent with the DFT calculations from [3].

In ultra-thin films the large separation in energy between the primed and the unprimed subbands even without stress leads to a de-population of the primed subbands. Tensile stress in [110] direction generates a shear component which changes the transport effective masses of the unprimed subbands and shifts the primed subbands with unfavorable effective masses up in energy (Fig. 4.11). With decreasing film thickness the decrease of the effective mass along [110] direction induced by shear strain becomes more pronounced enabling mobility enhancement even in ultra-thin films. Unfortunately, the density of states effective mass in unprimed subbands increases with shear strain and thus results in higher scattering rates which reduces the mobility gained due to the thickness-enhanced transport mass decrease at high stress values. However, the mobility enhancement remains significant [187].

---

# Modeling of Electrolytic Interfaces

---

**B**ERGVELD [188] introduced 1970 the first ion sensitive field-effect transistor. Since then the field of applications has developed to a versatile and fascinating area. In the sequel the basic properties of this kind of devices are discussed.

### 5.1 Electrochemistry of Ionic Solutions

Chemical and biological experiments are commonly carried out in ionic solutions [189]. The reason is that within polar solutions (e.g. water) the solvent molecules exhibit a non-vanishing dipole moment. This feature enables the reduction of the electric field between ionic bonds and allows to break up the initially strong ionic connections, leading to more chemically active reactants. Fig. 5.1 shows an example for a general structure of an ionic solution. It depicts a so called 1 : 1 solution [190], which implies that the valences' absolute value of the anion (negative ion) and the kation (positive ion) are equal. *NaCl* and *KCl* are two examples for a 1:1 solution/salt. The dissolved particles try to minimize the total energy of the system. This is accomplished by minimizing the repulsive forces between ions of equal charges. Thus, without external forces the charges are equally distributed across the electrolyte. Each ion is surrounded by an aggregate of water molecules. The charge of a water molecule is not symmetrically distributed, which causes a finite dipole moment. Therefore water is a *polar* solvent, and the polarity of water molecules enables it to dissolve ionic compounds by reducing the binding electric field between ions. The *water shell* around an ion changes the permittivity in it's vicinity and renders it less prone to electric fields originating from other ions. In this manner, the ions are free to move in the solvent, giving rise to a possible conduction path for an electrical current.

Not only the salt ions are dissolved in the solute but also the water molecules themselves can dissociate into ionic components. This is governed by the following chemical reaction [5]:



Assuming that the reaction (5.1) is reversible and in equilibrium the law of mass action can be

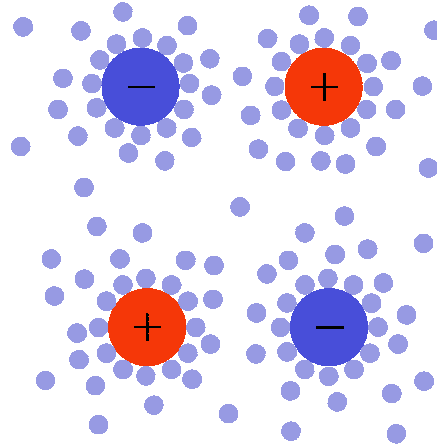


**Figure 5.1:** Most biological and chemical experiments are carried out in an ionic solution. Polar solutions (like water) can break up strong ionic bonds and ease chemical reactions. Each ion (red and dark blue) is surrounded by an aggregate of water molecules. The non-vanishing dipole moment of the water molecules weakens the electric field binding the ions together.

applied,

$$K_{\text{eq}} = \frac{[\text{H}^+][\text{OH}^-]}{[\text{H}_2\text{O}]} . \quad (5.2)$$

$K_{\text{eq}}$  denotes the equilibrium constant,  $[\text{H}^+]$  the hydrogen concentration,  $[\text{OH}^-]$  the hydroxyl concentration, and  $[\text{H}_2\text{O}]$  the water concentration, respectively. Further, taking the density of water as constant ( $1000 \frac{\text{g}}{\text{l}}$ ) the dependence of the ion concentrations on the equilibrium constants can be expressed directly:

$$K_{\text{eq}} = \frac{[\text{H}^+][\text{OH}^-]}{1000 \frac{\text{g}}{\text{l}} \cdot \frac{\text{mol}}{18\text{g}}} = \frac{[\text{H}^+][\text{OH}^-]}{55.56\text{M}} . \quad (5.3)$$

In this way we can define the dissociation constant of water as follows:

$$K_{\text{w}} = 55.56\text{M} \cdot K_{\text{eq}} = 1 \cdot 10^{-14} = [\text{H}^+][\text{OH}^-] . \quad (5.4)$$

The dissociation constant of water  $K_{\text{w}}$  has a value of  $10^{-14}$  at room temperature. Due to the large range for hydrogen and hydroxyl concentrations it is convenient to reformulate (5.4) to a logarithmic scale:

$$\log_{10}([\text{H}^+][\text{OH}^-]) = \text{pH} + \text{pOH} = 14 . \quad (5.5)$$

From (5.5) the widely in chemistry as a measure for the acidity of a solution used definition

$$\text{pH} = -\log_{10}(\text{H}^+) \quad (5.6)$$

can be deduced. This definition complies with the acid definition by Arrhenius, as a substance that increases the concentration of hydrogen ions. In Section 5.6 the influence of the hydrogen concentration on the operation of Ion-Sensitive Field-Effect Transistor (ISFET) devices will be enlightened by the site-binding model.

## 5.2 Charge Transport in Electrolytes

The electrical transport mechanisms in ionic solutions differ from that in metals/semiconductors: instead of electrons the current is sustained by ions. Additionally the ionic charge carriers are chemically active and able to contribute to chemical reactions at surfaces. Therefore, in the description of ionic conduction it is not sufficient to treat electrostatic effects solely, and chemical reactions must be included. Normally, conduction in electrolytes is caused by an externally applied bias at the electrodes/interfaces from an electronic circuit.

### 5.2.1 Bulk Transport

In the bulk only the ions are engaged in the charge transport. The charge transfer behaves similar to that in a resistor. Thus, it is adequate to find an accurate formulation for the resistivity of the bulk electrolyte in order to fully characterize transport. Often, the conductivity of electrolytes is expressed via their molar conductivity. Determining the molar conductivity is a delicate task, due to the many parameters influencing it. The ionic concentration and the valence in the solution play important roles in determining the conductivity of the bulk electrolyte. Furthermore, the degree of ionic dissociation also influences the total resistivity of the solution. For instance, 1 M of acetic acid  $CH_3COOH$  and  $NaCl$  exhibit different conductivities. Even though both solutions possess univalent bonds, their dissociation constants are different.  $CH_3COOH$  has a much smaller dissociation constant and, therefore, the number of ions is much smaller than that for the  $NaCl$  solution. Increasing the ion concentration of the solution raises the number of charge carriers. Increasing the number of charge carriers also means increasing the electrostatic interaction between the ions and thus decreasing the mobility. Kohlrausch's law covers this behavior for strong (fully dissolved) and dilute electrolytes [191]:

$$\Lambda_{\infty} = \Lambda^+ \nu^+ + \Lambda^- \nu^- , \quad (5.7)$$

where  $\Lambda_{\infty}$  denotes the molar conductivity of an electrolyte at infinite dilution.  $\Lambda^+$  and  $\Lambda^-$  are the molar conductivities for positive and negative ions, and  $\nu^+$  and  $\nu^-$  describe the valences of the corresponding ions. (5.7) presumes negligible ionic interactions between counterions for strong, dilute electrolytes and that the overall conductivity can be calculated via the sum of the positive and the negative molar conductivity weighted with their corresponding ion valence. The molar ionic conductivity is connected with the ionic mobility through:

$$\Lambda^+ = q n_A \mu^+ , \quad (5.8)$$

$$\Lambda^- = q n_A \mu^- . \quad (5.9)$$

Here,  $q$  denotes the elementary charge,  $n_A$  Avogadro's constant and  $\mu^{+/-}$  the ionic mobility for positive/negative ions. The molar conductivity at infinite dilution  $\Lambda_{\infty}$  presumes that ionic interactions have not yet started to impede the conductivity of the solution due to the *infinite*

distance between the ions. The following law allows an estimation of the relation between the effective conductivity  $\Lambda$  and the molar concentration  $[c]$ <sup>1</sup>:

$$\Lambda = \Lambda_{\infty} - K\sqrt{[c]} . \quad (5.10)$$

Since, similar forces affect the ions as those affecting electrons in metal resistors, the motion of the ions can be modeled by a resistor [191]. The value of the resistor can be deduced from (5.7)-(5.10) under the assumption of known concentrations and mobilities for the contributing ionic components.

### 5.2.2 Interface Transport

Despite the fact that the mobile charge carriers in the bulk of an electrolyte behave similar to the electrons in a resistor, the situation changes at surfaces. At least one metal-electrolyte interface is present in nearly all electrochemical experiments. The metal contact is usually called *electrode*. Compared to the charge transport phenomena in the bulk of the electrolyte or in the bulk of the electrode, the metal-electrolyte interface exhibits a quite deviating behavior. The charge carriers from the solute are not able to migrate into the metal and the electrons from the metal can not migrate into the solute without assistance. The only way to pass an electric current from the metal into the solute is a charge exchange at the interface via an electron transfer from the electrode to the ions in the liquid [190, 192]. This exchange can be utilized with a redox-reaction at the surface of the metal electrode. There are three distinguishable cases for electrodes [192]:

- *Inert Metal Electrodes*. One can think of them as ideally polarizable electrodes. These metals show high resistance to redox reactions and thus inhibit electronic transfer. This type of electrode-electrolyte interface does not allow charge transfer between the two phases and is equivalent to a capacitor.
- *Non-Polarizable Electrodes*. This type of electrodes do not exhibit any resistance to charge transfer from the electrode to the solute and therefore do not show charge accumulation at the interface. This characteristic is modeled with a short circuit or an extremely small resistor.
- *Partially Polarizable Electrodes*. These electrodes feature distinct levels of charge hindrance to the movement of the charge carriers and require a quite elaborate description of the interface.

Normally, metal-semiconductor electrodes are neither non-polarizable nor ideally polarized. Over a range of certain potentials, an interface can possess the properties of an ideally polarizable electrode, and outside of these potential intervals behave completely different [193]. The concept of an equilibrium potential is the key to describe the electric transport through the electrode interface. Every time an electrode is brought into contact with an electrolyte, redox-reactions take place and result in a certain amount of net charge in the electrolyte interface region and on the electrodes interface. This is caused by the two different chemical potentials

---

<sup>1</sup> $K$  denotes the Kohlrausch coefficient.

of the two phases [194]. The charge separation builds up an opposing electric field at the interface, thus blocking further redox-reactions. In conjunction with the excess charge a constant electrostatic potential will appear between the interface and the electrode, unless an external circuit or any other means of external charge removing process occurs. This potential can only be determined indirectly by measuring relative to another electrode. Normally, a standardized hydrogen electrode is employed as reference electrode and any standard electrode potential is measured against it [190].

Applying an external bias between the electrode and the electrolyte causes a fraction of the potential to oppose the built-in electrical potential and the rest of it, the so called *overpotential*, enables current transport through the interface. Tafel's equation [193,192] is a simplified model for the  $I - V$  characteristics:

$$i = i_0 e^{\frac{\alpha \nu q V_o}{k_B T}} . \quad (5.11)$$

$V_o$  denotes the overpotential value,  $\nu$  is the valence of the ionic species,  $\alpha$  describes a constant depending on the electrode's transfer kinetics, and  $i_0$  stands for a multiplicative constant related to the reaction rate and the exposed surface area. This description is only applicable for small voltages. Exposure to higher biases can open up paths for different phenomena and differing  $I - V$  profiles can be observed [193].

### 5.3 Insulator Surface Charge: The Double Layer

As mentioned in the Section 5.2.2, either by an externally applied voltage or by the equilibrium potential, charges gather at the electrode and in the surface area of electrolyte. The plentitude of charge carriers in the electrode lead to mutual repulsion and therefore all charge carriers will reside on the electrode surface. On the other hand, in the electrolyte the charge carriers are ions and these possess a larger radius compared to the charge carriers in the electrode (e.g. electrons in a metal). Therefore, a single layer of ions will not be able to compensate the surface charge of the electrode and a *diffusive* region of ions will form in the vicinity of the electrode surface. Due to the finite width of charges an electrostatic potential drop will arise in the *diffusive layer*. Combining concepts from electrostatic and statistical mechanics the *diffusive layer* can be described via the Poisson-Boltzmann equation. The *diffusive layer* is also known as Gouy-Chapman layer or electric double layer (depicted in Fig. 5.2). An extensive description of the Poisson-Boltzmann equation will be given in Section 6.2.1. Here, we will concentrate on the one-dimensional formulation for a 1 : 1 electrolyte:

$$\frac{d^2 \psi}{dx^2} = -\frac{1000 q n_A}{\epsilon_0 \epsilon_{sol}} ([c^+] - [c^-]) . \quad (5.12)$$

$\psi$  denotes the electrostatic potential,  $q$  the elementary charge,  $n_A$  Avogadro's constant, and  $[c^+], [c^-]$  the charge distributions for the positive and negative ions, in  $\frac{\text{mol}}{\text{l}}$  respectively. Assuming positive and negative ions in thermodynamical equilibrium with their neighborhood, their ionic densities can be related to the electrostatic potential by the following Boltzmann

distributions:

$$[c^+] = c_0 e^{-\frac{q\psi}{k_B T}} , \quad (5.13)$$

$$[c^-] = c_0 e^{\frac{q\psi}{k_B T}} . \quad (5.14)$$

Joining (5.12), (5.13) and (5.14) leads to the Poisson-Boltzmann equation for a 1 : 1 electrolyte:

$$\begin{aligned} \frac{d^2\psi}{dx^2} &= -\frac{q c_0}{\varepsilon_0 \varepsilon_{\text{sol}}} \left( e^{-\frac{q\psi}{k_B T}} - e^{\frac{q\psi}{k_B T}} \right) , \\ \frac{d^2\psi}{dx^2} &= -\frac{2q c_0}{\varepsilon_0 \varepsilon_{\text{sol}}} \sinh\left(\frac{q\psi}{k_B T}\right) . \end{aligned} \quad (5.15)$$

This ordinary non linear second order differential equation can only be solved analytically for very few cases and has to be treated with numerical methods.

The total charge density in the Gouy-Chapman layer can be calculated by ([192], derived in the Appendix C.):

$$\sigma_0 = \mp \sqrt{8\varepsilon_0 \varepsilon_{\text{sol}} k_B T c_0} \sinh\left(\frac{q\psi_0}{2k_B T}\right) . \quad (5.16)$$

## 5.4 Stern Modification

The potential distribution in the vicinity of the electrode-electrolyte interface can be approximated by the electrical double layer model. However, experimental data show deviations from the predicted values for the double layer charge and capacitance [190]. It was observed that the Gouy-Chapmann model overestimates the interface charge, and thus the capacitance for high-concentration electrolytes. Stern recognized that the ions in the electrolyte exhibit a certain *ionic radius* and, therefore, cannot approach the electrode surface closer than their *ionic radius* allows. This distance of closest approach is called the Outer Helmholtz Plane (OHP) [192]. The shell of water molecules around an ion also contributes to the distance of the closest approach. An extensive amount of energy would be necessary to release the water molecules from the aqueous shell of the ion. Therefore, close to the electrodes surface, a zone depleted of ionic charges will emerge and an additional constant contribution to the total capacitance will evolve. This so called Stern capacitance has a typical value of  $20 \frac{\mu\text{F}}{\text{cm}^2}$ . However, additionally to the Gouy-Chapmann and Stern contributions to the potential profile, several other effects exist. In general these effects are small and can be ignored. Some of these effects are (shown in Fig. 5.2):

- *Specific Adsorption of Ions on the Surface.* This is caused by (partially) freeing the ions from their solvation shell and thus allowing them to be closer to the interface than the OHP. This new radius of closest approach is called Inner Helmholtz Plane (IHP). The total model, handling IHP and OHP, is called Gouy-Chapman-Stern-Graham model [191].
- *Non-Specific Adsorption.* Here, the ions keep their solvation shell, but are adsorbed onto the surface due to distant coulombic attraction.
- *Polarization of Solvent.* In general, the effects of electric field weakening due to the dipole moment of the water molecules is handled by adjusting the relative permittivity. This

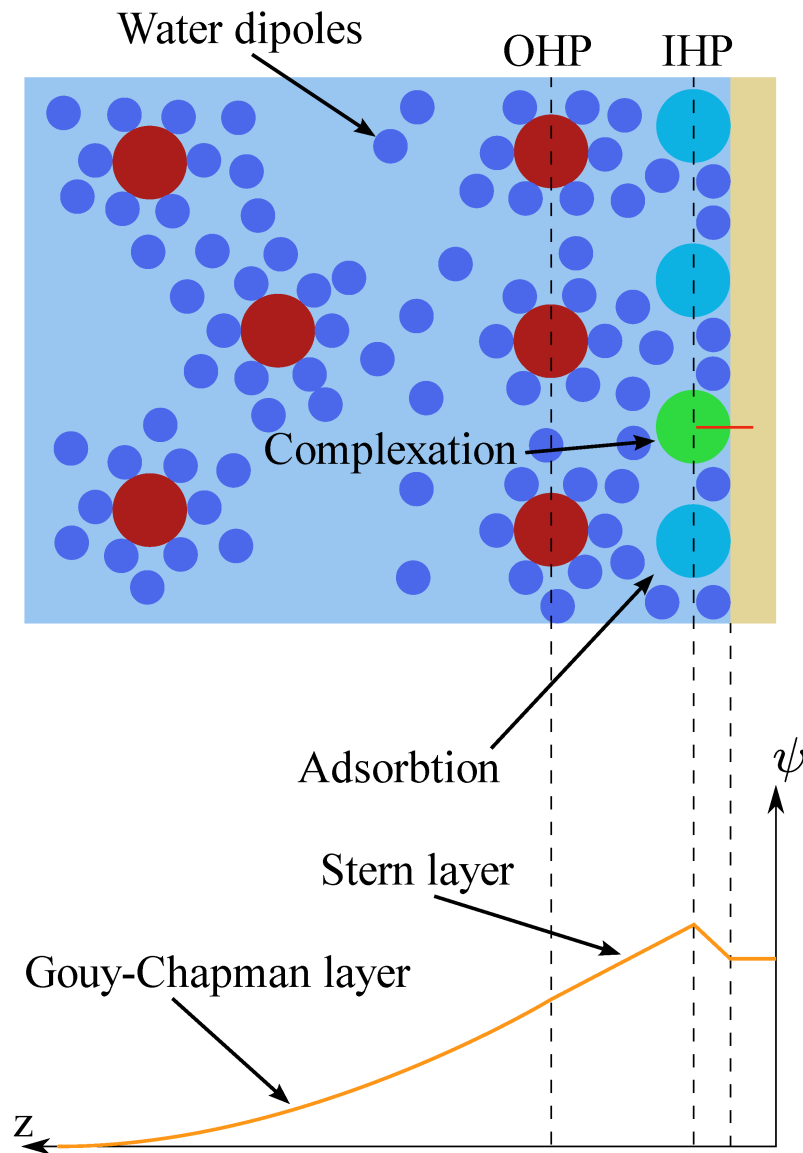


**Figure 5.2:** The different surface effects. The (*non-*) *specific adsorption*, due to (partial) release of the solvation shell and conjoint closer approach to the interface, the so called IHP, is depicted with blue circles. The effect of *surface complexation*, due to the high affinity of attracting counter ions, is shown by the green circle. The Stern layer ends at the OHP, the zone without counter ions exhibiting their full water shell (depicted with red circles, surrounded by small light blue circles), and is continued by the Gouy-Chapman layer.

works well for the bulk, but in the vicinity of the surface many water molecules are not able to adjust to the electric field. So the relative permittivity will not be the same as for the bulk and can cause differences in the results (e.g. potential and charge distribution). However, at high electric fields, the description of the dielectric constant can become more complicate, due to dielectric saturation<sup>2</sup>.

- *Surface Complexation.* Many charged surfaces exhibit an increased attraction to counter ions and enable the formation of complex compounds at the surface, changing the potential in their neighborhood.

## 5.5 Ionic Activity

It has been shown that chemical reactions are described by their equilibrium constants (q.v. Section 5.1), which are correlated to the concentrations of the reactants. The concentration of a certain reactant can differ in one area compared to other areas [196,197], for which the before discussed double layer is an example. Many different effects can cause an excess ion concentration. Here, only concentration changes caused by electrostatic potentials will be treated. In areas containing varying concentrations it would be incorrect to describe chemical reactions by their bulk concentration values. Instead, one must use the local concentration values of the corresponding reactants at the location of the short-range chemical reactions. The activity of ions based on their bulk values and related to their local electrostatic potential with respect to the bulk are:

$$\begin{aligned} [a^+] &= a_0 e^{-\frac{q\psi}{k_B T}} , \\ [a^-] &= a_0 e^{\frac{q\psi}{k_B T}} . \end{aligned} \tag{5.17}$$

(5.17) is exploited, when the site-binding model by Yates et al. [198] is derived (Section 5.6).

## 5.6 Insulator Surface Charge: Site-Binding Model

The Gouy-Chapman-Stern model describes the main contributions to the electric double layer. It relates the accumulated charge at the surface of the electrochemical interface to the applied potential. Despite the accurate description of the electrostatic interactions, there is no chemical interaction included in the model. Chemical reactions at the interface can lead to a net charge presence at the insulator's interface [198]. In this section the site-binding model will be investigated, allowing to include chemical processes at the insulator interface in the description. The inability of the regular double layer model to predict the correct net charge density in the electrolyte, shows the need for embracing chemical reactions at the interface with the site-binding model.

Unlike for electrostatic forces which act over long ranges, chemical reactions only occur within molecular distances. Therefore the assumption that chemical reactions are only possible within the OHP is chosen. Firstly, ionic species from the dissolved salt hold a water shell and cannot

---

<sup>2</sup>Polar fluids experience at high electric fields a non linear decrease in their permittivity [195].

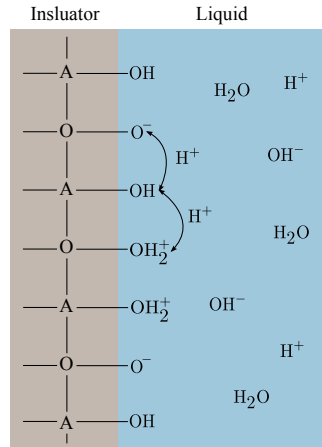


**Figure 5.3:** The insulator surface exhibits open binding sites due to the lack of insulator bonding partners at the surface. These binding sites can be either negatively/positively charged or neutral, depending on the properties of the liquid covering the surface. The surface charge density depends on the surface potential  $\psi_0$ , material properties, and the local hydrogen concentration  $[\text{H}^+]_b$ .

come closer to the interface than the OHP. Therefore, ions cannot contribute to the chemical reactions at the insulator interface (neglecting the possibility of specific adsorption of salt ions). Secondly, the much smaller hydrogen ions are not blocked by the OHP, due to their much smaller ionic radius and being not hydrated. They can approach the interface close enough to enable chemical reactions. As depicted in Fig. 5.3 the surface of an insulator inhabits a huge amount of unsaturated bonds. Neglecting unspecific adsorption, the only ions capable of bonding these sites are the hydrogen and hydroxyl ions [196, 197, 198], because they are not shielded by water layers. The following chemical reactions are dynamically balanced in the membrane, under the assumption of thermal equilibrium and without any net reaction<sup>3</sup>:



M denotes the insulator material, for instance,  $\text{SiO}_2$ . The first reaction tends to charge the oxide surface positively, while the second reaction tends to charge the insulator surface negatively. The final charge density on the insulator's surface is defined by the number of initial bonding sites (also known as amphoteric sites), and by the local density of hydrogen ions. The chemical reactions can be translated via the law of mass action into the following relations:

<sup>3</sup>chemical forward- and back-reaction rates are equal

$$K_a = \frac{[M - OH][H^+]}{[MH_2^+]} , \quad (5.20)$$

$$K_b = \frac{[M^-][H^+]}{[M - OH]} . \quad (5.21)$$

Calculating the surface charge from (5.20) and (5.21) one has to take care not to proceed with the bulk hydrogen concentrations. Since the surface potential is different from the bulk potential and the chemical reactions also take place directly at the surface, the ionic charge population of hydrogen at the surface is expected to be different from the bulk hydrogen concentration as well. Therefore, the activity of hydrogen should be used rather than the bulk hydrogen concentration. If the only affecting forces are of electrostatic nature, the activity of hydrogen can be formulated like in (5.17) and can be expressed for the positive hydrogen ions as:

$$[a_{H^+}] = [H^+]_b e^{-\frac{q\psi_0}{k_B T}} . \quad (5.22)$$

$$(5.23)$$

Substituting (5.22) into (5.20) and (5.21) facilitates the connection between the surface potential of the electrolyte and the charge density aggregated on the insulator's surface by the chemical reactions. The total surface charge density is given by:

$$\sigma_{Ox} = q ([MH_2^+] - [M^-]) , \quad (5.24)$$

while the total binding site density is give via

$$N_s = ([MH_2^+] + [M - OH] + [M^-]) . \quad (5.25)$$

Joining (5.20)-(5.25), the surface charge density due to the chemical reaction can be written as:

$$\sigma_{Ox} = qN_s \frac{\frac{[H^+]_b}{K_a} e^{-\frac{q\psi_0}{qk_B T}} - \frac{K_b}{[H^+]_b} e^{\frac{q\psi_0}{qk_B T}}}{1 + \frac{[H^+]_b}{K_a} e^{-\frac{q\psi_0}{qk_B T}} + \frac{K_b}{[H^+]_b} e^{\frac{q\psi_0}{qk_B T}}} . \quad (5.26)$$

Some parameter sets for the site-binding model are presented in Table 5.1 for several common materials. Fig. 5.4 shows the relation between the surface charge density and the surface potential for different gate dielectrics as described by (5.26). The maximum amount of surface charge is directly proportional to the number of surface sites per unit area and the steepness and width of the two appearing steps is related to the difference between the reaction rates  $pK_a$  and  $pK_b$ . That this charge accumulation at the surface will influence the charge distribution of the double layer and in the underlying semiconductor, due to the long range character of the electrostatic forces. The overall charge neutrality has to be guaranteed by:

$$\sigma_{Ox} + \sigma_0 + \sigma_s = 0 , \quad (5.27)$$

where  $\sigma_{Ox}$  denotes the charge density per unit area from the site-binding model,  $\sigma_0$  the charge density per unit area in the electrolytic double layer, and  $\sigma_s$  the charge density per unit area in the semiconductor. Adding (5.26) and (5.27) to the system of equations ((5.12) and (5.16)) the

**Table 5.1:** Parameters for the site-binding model commonly used for sensing ( $pK_i = -\log_{10}(K_i)$  analog to the definition of  $pH = -\log_{10}([H^+])$ ).

Oxide	$pK_a$	$pK_b$	$N_s [cm^{-2}]$	Reference
SiO <sub>2</sub>	-2	6	$5 \cdot 10^{14}$	[197]
Si <sub>3</sub> N <sub>4</sub>	-8.1	6.2	$5 \cdot 10^{14}$	[1]
Al <sub>2</sub> O <sub>3</sub>	6	10	$8 \cdot 10^{14}$	[197]
Ta <sub>2</sub> O <sub>5</sub>	2	4	$1 \cdot 10^{15}$	[200]
Gold surface	4.5	4.5	$1 \cdot 10^{18}$	[201]

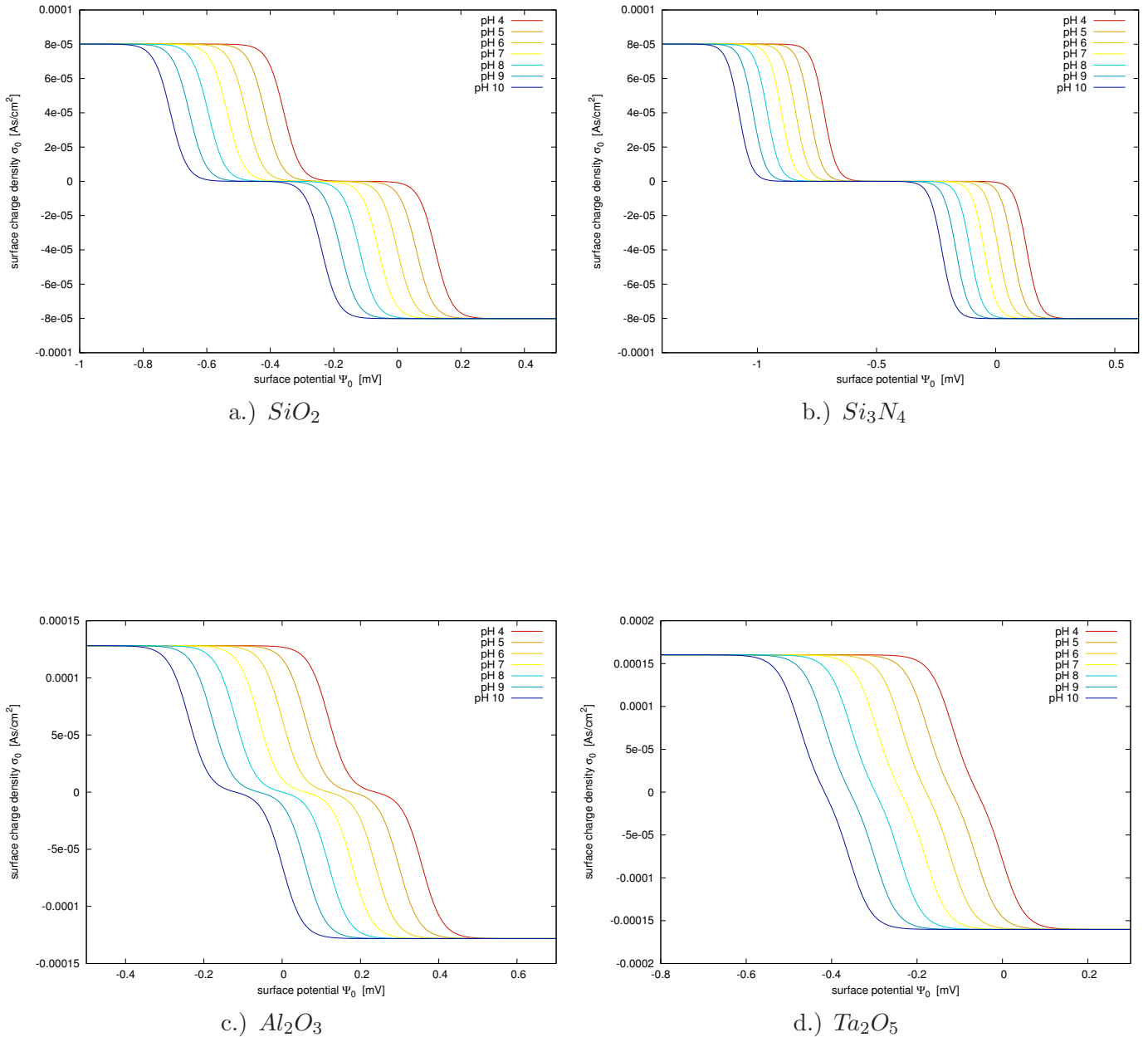
description is able to cover chemical reactions at the insulators surface. However, the aggregation of charge at the oxide surface can impose serious problems to the design of biosensors. At the same time, it can be exploited to facilitate very efficient pH sensors [199].

One may have wondered, why the hydrogen distribution is considered via the Boltzmann type terms at the interface within the site-binding region, while outside the OHP in the electric double layer the charge distribution of the salt ions is taken into account and the hydrogen distribution is neglected. This apparent contradiction can be resolved as follows: At the oxide surface the hydrogen concentration has a strong influence on the equilibrium constants for the reactions (5.20) and (5.21), while the hydrogen diffusive layer is much smaller than the ion diffusive layer. In a relatively dilute solution containing 1 mM of *NaCl*, the salt is completely dissolved into 1 mM  $Na^+$  and 1 mM  $Cl^-$ . Assuming a pH of 7, the hydrogen concentration in the electrolyte will be about 100 nM. This shows that the concentration difference between the hydrogen and the sodium is four orders of magnitude. Therefore, the hydrogen diffusive double layer has a negligible influence on the potential in the Gouy-Chapman layer compared to the site-binding region of the electrolyte.

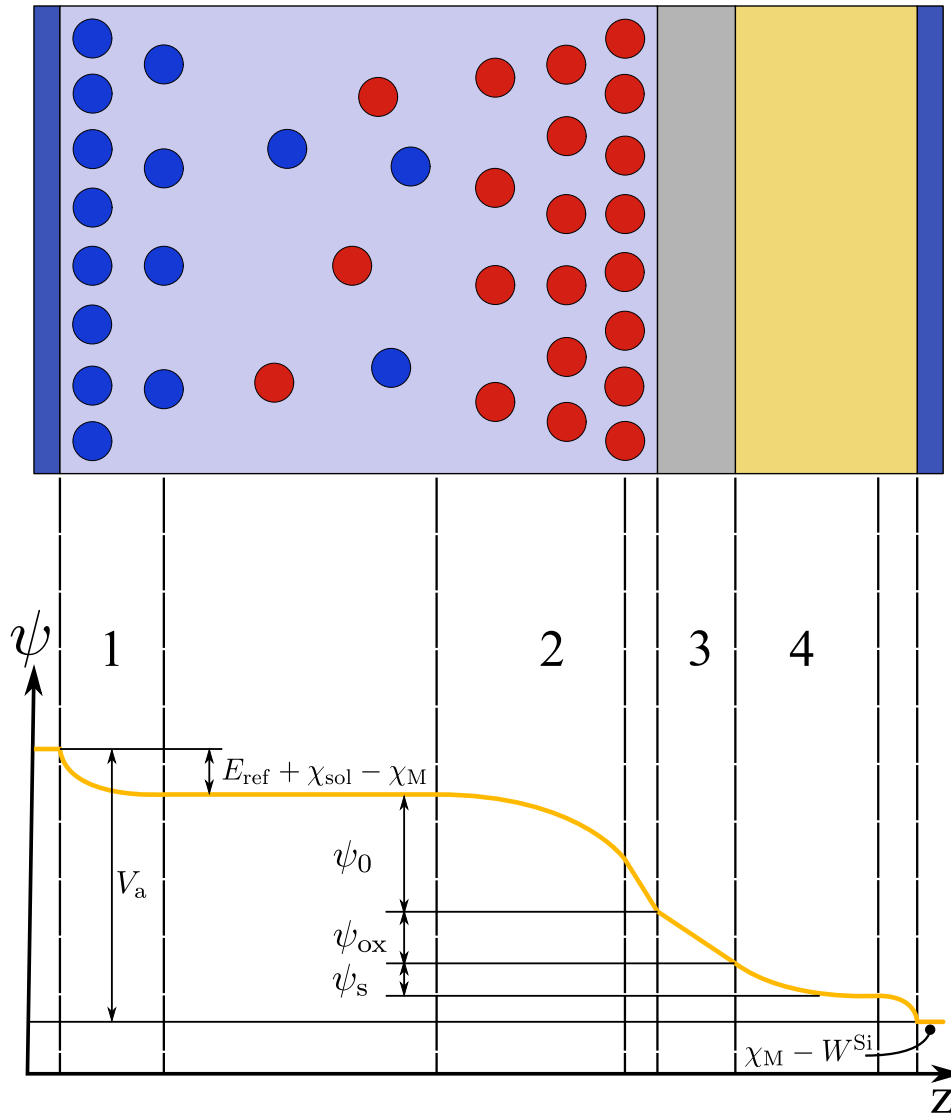
## 5.7 The Potential Diagram of an ISFET Gate Stack

Fig. 5.5 depicts a simplified diagram for the potential profile of an ISFET structure [16]. An ISFET consists of a regular MOSFET, possessing source, drain and body contacts. However, as explained in Section 2.5, for a Biologically sensitive Field-Effect Transistor (BioFET)/ISFET the gate contact is detached from the dielectric and replaced by an electrolytic solution and a reference electrode. The main purpose of this structure is to provide efficient coupling between the electrolytic area with the electronic substrate. This kind of structure enables electronic sensing of chemical and biological processes [202].

One of the major characteristics of a FET device is the flatband voltage, which is a part of the threshold voltage  $V_t$  in a MOSFET transistor. As derived in Appendix E., the flatband voltage  $V_{FB}$  of a MOSFET is related to the workfunction differences between the gate and the substrate materials, and to the amount of aggregated charge on the dielectric's surface and inner of the dielectric. Different circumstances can lead to a rise (or reduction) of the charges at the interface. This is reflected by the proportionality between the change in the amount of charge and the adjustment in the threshold voltage  $V_t$ . Small changes of charge can be sensed electrically. In the case of a correlation between a chemical or biological process and the modulation of charge, the ongoing process can be detected with high efficiency [203].



**Figure 5.4:** As illustrated in the panels a.) to d.), the higher the surface site density  $N_s$  is the bigger the maximal surface charge density  $\sigma_0$  will be. All curves show two distinct steps in the relation between surface charge density  $\sigma_0$  and surface potential  $\psi_0$ . The larger the difference between the forward positively charging reaction rate  $K_a$  and the negatively charging reaction rate  $K_b$  the more pronounced and steeper are these steps.



**Figure 5.5:** Potential profile in an ISFET structure for a cut along the z-axis.  
 1.) The potential drop at the electrode-electrolyte interface, caused by the Gouy-Chapman-Stern double layer ( $E_{\text{ref}} + \chi_{\text{sol}} - \chi_{\text{M}}$ ).  
 2.) The Gouy-Chapman-Stern double layer at the electrolyte-insulator interface ( $\psi_0$ ).  
 3.) The potential drop in the insulator ( $\psi_{\text{ox}}$ ).  
 4.) The potential drop due to the depletion charges in the semiconductor ( $\psi_{\text{s}}$ ).

By analogy to the analysis of a MOSFET, the bare ISFET has to be described via equations relating the occurring current in the channel to the applied voltages at the terminals. However, in addition a set of equations expressing the amount of immobilized charges via the appearing current, or, equivalently, the amount of immobilized charges via the observed shift in the threshold voltage, is needed [204].

In the following a one-dimensional model of the electrostatic potential distribution through the entire ISFET capacitor structure under a bias potential  $V_a$  is derived. There are several distinctive potential drops in the structure:

1. The potential drop caused by the Gouy-Chapman-Stern double layer at the electrode-electrolyte interface.
2. The potential drop caused by the Gouy-Chapman-Stern double layer at the electrolyte-insulator interface.
3. The potential drop within the insulator.
4. The potential drop caused by the depletion of charges in the semiconductor.

Fig. 5.5 shows the electrostatic potential difference occurring due to the charge diffusion driven by the differences in work functions. Due to the insulator, there is no current flowing through the structure under equilibrium conditions. Therefore, the potential drops between the metal and the semiconductor, and between the metal and the electrolyte, are constant and do not depend on the applied bias [205]. Additionally the potential drop from the Stern layer was conjoined with the potential drop across the electrolyte, shown in Fig. 5.5. For a given bias  $V_a$ <sup>4</sup>, the following electrochemical equilibrium equation arises [204]:

$$V_a = \tilde{u}_M - \tilde{u}_{Si} = \Phi_M - \frac{u_M}{q} - \Phi_{Si} + \frac{u_{Si}}{q} . \quad (5.28)$$

Here,  $\tilde{u}_M$  and  $\tilde{u}_{Si}$  denote the electrochemical potential for the metal and silicon, respectively.  $\Phi_M$  and  $\Phi_{Si}$  stand for the inner potentials of the metal electrode and silicon, while  $u_M$  and  $u_{Si}$  represent chemical potentials. The electrostatic potential drop in the electrode-electrolyte interface is constant and independent of the applied bias under equilibrium conditions and can be merged into a reference electrode potential  $E_{ref}$  [196]:

$$E_{ref} = \Phi_M - \Phi_{sol} - \frac{u_M}{q} . \quad (5.29)$$

This reference potential  $E_{ref}$  is fixed for a given salt concentration and a given electrode material. Substituting the definition of (5.29) into (5.28) yields:

$$V_a = E_{ref} + \frac{u_{Si}}{q} + \Phi_{sol} - \Phi_{Si} . \quad (5.30)$$

The potential difference  $\Phi_{sol} - \Phi_{Si}$  can be split into four different contributions:

---

<sup>4</sup>between the reference electrode and the bulk contact

1. The diffusive double layer (also known as Gouy-Chapman layer) within the electrolyte interface ( $\psi_0$ ).
2. The potential drop due to the depletion charge in the semiconductor ( $\psi_s$ ).
3. The potential drop through the dielectric ( $\psi_{ox}$ ).
4. The potential drop due to the different electron affinities between the solution and the semiconductor.

Taking all these components into account leads to [203, 206]:

$$V_a = E_{\text{ref}} + \frac{u_{\text{Si}}}{q} + \psi_{\text{ox}} + \psi_s + \psi_0 - \chi_{\text{sol}} - \chi_{\text{Si}} . \quad (5.31)$$

Again, all constant terms can be joined in one expression, analogously to the flatband voltage in a regular MOSFET structure,

$$V_{\text{FB}} = E_{\text{ref}} + \frac{u_{\text{Si}}}{q} + \chi_{\text{sol}} - \chi_{\text{Si}} . \quad (5.32)$$

Without parasitic charges and defects, the externally applied potential  $V_a$  in the ISFET and the accumulated potential drop in the electrolyte and the semiconductor can be related via:

$$V_a = V_{\text{FB}} + \psi_{\text{ox}} + \psi_s - \psi_0 . \quad (5.33)$$

In comparison to the standard MOSFET description, there is an extra entry  $\psi_0$  contributing to the overall potential drop across the structure. This potential drop is a function of the applied bias and cannot be merged into the flatband voltage. It represents the chemical and biological processes at the insulator-electrolyte interface and every biological or chemical reaction will be reflected by a modification of the potential drop  $\psi_0$ . Assuming a constant applied bias, a modulation in the potential drop  $\psi_0$  will cause an adjustment in the semiconductor surface potential  $\psi_s$  and in the dielectric potential drop  $\psi_{\text{ox}}$ , in a way consistent with (5.33). Accordingly the conductance of the channel will be modulated and a change in the source to drain current will be observed.

The three potential drops in (5.33) must be linked via two complementary conditions, in order to solve the equation system for the ISFET. One of these constraints is the charge neutrality for the whole device:

$$\sigma_0 + \sigma_s = 0 . \quad (5.34)$$

Supposing, there are no other charges in the system, the charges in the semiconductor side must be equal to the total charge of the double layer. The semiconductor charge is related to the surface potential by (7.54), see Appendix D., while the electric double layer charge relation (7.43) is derived in Appendix C.. Finally, the last condition is gained by the electric displacement field at the two insulator boundaries. This boundary condition demands a continuous and equal flux density at both insulator surfaces:

$$\varepsilon_{\text{Si}} \frac{d\psi_s}{dz} = \varepsilon_0 \frac{d\psi_0}{dz} \quad (5.35)$$

Combining the expression for the first derivative in Appendix D. and the expression for the second derivative in Appendix C., a third equation is gained, linking the potentials  $\psi_0$ ,  $\psi_s$ , and  $\psi_{ox}$ . These three equations can be solved self-consistently (by e.g. an iterative method), and the potential distribution and channel resistance can be determined.

If the modeled system exhibits a surface with dangling bonds able to bind hydrogen, the site-binding model (5.26) has to be taken into account. Accordingly, (5.34) has to be modified to (5.27), so that the charge accumulation due to the open oxide bonds is included.

## 5.8 The ISFET as a Sensor

The ability of changing the electrolyte surface potential in an ISFET device can be exploited for various sensor applications. The possible sensor types can be chemically, e.g. a  $CO_2$  sensor, as well as biologically, e.g. detecting the pH change due to cell metabolism, motivated. Depending on the type of sensor the mechanism changing the electrolytes surface potential varies. Most methods exploit a change in the charge population in the electrolyte. Commonly, depending on the nature of the experiment, reactants, or mechanisms leading to the modification of the charge distribution, ISFET devices are addressed as Chemically sensitive Field-Effect Transistor (CHEMFET), Enzyme Field-Effect Transistor (ENFET), DNA sensitive Field-Effect Transistor (DNAFET), or BioFET as a generic term.

There are two major concerns for efficient sensor designs: sensitivity and specificity. Specificity, is meant in the context of only responding to the selected species without any unwanted cross interactions. For instance, an ISFET sensor for  $Na^+$  must not react to any of  $Mg^{++}$  or  $Ca^{++}$  ions. However, as explained in the previous sections, an ISFET gate stack does not meet these requirements ad hoc: due to the electrostatic interaction any charge carrier will be sensed by the FET. There are ways to circumvent this obstacle as will be explained later. Sensitivity, used here in a chemical and biological context, is the minimum concentration of the target species required to generate a fair signal level at the sensor's output. Sensors designed for the same species, but exploiting different physical phenomena, can show different sensitivities. For instance, mass spectroscopy with a detection limit of  $\sim 10^{-8} \frac{g}{ml}$  is less sensitive than electrochemical sensors  $\sim 10^{-13} \frac{g}{ml}$  [207].

The manifold different techniques for permitting an ISFET gate stack to change its surface potential, can be divided for two distinct applications: affinity based sensors and catalytic sensors [199]. For *affinity* based sensors, the reaction at the surface of the insulator is caused by chemical and thermodynamic affinity, while for *catalytic* sensors the reaction is driven by certain locally constrained catalysts at the surface [208].

### 5.8.1 Sensing pH with an ISFET

ISFETs facilitate the detection of ions in a relatively easy way, thus, this application is most commonly used. The device relies on the chemical interaction between the surface binding sites and the hydrogen ions as explained in Section 5.6. This pH sensitivity was also the initial application by Bergveld [203]. The change in the flatband voltage per pH change in the solution determines the sensitivity of the ISFET device. The major criteria of the sensitivity of the oxide

**Table 5.2:** Sensitivity of ISFET devices for different gate dielectrics.

Sensitive layer	pH range	Sensitivity [ $\frac{mV}{pH}$ ]
$SiO_2$	4 – 10	24 – 36 [210]
$Al_2O_3$	2 – 12	54 – 56 [211]
$Si_3N_4$	4 – 11	52 – 58 [1]
$Ta_2O_5$	2 – 12	56 – 58 [211]

surfaces are determined by the surface binding site density  $N_s$  and the forward and backward reaction constants  $K_a$  and  $K_b$  (5.26). Table 5.2 shows some sensitivity values for different commonly used gate dielectric materials. Therefore, one can produce an efficient pH sensor by utilizing the open surface binding sites for detecting the dissolved protons. However, if large dissolved ions are desired for detection, due to their water shell, they cannot approach the interface closer than the OHP and thus the surface binding approach is not feasible. This problem can be circumvented by preparing a reaction medium in the ISFET gate stack such that the target species will generate excess hydrogen ions via a chemical reaction and thus change the pH of the solution. This method is particularly appealing for acid-base reactions, where the pH of the solution is directly affected by the reaction rate.  $CO_2$  sensing in an electrolytic solution is a good example of this type of mechanism [209]. Carbon dioxide  $CO_2$  reacts with water producing carbon acid and hydroxyl ions. The process is governed by the following reaction:



Utilizing this type of reactions enables the ISFET to detect different kinds of ions via the hydrogen dependent reaction at the empty dangling bonds of the oxide surface. With this type of sensor the ions are not sensed directly, because they can not interact with the surface. Only the excess hydrogen ions caused through the chemical reaction at the solvation of the desired ions will react with the dielectric interface.

Many different ionic sensors are based on their tendency to change the pH of a solution (act as a base or acid in an aqueous solution). In order to maintain the specificity of the sensor one has to take care that other eventually present ions do not contribute. Any change in the pH of the solution must be provoked from reactions concerning the target ions. This can be accomplished by adding a number of membranes to the ISFET chip, which are only transparent to the desired target ion [199] (as illustrated in Fig. 5.6). Applying this kind of additional layer, only the target ions will be able to reach the gate insulator and contribute to the local pH of the solution at the gate insulator interface.

### 5.8.2 Sensing via Catalysts

*Catalyst*-based detection is realized by immobilized catalyst agents on the surface of the insulator. The target is injected in a well prepared environment which only allows chemical reactions via the catalyst at the interface. The catalytic reaction (e.g. oxidation) yields a release of charge, which can be sensed by the ISFET. For instance, Kharitonov et al. [212] showed

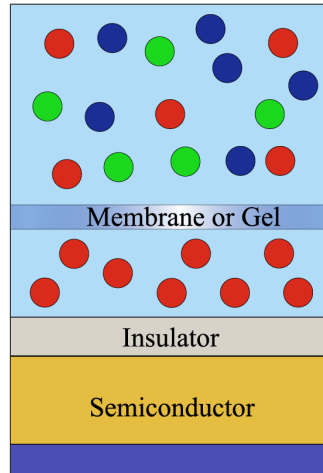
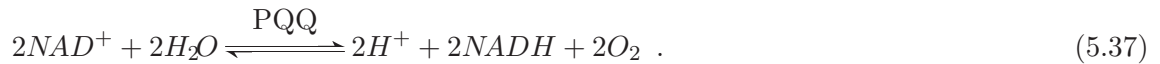


**Figure 5.6:** Introducing a membrane into the ISFET hinders unwanted ion-species to diffuse to the insulator interface. Thus, only the selected ion species can approach the gate insulator, and the selectivity of the ISFET is ensured.

a nicotinamide adenine dinucleotide ( $NAD^+$ ) detector, utilized by a pyrroloquinoline quinone (PQQ) catalyst. The chemical reaction is written as follows:



Catalyst spare the need for a selective membrane impeding diffusion of undesired ions to the surface area of the ISFET, due to its immobilization at the surface and restriction to the reaction (5.37). Therefore, such sensors exhibit a high degree of selectivity. However, the predicted and the measured pH level may slightly disagree due to the catalyst molecules introducing auxiliary effects at the insulator surface.

### 5.8.3 Examples for ISFETs as pH Sensor

An ISFET device as depicted in Fig. 2.9 has been simulated for different pH values. The studied device exhibits a channel length of  $15\ \mu\text{m}$  and thus fits well into the drift-diffusion regime of transport. Therefore, the Poisson equation in conjunction with the drift-diffusion model for current transport has been exploited within the semiconductor, while the Poisson-Boltzmann model was used in the solute. The experimentally determined voltage shifts per pH decade, are well reproduced by the site-binding model by Yates [198] without any special adjustments to the model parameters.

Fig. 5.7 shows the potential profile for a cut perpendicular to the gate dielectric. The predicted voltage shift per pH step for  $Si_3N_4$  has been reported in the range  $52 - 58\ \frac{\text{mV}}{\text{pH}}$  (Table 5.2). As can be seen in Fig. 5.7 the voltage shifts fit quite well the experimental data. Furthermore, the

influence of the incorporated Phosphate Buffered Saline (PBS) depends strongly on its concentration. A decreasing PBS concentration correlates to reduced screening within the solute and thus results in a longer decay of the potential in combination with saturation at higher pH levels. PBS is a buffer solution commonly used in biological research. This salty solution consists of sodium chloride and sodium phosphate and in some formulations additionally of potassium chloride and potassium phosphate. The buffer is normally applied to maintain constant pH and the osmolarity and ion concentrations of the solution match those of the human body. It is valuable due to its isotonicity and non-toxicity to cells and therefore is regularly employed for diluting substances or rinsing container holding cells. In the simulations carried out only potassium chloride was accounted for, because it represents  $\approx 90\%$  of the ingredients. Incorporating the whole buffer would have increased the computational effort without changing the results significantly.

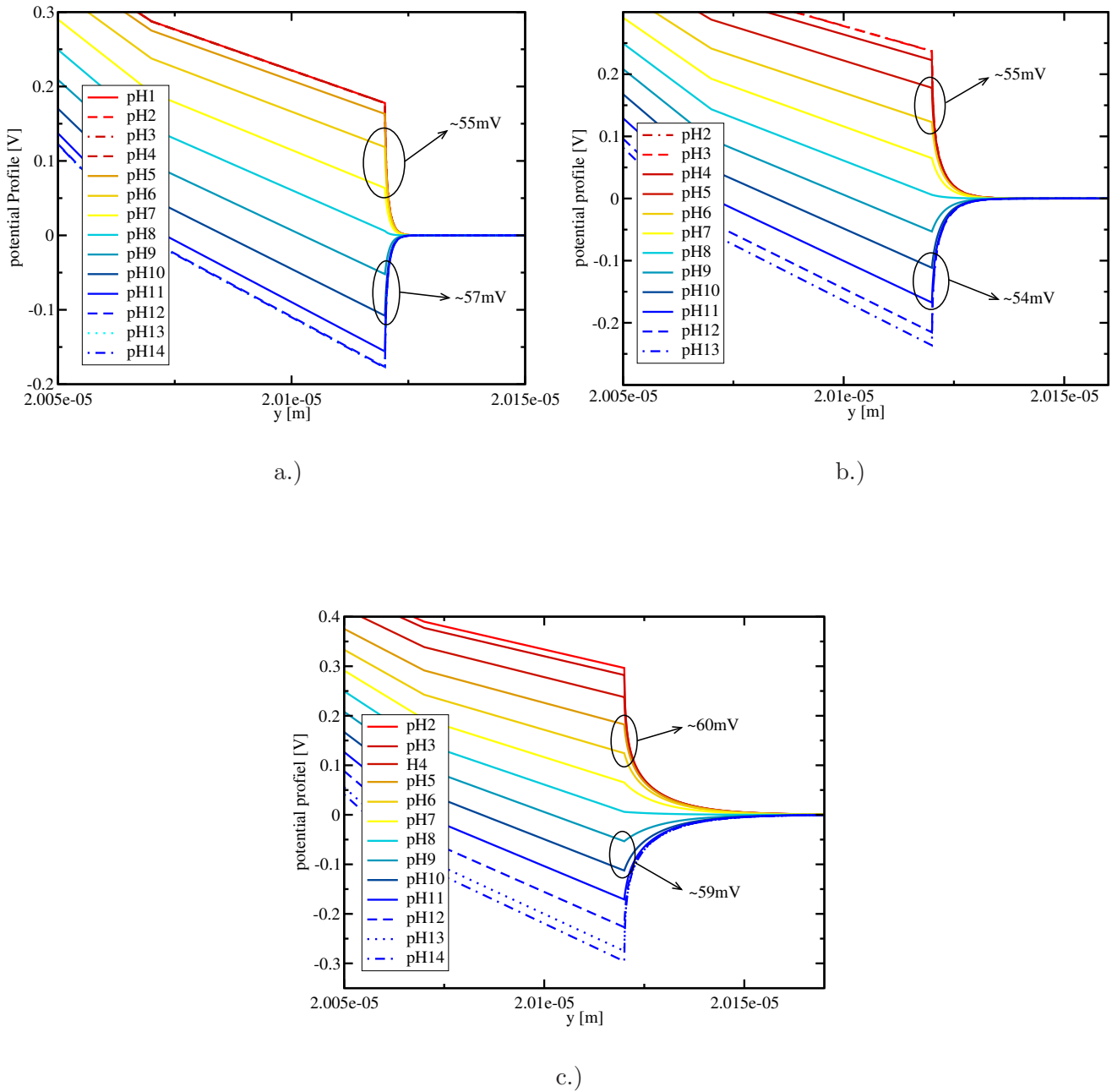


**Figure 5.7:** Potential profile for a cut perpendicular to the surface of the ISFET (beginning at the left border: semiconductor, dielectric, and solute). The simulations were carried out for a.) 100 mMol, b.) 10 mMol, and c.) 1 mMol phosphate buffered saline (PBS).  $Si_3N_4$  was utilized as gate dielectric at different pH values. Simulation results with the parameter set by Harame et al. [1], fit excellent the experimental values. With decreasing buffer concentration the screening is reduced and the saturation starts at higher pH values. The reduced screening is also reflected in the prolonged decay of the potential in the liquid.

---

# Generalization of the ISFET Concept

---

AS long as the chemical reaction is governed by relatively simple equations like (5.36) or (5.37), the methods described in the previous chapter are quite efficient, but there are cases where one wants to detect large charged molecules or organic polymers. These so called *macromolecules* exhibit certain structures determining their activity and other properties. In this case, the structure of the molecule is important. Therefore, even if a simple reaction able to change the pH of the solution is available, it is not effective, because it does not provide a way to determine the actual structure of the molecule. However, there is a possibility to utilize an ISFET device to determine the structure of a molecule via the so-called *long-range field-effect*.

### 6.1 Sensing via the Long-Range Field-Effect

Since most of the biological polymers are inherently charged, the key of the working principle is to exploit the intrinsic charges in the macromolecules. Therefore, if one is able to bring the macromolecule close enough to the surface of the dielectric, the intrinsic charges of the macromolecules will cause a formation of counter charges in the semiconductor by the field-effect. Due to the counter screening of the salt ions in the solute and the relatively wide distance (at least the OHP) compared to the hydrogen charges directly at the oxide interface, the sensitivity is expected to be lower than for an ISFET exploiting pH changes. Many effects, involving the ionic counter charge around the molecule and the surface charge of the dielectric, are able to diminish the field-effect of the macromolecule in the semiconductor. Therefore, it was believed that the detection of macromolecules like DNA is not feasible [196]. However, many experiments disproved this assumption and showed the practicability of such an approach [17, 152, 213]. Fig. 6.1 illustrates the long-range field-effect for large macromolecules e.g. proteins or DNA.

This device type, termed as BioFET, exhibits several advantages compared to currently established methods. The biggest advantage against common solutions is the label-free operation of BioFETs. Instead of labeling the analyte with fluorescent or radioactive probes and a subsequent readout step by an appropriate detection technique, the BioFET device allows a simplified

analyte preparation and a direct readout via an electrical signal, thus, saving time, expenses and laboratory equipment. Furthermore, the label-free technique, enables near real-time sensing and a high sensitivity. Exploiting the specificity of a given chemical reaction (“key-lock” principle), the sensor can be adapted for a wide range of molecule classes via exchanging the functionalization of the dielectric surface.

## 6.2 Modeling BioFETs

There exist two main approaches for the simulation in such devices. In the first approach the system is described via a set of differential equations and proper boundary conditions, while in the second one every molecule in the solute is described separately and is thus free to move within the solute, attempting to minimize acting forces (the energy of the system). This process is simulated via a stochastic Monte Carlo process [214]. The Monte Carlo approach allows a relatively easy description of the system via the fundamental interactions between single molecules/atoms, but needs a high amount of memory and offers an accuracy of the results of only  $\sim \frac{1}{\sqrt{N}}$  ( $N$  is the sample size). The high amount of memory is caused by the vast amount of molecules/atoms within the solute. For instance, 1 ml water contains about  $\approx 3.35 \times 10^{22}$  of water molecules. Even, restricting to the simulation of the macromolecules and describing the water molecules via a permittivity coefficient of  $\sim 80$ , the memory consumption remains on a high level, since macromolecules easily contain several thousand atoms. There are further approaches to reduce the memory need, but the overall memory consumption abides on a high level and the simulation domain is restricted to small volumes. Also the time scale

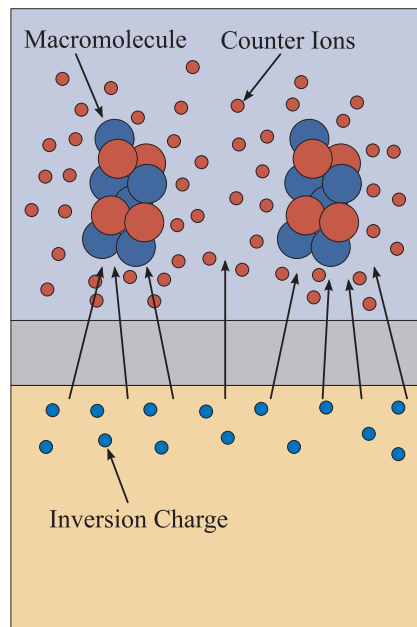


**Figure 6.1:** Sensing a macromolecule via the long-range field-effect.

such simulations can handle are quite small ( $\sim$  ps, [215,216]) and not comparable to time scales needed in real world applications (seconds to hours).

The differential equation approach on the contrary, is less memory and time consuming, but treats the quantities as continuous. This can cause misleading results for low buffer concentrations as will be shown later.

The difference between these two approaches originate from the different scales of the macromolecule and the FET device. Chemical reactions take place at the Angstrom length-scale, while the ISFET channel gate length is in the micrometer regime. Therefore, depending on the results to achieve one has to decide which approach is the more promising to conquer the multi-scale problem for his needs.

In this work the differential equation approach was chosen, because the emphasis was laid on the device behavior in conjunction with the preferred usage by engineers.

The simulation domain is split into several parts. There are the semiconducting region, the dielectric region, the Stern layer, the zone where the macromolecules are held, and the region containing the buffer (shown in Fig. 6.2). The device is in the micrometer regime and it is therefore possible to model transport in the semiconducting part via the drift-diffusion model [217,218]. The dielectric is modeled with the Laplace equation, assuming that there is no charge in the oxide. The Stern layer, ensuring a minimal distance of the charged zone containing the macromolecules to the oxide interface, is modeled with the Laplace equation and a relative permittivity of  $\epsilon_{\text{sol}} \approx 80$ . The presence of charge at the dielectric-electrolyte interface depends on the preparation of the device. Often the surface is passivated before the macromolecules are attached to it. The reasons for this are manifold: a need to suppress unwanted charge accumulation at the open oxide sites which could mask the charges from the macromolecules during detection, to avoid an unwanted pH dependence, and to prepare the surface in a way that the macromolecules can be linked (attached) to the surface. The charge density in the zone containing the macromolecules can either be determined by experimental data or must be estimated from the macromolecules structure itself derived from a protein data bank (e.g. [2]). This zone and the remaining electrolytic region are modeled with different approaches, described in the following sections.

### 6.2.1 Poisson-Boltzmann Model

The often employed Poisson-Boltzmann model is a good approximation for electrolytes from several mMol upwards. Assuming that the dissolved buffer ions are in thermodynamical equilibrium with their environment and their concentration only depends on the local potential, the charge contribution from the buffer can be written as sum over all ionic species of the buffer weighted with Boltzmann type terms  $e^{\frac{q\psi}{k_B T}}$  and their valences. The Poisson-Boltzmann model has been already introduced in Section 5.3 and is now generalized to a two-dimensional formulation<sup>1</sup>:

$$\epsilon_0 \nabla \cdot (\epsilon_{\text{sol}} \nabla \psi(x, y)) = - \sum_{\xi \in S} \xi q c_{\xi}^{\infty} e^{-\xi \frac{q}{k_B T} (\psi(x, y) - \psi_{\mu})} + \rho_{\text{Space}}(x, y) . \quad (6.1)$$

<sup>1</sup>In general this formulation can be extended to three dimensions, but due to the device geometry two-dimensional cuts are sufficient.

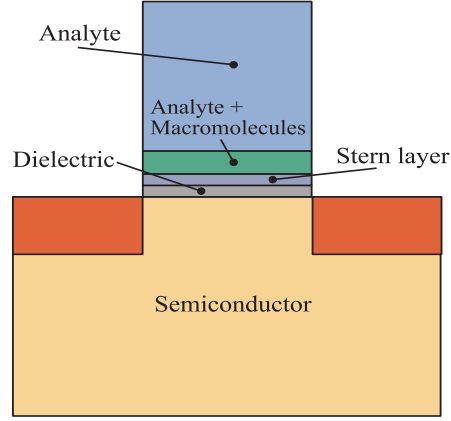


**Figure 6.2:** BioFET: different simulation zones.

$k_B$  denotes Boltzmann's constant,  $T$  the temperature in Kelvin, and  $\xi \in S$ , where  $S$  contains the valences of the ions in the electrolyte.  $\varepsilon_0$  is the permittivity of vacuum, and  $q$  denotes the elementary charge.  $\psi_\mu$  is the chemical potential.  $c_\xi^\infty$  is the ion concentration in equilibrium, while  $\varepsilon_{sol} \approx 80$  is the relative permittivity of water.  $\rho_{Space}$  represents the average space charge density in the simulation zone, where the charged macromolecules are held.

### 6.2.2 Poisson-Boltzmann Model with Sheet Charge

Looking at the region containing the charged macromolecules linked to the surface and not being dispensed in a gel, one recognizes that its height is typically in the deca nanometer regime. Thus, it is extremely thin compared to the rest of the device dimensions. Therefore, to save mesh points, one introduces the average charge density replacing this region with an equivalent sheet charge  $\sigma_{Sheet}(x)$  at the surface  $y_0$ .

$$\varepsilon_0 \nabla \cdot (\varepsilon_{sol} \nabla \psi(x, y)) = - \sum_{\xi \in S} \xi q c_\xi^\infty e^{-\xi \frac{q}{k_B T} (\psi(x, y) - \psi_\mu)} + \sigma_{Sheet}(x) \delta(y - y_0) \quad (6.2)$$

### 6.2.3 Poisson-Boltzmann Model with Homogenized Interface Conditions

A similar but somewhat refined model was derived in [219, 220, 221]. The authors solved the multi-scale problem by exchanging the fast varying charge distribution at the surface (e.g. Proteins or DNA fragments scattered over the functionalized surface) by two interface conditions. These interface conditions describe the effects of the charge and the dipole moment of the bio-functionalized layer, including the charged macromolecules:

$$\varepsilon_{\text{Oxid}} \partial_y \psi(0-, x) - \varepsilon_{\text{sol}} \partial_y \psi(0+, x) = -\frac{C(x)}{\varepsilon_0}, \quad (6.3)$$

$$\psi(0-, x) - \psi(0+, x) = -\frac{D_y(x)}{\varepsilon_{\text{sol}} \varepsilon_0}. \quad (6.4)$$

Here,  $\psi(0-)$  describes the potential at the dielectric-electrolyte interface from the oxide, while  $\psi(0+)$  denotes the interface potential from the solute. The first equation describes the jump in the field, while the second introduces a dipole moment which causes a shift of the potential.  $C(x)$  is the averaged (homogenized) charge density at the dielectric-electrolyte interface and can either be determined by experimental data or derived from first principle calculations via a data set from a protein data bank [2].  $D_y(x)$  is the averaged dipole moment density and has to be gained from first principle calculations. For instance, the *adaptive Poisson-Boltzmann solver* (APBS) [222, 223, 224] allows to assign partial charges to every atom belonging to the desired macromolecule, and therefore the calculation of the overall charge and in conjunction with the relative distances between the atoms also the dipole moment of the molecule. This charge and dipole moment can be linked to the mean charge and mean dipole moment assuming an average distance between the macromolecules.

#### 6.2.4 Extended Poisson-Boltzmann Model

The extended Poisson-Boltzmann model [225] incorporates the average closest possible distance two ions within the liquid can approach. This allows to include the Stern layer within this formulation without the need to add an ion free zone between the dielectric and the region where the Poisson Boltzmann model is working. Furthermore, the closest possible approach between two ions  $a$  is in this model a fit parameter and can therefore account for the varying screening behavior at different ionic concentrations:

$$\varepsilon_0 \nabla \cdot (\varepsilon_{\text{sol}} \nabla \psi) = 2q c_0^\infty \frac{\left( a - (a-1) \cosh\left(\frac{q\psi}{2k_{\text{B}}T}\right) \right) \sinh\left(\frac{q\psi}{2k_{\text{B}}T}\right)}{\left( (1-a) + a \cosh\left(\frac{q\psi}{2k_{\text{B}}T}\right) \right)^3}. \quad (6.5)$$

Here,  $c_0^\infty$  denotes the bulk ion concentration for a 1 : 1 salt. In the limit  $\lim_{a \rightarrow 0}$  the Poisson Boltzmann expression is recovered. One has to mention that this formulatin is limited to 1 : 1 electrolytes and therefore can not be applied to an arbitrary solute. In Section 6.3 some examples will be considered.

#### 6.2.5 Debye-Hückel Model

The Poisson-Boltzmann equation constitutes a nonlinear differential equation for the electrostatic potential. Frequently one is interested in a formulation which is numerically less demanding or even an analytical solution. This has been done by Debye and Hückel [226] in 1923, who derived a linearized version of the Poisson-Boltzmann equation. Starting with the corresponding thermodynamical potential, they rigorously deduced the Poisson-Boltzmann model and from

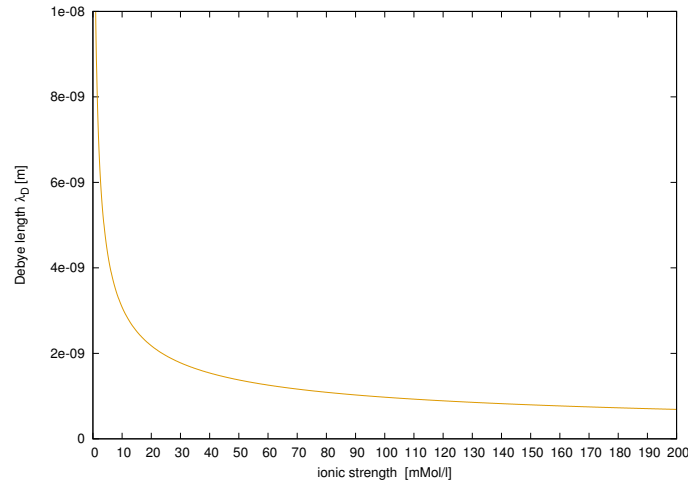


**Figure 6.3:** The dependence of the Debye length on ion concentration for a 1 : 1 electrolytic solution. Higher salt concentration reduces the repulsion between complementary DNA strands, and thus accelerates the hybridization events, but, at the same time, decreases the Debye length  $\lambda_D$  and therefore the device signal.

this their Debye-Hückel equation by Taylor expansion of the exponential terms, neglecting contributions higher than first order. This model is valid only for small potentials in relatively dilute electrolytes:

$$\epsilon_0 \nabla \cdot (\epsilon_{\text{sol}} \nabla \psi(x, y)) = \frac{q^2}{k_B T} (\psi(x, y) - \psi_\mu) \sum_{\xi \in S} \xi^2 c_\xi^\infty + \rho_{\text{Space}}(x, y) \quad (6.6)$$

From (6.6) two important properties can be gained. Firstly, the Debye length  $\lambda_D$ :

$$\lambda_D = \sqrt{\frac{k_B T \epsilon_0 \epsilon_{\text{sol}}}{q^2 \sum_{\xi \in S} \xi^2 c_\xi^\infty}} \quad \text{or in terms of ionic strength } I(\vec{x}) \quad (6.7)$$

$$= \sqrt{\frac{k_B T \epsilon_0 \epsilon_{\text{sol}}}{2 q^2 I(\vec{x})}}. \quad (6.8)$$

The Debye length  $\lambda_D$  is the characteristic length of the electrolytic system. It is the length at which the charge density and also the electric potential of an ion atmosphere reduces to  $1/e$ .

The Debye length  $\lambda_D$  is also an important parameter in the sense of giving a rule of thumb on how far a charged macromolecule can be away from the dielectric-electrolyte interface without being completely shielded by the ions in the electrolyte. It is also a measure of how much of the macromolecule's charge is actually able to couple to the semiconductor without being screened for very large macromolecules (e.g. DNA). The Debye length  $\lambda_D$  affects the double layer thickness. Increasing the concentration or valence of the counterions compresses the double layer and raises the potential gradient.

The second parameter is already introduced in (6.8) and describes the ionic strength of the electrolyte defined as:

$$I(\vec{x}) = \frac{1}{2} \sum_{\xi \in S} \xi^2 c_{\xi}^{\infty}(\vec{x}) \quad (6.9)$$

The ionic strength of a solution is a measure of the concentration of ions in the solution. The ionic compounds (e.g. salts), dissociate into ions, when they are dissolved in water. Ionic strength is one of the main characteristics of a solution with dissolved ions, which influences many important properties like, the dissociation or solubility of different salts and the double layer thickness. The ionic strength is utilized to describe the strong deviations from the ideality typically experienced in ionic solutions via the Debye-Hückel theory. It is furthermore related to electrokinetic phenomena, electroacoustic phenomena in colloids and other heterogeneous systems and linked to the electric double layer (eq. (6.8)). The Debye length  $\lambda_D$  is inversely proportional to the square root of the ionic strength Fig. 6.3.

In order to minimize changes during a titration<sup>2</sup> in the activity quotient of solutes at lower concentrations, media with high ionic strength are employed. Natural waters such as seawater have a non-zero ionic strength due to the presence of dissolved salts which significantly affects their properties.

## 6.2.6 Buffers and Ionic Strength

Normally, the experiment is carried out in a so called *buffer* solution. There are several reasons for this. For instance, enzyme reactions are very sensitive to the local temperature, the local substrate concentration, and also to their *chemical* environment (e.g. pH). In this case the buffer fulfills the function of stabilizing the pH of the solution at a certain point and thus keeping the enzyme activity at its maximum. If DNA is going to be hybridized<sup>3</sup>, the ions in the buffer gather around the single DNA strands and screen partially the DNA charge. The repulsion between the two negatively charged single DNA strands is reduced and they can approach each other close enough to enable the hybridization reaction.

The utilization of buffers is a path way to control the chemical properties of the environment in which the chemical reaction is conducted. Therefore, buffers are also a significant ingredient in the description of BioFETs and a method to calculate the ion concentrations and the ionic strength for an arbitrary buffer will be given. Beynon and Easterby published a book about buffer solutions, giving an exhaustive and easy introduction into this topic [5].

### 6.2.6.1 Temperature Effects on Buffers

$pK_a = -\log_{10}(K_a)$  is, analogously to the definition of the pH of a solution, for the reaction  $a$ . Since the equilibrium constant of a buffer is determined by the laws of thermodynamics, it has to depend on temperature. This is described by  $\frac{dpK_a}{dT}$ , the change of  $pK_a$  with temperature.

<sup>2</sup>Titration is an often employed laboratory method of quantitative chemical analysis, used to determine the unknown concentration of a known reactant.

<sup>3</sup>Nucleic acid hybridization is the process of joining two complementary strands of DNA

The logarithmized equilibrium constant depends on the applied buffer and can exhibit positive or negative values, or even being close to zero. Therefore,

$$pK_{a,T} = pK_a + \frac{dpK_a}{dT} (T - 298.15 \text{ K}) , \quad (6.10)$$

$T$  denotes the temperature and  $pK_a$  represents the *thermodynamic*  $pK_a$  value for  $25^\circ\text{C}$ .

### 6.2.6.2 Debye-Hückel Relationship

Biological sensors are typically employed at a certain pH. The pH can be adjusted by titration and monitored by measurement. Hence, pH is an input parameter for the simulation. Starting with a given pH, the buffer ion concentrations can be calculated including temperature effects and the ionic strength of the solution.  $pK'_{a,T}$  determines the buffer ion concentrations but also depends on the ionic strength  $I(\vec{x})$  and temperature  $T$ . Since the ionic strength also depends on the buffer ion concentration, this nonlinear equation system has to be solved self-consistently. The effect of the ionic strength  $I(\vec{x})$  on  $pK'_a$  can be compressed in one relation (also known as the Debye-Hückel relationship):

$$pK'_{a,T} = pK_{a,T} + (2\xi_a - 1) \left[ \frac{A\sqrt{I}}{1 + \sqrt{I}} - 0.1 I \right] . \quad (6.11)$$

$pK'_{a,T}$  is termed as *modified*, *working*, or *practical*  $pK_a$  value,  $\xi_a$  is the charge on the conjugate acid species and  $A(T)$  is a temperature dependent constant.  $A$  is normally around  $\sim 0.5$  (at  $T = 0^\circ\text{C}$   $A = 0.4918$  and at  $T = 100^\circ\text{C}$   $A = 0.6086$ ). Furthermore,  $pK'_{a,T}(\vec{x})$  is a function of position, because the ionic strength exhibits a position dependence, while  $pK_{a,T}$  is only related to temperature.

### 6.2.6.3 Henderson-Hasselbach Equation

The Henderson-Hasselbach equation connects the relative concentrations of acid and base and the  $pK'_{a,T}$  of the conjugate acid/base pair to the pH of the electrolyte,

$$pH = pK'_{a,T} + \log_{10} \left( \frac{[\text{acid}]}{[\text{base}]} \right) . \quad (6.12)$$

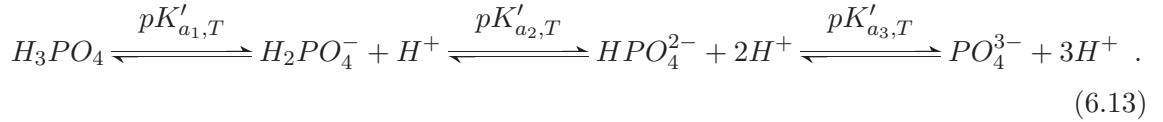
On account of the spatial coordinate dependence of all input quantities, the local pH is also a function of position. In the vicinity of the interface the pH value will deviate from the pH value in the bulk electrolyte. Remembering that the ion concentrations are also related to the local potential via the Poisson-Boltzmann equation, further complicates the situation. In order to include all effects one has to employ a numerical approach and solve the equations in a self-consistent manner.

A feasible algorithm works as follows:

1. Define the temperature  $T$  and the bulk pH value.
2. Define a buffer. Normally there is already one specified from an experiment. If none is available, choose a buffer with a  $pK_a$  near to the required pH.
3. Correct the  $pK_a$  values to the given temperature  $T$ .
4. Calculate the concentrations of the conjugate base and acid via the Henderson-Hasselbach equation.
5. Calculate the ionic strength  $I$  of the buffer, including counter ions.
6. Calculate  $pK'_a$  from  $pK_{a,T}$  with the ionic strength from the step before.
7. Return to Step 4 and calculate the ionic strength  $I$  again, but this time with the *refined*  $pK'_a$  values.
8. Calculate the  $pK'_a$  values again with the new ionic strength from the step before.
9. Repeat Step 7 and Step 8 until convergence is reached. Typically four cycles are enough to reach a relative error of  $\sim 10^{-3}$ .

#### 6.2.6.4 PBS as an Example

In order to further clarify the procedure, how to calculate the ionic strength and the different ion concentrations in the buffer, the procedure for a PBS will be presented. PBS contains orthophosphoric acid  $H_3PO_4$  and exhibits three dissociation reactions:



Applying the Henderson-Hasselbach equation to (6.13) and utilizing charge conservation to gain the sodium concentration leads to the following set of equations:

$$[H_3PO_4] = \frac{[PBS]}{1 + 10^{pH - pK'_{a1,T}} \left( 1 + 10^{pH - pK'_{a2,T}} \left( 1 + 10^{pH - pK'_{a3,T}} \right) \right)} , \quad (6.14)$$

$$[H_2PO_4^-] = [H_3PO_4] 10^{pH - pK'_{a1,T}} , \quad (6.15)$$

$$[HPO_4^{2-}] = [H_2PO_4^-] 10^{pH - pK'_{a2,T}} , \quad (6.16)$$

$$[PO_4^{3-}] = [HPO_4^{2-}] 10^{pH - pK'_{a3,T}} , \quad (6.17)$$

$$[Na^+] = -\xi_1 [H_2PO_4^-] - \xi_2 [HPO_4^{2-}] - \xi_3 [PO_4^{3-}] . \quad (6.18)$$

Here,  $\xi_1$ ,  $\xi_2$ , and  $\xi_3$  are the valencies of the  $H_2PO_4^-$ ,  $HPO_4^{2-}$ , and  $PO_4^{3-}$ , respectively, and the concentration of the PBS and the pH value in the bulk electrolyte is kept fixed. The iteration procedure given before with the values in Table 6.1 yields the ion concentrations depicted in

**Table 6.1:** Parameters for the chosen phosphate buffer saline (PBS) [5].

Symbol	value	unit
$pK_{a_1}$	2.15	
$pK_{a_2}$	7.21	
$pK_{a_3}$	12.33	
$dpK_{a_1}$	0.0044	1/K
$dpK_{a_2}$	-0.0028	1/K
$dpK_{a_3}$	-0.0026	1/K
$\xi_{a_1}$	0.0	
$\xi_{a_1}$	-1.0	
$\xi_{a_1}$	-2.0	
$A$	0.5114	
$T$	25 + 273.15	K

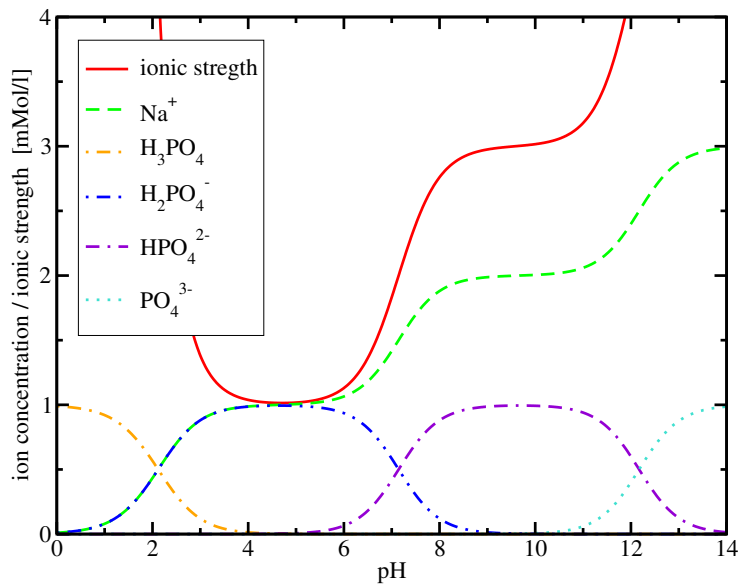
**Figure 6.4:** The dependence of the concentrations for different ionic components and the ionic strength on the local pH.

Fig. 6.4, which illustrates the buffer ion concentrations and the ionic strength as a function of pH at  $25^\circ\text{C}$  and  $1 \frac{\text{mMol}}{\text{l}}$ . The ionic strength rises strongly for small pH values (high  $[\text{H}_3\text{O}^+]$  concentration) and high pH values (high  $\text{OH}^-$  concentration). Furthermore, the influence of the valence on the ionic strength is very pronounced due to the quadratic dependence in (6.9).

### 6.3 Analytical Comparison between the Poisson-Boltzmann, the Extended Poisson-Boltzmann, and the Debye-Hückel Model

For better comparison between the Poisson-Boltzmann, the extended Poisson-Boltzmann, and the Debye-Hückel model we study their one-dimensional analytical solutions without any charges from macromolecules or due to the site-binding effect at the oxide surface. The surface potential  $\varphi_0$  will be chosen in a way that all models exhibit the same charge at the surface and that the potential  $\varphi$  and the electric field  $\mathcal{E}$  vanish in the limit of infinite distance away from the surface. In the first step all equations are transformed to dimensionless units.

Reformulating the Laplace term

$$\frac{d\varphi^2}{dz^2} = -\frac{d\mathcal{E}}{dz} = \mathcal{E} \cdot \frac{d\mathcal{E}}{d\varphi} \quad (6.19)$$

and transforming the equations with

$$\varphi = \frac{q\psi}{k_B T} \quad \text{and} \quad (6.20)$$

$$\frac{1}{\lambda_D^2} = \frac{2q^2 c_0}{k_B T \varepsilon_0 \varepsilon_{\text{sol}}} \quad , \quad (6.21)$$

leads to the following differential equations:

$$\mathcal{E} \cdot \frac{d\mathcal{E}}{d\varphi} = \frac{1}{\lambda_D^2} \sinh(\varphi) \quad (6.22)$$

for the Poisson-Boltzmann model,

$$\mathcal{E} \cdot \frac{d\mathcal{E}}{d\varphi} = \frac{2}{\lambda_D^2} \frac{(a + (1-a) \cosh(\varphi/2)) \sinh(\varphi/2)}{((1-a) + a \cosh(\varphi/2))^3} \quad (6.23)$$

for the extended Poisson-Boltzmann model and

$$\mathcal{E} \cdot \frac{d\mathcal{E}}{d\varphi} = \frac{1}{\lambda_D^2} \varphi \quad , \quad (6.24)$$

for the Debye-Hückel model.

Assuming vanishing potential  $\varphi$  and vanishing electric field  $\mathcal{E}$  for large distances  $z \rightarrow \infty$ , integrating these equations twice results in the following solutions:

$$\varphi(z) = 2 \ln \left( \frac{1 - e^{-z/\lambda_D} \tanh(\varphi_0/4)}{1 + e^{-z/\lambda_D} \tanh(\varphi_0/4)} \right) \quad (6.25)$$

$$\mathcal{E}(z) = \frac{4}{\lambda_D} \frac{e^{-z/\lambda_D} \tanh(\varphi_0/4)}{1 - e^{-2z/\lambda_D} \tanh^2(\varphi_0/4)} \quad , \quad (6.26)$$

for the Poisson-Boltzmann model [227],

$$z(\varphi) = -\lambda_D \ln \left| \frac{\tanh^{1-a} \left( \frac{\varphi}{4} \right) \sinh^a \left( \frac{\varphi}{2} \right)}{\tanh^{1-a} \left( \frac{\varphi_0}{4} \right) \sinh^a \left( \frac{\varphi_0}{2} \right)} \right|, \text{ or with only } \varphi/2 \quad (6.27)$$

$$-\lambda_D \ln \left| \frac{(\cosh \left( \frac{\varphi}{2} \right) + 1)^{a-1} \sinh \left( \frac{\varphi}{2} \right)}{(\cosh \left( \frac{\varphi_0}{2} \right) + 1)^{a-1} \sinh \left( \frac{\varphi_0}{2} \right)} \right|, \quad (6.28)$$

or via  $\mathcal{E}$  as a function of  $\varphi$

$$\mathcal{E}(\varphi) = \frac{2}{\lambda_D} \frac{\sinh(\varphi/2)}{1 - a + a \cosh(\varphi/2)}, \quad (6.29)$$

for the extended Poisson-Boltzmann model [225], and

$$\varphi(z) = \varphi_0 e^{-z/\lambda_D} \quad (6.30)$$

$$\mathcal{E}(z) = \varphi_0/\lambda_D e^{-z/\lambda_D} \quad (6.31)$$

for the Debye-Hückel model [226].

Unfortunately the analytical expression (6.27) is not as handy as the expressions (6.30) for the Debye-Hückel model and (6.25) for the Poisson-Boltzmann model. As can be seen in (6.27), only for the position  $z$  as a function of the potential  $\varphi$  it is possible to write down a compact analytical expression, while for the inverse function one has to use numerical approaches. However, in the limit  $a \rightarrow 0$  the solution for the Poisson-Boltzmann model is recovered [225].

In the next step we assume an equivalent surface charge  $\sigma_0$  for all three models, in order to accomplish a better comparison between them. This is realized by choosing an arbitrary charge at the surface and applying Gauß's law. This way, a surface potential  $\varphi_0$  related to the same surface charge can be found.

The corresponding surface potentials are:

$$\varphi_0 = \varphi(0) = 2 \ln \left( \frac{1 - \zeta}{1 + \zeta} \right) \text{ with} \quad (6.32)$$

$$\zeta = \frac{1}{\lambda_D \sigma_0} \left( 2 + \sqrt{4 + \lambda_D^2 \sigma_0^2} \right), \quad (6.33)$$

for the Poisson-Boltzmann model [227],

$$\varphi_0 = \varphi(0) = -2 \operatorname{arccosh} \left( \frac{(1-a) a \frac{\lambda_D^2 \sigma_0^2}{4} - \sqrt{1 + \frac{\lambda_D^2 \sigma_0^2}{4} - a \frac{\lambda_D^2 \sigma_0^2}{2}}}{1 - a^2 \frac{\lambda_D^2 \sigma_0^2}{4}} \right), \quad (6.34)$$

for the extended Poisson-Boltzmann model [225], and

$$\varphi_0 = \varphi(0) = \lambda_D \sigma_0, \quad (6.35)$$

the Debye-Hückel model, respectively.

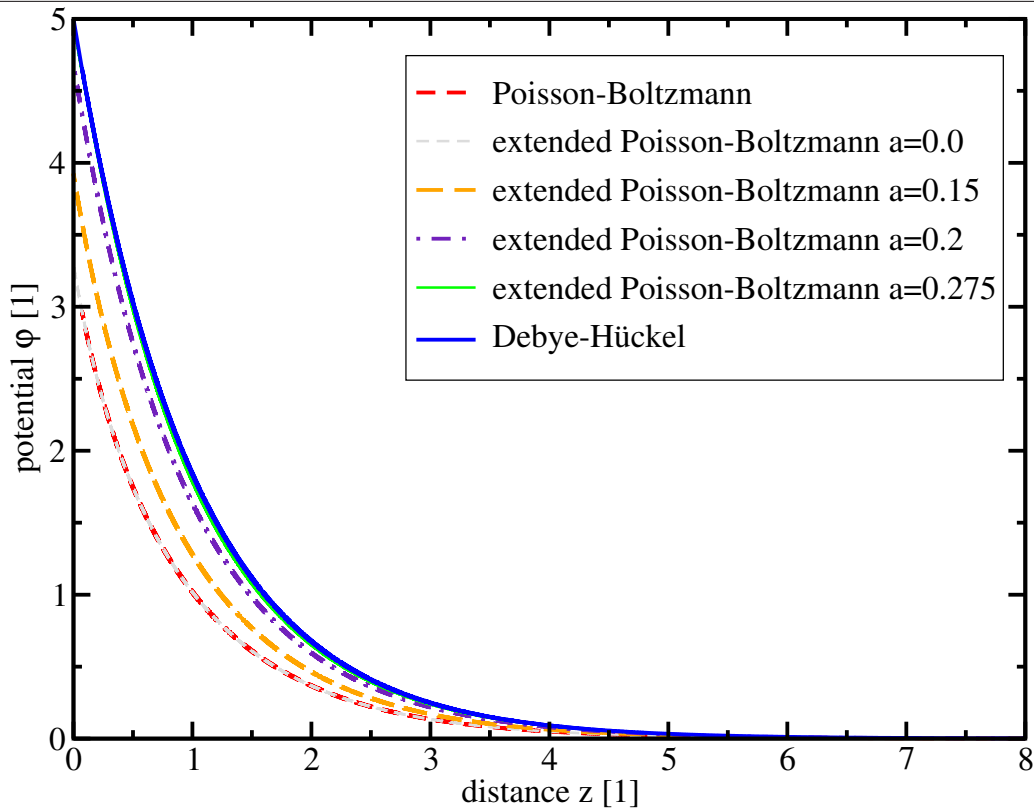


**Figure 6.5:** Illustrating the different screening characteristics for the Poisson-Boltzmann, the extended Poisson-Boltzmann, and the Debye-Hückel model. In the limit of  $a \rightarrow 0$  the extended Poisson-Boltzmann model rejoins the Poisson-Boltzmann model, while for increasing closest possible ion distance  $a$ , which corresponds to a decreasing salt concentration, the screening is reduced and resembles for  $a = 0.275$  the Debye-Hückel model.

Fig. 6.5 shows a comparison between the Poisson-Boltzmann, the extended Poisson-Boltzmann, and the Debye-Hückel model. As already mentioned before, one can see that for  $a \rightarrow 0$  the extended Poisson-Boltzmann model and the Poisson-Boltzmann model coincide. Increasing the closest possible approach  $a$  between two ions, leads to a reduction in screening and thus higher surface potential  $\varphi_0$ . Furthermore, for  $a = 0.275$  the extended Poisson-Boltzmann model aligns quite well with the Debye-Hückel model. This shows that the extended Poisson-Boltzmann model is able to cover a wider range of screening behavior than the Poisson-Boltzmann and the Debye-Hückel model.

## 6.4 BioFET Examples

In this section possible surface modifications for a BioFET are demonstrated. Several examples regarding BioFETs functionalization with single stranded DNA, utilizing the different models outlined in Section 6.2, followed by a second BioFET functionalized for a biotin-streptavidin reaction, using a SGFET with different dielectric materials is discussed.

### 6.4.1 DNAFET

The ability of ISFETs to sense the charge in deoxyribonucleic acid (DNA) can be exploited to craft biosensors able to detect specific DNA sequences [189,196,208]. This possibility has a vast impact in many areas, like food and environmental monitoring, development of patient-specific drugs, and gene expression experiments. Therefore, the simulation of so called *DNAFETs* is currently extremely interesting. However, in order to give a better overview about DNAFETs, a small introduction to DNA and the currently established detection methods will be given prior to the simulation results.

#### 6.4.1.1 DNA Structure

DNA and proteins are regularly addressed as the main active components in all living organisms [228]. The DNA stores via molecular sequences in the polymere all genetic information. Watson and Crick found that DNA consists of a double helix structure. Each helix is a compound of a repeating structure, containing a sugar polymer, a nitrogen base and a phosphate ion. The nitrogen base can be one of four select bases. Namely, adenine (A), thymine (T), cytosine (C), and guanine (G). A DNA strand may consist of several millions of such base pairs and the specific sequence of bases within the DNA strand allows to encode specific genetic information concerning an organism. A *species signature* can be build from particular subsequences of an organism's DNA, thus providing a genetic finger print [189,228]. The two helical strands are bound together by weak hydrogen bonds formed between the bases. The bonds between A and T, and between C and G have been found to be thermodynamical favorable. Therefore, only helical DNA strands with complementary bases will be able to fully bind and form a thermodynamically stable compound. The process of double helix formation, called *hybridization*, is a fundamental part in the life cycle of any living organism, facilitating the multiplication of genetic code.

### 6.4.2 DNA Hybridization Sensors

#### 6.4.2.1 Studying the Angular Dependence of DNA in Relation to the Surface on the Device Characteristics

Fig. 6.6a and Fig. 6.6b sketch a DNAFET with a functionalized surface, exhibiting single DNA strands containing 12 phosphate groups. Every phosphate group possesses one elementary charge ( $-1e$ ). Thus, the unbound single stranded DNA is charged with  $-12e$  elementary charges (Fig. 6.6), while the hybridized DNA strand features  $-24e$  elementary charges.

Here, the Poisson-Boltzmann model with homogenized interface conditions (see Section 6.2.3)

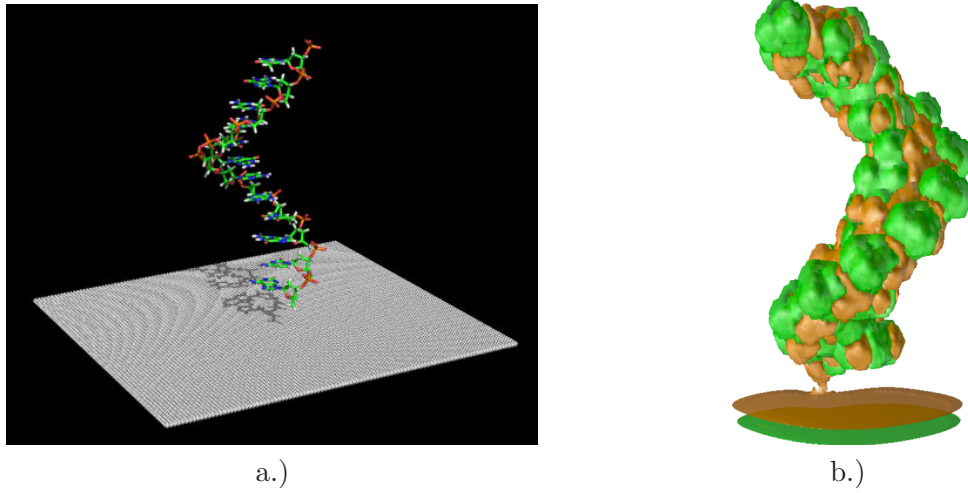


**Figure 6.6:** a.) The unbound single-stranded DNA at the surface of the dielectric.  
 b.) Single-stranded DNA on the oxide surface. Two iso-surfaces for plus and minus  $0.2 \frac{k_B T}{qA^2}$  are shown.

has been applied. It allows to introduce the angular dependence of the molecule orientation in relation to the surface by its mean dipole moment. Starting with a data set from a protein data bank [2], one can calculate the overall charge and the dipole moment for a single DNA strand. Since, only the dipole moment perpendicular to the surface enters in (6.4), one has to calculate the perpendicular dipole moment for different inclination angles of the DNA. The charge and dipole moment of the single (unbound) and the double (bound/hybridized) DNA strand can be related to average charge densities and dipole moments by introducing an average distance between the macromolecules.

Simulations were carried out for two average distances  $\lambda$  (10 nm and 15 nm). For each mean distance the potential profiles and output characteristics at different states were simulated. The states were: the unprepared surface, where no DNA is attached, the prepared but unbound state, where single-stranded DNA is attached to the surface, and the bound state, when the single-stranded DNA has been hybridized to double-stranded DNA. Additionally, calculations for  $0^\circ$  (dipole moment perpendicular to the surface) and  $90^\circ$  (dipole moment parallel to the surface) were carried out. 100% binding efficiency was assumed.  $SiO_2$  was chosen as dielectric. The potential at the reference electrode was set to 0.4 V, setting the nMOS to moderate inversion as proposed by [160].

Fig. 6.7a illustrates the potential profile in the BioFET including the solute. Fig. 6.7b shows the potential profile for a cut throughout the middle of the device orthogonal to the interface of the dielectric, for the unprepared state and the bound state. As can be seen, when the negatively charged DNA is attached to the interface, the potential in the channel changes. This upward shift is related to a threshold voltage decrease, and in conjunction with this, an increase in the channel resistance. Fig. 6.8a shows the influence of the DNA surface concentration on the output curves for single-stranded DNA (unbound state), while Fig. 6.8b depicts the relation of the DNA surface concentration to the output curves for double-stranded DNA (bound state). Comparing these two figures shows that for higher concentrations (smaller  $\lambda$ ) the change in the

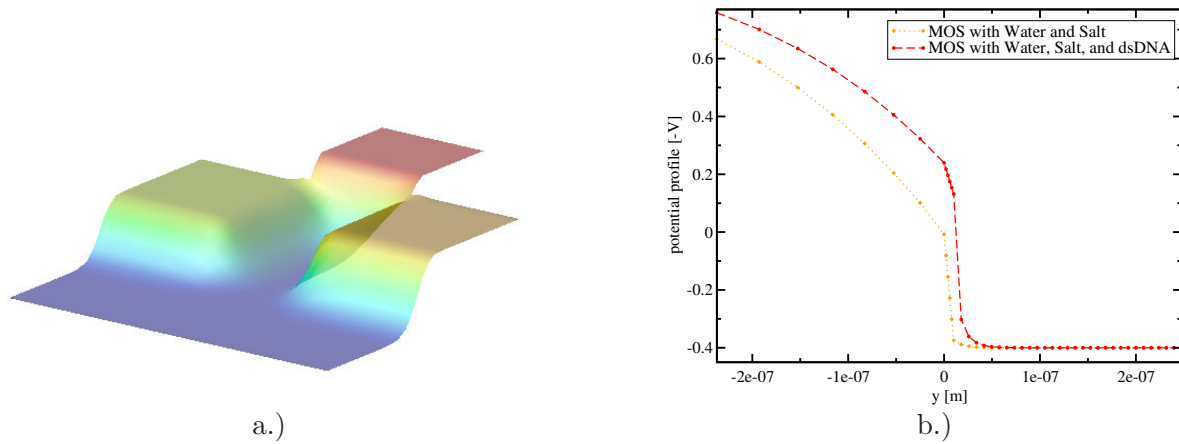


**Figure 6.7:** a.) Potential profile in the whole device for double-stranded DNA perpendicular to surface.  
 b.) Potential profile at the interface (from left to right: semiconductor, oxide, solute).

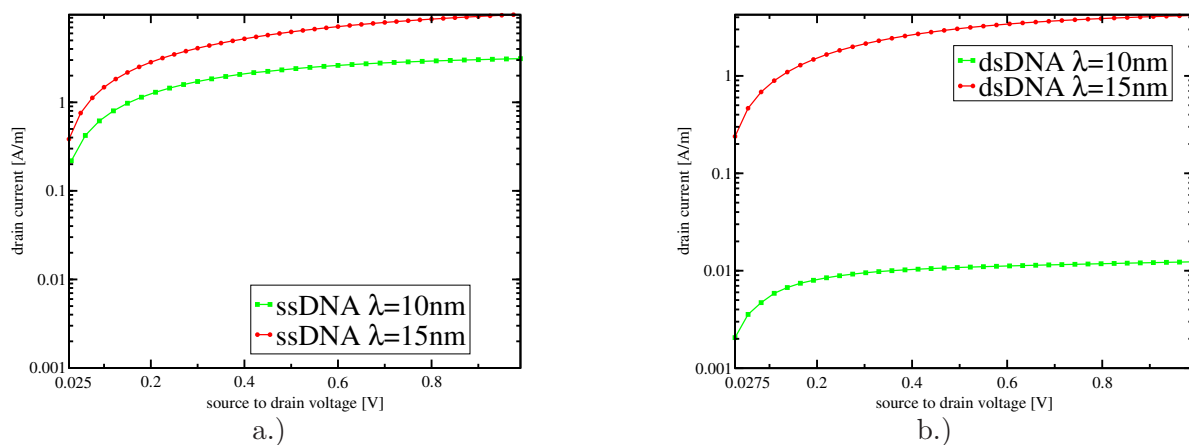


**Figure 6.8:** a.) Output characteristics before hybridization for a mean distance  $\lambda = 10nm$  and  $\lambda = 15nm$  without dipole moment.  
 b.) Output characteristics after hybridization for a mean distance  $\lambda = 10nm$  and  $\lambda = 15nm$  without dipole moment.

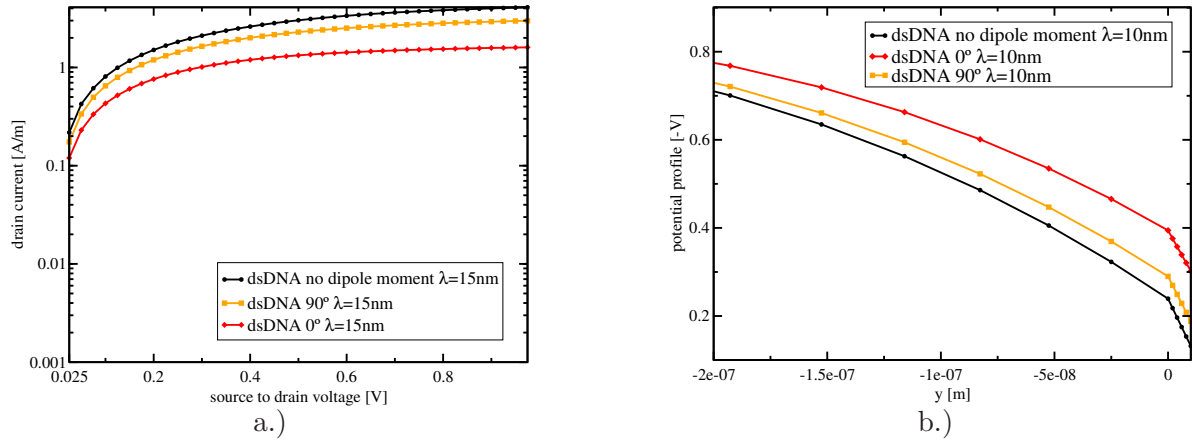


**Figure 6.9:** a.) Output characteristics after hybridization for a mean distance  $\lambda = 15nm$ : without dipole moment, with  $0^\circ$ , and  $90^\circ$ .  
b.) Potential profile from semiconductor to oxide (left to right).

output curves increases. The unbound state (single-stranded DNA) exhibits  $-12e$  elementary charges, while the bound state (double-stranded DNA) possesses twice the charge, equal to  $-24e$  elementary charges. Therefore, the bound state of double-stranded DNA features a larger negative surface charge, which results in a reduced current. This reduction is more pronounced for higher DNA concentration as demonstrated in Fig. 6.8a and Fig. 6.8b.

Fig. 6.9 illustrates the influence of the DNA orientation on the output curves of the DNAFET. It demonstrates that the orientation perpendicular to the surface ( $0^\circ$ ) possesses the highest resistance in comparison to the other curves. Also the DNA orientation parallel to the surface shows an increased resistance in comparison to the curve without dipole moment. This is caused by the inhomogeneously distributed charge along the DNA strand and linked to this the non-vanishing dipole moment. For the orientation perpendicular ( $0^\circ$ ) to the surface the threshold voltage shift is the most negative one, while for the orientation parallel to the surface ( $90^\circ$ ) it is almost absent as compared to the case without dipole moment.

Over several years there was a discussion, whether the orientation of the molecules attached to the surface affects sensing [229, 230, 231, 232, 233]. Indeed biomolecules exhibit an inhomogeneous charge distribution and therefore possess a dipole moment. The orientation of the biomolecule must obey the energy minimization principle and, therefore, there is an orientation that is preferred over others.

In the works [229, 230, 231, 232, 233] the change of orientation has been resolved, optical techniques to detect DNA were applied. Although extra study is needed, one should mention that for optical detection techniques it is more important to choose the linking molecule in a way that the reaction is not impeded by steric effects (receptors blocking each other) or the binding sites are obstructed or even destroyed by the crosslinker. However, in the case of DNAFETs, a field-effect as working principle is exploited. Thus it is decisive to provide a linker which is as short as possible, so that the molecule is closer to the surface. In order to increase the signal to noise ratio, the linker should have as little charge as possible.

### 6.4.2.2 Studying different Models for DNA Sensing with Low Concentrated Buffers in SGFETs

The experimental data of a suspend gate field-effect transistor (SGFET) have been investigated via three different modeling approaches. A SGFET is basically a standard MOSFET except it possesses an elevated gate with a hollow below it. The resulting bare gate-oxide layer is biofunctionalized with single stranded DNA, which is able to hybridize with a complementary strand in a subsequent process step. As already mentioned, caused by the intrinsic charge of the phosphate groups (minus one elementary charge per group) of the DNA, big shifts in the transfer characteristics are generated. This way, label-free, time-resolved, and in-situ detection of DNA is possible.

At first, I will take a short review on the experiment carried out by Harnois et al. [234] to build the basis for a better understanding of the behavior of the system. In their work 60 oligodeoxynucleotides (ODN), also known as single stranded DNA, were attached onto a glutaraldehyde coated nitride layer. Subsequently, one test run with mismatched ODNs and one test run with matching ODNs were performed. The test samples with the mismatching DNA sequences display no relevant change in the output curves, while for the matching single stranded DNA a big shift in the threshold voltage is observed. The outcome of their experimental series features two interesting properties. Firstly, they exhibit a threshold voltage shift of about 800 mV between the probe curve and the target transfer curve and, secondly, the probe transfer curve is situated in the center between the target and the reference curve. A typical threshold voltage shift lies within a range from several mV to 100 mV [235], determined by the featured buffer concentration. Therefore, the 800mV shift is quite big and additionally the Poisson-Boltzmann regime shows commonly a big shift between the reference and the probe/target ( $\sim 100$  mV), but a much smaller shift between probe and target curves (10 – 20 mV) [149]<sup>4</sup>.

In order to reproduce the device behavior, the Poisson-Boltzmann model in combination with a space charge representing the charged DNA (60 base pairs *probe* and 120 base pairs *target*), the Poisson-Boltzmann model with a sheet charge describing the DNA, and the Debye-Hückel model with a corresponding space charge were investigated, trying to match the device transfer curves.

Fig. 6.10a,b,c illustrate the transfer characteristics for the unprepared SGFET (reference), the prepared but unbound (probe), and after the DNA has bound to functionalized surface (target), respectively. The curves of the experiment are indicated by discrete grey dots. As shown by Fig. 6.10a and Fig. 6.10b, even for the very low salt concentration of 0.6 mmol, the shift between the reference curve and the probe/target is bigger than between the probe and target curves.

This behavior abides with the observations by [149] and is assigned to the nonlinear screening of the used models. Studying Fig. 6.11 and Fig. 6.12 reveals that doubling the charge at the interface does not cause twice the potential shift. There is also a bigger shift for the sheet charge model due to the description of the DNA charge as sheet with infinitely small height observable. This is the result of lesser screening compared to the space charge model which spreads the same amount of charge over 20 nm.

However, it is impossible to fit the experimental data by only decreasing the salt concentration. On the other hand the Debye-Hückel model shows acceptable agreement for the same parameter

---

<sup>4</sup>Due to the strong non linear screening in the Poisson-Boltzmann regime doubling the charge does not lead to twice the potential shift.

set as for the Poisson-Boltzmann models (Fig. 6.10). For the Debye-Hückel model, doubling the charge is reflected in twice the potential shift (Fig. 6.13), due to the linear screening behavior of the model (6.6).

Understanding the failure of the Poisson-Boltzmann model and the success of the Debye-Hückel model demands a second look at the models and checking the validity constraints of their formulation. One can get a feeling for the problem by assuming a single 60 bases DNA strand contained in a box of  $10 \cdot 10 \cdot 20 \text{ nm}^3$  at one mmol sodium-chloride bulk concentration. In this volume there will be only one sodium/chlorine ion on average. Therefore, strong nonlinear screening is extremely unlikely in such cases. The Poisson-Boltzmann model is a continuum model, which describes the salt concentration as a continuous quantity. This is the reason why it overestimates the screening and, therefore, it is not valid for small salt concentrations.

The Debye-Hückel model is derived by expanding the exponential terms into a Taylor series and neglecting all terms higher than second order [226]. Taking the laws of series expansion into account,  $\frac{q\psi}{k_B T} \ll 1$ , thus the potential has to be small compared to the thermal energy. Furthermore, treating the ions as infinite small point charges leads to a big mean distance between the ions in the solution and, in conjunction with this, to a low bulk salt concentration. However, even though only one of the constraints is fulfilled, the Debye-Hückel model is able to fit the data. One possible explanation is that in this case the extended Poisson-Boltzmann model and the Debye-Hückel model coincide as shown in Section 6.3 (Fig. 6.5) and thus the screening is controlled by the average closest possible approach.

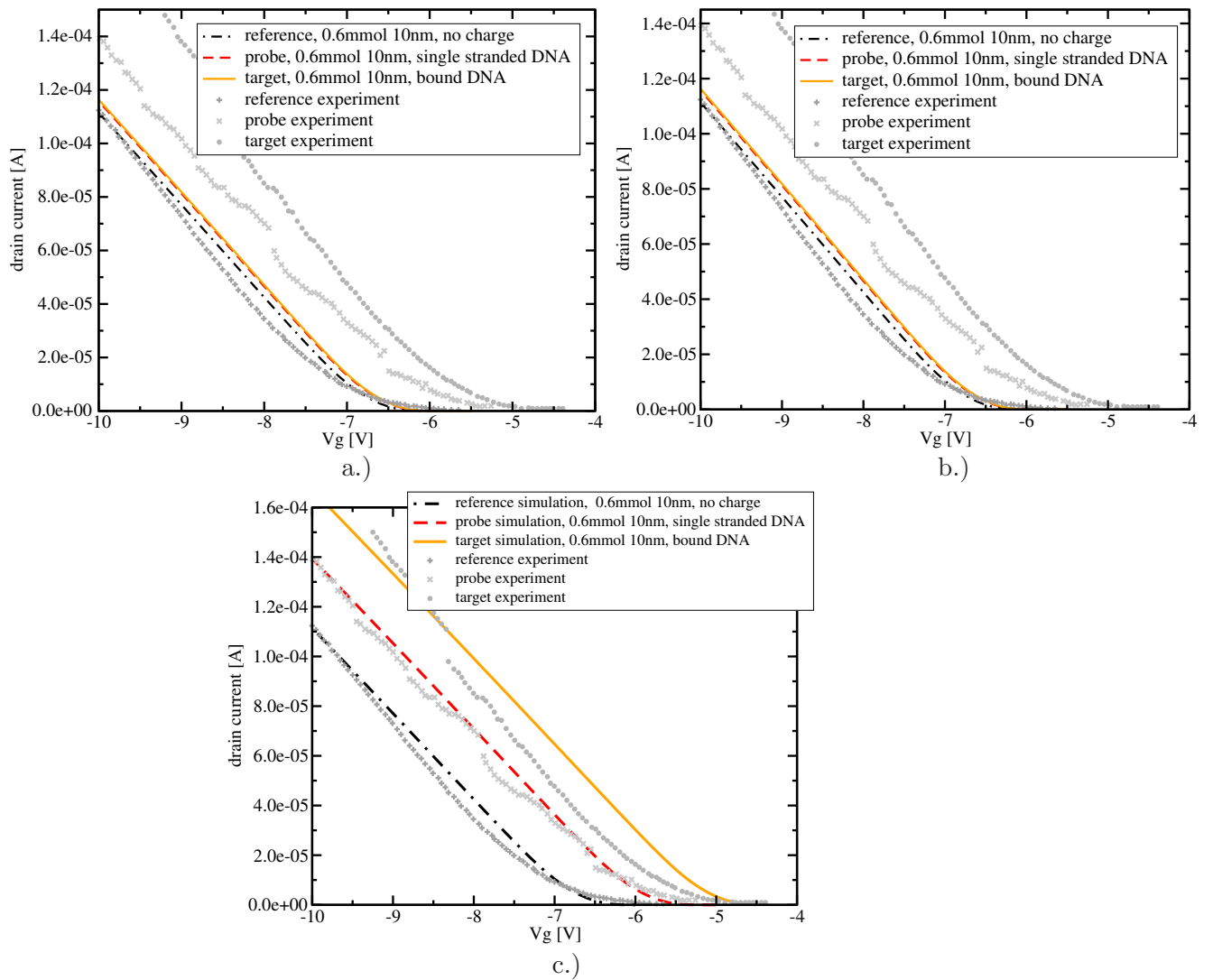


**Figure 6.10:** a.) Transfer characteristics of a SGFET for Poisson-Boltzmann model and DNA charge modeled via space charge density.  
 b.) Transfer characteristics of a SGFET for Poisson-Boltzmann model and DNA charge modeled via sheet charge density.  
 c.) Transfer characteristics of a SGFET for Debye-Hückel model and DNA charge modeled via space charge density.

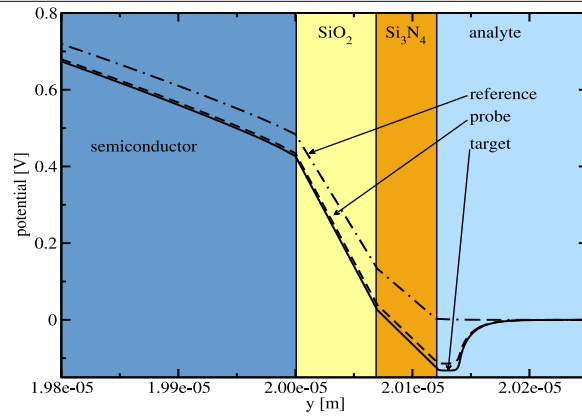


**Figure 6.11:** Potential for the Poisson-Boltzmann model with space charge, starting from the semiconductor (left) and ending in the analyte (right). It can be seen that doubling the charge does not lead to twice the potential shift due to nonlinear screening.

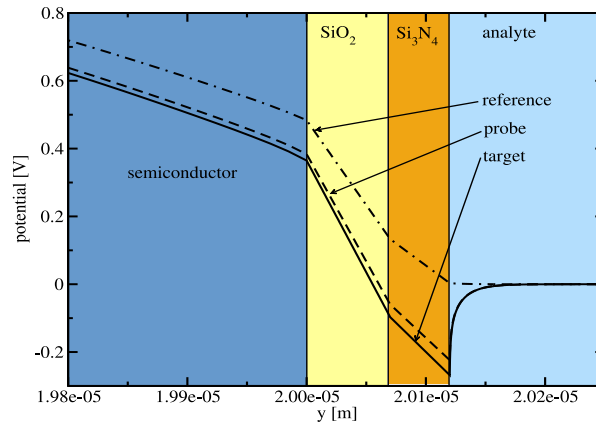


**Figure 6.12:** Potential for the Poisson-Boltzmann model with sheet charge, starting from the semiconductor (left) and ending in the analyte (right). Here the shift is a bit increased but far away from the values from the measurement. However, also here doubling the charge does not lead to twice the potential shift due to nonlinear screening.

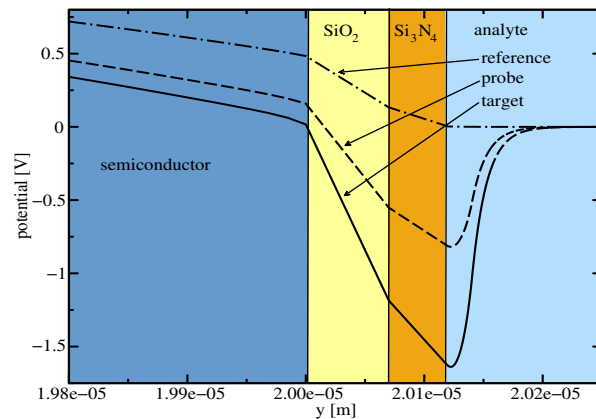


**Figure 6.13:** Potential for the Debye-Hückel model with space charge, starting from the semiconductor (left) and ending in the analyte (right). It can be seen that doubling the charge leads to twice the potential shift due to the weaker linear screening.

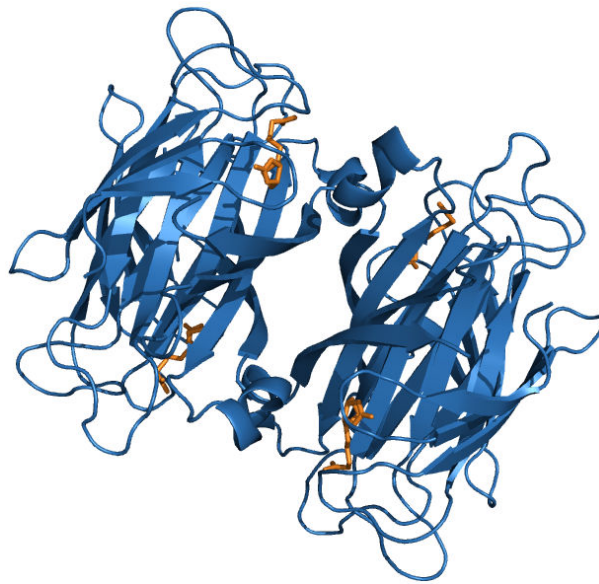


**Figure 6.14:** Scheme of the tetrameric protein streptavidin and biotin.

### 6.4.3 Protein-FET - Streptavidin-Biotin-FET

The chemist Gerhardus Johannes Mulder was the first to describe proteins and Jöns Jakob Berzelius the first naming them in 1838. Proteins play a key role in living organisms. They are like other biological macromolecules, such as polysaccharides and nucleic acids, essential parts of an organism and participate in an endless list of processes within a cell. Numerous proteins are enzymes catalyzing biochemical reactions and thus vital to metabolism. They also exhibit structural or mechanical functions, such as actin and myosin in muscles or the proteins in the cytoskeleton forming a system of scaffolding which maintains the cell shape. Proteins are also substantial in cell signaling, immune responses, cell adhesion, and the cell cycle.

Proteins are linear polymers and consist of a series of up to 20 different L- $\alpha$ -amino acids. All amino acids exhibit common structural features like an  $\alpha$ -carbon bonded to an amino group, a carboxyl group, and a variable side chain. Their three-dimensional structures were first determined by Perutz and Kendrew via x-ray diffraction analysis in 1962, awarded with the Nobel prize in chemistry for their discoveries.

Streptavidin is a tetrameric protein purified from the bacterium *streptomyces avidinii* and each subunit is able to bind biotin with equal affinity (Fig. 6.14, Fig. 6.15). It is exploited widely in molecular biology through its extraordinarily strong affinity for biotin. It also possesses one of the strongest non-covalent interactions known in nature. Among the most common uses are the purification or detection of various biomolecules. The strong streptavidin-biotin bond can be utilized to attach various biomolecules to one another or onto a solid support.

As mentioned before proteins play a major role in a living organism. Therefore, various kinds of reaction pairs are of interest and have been studied comprehensively, like detection of DNA [17], [150], [151], cancer markers [152], proteins, e.g. biotin-streptavidin [153], [154], [155], [156], albumin [157], and transferrin [158].

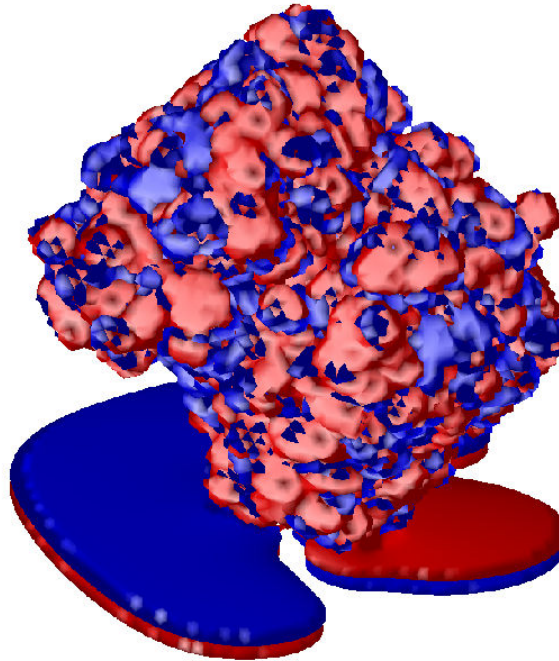


**Figure 6.15:** Biotin-streptavidin complex [2] on the oxide surface. Two iso-surfaces for plus and minus  $0.03 k_B T / q \text{\AA}^2$  are shown.

The biotin-streptavidin reaction pair is modeled with the physics-based bottom-up approach of Section 6.4.2.1. Here, once more the charge and dipole moment for a single molecule (biotin/streptavidin) (see for example Figure 6.15, [235]) is obtained and extrapolated to the mean charge density and the mean dipole moment density of the boundary layer, bridging the gap between the Angstrom length scale of the biomolecules and the micrometer dimensions of the FET [219], [220], [236]. The x-axis is chosen parallel to the oxide surface, while the y-axis points into the liquid.  $\psi(0-)$  describes the potential in the oxide, while  $\psi(0+)$  relates to the potential in the solute. The first equation (6.3) introduces the jump in the field, while the second (6.4) describes the dipole moment which causes a shift of the potential taken into account by adjusting the potential in the analyte.

Three different oxid types were utilized as dielectric.  $SiO_2$  as a reference,  $Al_2O_3$ , and  $Ta_2O_5$  as possible high-k materials, with relative permittivities of 3.9, 10, and 25 respectively. Sodium chloride was chosen as solute at pH 7. For each dielectric several simulation runs were performed such as the unprepared state (only water and salt), the prepared but unbound state (water, salt and biotin), and the bound state, when the chemical reaction has occurred (water, salt, and biotin-streptavidin). Furthermore, for every dielectric two sets of mean distances between the molecules ( $\lambda = 10\text{nm}$ ,  $\lambda = 15\text{nm}$ ) and two different orientations in relation to the surface ( $0^\circ \dots$  perpendicular to the surface and  $90^\circ \dots$  parallel to the surface) were considered. The data for biotin and streptavidin were obtained from [2] and exploited for their charges and dipole moments. The ProteinFETs output curves were computed for every parameter combination mentioned before, under the assumption of a 100% binding efficiency. The potential of the reference electrode was set to 0.4V, shifting the FET into moderate inversion as proposed by [160].

Fig. 6.16, Fig. 6.17, and Fig. 6.18 show a decrease in the output current for biotin attached to the surface in comparison to the unprepared surface. This downward shift for the bound state in comparison to the unbound state is caused by the increase of negative charges at the interface, which is consistent with the difference between the curves for  $\lambda = 10\text{nm}$  and  $\lambda = 15\text{nm}$ , since for 10nm the molecules are more dense than by 15nm.

One can learn from Fig. 6.16, Fig. 6.17, and Fig. 6.18 the bigger the  $\varepsilon_r$  of the dielectric the bigger is the output current. Thus high-k materials enable stronger output signals. However, according to [237], higher  $\varepsilon_r$  dielectric constants may be influenced by higher trap densities and thus lead to a decreased signal-to-noise ratio. Therefore a compromise between an increased output signal and a good signal-to-noise ratio has to be found.

Fig. 6.19 illustrates the output curves as a function of dielectric and molecule orientation ( $0^\circ$  denotes perpendicular to the surface and  $90^\circ$  lying flat on the interface) yielding the lowest output curves for  $0^\circ$  followed by  $90^\circ$  and the curves without dipole moment for each group. Fig. 6.20 and Fig. 6.21 display the small signal resistance as a function of dielectric and molecule orientation, showing smaller values for higher relative permittivity  $\varepsilon_r$ . In agreement with the previous results depicted in Fig. 6.16, Fig. 6.17, and Fig. 6.18, a somewhat larger differential resistance is observed for the perpendicular molecule orientation. This has to be apprehended in the sense of the inhomogeneously charged biomolecules and in conjunction to the occurring dipole moment entering into the boundary conditions (6.4), thus yielding a difference in the output curves of the BioFET for different orientation angles in relation to the surface.

In order to increase the signal-to-noise ratio, the linker should be neutral or at least possess as little charge as possible. For instance, in the case of detecting streptavidin, biotin can be used as a binding agent. So biotin molecules are attached to the surface via a neutral linker. Streptavidin is then able to bind biotin and form a bound state at the interface. The charge difference between the unbound state of a single biotin, which is negatively charged with one single elementary charge and the bound state of biotin-streptavidin, which is negatively charged with five elementary charges, is large enough for detection. One also has to mention that due to the tetrameric nature of streptavidin it exhibits four binding sites for biotin as shown in Fig. 6.14. Thus, the linker for binding biotin to the surface should be short enough to impede binding several biotin molecules to a single molecule of streptavidin. If one has the freedom of choice in deciding, if biotin or streptavidin is initially attached to the surface, I would recommend to attach biotin in advance of streptavidin. The relative change in charge will be bigger this way (from minus one elementary charge to minus five elementary charges) leading to an more pronounced change in the output signal and allows to attach further biotinylated molecules close to the interface<sup>5</sup>.

The model shows a strong dependence on surface charges and indicates a detectable shift in the threshold voltage depending on their orientation related to the surface. It would be interesting to study an experimental setup introducing an additional electric field parallel to the surface (e.g. extra isolated plates on the left and right side wall of the microfluidic), which enables to bend the molecules out of their equilibrium position into an arbitrary direction allowing the comparison with the results obtained from the simulations.

---

<sup>5</sup>due to the three remaining open binding sites of streptavidin for biotin

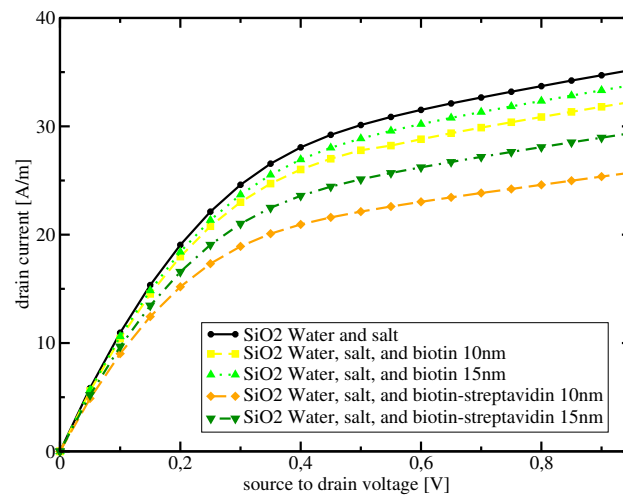


**Figure 6.16:** Output curve for  $\text{SiO}_2$  for unprepared, prepared but unbound, and bound state at  $\lambda = 10\text{nm}$  and  $\lambda = 15\text{nm}$ , respectively.

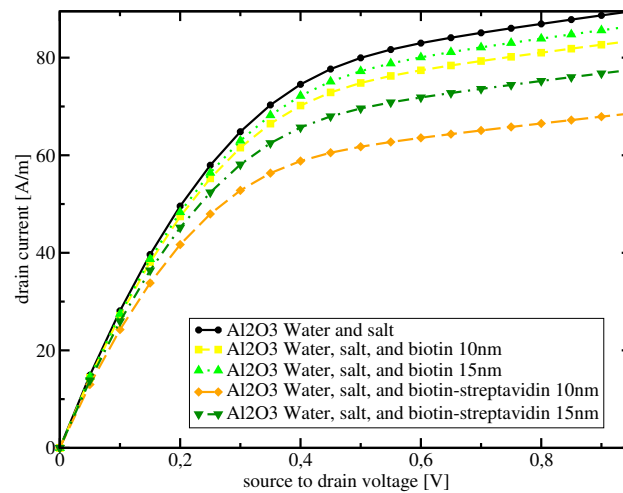


**Figure 6.17:** Output curve for  $\text{Al}_2\text{O}_3$  for unprepared, prepared but unbound, and bound state at  $\lambda = 10\text{nm}$  and  $\lambda = 15\text{nm}$ , respectively.

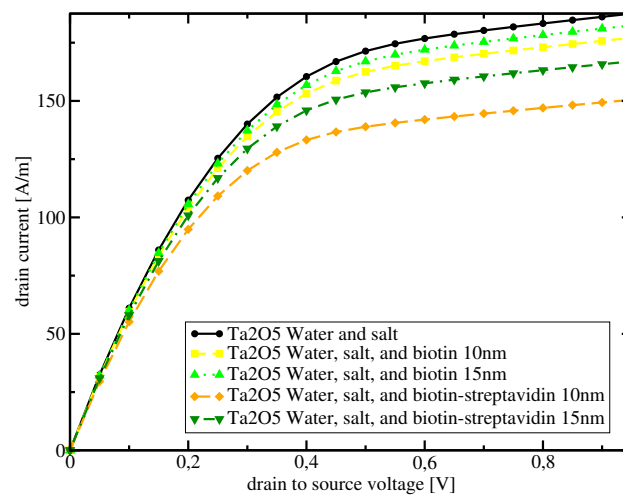


**Figure 6.18:** Output curve for  $\text{Ta}_2\text{O}_5$  for unprepared, prepared but unbound, and bound state at  $\lambda = 10\text{nm}$  and  $\lambda = 15\text{nm}$ , respectively.

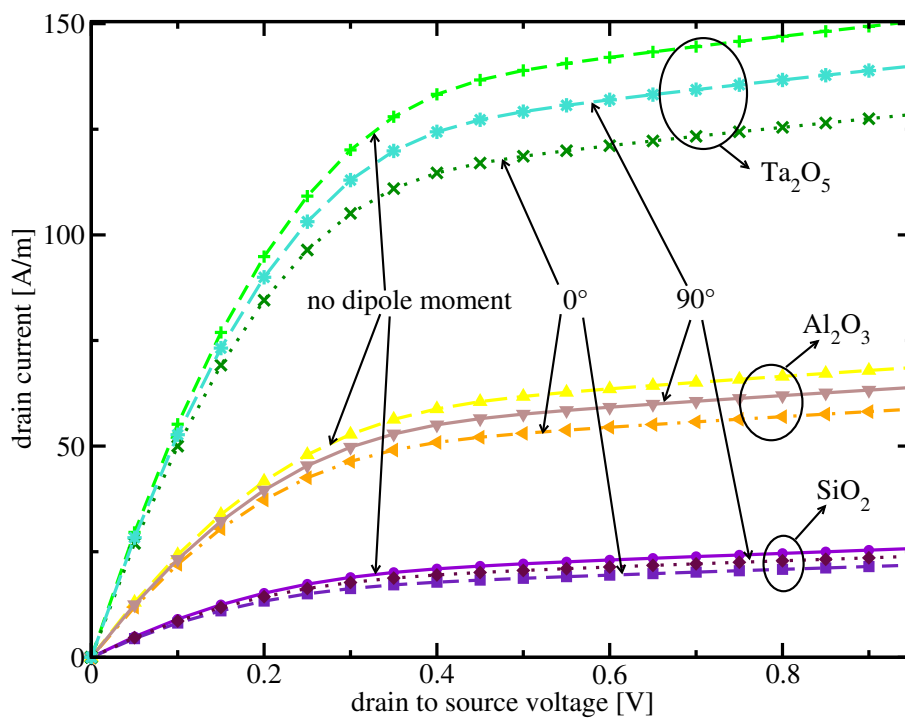


**Figure 6.19:** Output curves for  $\text{SiO}_2$ ,  $\text{Al}_2\text{O}_3$ , and  $\text{Ta}_2\text{O}_5$  for calculation without dipole moment,  $0^\circ$  (perpendicular to surface), and  $90^\circ$  (parallel to surface).

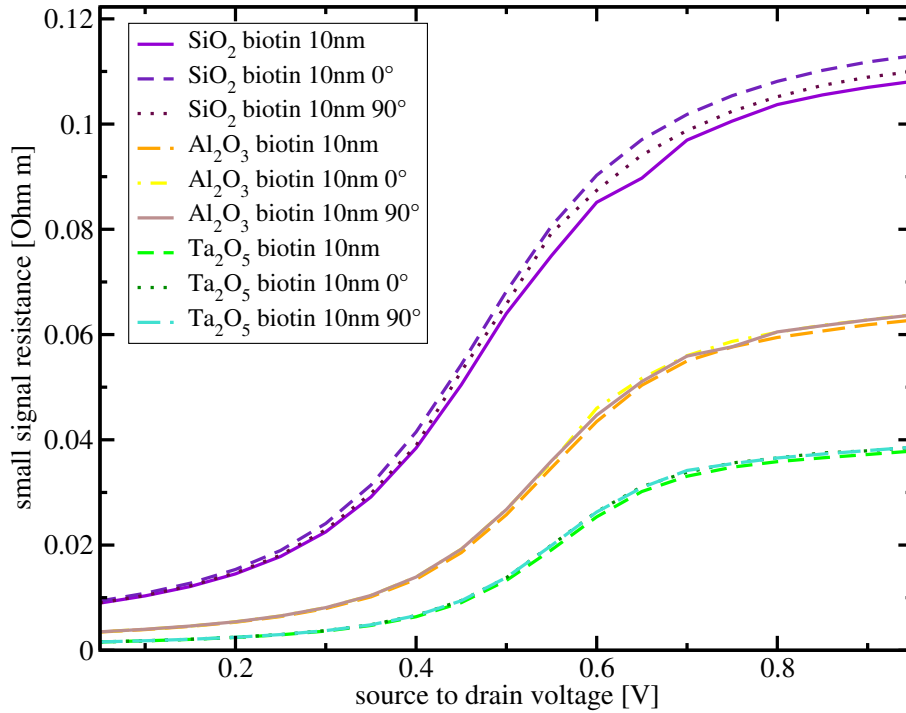


**Figure 6.20:** Small signal resistance for  $SiO_2$ ,  $Al_2O_3$ , and  $Ta_2O_5$  for calculation without dipole moment,  $0^\circ$  (perpendicular to surface), and  $90^\circ$  (parallel to surface) at biotin only.

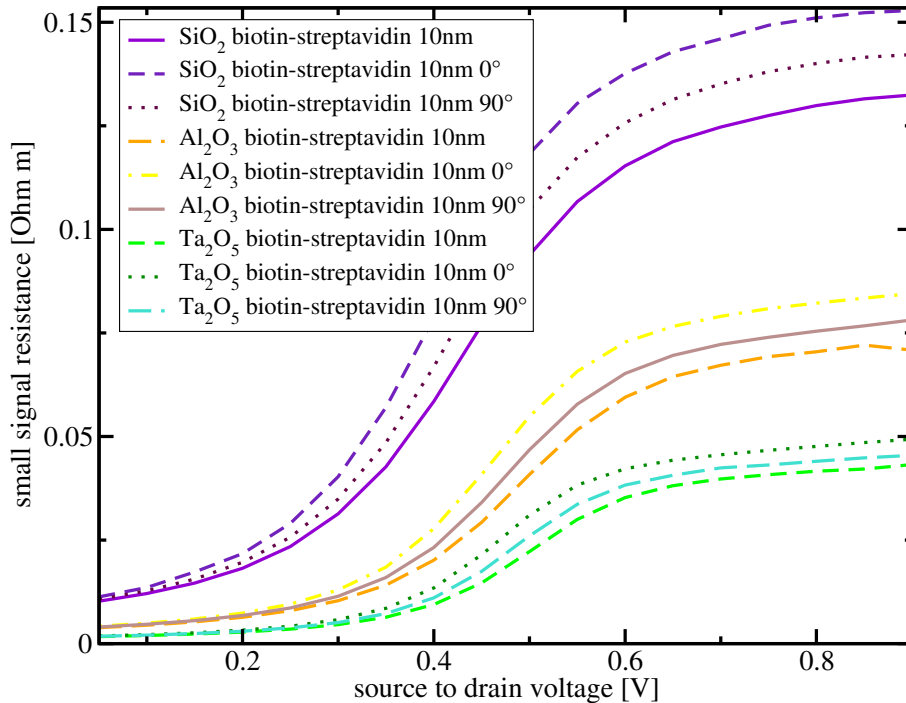


**Figure 6.21:** Small signal resistance for  $SiO_2$ ,  $Al_2O_3$ , and  $Ta_2O_5$  for calculation without dipole moment,  $0^\circ$  (perpendicular to surface), and  $90^\circ$  (parallel to surface) at bound state (biotin-streptavidin).

---

# Summary and Outlook

---

**B**EGINNING WITH high-k gate stacks employed in modern CPUs and flash memories, gate stacks with strained interfaces, in order to boost the carriers mobility, ferroelectric gate stacks, for novel non-volatile memories, and electrolytic gate stacks, enabling new biochemical sensors, the versatility of the field-effect has been shown.

An overview of state of the art strained interface gate stacks is given and their mathematical description with the aid of the  $\mathbf{k}\cdot\mathbf{p}$  method is presented. The description of the influence of strain on the semiconductor is extended to ultra-thin body FETs with the help of a confinement potential and a two-band  $\mathbf{k}\cdot\mathbf{p}$  model. The effects on the dispersion relation, energy splitting, and effective masses for ultra-thin body FETs along [001] for primed and unprimed subbands with respect to the  $X$ -point at different strain levels and body thicknesses are studied. The utilized two-band  $\mathbf{k}\cdot\mathbf{p}$  Hamiltonian accurately describes the band structure up to energies of  $\sim 0.5$  eV and incorporates a shear strain component, neglected in the parabolic approximation. Due to the modification of the effective mass by shear strain it is an important source of mobility enhancement one has to account for in ultra-thin silicon films.

It is shown that the effective masses along [110] and  $[\bar{1}\bar{1}0]$  become different for decreasing film thickness. In ultra-thin films the large separation in energy between the primed and the unprimed subbands even without stress leads to a de-population of the primed subbands. Tensile stress in [110] direction generates a shear component which changes the transport effective masses of the unprimed subbands and shifts the primed subbands with unfavorable effective masses up in energy. With decreasing film thickness the decrease of the effective mass along [110] direction induced by shear strain becomes more pronounced enabling mobility enhancement even in ultra-thin films. Unfortunately, the density of states effective mass in unprimed subbands increases with shear strain and thus results in higher scattering rates, which reduces the mobility gained due to the thickness-enhanced transport mass decrease at high stress values. However, the mobility enhancement remains significant.

Thereafter, a detailed introduction into the modeling of electrolytic interfaces is presented and its peculiarities like, the double layer, the Stern layer, the site-binding model, and the different available models for the electrolyte are elaborated. Several examples illustrate the exploitation of electrolytic gate stacks for pH, DNA, and biotin-streptavidin sensitive devices. The presented pH sensor (ISFET) was the first device utilizing an electrolytic gate stack. The simulations

performed show good agreement with the values reported in literature. The examples for detecting DNA predict an angular dependence of the DNA molecule orientation with respect to the surface and show that for low salt concentrations the commonly employed Poisson-Boltzmann model can not reproduce the screening of the DNA in the electrolyte correctly, while the Debye-Hückel model is able to fit the experimental data. This can be explained by the in this work introduced extended Poisson-Boltzmann model, which is able to adjust the screening behavior with respect to the average closest possible distance between two ions. Finally, a BioFET for detecting biotin-streptavidin is analyzed, studying the influence of several dielectric materials, molecule surface density, and molecule orientation with respect to the surface.

Even though the end of *scaling* is beginning to rise on the horizon, there are plenty of white spots on the map of microelectronics and there is more than enough room for further improvements and fascinating new applications.

---

# Appendix

---

## A. Re-expressing $X_1$ as a Function of $X_2$

In the first step the Hamiltonian (4.1) and the energy dispersion (4.4) are transformed into dimensionless units with the expressions:

$$\begin{aligned} X &= \frac{k_z}{k_0}, & E_0 &= \frac{\hbar^2 k_0^2}{m_1} \\ \mathcal{E} &= \frac{E}{E_0}, & \zeta &= \frac{\delta}{E_0}. \end{aligned} \quad (7.1)$$

The energy dispersion then takes the following form:

$$\mathcal{E}(X) = \frac{X^2}{2} \pm \sqrt{\zeta^2 + X^2} + \frac{m_l(k_x^2 + k_y^2)}{2m_t k_0^2}. \quad (7.2)$$

Setting the determinant of the dimensionless Hamiltonian to zero allows to express  $X$  as a function of energy  $\mathcal{E}$ :

$$\begin{aligned} \left(\frac{X^2}{2} - X - \mathcal{E}\right) \left(\frac{X^2}{2} + X - \mathcal{E}\right) - \zeta^2 &= 0 \\ \text{or } \left(\frac{X^2}{2} - \mathcal{E}\right)^2 - X^2 - \zeta^2 &= 0. \end{aligned} \quad (7.3)$$

Re-expressing the fourth order equation (7.3) as a second order equation  $\frac{\nu^2}{4} - \nu\mathcal{E} + \mathcal{E}^2 - \nu - \zeta^2 = 0$  by

$$\nu = X^2, \quad (7.4)$$

we find the solution,

$$\begin{aligned} \nu &= 2(1 + \mathcal{E}) \pm \sqrt{4(1 + \mathcal{E})^2 - 4(\mathcal{E}^2 - \zeta^2)} \quad \text{or} \\ \nu &= 2(1 + \mathcal{E}) \pm 2\sqrt{1 + 2\mathcal{E} + \zeta^2}. \end{aligned} \quad (7.5)$$

This formulation preserves all four solutions for  $X$ . Embracing two sets of  $X$  values in two separate equations leads to the following expressions:

$$\nu = \left(1 \pm \sqrt{1 + 2\mathcal{E} + \zeta^2}\right)^2 - \zeta^2 \quad (7.6)$$

$$X_1^2 = \left(1 + \sqrt{1 + 2\mathcal{E} + \zeta^2}\right)^2 - \zeta^2 \quad (7.7)$$

$$X_2^2 = \left(1 - \sqrt{1 + 2\mathcal{E} + \zeta^2}\right)^2 - \zeta^2 . \quad (7.8)$$

Using the following identities:

$$\frac{X_1^2 + X_2^2}{2} = 2(1 + \mathcal{E}) , \quad (7.9)$$

$$\frac{X_1^2 - X_2^2}{2} = 2\sqrt{1 + 2\mathcal{E} + \zeta^2} , \quad (7.10)$$

leads to the desired expressions  $X_1(X_2)$  and  $X_2(X_1)$ .

$$X_1^2 = \left(1 + \frac{X_1^2 - X_2^2}{4}\right)^2 - \zeta^2 , \quad (7.11)$$

$$X_2^2 = \left(1 - \frac{X_1^2 - X_2^2}{4}\right)^2 - \zeta^2 \text{ or} \quad (7.12)$$

$$X_1^2 = X_2^2 + 4 + 4\sqrt{X_2^2 + \zeta^2} , \quad (7.13)$$

$$X_2^2 = X_1^2 + 4 - 4\sqrt{X_1^2 + \zeta^2} . \quad (7.14)$$

The transformation to dimensionless units of the corresponding expression for  $c(X)$  is:

$$c(X) = -\frac{X}{\zeta \pm \sqrt{\zeta^2 + X^2}} . \quad (7.15)$$

## B. Expressing the Equations (4.18) and (4.19)

In order to write (4.25) as a function of  $y_n$  the following set of rules is needed:

$$(\bar{y}_n + y_n) = X_1 , \quad (7.16)$$

$$(\bar{y}_n - y_n) = X_2 , \quad (7.17)$$

or

$$\frac{X_1 + X_2}{2} = y_n , \quad (7.18)$$

$$\frac{X_1 - X_2}{2} = \bar{y}_n . \quad (7.19)$$

The following identities ((7.11),(7.12)):

$$(\bar{y}_n \pm y_n)^2 + \zeta^2 = \left(1 \pm \frac{X_1^2 - X_2^2}{4}\right)^2, \quad (7.20)$$

$$\bar{y}_n^2 + y_n^2 + \zeta^2 = 1 + \frac{X_1^2 - X_2^2}{4}, \quad (7.21)$$

$$\bar{y}_n y_n = \frac{X_1^2 - X_2^2}{4}, \quad (7.22)$$

allow to write  $\bar{y}_n$  as function of  $y_n$ ,

$$\bar{y}_n^2 + y_n^2 + \zeta^2 = 1 + \bar{y}_n^2 y_n^2, \quad (7.23)$$

$$\bar{y}_n^2 (1 - y_n^2) = 1 - y_n^2 - \zeta^2, \quad (7.24)$$

$$\bar{y}_n^2 = \frac{1 - y_n^2 - \zeta^2}{1 - y_n^2}, \quad (7.25)$$

and  $y_n$  as function of  $\bar{y}_n$ ,

$$\bar{y}_n^2 + y_n^2 + \zeta^2 = 1 + \bar{y}_n^2 y_n^2, \quad (7.26)$$

$$y_n^2 (1 - \bar{y}_n^2) = 1 - \bar{y}_n^2 - \zeta^2, \quad (7.27)$$

$$y_n^2 = \frac{1 - \bar{y}_n^2 - \zeta^2}{1 - \bar{y}_n^2}. \quad (7.28)$$

Starting with the fraction of (4.26) in dimensionless form  $I \equiv \frac{c(X_2) - c(X_1)}{c(X_2) + c(X_1)}$ , and putting in the definition of  $c(X)$ , leads to the term below:

$$I \equiv \frac{X_2 \left(\zeta \pm \sqrt{\zeta^2 + X_1^2}\right) - X_1 \left(\zeta \pm \sqrt{\zeta^2 + X_2^2}\right)}{X_2 \left(\zeta \pm \sqrt{\zeta^2 + X_1^2}\right) + X_1 \left(\zeta \pm \sqrt{\zeta^2 + X_2^2}\right)}. \quad (7.29)$$

Proceeding by substituting  $X_1$  with (7.16) and  $X_2$  with (7.17), and using the identity:

$$\sqrt{X_{1,2}^2 + \zeta^2} = \left|1 \pm \frac{X_1^2 - X_2^2}{4}\right| = |1 \pm \bar{y}_n y_n|, \quad (7.30)$$

the term (7.29) can be written as a function of  $\bar{y}_n$  and  $y_n$ ,

$$I \equiv \frac{(\bar{y}_n - y_n) (\zeta \pm (1 + \bar{y}_n y_n)) - (\bar{y}_n + y_n) (\zeta \pm (1 - \bar{y}_n y_n))}{(\bar{y}_n - y_n) (\zeta \pm (1 + \bar{y}_n y_n)) + (\bar{y}_n + y_n) (\zeta \pm (1 - \bar{y}_n y_n))}, \quad (7.31)$$

Expanding the brackets and reorganizing the expression results in:

$$I \equiv -\frac{y_n (\zeta \pm 1 \mp \bar{y}_n^2)}{\bar{y}_n (\zeta \pm 1 \mp y_n^2)}. \quad (7.32)$$

After substituting  $\sqrt{\frac{1 - y_n^2 - \zeta^2}{1 - y_n^2}}$  for  $\bar{y}_n$  the expression simplifies to:

$$I \equiv \frac{-y_n \zeta \left(1 \pm \frac{\zeta}{1 - y_n^2}\right)}{(\zeta \pm 1 \mp y_n^2) \sqrt{\frac{1 - y_n^2 - \zeta^2}{1 - y_n^2}}}, \quad (7.33)$$

and can be reformulated to the term used in (4.28):

$$I \equiv \mp \frac{y_n \zeta}{\sqrt{(1 - y_n^2)(1 - y_n^2 - \zeta^2)}} . \quad (7.34)$$

### C. Estimating the Total Charge in the Diffusive Layer

The Poisson-Boltzmann equation can be solved for the total charge in the diffusive layer in a similar manner the way it is done for the semiconductor surface potential. Beginning with (5.15):

$$\frac{d^2\psi}{dz^2} = \frac{2q c_0}{\epsilon_0 \epsilon_{sol}} \sinh\left(\frac{q\psi}{k_B T}\right) . \quad (7.35)$$

Reexpressing it via the Debye length,

$$\lambda_D^2 = \frac{k_B T \epsilon_0 \epsilon_{sol}}{2q^2 c_0} , \quad (7.36)$$

leads to the following expression:

$$\frac{d^2\psi}{dz^2} = \frac{k_B T}{q \lambda_D^2} \sinh\left(\frac{q\psi}{k_B T}\right) . \quad (7.37)$$

This equation can be rewritten by applying the following identity:

$$2 \frac{d\psi^2}{dz^2} \frac{d\psi}{dz} = \frac{d}{dz} \left( \frac{d\psi}{dz} \right)^2 . \quad (7.38)$$

Substituting (7.38) into (7.37) leads to a first order differential equation:

$$\begin{aligned} \frac{d^2\psi}{dz^2} &= \frac{1}{2} \frac{1}{\psi'} \frac{d}{dz} (\psi')^2 = \frac{k_B T}{q \lambda_D^2} \sinh\left(\frac{q\psi}{k_B T}\right) \text{ or} \\ \frac{d}{dz} (\psi')^2 &= \frac{2k_B T}{q \lambda_D^2} \psi' \sinh\left(\frac{q\psi}{k_B T}\right) \end{aligned} \quad (7.39)$$

(7.39) can be solved via separation of variables. Under the condition of a vanishing electric field for  $z \rightarrow \infty$  the following solution can be derived:

$$\begin{aligned} (\psi')^2 &= \frac{2k_B T}{q \lambda_D^2} \int_{-\infty}^{z_0} \psi' \sinh\left(\frac{q\psi}{k_B T}\right) dz \\ &= \frac{2k_B T}{q \lambda_D^2} \int_0^{\psi_0} \sinh\left(\frac{q\psi}{k_B T}\right) d\psi = \frac{2(k_B T)^2}{q^2 \lambda_D^2} \cosh\left(\frac{q\psi}{k_B T}\right) \Big|_0^{\psi_0} = \\ &= \frac{2(k_B T)^2}{q^2 \lambda_D^2} \left( \cosh\left(\frac{q\psi_0}{k_B T}\right) - 1 \right) \end{aligned} \quad (7.40)$$

Exploiting the identity  $2 \sinh^2(x/2) = \cosh(x) - 1$ , the expression for  $(\psi')^2$  can be formulated as:

$$(\psi'_0)^2 = \frac{4(k_B T)^2 \sinh^2\left(\frac{q\psi_0}{k_B T}\right)}{\lambda_D^2 q^2}, \quad (7.41)$$

$$\psi'_0 = \frac{\pm 2k_B T \sinh\left(\frac{q\psi_0}{k_B T}\right)}{\lambda_D q} \quad (7.42)$$

In the last calculation step Gauß's law is utilized to express the total charge per unit area in the Gouy-Chapman layer:

$$\sigma_0 = -\varepsilon_0 \varepsilon_{sol} \psi'_0 = \mp \sqrt{8\varepsilon_0 \varepsilon_{sol} k_B T c_0} \sinh\left(\frac{q\psi_0}{2k_B T}\right). \quad (7.43)$$

## D. Relation Between Charge Density and Potential Drop in the MOSFET Channel

The relation between the charge density in the MOSFET channel and the potential drop (assuming an n-channel MOS transistor) can be obtained from the Poisson equation using the prerequisite of the validity of Boltzmann distributed electrons and holes. Interestingly, this leads to an equation very similar to the Poisson-Boltzmann model of the electrolyte:

$$\frac{d^2\psi}{dz^2} = -\frac{q}{\varepsilon_0 \varepsilon_{Si}} \left( p_0 e^{-\frac{q\psi}{k_B T}} - n_0 e^{\frac{q\psi}{k_B T}} - N_A \right). \quad (7.44)$$

Since, the overall charge has to be zero,  $N_A = p_0 - n_0$  must be fulfilled. Substituting  $N_A$  by the relation before the following expression is derived:

$$\frac{d^2\psi}{dz^2} = -\frac{q}{\varepsilon_0 \varepsilon_{Si}} \left( p_0 e^{-\frac{q\psi}{k_B T}} - n_0 e^{\frac{q\psi}{k_B T}} - p_0 + n_0 \right). \quad (7.45)$$

Now, grouping the expressions containing  $p_0$  and  $n_0$ :

$$\frac{d^2\psi}{dz^2} = -\frac{q}{\varepsilon_0 \varepsilon_{Si}} \left( p_0 \left( e^{-\frac{q\psi}{k_B T}} - 1 \right) + n_0 \left( 1 - e^{\frac{q\psi}{k_B T}} \right) \right), \quad (7.46)$$

followed by the relation  $\frac{n_0}{p_0} = \frac{n_i^2}{p_0^2}$  and the assumption that  $N_A \approx p_0$ , (p-doped), we get:

$$\frac{d^2\psi}{dz^2} = -\frac{qN_A}{\varepsilon_0 \varepsilon_{Si}} \left( e^{-\frac{q\psi}{k_B T}} - 1 + \frac{n_i^2}{N_A^2} \left( 1 - e^{\frac{q\psi}{k_B T}} \right) \right). \quad (7.47)$$

The equation connecting the potential and the doping can now be deduced. The identity:

$$2 \frac{d\psi^2}{dz^2} \frac{d\psi}{dz} = \frac{d}{dz} \left( \frac{d\psi}{dz} \right)^2 \quad (7.48)$$

is introduced in order to rewrite (7.47) as a differential equation of first order:

$$\begin{aligned} \frac{d}{dz} (\psi')^2 &= -\frac{2qN_A\psi'}{\varepsilon_0\varepsilon_{\text{Si}}} \left( e^{-\frac{q\psi}{k_B T}} - 1 + \frac{n_i^2}{N_A^2} \left( 1 - e^{\frac{q\psi}{k_B T}} \right) \right) \\ (\psi')^2 &= -\frac{2qN_A}{\varepsilon_0\varepsilon_{\text{Si}}} \int \left( e^{-\frac{q\psi}{k_B T}} - 1 + \frac{n_i^2}{N_A^2} \left( 1 - e^{\frac{q\psi}{k_B T}} \right) \right) \psi' dz . \end{aligned} \quad (7.49)$$

The boundary conditions are set to  $\psi_s$  at the surface, and 0 for  $z \rightarrow \infty$ :

$$(\psi')^2 = -\frac{2qN_A}{\varepsilon_0\varepsilon_{\text{Si}}} \int_0^{\psi_s} e^{-\frac{q\psi}{k_B T}} - 1 + \frac{n_i^2}{N_A^2} \left( 1 - e^{\frac{q\psi}{k_B T}} \right) d\psi . \quad (7.50)$$

After the integration the following relation is gained:

$$(\psi')^2 = \frac{2qN_A}{\varepsilon_0\varepsilon_{\text{Si}}} \left( \frac{k_B T}{q} e^{-\frac{q\psi_s}{k_B T}} + \psi_s - \frac{k_B T}{q} + \frac{n_i^2}{N_A^2} \left( \frac{k_B T}{q} e^{-\frac{q\psi_s}{k_B T}} - \psi_s - \frac{k_B T}{q} \right) \right) . \quad (7.51)$$

Since the electric field is related to the potential via  $\mathcal{E} = -\frac{d\psi}{dz}$ , the derived expression describes the dependence of the electric field on the surface potential:

$$\mathcal{E} = \mp \sqrt{\frac{2qN_A}{\varepsilon_0\varepsilon_{\text{Si}}}} \sqrt{\frac{k_B T}{q} e^{-\frac{q\psi_s}{k_B T}} + \psi_s - \frac{k_B T}{q} + \frac{n_i^2}{N_A^2} \left( \frac{k_B T}{q} e^{-\frac{q\psi_s}{k_B T}} - \psi_s - \frac{k_B T}{q} \right)} . \quad (7.52)$$

Applying Gauß's law:

$$\mathcal{E} = \frac{\sigma_s}{\varepsilon_0\varepsilon_{\text{Si}}} , \quad (7.53)$$

leads to the desired formulaion, connecting the surface charge density  $\sigma_s$  with the surface potential  $\psi_s$ :

$$\sigma_s = -\sqrt{2qN_A\varepsilon_0\varepsilon_{\text{Si}}} \sqrt{\frac{k_B T}{q} e^{-\frac{q\psi_s}{k_B T}} + \psi_s - \frac{k_B T}{q} + \frac{n_i^2}{N_A^2} \left( \frac{k_B T}{q} e^{-\frac{q\psi_s}{k_B T}} - \psi_s - \frac{k_B T}{q} \right)} . \quad (7.54)$$

## E. Flatband Potential and MOSFET Properties

Applying a potential between drain and source leads to a charge transport and the thermal equilibrium distribution under the assumption of Boltzmann statistics is not applicable anymore. One can evade this hitch by assuming stationary conditions, meaning there is no change in charge density over time, so the carrier density can be reformulated to:

$$n(\psi) = n_0 e^{\frac{q(\psi - V_{\text{CB}})}{k_B T}} , \quad (7.55)$$

where  $V_{CB}$  denotes the potential value at a location C in the channel. A procedure analogous to the one in Appendix D. yields the following expression for the total semiconductor charge:

$$\sigma_s(V_{CB}) = -\sqrt{2q\varepsilon_0\varepsilon_{Si}N_A} \cdot \sqrt{\frac{k_B T}{q} e^{-\frac{q\psi_s}{k_B T}} + \psi_s - \frac{k_B T}{q} + \frac{n_i^2}{N_A^2} \left( \frac{k_B T}{q} e^{-\frac{q(\psi_s - V_{CB})}{k_B T}} - \psi_s - \frac{k_B T}{q} e^{-\frac{qV_{CB}}{k_B T}} \right)} . \quad (7.56)$$

This shows that the charge density depends on the value of  $V_{CB}$  within the channel. In order to calculate the current in the channel, one has to define the channel width  $W$  and the channel length  $L$ . The current consists of a drift and a diffusive component:

$$I_{\text{Drift}}(x) = -\mu_n W \sigma_I \frac{d\psi_s}{dx} , \quad (7.57)$$

$$I_{\text{Diff}}(x) = \mu_n W \frac{k_B T}{q} \frac{\sigma_I}{dx} . \quad (7.58)$$

$\mu_n$  is the channel mobility, while  $\sigma_I$  describes the inversion charge density. The total current is given by the sum of the diffusive and drift part and can be calculated by averaging all infinitesimal contributions along the channel.

$$I = I_{\text{Drift}} + I_{\text{Diff}} = \frac{1}{L} \int_0^L I_{\text{Drift}}(x) + I_{\text{Diff}}(x) dx \quad (7.59)$$

Unfortunately, the inversion charge density  $\sigma_I$  and the semiconductor surface potential  $\psi_s$  are not easily accessible and in conjunction the integration is not possible without further assumptions. The charge-sheet model arrogates that the inversion charge is represented by an infinitesimal thin sheet of charge, positioned at the surface of the channel. Due to its infinitesimal thickness, it does not contribute to any vertical potential drop. The rest of the charge is embraced as depletion charge without majority carrier contributions, leading to potential variations defined by a constant density depletion charge. Furthermore, the depletion layer is postulated to exhibit a sharp edge. With all these constraints, one can derive a closed form expression for the inversion charge as a function of the surface potential. The potential drop from the gate to the body, perpendicular to the MOSFET structure, is given by:

$$\begin{aligned} V_{GB} &= \Phi_{MS} + \psi_{Ox} + \psi_s , \\ V_{GB} &= \Phi_{MS} + \psi_s - \frac{\sigma_I + \sigma_B}{C_{ox}} - \frac{\sigma_0}{C_{ox}} , \\ V_{GB} &= V_{FB} + \psi_s - \frac{\sigma_B + \sigma_I}{C_{ox}} . \end{aligned} \quad (7.60)$$

Now, the descriptions for  $\sigma_I$  and  $\sigma_B$  have to be calculated. Applying Gauß's law on the region containing only depletion charges, one can see:

$$\begin{aligned}
 \frac{d^2\psi}{dz^2} &= -\frac{qN_A}{\varepsilon_0\varepsilon_{Si}} , \\
 \psi_s &= \frac{qN_A}{\varepsilon_0\varepsilon_{Si}} (L_b)^2 , \\
 L_b &= \sqrt{\frac{qN_A}{\varepsilon_0\varepsilon_{Si}}} \sqrt{\psi_s} , \\
 \sigma_B &= -qN_AL_b = -\sqrt{2qN_A\varepsilon_0\varepsilon_{Si}} \sqrt{\psi_s} ,
 \end{aligned} \tag{7.61}$$

thus, the charge density  $\sigma_B$  is linked to the surface potential  $\psi_s$  via a square root dependence. The expression for the inversion charge density can be written as follows:

$$\begin{aligned}
 \sigma_I &= -C_{ox} \left( V_{GB} - V_{FB} - \psi_s + \frac{\sigma_B}{C_{ox}} \right) , \\
 \sigma_I &= -C_{ox} \left( V_{GB} - V_{FB} - \psi_s - \frac{\sqrt{2qN_A\varepsilon_0\varepsilon_{Si}}}{C_{ox}} \sqrt{\psi_s} \right) , \\
 \sigma_I &= -C_{ox} \left( V_{GB} - V_{FB} - \psi_s - \gamma \sqrt{\psi_s} \right) ,
 \end{aligned} \tag{7.62}$$

where the body effect coefficient is in units of  $V^{-1}$  defined as:

$$\gamma = \frac{\sqrt{2qN_A\varepsilon_0\varepsilon_{Si}}}{C_{ox}} . \tag{7.63}$$

Knowing all needed relations, the integrations for the drain current can be performed. Starting with the determination of the diffusive part of the current,

$$\begin{aligned}
 I_{\text{Diff}} &= \mu_n \frac{W}{L} \frac{k_B T}{q} \int_0^L \frac{d\sigma_I}{dx} dx \\
 &= \mu_n \frac{W}{L} \frac{k_B T}{q} \int_{\sigma_{I,s}}^{\sigma_{I,d}} d\sigma_I \\
 &= \mu_n \frac{W}{L} \frac{k_B T}{q} C_{ox} \left( \psi_{s, \text{source}} - \psi_{d, \text{source}} + \gamma \left( \sqrt{\psi_{s, \text{source}}} - \sqrt{\psi_{d, \text{source}}} \right) \right) ,
 \end{aligned} \tag{7.64}$$

and followed by the drift part of the drain current,

$$\begin{aligned}
I_{\text{Drift}} &= -\mu_n \frac{W}{L} \int_0^L \sigma_I \frac{d\psi_s}{dx} dx \\
&= -\mu_n \frac{W}{L} \int_{\psi_{s, \text{source}}}^{\psi_{s, \text{drain}}} \sigma_I d\psi_s \\
&= -\mu_n \frac{W}{L} C_{\text{ox}} \int_{\psi_{s, \text{source}}}^{\psi_{s, \text{drain}}} (V_{\text{GB}} - V_{\text{FB}} - \psi_s - \gamma \sqrt{\psi_s}) d\psi_s \\
&= -\mu_n \frac{W}{L} C_{\text{ox}} \left[ (V_{\text{GB}} - V_{\text{FB}}) (\psi_{s, \text{drain}} - \psi_{s, \text{source}}) - \frac{1}{2} (\psi_{s, \text{drain}}^2 - \psi_{s, \text{source}}^2) - \right. \\
&\quad \left. - \frac{2}{3} \gamma (\psi_{s, \text{drain}}^{3/2} - \psi_{s, \text{source}}^{3/2}) \right] , \tag{7.65}
\end{aligned}$$

one completes the equation system. The surface potentials  $\psi_{s, \text{source}}$  and  $\psi_{s, \text{drain}}$  can be determined by iterating the subsequent equations:

$$\begin{aligned}
\psi_{s, \text{source}} &= V_{\text{GB}} - V_{\text{FB}} - \gamma \\
&\times \sqrt{\frac{k_{\text{B}}T}{q} e^{-\frac{q\psi_{s, \text{source}}}{k_{\text{B}}T}} + \psi_{s, \text{source}} - \frac{k_{\text{B}}T}{q} + \frac{n_i^2}{N_{\text{A}}^2} \left( \frac{k_{\text{B}}T}{q} e^{-\frac{q(\psi_{s, \text{source}} - V_{\text{SB}})}{k_{\text{B}}T}} - \psi_{s, \text{source}} - \frac{k_{\text{B}}T}{q} e^{-\frac{qV_{\text{SB}}}{k_{\text{B}}T}} \right)} , \tag{7.66}
\end{aligned}$$

$$\begin{aligned}
\psi_{s, \text{drain}} &= V_{\text{GB}} - V_{\text{FB}} - \gamma \\
&\times \sqrt{\frac{k_{\text{B}}T}{q} e^{-\frac{q\psi_{s, \text{drain}}}{k_{\text{B}}T}} + \psi_{s, \text{drain}} - \frac{k_{\text{B}}T}{q} + \frac{n_i^2}{N_{\text{A}}^2} \left( \frac{k_{\text{B}}T}{q} e^{-\frac{q(\psi_{s, \text{drain}} - V_{\text{DB}})}{k_{\text{B}}T}} - \psi_{s, \text{drain}} - \frac{k_{\text{B}}T}{q} e^{-\frac{qV_{\text{DB}}}{k_{\text{B}}T}} \right)} , \tag{7.67}
\end{aligned}$$

where  $V_{\text{SB}}$  and  $V_{\text{DB}}$  denote the source and drain biases with respect to the bulk, respectively.

---

# Bibliography

---

- [1] D. Hareme, L. Bousse, J. Shott, and J. Meindl, “Ion-Sensing Devices with Silicon Nitride and Borosilicate Glass Insulators,” *IEEE Trans. Electron Devices*, vol. 34, no. 8, pp. 1700–1707, Aug 1987.
- [2] <http://www.pdb.org>.
- [3] A. Martinez, K. Kalna, P. Sushko, A. Shluger, J. Barker, and A. Asenov, “Impact of Body-Thickness-Dependent Band Structure on Scaling of Double-Gate MOSFETs: A DFT/NEGF Study,” *IEEE Trans. Nanotechnology*, vol. 8, no. 2, pp. 159–166, March 2009.
- [4] J.-L. van der Steen, D. Esseni, P. Palestri, L. Selmi, and R. Hueting, “Validity of the Parabolic Effective Mass Approximation in Silicon and Germanium n-MOSFETs with Different Crystal Orientations,” *IEEE Trans. Electron Devices*, vol. 54, no. 8, pp. 1843–1851, Aug 2007.
- [5] R. Beynon and J. Easterby, *Buffer Solutions the Basics*. Oxford University Press, Oxford New York Tokyo, 1996.
- [6] “International Technology Roadmap for Semiconductors: 2009 Edition,” 2009. <http://www.itrs.net/Links/2009ITRS/Home2009.htm>.
- [7] T. Bohr, “Intel 32 nm Technology,” tech. rep., Intel Logic Technology Development, Feb 2009.
- [8] C.-H. Jan, P. Bai, S. Biswas, M. Buehler, Z.-P. Chen, G. Curello, S. Gannavaram, W. Hafez, J. He, J. Hicks, U. Jalan, N. Lazo, J. Lin, N. Lindert, C. Litteken, M. Jones, M. Kang, K. Komeyli, A. Mezhiba, S. Naskar, S. Olson, J. Park, R. Parker, L. Pei, I. Post, N. Pradhan, C. Prasad, M. Prince, J. Rizk, G. Sacks, H. Tashiro, D. Towner, C. Tsai, Y. Wang, L. Yang, J.-Y. Yeh, J. Yip, and K. Mistry, “A 45nm Low Power System-On-Chip Technology with Dual Gate (Logic and I/O) High-K/Metal Gate Strained Silicon Transistors,” in *IEEE Proc. Intl. Electron Devices Meeting*, pp. 1–4, Dec 2008.
- [9] S. Borkar, “Design Challenges for 22 nm CMOS and Beyond,” in *IEEE Proc. Intl. Electron Devices Meeting*, p. 18.2.1, Dec 2009.

## BIBLIOGRAPHY

---

- [10] S. Hofstein and F. Heiman, "The Silicon Insulated-Gate Field-Effect Transistor," in *Proc.IEEE*, vol. 51, pp. 1190–1202, Sep 1963.
- [11] C. Jan, M. Agostinelli, M. Buehler, Z.-P. Chen, S.-J. Choi, G. Curello, H. Deshpande, S. Gannavaram, W. Hafez, U. Jalan, M. Kang, P. Kolar, K. Komeyli, B. Landau, A. Lake, N. Lazo, S.-H. Lee, T. Leo, J. Lin, N. Lindert, S. Ma, L. McGill, C. Meining, A. Paliwal, J. Park, K. Phoa, I. Post, N. Pradhan, M. Prince, A. Rahman, J. Rizk, L. Rockford, G. Sacks, A. Schmitz, H. Tashiro, C. Tsai, P. Vandervoorn, J. Xu, L. Yang, J.-Y. Yeh, J. Yip, K. Zhang, Y. Zhang, and P. Bai, "A 32nm SoC Platform Technology with 2<sup>nd</sup> Generation High-k/Metal Gate Transistors Optimized for Ultra Low Power, High Performance, and High Density Product Applications," in *IEEE Proc. Intl. Electron Devices Meeting*, pp. 647–650, Dec 2009.
- [12] Intel Cooperation, *Intel<sup>®</sup> Core™ i7 Processor Extreme and Intel<sup>®</sup> Core™ i7 Processor, Datasheet, Volume 1*, Nov 2008.
- [13] B. Stackhouse, S. Bhimji, C. Bostak, D. Bradley, B. Cherkauer, J. Desai, E. Francom, M. Gowan, P. Gronowski, D. Krueger, C. Morganti, and S. Troyer, "A 65 nm 2-Billion Transistor Quad-Core Itanium Processor," *IEEE Journal of Solid-State Circuits*, vol. 44, no. 1, pp. 18–31, Jan 2009.
- [14] N. Flaherty, "Flash [computer memory]," *IEEE Review*, vol. 49, no. 11, pp. 50–53, Nov 2003.
- [15] K. Itoh, T. Watanabe, S. Kimura, and T. Sakata, "Reviews and Prospects of High-Density RAM Technology," in *Proc. Intl. Semiconductor Conference CAS*, vol. 1, pp. 13–22, 2000.
- [16] P. Bergveld, "Thirty Years of ISFETology: What Happened in the Past 30 Years and What May Happen in the Next 30 Years," *Sensors and Actuators B: Chemical*, vol. 88, no. 1, pp. 1–20, 2003.
- [17] Z. Gao, A. Agarwal, A. Trigg, N. Singh, C. Fang, C.-H. Tung, Y. Fan, K. Buddhharaju, and J. Kong, "Silicon Nanowire Arrays for Label-Free Detection of DNA," *Analytical Chemistry*, vol. 79, no. 9, pp. 3291–3297, April 2007. doi: 10.1021/ac061808q.
- [18] G. E. Moore, "Cramming More Components onto Integrated Circuits," *Electronics*, vol. 38, no. 8, pp. 114–117, 1965.
- [19] B. V. Zeghbroeck, *Principles of Semiconductor Devices*. online course, 2007. <http://ece-www.colorado.edu/~bart/book/>.
- [20] "International Technology Roadmap for Semiconductors: 2008 Update," 2008. <http://www.itrs.net/Links/2008ITRS/Home2008.htm>.
- [21] K. Mistry, C. Allen, C. Auth, B. Beattie, D. Bergstrom, M. Bost, M. Brazier, M. Buehler, A. Cappellani, R. Chau, C. . Choi, G. Ding, K. Fischer, T. Ghani, R. Grover, W. Han, D. Hanken, M. Hattendorf, J. He, J. Hicks, R. Huessner, D. Ingerly, P. Jain, R. James, L. Jong, S. Joshi, C. Kenyon, K. Kuhn, K. Lee, H. Liu, J. Maiz, B. McIntyre, P. Moon, J. Neiryneck, S. Pae, C. Parker, D. Parsons, C. Prasad, L. Pipes, M. Prince, P. Rarade, T. Reynolds, J. Sandford, L. Shifren, J. Sebastian, J. Seiple, D. Simon, S. Sivakumar, P. Smith, C. Thomas, T. Troeger, P. Vandervoorn, S. Williams, and K. Zawadzki, "A

## BIBLIOGRAPHY

---

- 45nm Logic Technology with High-k+ Metal Gate Transistors, Strained Silicon, 9 Cu Interconnect Layers, 193nm Dry Patterning, and 100% Pb-free Packaging,” in *IEEE Proc. Intl. Electron Devices Meeting*, pp. 247–250, Dec 2007.
- [22] K. Mistry, M. Armstrong, C. Auth, S. Cea, T. Coan, T. Ghani, T. Hoffmann, A. Murthy, J. Sandford, R. Shaheed, K. Zawadzki, K. Zhang, S. Thompson, and M. Bohr, “Delaying Forever: Uniaxial Sstrained Silicon Transistors in a 90 nm CMOS Technology,” in *IEEE Symposium on VLSI Technology Digest of Technical Papers*, pp. 50–51, June 2004.
- [23] P. Bai, C. Auth, S. Balakrishnan, M. Bost, R. Brain, V. Chikarmane, R. Heussner, M. Hussein, J. Hwang, D. Ingerly, R. James, J. Jeong, C. Kenyon, E. Lee, S.-H. Lee, N. Lindert, M. Liu, Z. Ma, T. Marieb, A. Murthy, R. Nagisetty, S. Natarajan, J. Neiryneck, A. Ott, C. Parker, J. Sebastian, R. Shaheed, S. Sivakumar, J. Steigerwald, S. Tyagi, C. Weber, B. Woolery, A. Yeoh, K. Zhang, and M. Bohr, “A 65 nm Logic Technology Featuring 35 nm Gate Lengths, Enhanced Channel Strain, 8 Cu Interconnect Layers, Low-k ILD and  $0.57\ \mu\text{m}^2$  SRAM Cell,” in *IEEE Proc. Intl. Electron Devices Meeting*, pp. 657–660, Dec 2004.
- [24] P. Packan, S. Akbar, M. Armstrong, D. Bergstrom, M. Brazier, H. Deshpande, K. Dev, G. Ding, T. Ghani, O. Golonzka, W. Han, J. He, R. Heussner, R. James, J. Jopling, C. Kenyon, S. Lee, M. Liu, S. Lodha, B. Mattis, A. Murthy, L. Neiberg, J. Neiryneck, S. Pae, C. Parker, L. Pipes, J. Sebastian, J. Seiple, B. Sell, A. Sharma, S. Sivakumar, B. Song, A. Amour, K. Tone, T. Troeger, C. Weber, K. Zhang, Y. Luo, and S. Natarajan, “High Performance 32 nm Logic Technology Featuring 2<sup>nd</sup> Generation High-k + Metal Gate Transistors,” in *IEEE Proc. Intl. Electron Devices Meeting*, pp. 659–662, Dec 2009.
- [25] M. Frank, S. Kim, S. Brown, J. Bruley, M. Copel, M. Hopstaken, M. Chudzik, and V. Narayanan, “Scaling the MOSFET Gate Dielectric: From High-k to Higher-k? (Invited Paper),” *Microelectronic Engineering*, vol. 86, no. 7–9, pp. 1603–1608, 2009. INFOS 2009.
- [26] S. Rhee, C. Kang, C. Choi, C. Kang, S. Krishnan, M. Zhang, M. Akbar, and J. Lee, “Improved Electrical and Material Characteristics of Hafnium Titanate Multi-Metal Oxide n-MOSFETs with Ultra-Thin EOT ( $\sim 8\text{\AA}$ ) Gate Dielectric Application,” in *IEEE Proc. Intl. Electron Devices Meeting*, pp. 837–840, Dec 2004.
- [27] X. Guo, X. Wang, Z. Luo, T. Ma, and T. Tamagawa, “High Quality Ultra-Thin (1.5 nm)  $TiO_2 - Si_3N_4$  Gate Dielectric for Deep Sub-Micron CMOS Technology,” in *IEEE Proc. Intl. Electron Devices Meeting*, pp. 137–140, Dec 1999.
- [28] D. Triyoso, R. Hegde, X.-D. Wang, M. Stoker, R. Rai, M. Ramon, J. B.E. White, and P. Tobin, “Characteristics of Mixed Oxides and Nanolaminates of Atomic Layer Deposited  $HfO_2 - TiO_2$  Gate Dielectrics,” *J.Electrochem.Soc.*, vol. 153, no. 9, pp. G834–G839, 2006.
- [29] S. Kim, S. Brown, S. Rossnagel, J. Bruley, M. Copel, M. Hopstaken, V. Narayanan, and M. Frank, “Oxygen Migration in  $TiO_2$ -Based Higher-k Gate Stacks,” *J.Appl.Phys.*, vol. 107, p. 054102, 2010.
- [30] H.-H. Tseng, P. Kirsch, C. Park, G. Bersuker, P. Majhi, M. Hussain, and R. Jammy, “The Progress and Challenges of Threshold Voltage Control of High-k/Metal-Gated Devices for Advanced Technologies (Invited Paper),” *Microelectronic Engineering*, vol. 86, no. 7–9, pp. 1722–1727, 2009.

## BIBLIOGRAPHY

---

- [31] K. Kita and A. Toriumi, "Intrinsic Origin of Electric Dipoles Formed at High-k/ $SiO_2$  Interface," in *IEEE Proc. Intl. Electron Devices Meeting*, pp. 1–4, Dec 2008.
- [32] P. Sivasubramani, T. Boscke, J. Huang, C. Young, P. Kirsch, S. Krishnan, M. Quevedo-Lopez, S. Govindarajan, B. Ju, H. Harris, D. Lichtenwalner, J. Jur, A. Kingon, J. Kim, B. Gnade, R. Wallace, G. Bersuker, B. Lee, and R. Jammy, "Dipole Moment Model Explaining nFET Vt Tuning Utilizing La, Sc, Er, and Sr Doped  $HfSiON$  Dielectrics," in *IEEE Symposium on VLSI Technology Digest of Technical Papers*, pp. 68–69, June 2007.
- [33] P. D. Kirsch, P. Sivasubramani, J. Huang, C. D. Young, M. A. Quevedo Lopez, H. C. Wen, H. Alshareef, K. Choi, C. S. Park, K. Freeman, M. M. Hussain, G. Bersuker, H. R. Harris, P. Majhi, R. Choi, P. Lysaght, B. H. Lee, H.-H. Tseng, R. Jammy, T. S. Böske, D. J. Lichtenwalner, J. S. Jur, and A. I. Kingon, "Dipole Model Explaining High-k/Metal Gate Field Effect Transistor Threshold Voltage Tuning," *Appl.Phys.Lett.*, vol. 92, no. 9, p. 092901, 2008.
- [34] F. Masuoka and H. Iizuka, "Semiconductor Memory Device and Method for Manufacturing the Same," July 1985. Patent: US4531203 (A).
- [35] Y. Chen, "Flash Memory Reliability NEPP 2008 Task Final Report," Tech. Rep. 09-09, Jet Propulsion Laboratory, National Aeronautics and Space Administration, Pasadena, California, USA, March 2009. <http://hdl.handle.net/2014/41262>.
- [36] SanDisk Corporation, "SanDisk Announces Worlds Largest Mobile Phone Memory Card Capacity with 16GB MicroSDHC and M2," press release, <http://www.sandisk.com/Corporate/PressRoom/PressReleases/PressRelease.aspx?ID=4398>, 2008.
- [37] K. Kim, "Technology for Sub-50nm DRAM and NAND Flash Manufacturing," in *IEEE Proc. Intl. Electron Devices Meeting*, pp. 323–326, Dec 2005.
- [38] D. DiMaria and E. Cartier, "Mechanism for Stress-Induced Leakage Currents in Thin Silicon Dioxide Films," *J.Appl.Phys.*, vol. 78, no. 6, pp. 3883–3894, 1995.
- [39] J. Kittl, K. Opsomer, M. Popovici, N. Menou, B. Kaczer, X. Wang, C. Adelman, M. Pawlak, K. Tomida, A. Rothschild, B. Govoreanu, R. Degraeve, M. Schaekers, M. Zahid, A. Delabie, J. Meersschant, W. Polspoel, S. Clima, G. Pourtois, W. Knaepen, C. Detavernier, V. Afanas'ev, T. Blomberg, D. Pierreux, J. Swerts, P. Fischer, J. Maes, D. Manger, W. Vandervorst, T. Conard, A. Franquet, P. Favia, H. Bender, B. Brijs, S. Van Elshocht, M. Jurczak, J. Van Houdt, and D. Wouters, "High-k Dielectrics for Future Generation Memory Devices (Invited Paper)," *Microelectronic Engineering*, vol. 86, no. 7-9, pp. 1789–1795, 2009. INFOS 2009.
- [40] V. V. Afanas'ev and A. Stesmans, "Internal Photoemission at Interfaces of High- $\kappa$  Insulators with Semiconductors and Metals," *J.Appl.Phys.*, vol. 102, no. 8, p. 081301, 2007.
- [41] B. Govoreanu, D. Wellekens, L. Haspeslagh, D. Brunco, J. D. Vos, D. R. Aguado, P. Blomme, K. van der Zanden, and J. V. Houdt, "Performance and Reliability of  $HfAlO_x$ -based Interpoly Dielectrics for Floating-Gate Flash Memory," *Solid-State Electron.*, vol. 52, no. 4, pp. 557–563, April 2008.

## BIBLIOGRAPHY

---

- [42] R. Steimle, R. Muralidhar, R. Rao, M. Sadd, C. Swift, J. Yater, B. Hradsky, S. Straub, H. Gasquet, L. Vishnubhotla, E. Prinz, T. Merchant, B. Acred, K. Chang, B. White, and Jr., "Silicon Nanocrystal Non-Volatile Memory for Embedded Memory Scaling," *Microelectron.Reliab.*, vol. 47, no. 4–5, pp. 585–592, 2007.
- [43] C. Gerardi, V. Ancarani, R. Portoghese, S. Giuffrida, M. Bileci, G. Bimbo, O. Brafa, D. Mello, G. Ammendola, E. Tripiciano, R. Puglisi, and S. Lombardo, "Nanocrystal Memory Cell Integration in a Stand-Alone 16-Mb NOR Flash Device," *IEEE Trans. Electron Devices*, vol. 54, no. 6, pp. 1376–1383, June 2007.
- [44] R. A. Puglisi, S. Lombardo, D. Corso, I. Crupi, G. Nicotra, L. Perniola, B. De Salvo, and C. Gerardi, "Effects of Partial Self-Ordering of Si Dots Formed by Chemical Vapor Deposition on the Threshold Voltage Window Distribution of Si Nanocrystal Memories," *J. Appl. Phys.*, vol. 100, no. 8, p. 086104, 2006.
- [45] R. Ohba, Y. Mitani, N. Sugiyama, and S. Fujita, "10 nm Bulk-Planar SONOS-Type Memory with Double Tunnel Junction and Sub-10 nm Scaling Utilizing Source to Drain Direct Tunnel Sub-Threshold," in *IEEE Proc. Intl. Electron Devices Meeting*, pp. 1–4, Dec 2008.
- [46] S. Lombardo, C. Gerardi, L. Breuil, C. Jahan, L. Perniola, G. Cina, D. Corso, E. Tripiciano, V. Ancarani, G. Iannaccone, G. Iacono, C. Bongiorno, J. Razafindramora, C. Garozzo, P. Barbera, E. Nowak, R. Puglisi, G. Costa, C. Coccorese, M. Vecchio, E. Rimini, J. Van Houdt, B. De Salvo, and M. Melanotte, "Advantages of the FinFET Architecture in SONOS and Nanocrystal Memory Devices," in *IEEE Proc. Intl. Electron Devices Meeting*, pp. 921–924, Dec 2007.
- [47] A. Marent, M. Geller, A. Schliwa, D. Feise, K. Pötschke, D. Bimberg, N. Akçay, and N. Öncan, "10<sup>6</sup> Years Extrapolated Hole Storage Time in *GaSb/AlAs* Quantum Dots," *Appl. Phys. Lett.*, vol. 91, no. 24, p. 242109, 2007.
- [48] W. Haensch, E. Nowak, R. Dennard, P. Solomon, A. Bryant, O. Dokumaci, A. Kumar, X. Wang, J. Johnson, and M. V. Fischetti, "Silicon CMOS Devices Beyond Scaling," *IBM J. Res. Dev.*, vol. 50, no. 4/5, pp. 339–361, 2006.
- [49] B. Hoeneisen and C. Mead, "Fundamental Limitations in Microelectronics—I. MOS Technology," *Solid-State Electron.*, vol. 15, no. 7, pp. 819–829, July 1972.
- [50] J. Wallmark, "Fundamental Physical Limitations in Integrated Electronic Circuits," in *Inst. Phys. Conf. Ser.*, vol. 25, pp. 133–167, 1975.
- [51] C. Hu, "Gate Oxide Scaling Limits and Projection," in *IEEE Proc. Intl. Electron Devices Meeting*, pp. 319–322, Dec 1996.
- [52] J. Stathis and D. DiMaria, "Reliability Projection for Ultra-Thin Oxides at Low Voltage," in *IEEE Proc. Intl. Electron Devices Meeting*, pp. 167–170, Dec 1998.
- [53] K. Rim, J. Chu, H. Chen, K. Jenkins, T. Kanarsky, K. Lee, A. Mocuta, H. Zhu, R. Roy, J. Newbury, J. Ott, K. Petrarca, P. Mooney, D. Lacey, S. Koester, K. Chan, D. Boyd, M. Jeong, and H.-S. Wong, "Characteristics and Device Design of Sub-100 nm Strained *Si* n- and nMOSFETs," in *IEEE Symposium on VLSI Technology Digest of Technical Papers*, pp. 98–99, 2002.

## BIBLIOGRAPHY

---

- [54] S. Thompson, M. Armstrong, C. Auth, S. Cea, R. Chau, G. Glass, T. Hoffmann, J. Klaus, Z. Ma, B. McIntyre, A. Murthy, B. Obradovic, L. Shifren, S. Sivakumar, S. Tyagi, T. Ghani, K. Mistry, M. Bohr, and Y. El-Mansy, "A Logic Nanotechnology Featuring Strained-Silicon," *IEEE Electron Device Lett.*, vol. 25, no. 4, pp. 191–193, 2004.
- [55] H. Hall, J. Bardeen, and G. Pearson, "The Effects of Pressure and Temperature on the Resistance of  $p-n$  Junctions in Germanium," *Physical Review*, vol. 84, no. 1, pp. 129–132, Oct 1951.
- [56] C. Smith, "Piezoresistance Effect in Germanium and Silicon," *Physical Review*, vol. 94, no. 1, pp. 42–49, April 1954.
- [57] E. Fitzgerald, Y. Xie, M. Green, D. Brasen, A. Kortan, J. Michel, Y. Mii, and B. Weir, "Totally Relaxed  $\text{Ge}_x\text{Si}_{1-x}$  Layers with Low Threading Dislocation Densities Grown on Si Substrates," *Appl.Phys.Lett.*, vol. 59, no. 7, pp. 811–813, 1991.
- [58] J. Welser, J. Hoyt, and J. Gibbons, "NMOS and PMOS Transistors Fabricated in Strained Silicon/Relaxed Silicon-Germanium Structures," in *IEEE Proc. Intl. Electron Devices Meeting*, pp. 1000–1002, Dec 1992.
- [59] J. Welser, J. Hoyt, and J. Gibbons, "Electron Mobility Enhancement in Strained-Si n-Type Metal-Oxide-Semiconductor Field-Effect Transistors," *IEEE Electron Device Lett.*, vol. 15, no. 3, pp. 100–102, March 1994.
- [60] Z.-Y. Cheng, M. Currie, C. Leitz, G. Taraschi, E. Fitzgerald, J. Hoyt, and D. Antoniadis, "Electron Mobility Enhancement in Strained-Si n-MOSFETs Fabricated on SiGe-On-Insulator (SGOI) Substrates," *IEEE Electron Device Lett.*, vol. 22, no. 7, pp. 321–323, July 2001.
- [61] B. Ghyselen, J. Hartmann, T. Ernst, C. Aulnette, Y. Osternaud, B. and Bogumilowicz, A. Abbadie, P. Besson, O. Rayssac, and A. Tiberj, "Engineering Strained Silicon on Insulator Wafers with the Smart Cut™ Technology," *Solid-State Electron.*, vol. 48, no. 8, pp. 1285–1296, Aug 2004.
- [62] M. Sadaka, A. Thean, A. Barr, D. Tekleab, S. Kalpat, and T. White, "Fabrication and Operation of Sub-50 nm Strained-Si on  $\text{Si}_{1-x}\text{Ge}_x$  on Insulator (SGOI) CMOSFETs," in *IEEE Intl. SOI Conference*, pp. 209–211, 2004.
- [63] F. Andrieu, T. Ernst, O. Faynot, O. Rozeau, Y. Bogumilowicz, J. M. Hartmann, L. Brevard, A. Toffoli, D. Lafond, and B. Ghyselen, "Performance and Physics of Sub-50 nm Strained Si on  $\text{Si}_{1-x}\text{Ge}_x$  on Insulator (SGOI) nMOSFETs," *Solid-State Electron.*, vol. 50, no. 4, pp. 566–572, April 2006.
- [64] L.-J. Huang, J. Chu, S. Goma, C. D'Emic, S. Koester, D. Canaperi, P. Mooney, S. Cordes, J. Speidell, R. Anderson, and H.-S. Wong, "Carrier Mobility Enhancement in Strained Si-On-Insulator Fabricated by Wafer Bonding," in *IEEE Symposium on VLSI Technology Digest of Technical Papers*, pp. 57–58, 2001.
- [65] K. Rim, K. Chan, L. Shi, D. Boyd, J. Ott, N. Klymko, F. Cardone, L. Tai, S. Koester, M. Cobb, D. Canaperi, B. To, E. Duch, I. Babich, R. Carruthers, P. Saunders, G. Walker,

## BIBLIOGRAPHY

---

- Y. Zhang, M. Steen, and M. Jeong, "Fabrication and Mobility Characteristics of Ultra-Thin Strained Si Directly on Insulator (SSDOI) MOSFETs," in *IEEE Proc. Intl. Electron Devices Meeting*, pp. 49–52, Dec 2003.
- [66] S. Uppal, M. Bollani, A. Willoughby, J. Bonar, R. Morris, and M. Dowsett, "Boron Diffusion in High Ge Content SiGe Alloys," in *Electrochemical Society Proceedings*, vol. 7, pp. 159–165, Electrochemical Society Inc., 2004.
- [67] K. Rim, J. Hoyt, and J. Gibbons, "Fabrication and Analysis of Deep Submicron Strained-Si n-MOSFET's," *IEEE Trans. Electron Devices*, vol. 47, no. 7, pp. 1406–1415, July 2000.
- [68] B. Haugerud, L. Bosworth, and R. Belford, "Mechanically Induced Strain Enhancement of Metal–Oxide–Semiconductor Field Effect Transistors," *J. Appl. Phys.*, vol. 94, no. 6, pp. 4102–4107, 2003.
- [69] R. E. Belford, "Uniaxial, Tensile-Strained Si Devices," *J. Electron. Mater.*, vol. 30, no. 7, pp. 807–811, 2001.
- [70] L. Bera, W. Loh, L. Guo, X. Zhang, G. Lo, N. Balasubramanian, and D.-L. Kwong, "The Impact of Uniform Strain Applied Via Bonding Onto Plastic Substrate on MOSFET Performance," *IEEE Electron Device Lett.*, vol. 27, no. 1, pp. 58–61, Jan 2006.
- [71] G. Scott, J. Lutze, M. Rubin, F. Nouri, and M. Manley, "NMOS Drive Current Reduction Caused by Transistor Layout and Trench Isolation Induced Stress," in *IEEE Proc. Intl. Electron Devices Meeting*, pp. 827–830, Dec 1999.
- [72] T. Matsumoto, S. Maeda, H. Dang, T. Uchida, K. Ota, Y. Hirano, H. Sayama, T. Iwamatsu, T. Ipposhi, H. Oda, S. Maegawa, Y. Inoue, , and T. Nishimura, "Novel SOI Wafer Engineering using Low Stress and High Mobility CMOSFET with  $\langle 100 \rangle$  Channel for Embedded RF/Analog Applications," in *IEEE Proc. Intl. Electron Devices Meeting*, pp. 663–666, Dec 2002.
- [73] A. Steegen, M. Stucchi, A. Lauwers, and K. Maex, "Silicide Induced Pattern Density and Orientation Dependent Transconductance in MOS Transistors," in *IEEE Proc. Intl. Electron Devices Meeting*, pp. 497–500, Dec 1999.
- [74] S. Ito, H. Namba, K. Yamaguchi, T. Hirata, K. Ando, S. Koyama, S. Kuroki, N. Ikezawa, T. Suzuki, T. Saitoh, and T. Horiuchi, "Mechanical Stress Effect of Etch-Stop Nitride and its Impact on Deep Submicron Transistor Design," in *IEEE Proc. Intl. Electron Devices Meeting*, pp. 247–251, Dec 2000.
- [75] A. Shimizu, K. Hachimine, N. Ohki, H. Ohta, M. Koguchi, Y. Nonaka, H. Sato, , and F. Ootsuka, "Local Mechanical-Stress Control (LMC): A New Technique for CMOS-Performance Enhancement," in *IEEE Proc. Intl. Electron Devices Meeting*, pp. 433–436, Dec 2001.
- [76] R. Khamankar, H. Bu, C. Bowen, S. Chakravarthi, P. Chidambaram, M. Bevan, A. Krishnan, H. Niimi, B. Smith, J. Blatchford, B. Hornung, J. Lu, P. Nicollian, B. Kirkpatrick, D. Miles, M. Hewson, D. Farber, L. Hall, H. Alshareef, A. Varghese, A. Gurba, V. Ukraintsev, B. Rath sack, J. De Loach, J. Tran, C. Kaneshige, M. Somervell, S. Aur, C. Machala, and T. Grider, "An Enhanced 90nm High Performance Technology with

- Strong Performance Improvements from Stress and Mobility Increase Through Simple Process Changes,” in *IEEE Symposium on VLSI Technology Digest of Technical Papers*, pp. 162–163, June 2004.
- [77] J.-S. Lim, S. Thompson, and J. Fossum, “Comparison of Threshold-Voltage Shifts for Uniaxial and Biaxial Tensile-Stressed n-MOSFETs,” *IEEE Electron Device Lett.*, vol. 25, no. 11, pp. 731–733, Nov 2004.
- [78] S. Eneman, P. Verheyen, R. Rooyackers, F. Nouri, L. Washington, R. Degraeve, B. Kaczer, V. Moroz, A. De Keersgieter, R. Schreutelkamp, M. Kawaguchi, Y. Kim, A. Samoilo, L. Smith, P. Absil, K. De Meyer, M. Jurczak, and S. Biesemans, “Layout Impact on the Performance of a Locally Strained PMOSFET,” in *IEEE Symposium on VLSI Technology Digest of Technical Papers*, pp. 22–23, June 2005.
- [79] H. Yang, R. Malik, S. Narasimha, Y. Li, R. Divakaruni, P. Agnello, S. Allen, A. Antreasyan, J. C. Arnold, K. Bandy, M. Belyansky, A. Bonnoit, G. Bronner, V. Chan, X. Chen, Z. Chen, D. Chidambarrao, A. Chou, W. Clark, S. W. Crowder, B. Engel, H. Harifuchi, S. F. Huang, R. Jagannathan, F. F. Jamin, Y. Kohyama, H. Kuroda, C. W. Lai, H. K. Lee, W. H. Lee, E. H. Lim, W. Lai, A. Mallikarjunan, K. Matsumoto, A. McKnight, J. Nayak, H. Y. Ng, S. Panda, R. Rengarajan, M. Steigerwalt, S. Subbanna, K. Subramanian, J. Sudijono, G. Sudo, S. P. Sun, B. Tessier, Y. Toyoshima, P. Tran, R. Wise, R. Wong, I. Y. Yang, C. H. Wann, L. T. Su, M. Horstmann, T. Feudel, A. Wei, K. Frohberg, G. Burbach, M. Gerhardt, M. Lenski, R. Stephan, K. Wiczorek, M. Schaller, H. Salz, J. Hohage, H. Ruelke, J. Klais, P. Huebler, S. Luning, R. van Bentum, G. Grasshoff, C. Schwan, E. Ehrichs, S. Goad, J. Buller, S. Krishnan, D. Greenlaw, M. Raab, and N. Kepler, “Dual Stress Liner for High Performance Sub-45 nm Gate Length SOI CMOS Manufacturing,” in *IEEE Proc. Intl. Electron Devices Meeting*, pp. 1075–1077, Dec 2004.
- [80] C. Sheraw, M. Yang, D. Fried, G. Costrini, T. Kanarsky, W. Lee, V. Chan, M. Fischetti, J. Holt, L. Black, M. Naeem, S. Panda, L. Economikos, J. Groschopf, A. Kapur, Y. Li, R. T. Mo, A. Bonnoit, D. Degraw, S. Luning, D. Chidambarrao, X. Wang, A. Bryant, D. Brown, C.-Y. S. P. Agnello, M. I. S.-F. Huang, X. Chen, and M. Khare, “Dual Stress Liner Enhancement in Hybrid Orientation Technology,” in *IEEE Symposium on VLSI Technology Digest of Technical Papers*, pp. 12–13, 2005.
- [81] R. Arghavani, L. Xia, H. Saad, M. Balseanu, G. Karunasiri, A. Mascarenhas, , and S. Thompson, “A Reliable and Manufacturable Method to Induce a Stress of  $\geq 1$  GPa on a p-Channel MOSFET in High Volume Manufacturing,” *IEEE Electron Device Lett.*, vol. 27, no. 2, pp. 114–116, 2006.
- [82] K. Ota, K. Sugihara, H. Sayama, T. Uchida, H. Oda, T. Eimori, H. Morimoto, and Y. Inoue, “Novel Locally Strained Channel Technique for High Performance 55nm CMOS,” in *IEEE Proc. Intl. Electron Devices Meeting*, pp. 27–30, Dec 2002.
- [83] Chien-Hao Chen, T. Lee, T. Hou, C. Chen, C. Chen, J. Hsu, K. Cheng, Y. Chiu, H. Tao, Y. Jin, C. Diaz, S. Chen, and M.-S. Liang, “Stress Memorization Technique (SMT) by Selectively Strained-Nitride Capping for Sub-65nm High-Performance Strained-Si Device Application,” in *IEEE Symposium on VLSI Technology Digest of Technical Papers*, pp. 56–57, June 2004.

## BIBLIOGRAPHY

---

- [84] M. Horstmann, A. Wei, T. Kammler, J. Höntschel, H. Bierstedt, T. Feudel, K. Frohberg, M. Gerhardt, A. Hellmich, K. Hempel, J. Hohage, P. Javorika, J. Klais, G. Koerner, M. Lenski, A. Neu, R. Otterbach, P. Press, C. Reichel, M. Trentsch, B. Trui, H. Salz, M. Schaller, H.-J. Engelmann, O. Herzog, H. Ruelke, P. Hübler, R. Stephan, D. Greenlaw, M. Raab, and N. Kepler, "Integration and Optimization of Embedded-SiGe, Compressive and Tensile Stressed Liner Films, and Stress Memorization in Advanced SOI CMOS Technologies," in *IEEE Proc. Intl. Electron Devices Meeting*, pp. 233–236, Dec 2005.
- [85] V. Chan, K. Rim, M. Jeong, S. Yang, R. Malik, Y. W. Teh, M. Yang, and Qiqing, "Strain for CMOS Performance Improvement," in *Custom Integrated Circuits Conference, 2005. Proceedings of the IEEE 2005*, pp. 667–674, Sep 2005.
- [86] P. Chidambaram, C. Bowen, S. Chakravarthi, C. Machala, and R. Wise, "Fundamentals of Silicon Material Properties for Successful Exploitation of Strain Engineering in Modern CMOS Manufacturing," *IEEE Trans. Electron Devices*, vol. 53, no. 5, pp. 944–964, May 2006.
- [87] S. Thompson, M. Armstrong, C. Auth, M. Alavi, M. Buehler, R. Chau, S. Cea, T. Ghani, G. Glass, T. Hoffmann, C.-T. Jan, C. Kenyon, J. Klaus, K. Kuhn, Z. Ma, B. McIntyre, K. Mistry, A. Murthy, B. Obradovic, R. Nagisetty, P. Nguyen, S. Sivakumar, R. Shaheed, L. Shifren, B. Tufts, S. Tyagi, M. Bohr, and Y. El-Mansy, "A 90-nm Logic Nanotechnology Featuring Strained-Silicon," *IEEE Trans. Electron Devices*, vol. 51, no. 11, pp. 1790–1797, Nov 2004.
- [88] Q. Ouyang, M. Yang, J. Holt, S. Panda, H. Chen, H. Utomo, M. Fischetti, N. Rovedo, J. Li, N. Klymko, H. Wildman, T. Kanarsky, G. Costrini, D. Fried, A. Bryant, J. Ott, M. Jeong, and C. Sung, "Investigation of CMOS Devices with Embedded SiGe Source/Drain on Hybrid Orientation Substrates," in *IEEE Trans. VLSI Systems*, pp. 28–29, June 2005.
- [89] K.-W. Ang, K. Chui, V. Bliznetsov, A. Du, N. Balasubramanian, M. Li, G. Samudra, and Y.-C. Yeo, "Enhanced Performance in 50 nm n-MOSFETs with Silicon-Carbon Source/Drain Regions," in *IEEE Proc. Intl. Electron Devices Meeting*, pp. 1069–1071, Dec 2004.
- [90] K.-J. Chui, K.-W. Ang, N. Balasubramanian, M.-F. Li, G. Samudra, and Y.-C. Yeo, "n-MOSFET With SiliconCarbon Source/Drain for Enhancement of Carrier Transport," *IEEE Trans. Electron Devices*, vol. 54, no. 2, pp. 249–256, Feb 2007.
- [91] Y. Wang, D. Scott, J. Wu, J. Waller, J. Hu, K. Liu, and V. Ukraintsev, "Effects of Uniaxial Mechanical Stress on Drive Current of 0.13  $\mu\text{m}$  MOSFETs," *IEEE Trans. Electron Devices*, vol. 50, no. 2, pp. 529–531, Feb 2003.
- [92] V. Chan, R. Rengarajan, N. Rovedo, W. Jin, T. Hook, P. Nguyen, J. Chen, E. Nowak, X.-D. Chen, D. Lea, A. Chakravarti, V. Ku, S. Yang, A. Steegen, C. Baiocco, P. Shafer, H. Ng, S.-F. Huang, and C. Wann, "High Speed 45nm Gate Length CMOSFETs Integrated Into a 90 nm Bulk Technology Incorporating Strain Engineering," in *IEEE Proc. Intl. Electron Devices Meeting*, pp. 3.8.1–3.8.4, Dec 2003.
- [93] D. Zhang, B. Nguyen, T. White, B. Goolsby, T. Nguyen, V. Dhandapani, J. Hildreth, M. Foisy, V. Adams, Y. Shiho, A. Thean, D. Theodore, M. Canonico, S. Zollner, S. Bagchi,

## BIBLIOGRAPHY

---

- S. Murphy, R. Rai, J. Jiang, M. Jahanbani, R. Noble, M. Zavala, R. Cotton, D. Eades, S. Parsons, P. Montgomery, A. Martinez, B. Winstead, M. Mendicino, J. Cheek, J. Liu, P. Grudowski, N. Ranami, P. Tomasini, C. Arena, C. Werkhoven, H. Kirby, C. Chang, C. Lin, H. Tuan, Y. See, S. Venkatesan, V. Kolagunta, N. Cave, and J. Mogab, "Embedded SiGe S/D PMOS on Thin Body SOI Substrate with Drive Current Enhancement," in *IEEE Symposium on VLSI Technology Digest of Technical Papers*, pp. 26–27, June 2005.
- [94] N. Mohta and S. Thompson, "Mobility Enhancement," *IEEE Circuits & Devices*, vol. 21, no. 5, pp. 18–23, Sep–Oct 2005.
- [95] S. Pidin, T. Mori, K. Inoue, S. Fukuta, N. Itoh, E. Mutoh, K. Ohkoshi, R. Nakamura, K. Kobayashi, K. Kawamura, T. Saiki, S. Fukuyama, S. Satoh, M. Kase, and K. Hashimoto, "A Novel Strain Enhanced CMOS Architecture Using Selectively Deposited High Tensile and High Compressive Silicon Nitride Films," in *IEEE Proc. Intl. Electron Devices Meeting*, pp. 213–216, Dec 2004.
- [96] C.-H. Jan, P. Bai, J. Choi, G. Curello, S. Jacobs, J. Jeong, K. Johnson, D. Jones, S. Klop-  
cic, J. Lin, N. Lindert, A. Lio, S. Natarajan, J. Neiryneck, P. Packan, J. Park, I. Post, M. Patel, S. Ramey, P. Reese, L. Rockford, A. Roskowski, G. Sacks, B. Turkot, Y. Wang, L. Wei, J. Yip, I. Young, K. Zhang, Y. Zhang, M. Bohr, and B. Holt, "A 65 nm Ultra Low Power Logic Platform Technology Using Uni-Axial Strained Silicon Transistors," in *IEEE Proc. Intl. Electron Devices Meeting*, pp. 60–63, Dec 2005.
- [97] N. Setter, D. Damjanovic, L. Eng, G. Fox, S. Gevorgian, S. Hong, A. Kingon, H. Kohlstedt, N. Park, G. Stephenson, I. Stolitchnov, A. Tagansteve, D. Taylor, T. Yamada, and S. Streiffer, "Ferroelectric Thin Films: Review of Materials, Properties, and Applications," *J.Appl.Phys.*, vol. 100, no. 5, p. 051606, 2006.
- [98] D. Chapman, "Some Thin-Film Properties of a New Ferroelectric Composition," *J.Appl.Phys.*, vol. 40, no. 6, pp. 2381–2385, 1969.
- [99] M. Francombe, "Ferroelectric films and Their Device Applications," *Thin Solid Films*, vol. 13, no. 2, pp. 413–433, 1972.
- [100] B. Sharma, S. Vogel, and P. Prentky, "Retention in Thin Ferroelectric Films," *Ferroelectrics*, vol. 5, no. 1, pp. 69–75, 1973.
- [101] W. Känzig, *Solid State Physics: Advances in Research and Applications*, vol. 4. Academic Press Inc., 1957.
- [102] M. Lines and A. Glass, *Principles and Applications of Ferroelectrics and Related Materials*. Clarendon Press, Oxford, 1979.
- [103] J. Valasek, "Piezo-Electric and Allied Phenomena in Rochelle Salt," *Physical Review*, vol. 17, no. 4, pp. 475–481, April 1921.
- [104] J. Valasek, "Minutes of the Washington Meeting, April 23 and 24, 1920: Piezoelectric and Allied Phenomena in Rochelle Salt," *Physical Review*, vol. 15, no. 6, p. 537, June 1920.
- [105] A. Tagantsev, I. Stolichnov, E. Colla, and N. Setter, "Polarization Fatigue in Ferroelectric Films: Basic Experimental Findings, Phenomenological Scenarios, and Microscopic Features," *J.Appl.Phys.*, vol. 90, no. 3, pp. 1387–1402, 2001.

## BIBLIOGRAPHY

---

- [106] H. Al-Shareef, D. Dimos, W. Warren, and B. Tuttle, “Voltage Offsets and Imprint Mechanism in  $SrBi_2Ta_2O_9$  Thin Films,” *J.Appl.Phys.*, vol. 80, no. 8, pp. 4573–4577, 1996.
- [107] M. Grossmann, O. Lohse, D. Bolten, U. Boettger, R. Waser, W. Hartner, M. Kastner, and G. Schindler, “Lifetime Estimation Due to Imprint Failure in Ferroelectric  $SrBi_2Ta_2O_9$  Thin Films,” *Appl.Phys.Lett.*, vol. 76, no. 3, pp. 363–365, 2000.
- [108] A. Gruverman, B. Rodriguez, A. Kingon, R. Nemanich, J. Cross, and M. Tsukada, “Spatial Inhomogeneity of Imprint and Switching Behavior in Ferroelectric Capacitors,” *Appl.Phys.Lett.*, vol. 82, no. 18, pp. 3071–3073, 2003.
- [109] B. H. Park, B. S. Kang, S. D. Bu, T. W. Noh, J. Lee, and W. Jo, “Lanthanum-Substituted Bismuth Titanate for Use in Non-Volatile Memories,” *Nature*, vol. 401, no. 6754, pp. 682–684, Oct 1999.
- [110] A. Lin, X. Hong, V. Wood, A. A. Verevkin, C. H. Ahn, R. A. McKee, F. J. Walker, and E. D. Specht, “Epitaxial Growth of  $Pb(Zr_{0.2}Ti_{0.8})O_3$  on Si and its Nanoscale Piezoelectric Properties,” *Appl.Phys.Lett.*, vol. 78, no. 14, pp. 2034–2036, 2001.
- [111] M. Dawber, K. Rabe, and J. Scott, “Physics of Thin-Film Ferroelectric Oxides,” *Rev. Mod. Phys.*, vol. 77, no. 4, pp. 1083–1130, Oct 2005.
- [112] H. Ishiwara, M. Okuyama, and Y. Arimoto, *Ferroelectric Random Access Memories: Fundamentals and Applications*, vol. 93 of *Topics in Applied Physics*. Springer, 2004.
- [113] S. Eaton, D. Butler, M. Parris, D. Wilson, and H. McNeillie, “A Ferroelectric Nonvolatile Memory,” in *IEEE Intl. Solid-State Circuits Conference*, p. 130, Feb 1988.
- [114] R. Womack and D. Dolsch, “A 16 Kb Ferroelectric Nonvolatile Memory with a Bit Parallel Architecture,” in *IEEE Intl. Solid-State Circuits Conference*, pp. 242–243, Feb 1989.
- [115] J. Scott and C. P. de Araujo, “Ferroelectric Memories,” *Science*, vol. 246, no. 4936, pp. 1400–1405, 1989.
- [116] C. P. de Araujo, J. Cuchiaro, L. McMillan, M. Scott, and J. Scott, “Fatigue-Free Ferroelectric Capacitors with Platinum Electrodes,” *Letters to Nature*, vol. 374, pp. 627–629, April 1995.
- [117] E. Choi, N. Kim, S. Kweon, H. Sun, S. Yeom, J. Kim, J. Roh, J. Kim, and Y. Park, “Integration of Novel Capacitor Structure for High Density FeRAM with Barrier Metal  $TiAlN$  and  $(Bi, La)_4Ti_3O_{12}$ ,” *Integrated Ferroelectrics: An International Journal*, vol. 66, no. 1, pp. 107–113, 2004.
- [118] S. Sinharoy, H. Buhay, D. Lampe, and M. Francombe, “Integration of Ferroelectric Thin Films Into Nonvolatile Memories,” *J.Vac.Sci.Technol.A*, vol. 10, no. 4, pp. 1554–1561, 1992.
- [119] H. Volz, K. Koger, and H. Schmitt, “Preparation, Properties and Application of Thin Ferroelectric Films of PLZT,” *Ferroelectrics*, vol. 56, no. 1, pp. 1165–1168, 1984.

## BIBLIOGRAPHY

---

- [120] T. Hayashi, Y. Igarashi, D. Inomata, T. Ichimori, T. Mitsuhashi, K. Ashikaga, T. Ito, M. Yoshimaru, M. Nagata, S. Mitarai, H. Godaiin, T. Nagahama, C. Isobe, H. Moriya, M. Shoji, Y. Ito, H. Kuroda, and M. Sasaki, “A Novel Stack Capacitor Cell for High Density FeRAM Compatible with CMOS Logic,” in *IEEE Proc. Intl. Electron Devices Meeting*, pp. 543–546, Dec 2002.
- [121] H. Kim, S. Yamamoto, and H. Ishiwara, “Improvement of Data Readout Disturbance Effect in 1T2C-Type Ferroelectric Memory,” *Integrated Ferroelectrics: An International Journal*, vol. 67, no. 1, pp. 271–280, 2004.
- [122] F. Chu, G. Fox, and T. Davenport, “High Endurance Scaled PLZT Thin Films for FRAM Applications,” *Integrated Ferroelectrics: An International Journal*, vol. 36, no. 1, pp. 43–52, 2001.
- [123] F. Chu, G. Fox, T. Davenport, Y. Miyaguchi, and K. Suu, “The Control of Pb Loss for PZT Based FRAM,” *Integrated Ferroelectrics: An International Journal*, vol. 48, no. 1, pp. 161–169, 2002.
- [124] A. Itoh, Y. Hikosaka, T. Saito, H. Naganuma, H. Miyazawa, Y. Ozaki, Y. Kato, S. Mi-hara, H. Iwamoto, S. Mochizuki, M. Nakamura, and T. Yamazaki, “Mass-Productive High Performance 0.5  $\mu\text{m}$  Embedded FRAM Technology with Triple Layer Metal,” in *IEEE Symposium on VLSI Technology Digest of Technical Papers*, pp. 32–33, 2000.
- [125] W. Kraus, L. Lehman, D. Wilson, T. Yamazaki, C. Ohno, E. Nagai, H. Tamazaki, and H. Suzuki, “A 42.5 mm<sup>2</sup> 1 Mb Nonvolatile Ferroelectric Memory Utilizing Advanced Architecture for Enhanced Reliability,” in *IEEE Symposium on VLSI Curcuits Technology Digest of Technical Papers*, pp. 242–245, June 1998.
- [126] E. Fujii and K. Uchiyama, “First 0.18  $\mu\text{m}$  SBT-Based Embedded FeRAM Technology with Hydrogen Damage Free Stacked Cell Structure,” *Integrated Ferroelectrics: An International Journal*, vol. 53, no. 1, pp. 317–323, 2003.
- [127] H. Joo, Y. Song, H. Kim, S. Kang, J. Park, Y. Kang, H. Rhie, S. Lee, and K. Kim, “Improvement in Reliability of 0.25  $\mu\text{m}$  15 F<sup>2</sup> FRAM Using Novel MOCVD PZT Technology,” *Integrated Ferroelectrics: An International Journal*, vol. 68, no. 1, pp. 139–145, 2004.
- [128] Y. Horii, Y. Hikosaka, A. Itoh, K. Matsuura, M. Kurasawa, G. Komuro, K. Maruyama, T. Eshita, and S. Kashiwagi, “4 Mbit Embedded FRAM for High Performance System on Chip (SoC) with Large Switching Charge, Reliable Retention and High Imprint Resistance,” in *IEEE Proc. Intl. Electron Devices Meeting*, pp. 539–542, Dec 2002.
- [129] T. Moise, S. Summerfelt, G. Xing, L. Colombo, T. Sakoda, S. Gilbert, A. Loke, S. Ma, R. Kavari, L. Wills, T. Hsu, J. Amano, S. Johnston, D. Vestyck, M. Russell, and S. Bilodeau, “Electrical Properties of Submicron (&ges; 0.13  $\mu\text{m}^2$ ) Ir/PZT/Ir Capacitors Formed on W Plugs,” in *IEEE Proc. Intl. Electron Devices Meeting*, pp. 940–942, Dec 1999.
- [130] D. Takashima and Y. Oowaki, *Ferroelectric Random Access Memories*, vol. 93 of *Topics in Applied Physics*. Springer, 2004.

## BIBLIOGRAPHY

---

- [131] H. McAdams, R. Acklin, T. Blake, X.-H. Du, J. Eliason, J. Fong, W. Kraus, D. Liu, S. Madan, T. Moise, S. Natarajan, N. Qian, Y. Qiu, K. Remack, J. Rodriguez, J. Roscher, A. Seshadri, and S. Summerfelt, "A 64-Mb Embedded FRAM Utilizing a 130-nm 5LM Cu/FSG Logic Process," *IEEE J.Solid-State Circuits*, vol. 39, no. 4, pp. 667–677, April 2004.
- [132] T. Moise, S. Summerfelt, H. McAdams, S. Aggarwal, K. Udayakumar, F. Celii, J. Martin, G. Xing, L. Hall, K. Taylor, T. Hurd, J. Rodriguez, K. Remack, M. Khan, K. Boku, G. Stacey, M. Yao, M. Albrecht, E. Zielinski, M. Thakre, S. Kuchimanchi, A. Thomas, B. McKee, J. Rickes, A. Wang, J. Grace, J. Fong, D. Lee, C. Pietrzyk., R. Lanham, S. Gilbert, D. Taylor, J. Amano, R. Bailey, F. Chu, G. Fox, S. Sun, and T. Davenport, "Demonstration of a 4 Mb, High Density Ferroelectric Memory Embedded within a 130 nm, 5 LM Cu/FSG Logic Process," in *IEEE Proc. Intl. Electron Devices Meeting*, pp. 535–538, Dec 2002.
- [133] H. Kohlsted and H. Ishiwara, *Nanoelectronics and Information Technology: Advanced Electronic Materials and Novel Devices*. Wiley-VCH, Dec 2003.
- [134] H. Ishiwara, "Current Status of Fabrication and Integration of Ferroelectric-Gate FET's," in *Ferroelectric Thin Films VII*, vol. 596, 1999.
- [135] Y. Arimoto and H. Ishiwara, "Current Status of Ferroelectric Random-Access Memory," *Materials Research Society Bulletin*, vol. 29, no. 11, pp. 823–828, Nov 2004.
- [136] I. Ross, "Semiconductive Translating Device," May 1957. Patent: 2791760.
- [137] K. Takahashi, K. Manabe, A. Morioka, T. Ikarashi, T. Yoshihara, H. Watanabe, and T. Tatsumi, "High-Mobility Dual Metal Gate MOS Transistors with High-k Gate Dielectrics," *Japanese Journal of Applied Physics*, vol. 44, no. 4B, pp. 2210–2213, 2005.
- [138] S. Chambers, Y. Liang, Z. Yu, R. Droopad, J. Ramdani, and K. Eisenbeiser, "Band Discontinuities at Epitaxial  $SrTiO_3/Si$  (001) Heterojunctions," *Appl.Phys.Lett.*, vol. 77, no. 11, pp. 1662–1664, 2000.
- [139] C. Först, C. Ashman, K. Schwarz, and P. Blöchl, "The Interface Between Silicon and a High-k Oxide," *Nature*, vol. 427, no. 6969, pp. 53–56, Jan 2004.
- [140] R. McKee, F. Walker, and M. Chisholm, "Crystalline Oxides on Silicon: The First Five Monolayers," *Physical Review Letters*, vol. 81, no. 14, pp. 3014–3017, Oct 1998.
- [141] T. Furukawa, "Ferroelectric Properties of Vinylidene Fluoride Copolymers," *Phase Transitions: A Multinational Journal*, vol. 18, no. 3, pp. 143–211, 1989.
- [142] T. Furukawa, S. Kanai, A. Okada, Y. Takahashi, and R. Yamamoto, "Ferroelectric Switching Dynamics in VDF-TrFE Copolymer Thin Films Spin Coated on Si Substrate," *J.Appl.Phys.*, vol. 105, no. 6, p. 061636, 2009.
- [143] S. Lim, A. Rastogi, and S. Desu, "Electrical Properties of Metal-Ferroelectric-Insulator-Semiconductor Structures Based on Ferroelectric Polyvinylidene Fluoride Copolymer Film Gate for Nonvolatile Random Access Memory Application," *J.Appl.Phys.*, vol. 96, no. 10, pp. 5673–5682, 2004.

## BIBLIOGRAPHY

---

- [144] T. Reece, S. Ducharme, A. Sorokin, and M. Poulsen, “Nonvolatile Memory Element Based on a Ferroelectric Polymer Langmuir–Blodgett Film,” *Appl.Phys.Lett.*, vol. 82, no. 1, pp. 142–144, 2003.
- [145] R. Naber, C. Tanase, P. Blom, G. Gelinck, A. Marsman, F. Touwslager, S. Setayesh, and D. de Leeuw, “High-Performance Solution-Processed Polymer Ferroelectric Field-Effect Transistors,” *Nat. Mater.*, vol. 4, no. 3, pp. 243–248, March 2005.
- [146] G. Gelinck, A. Marsman, F. Touwslager, S. Setayesh, D. de Leeuw, R. Naber, and P. Blom, “All-Polymer Ferroelectric Transistors,” *Appl.Phys.Lett.*, vol. 87, no. 9, p. 092903, 2005.
- [147] R. Schroeder, L. Majewski, and M. Grell, “All-Organic Permanent Memory Transistor Using an Amorphous, Spin-Cast Ferroelectric-like Gate Insulator,” *Advanced Materials*, vol. 16, no. 7, pp. 633–636, 2004.
- [148] Michael C. Pirrung, “How to Make a DNA Chip,” *Angew. Chem. Int. Ed.*, vol. 41, pp. 1276–1289, 2002.
- [149] M. W. Shinwari, M. J. Deen, and D. Landheer, “Study of the Electrolyte-Insulator-Semiconductor Field-Effect Transistor (EISFET) with Applications in Biosensor Design,” *Microelectronics Reliability*, vol. 47, no. 12, pp. 2025–2057, Dec 2007.
- [150] J. Fritz, E. Cooper, S. Gaudet, P. Soger, and S. Manalis, “Electronic Detection of DNA by its Intrinsic Molecular Charge,” *PNAS*, vol. 99, no. 22, pp. 1412–1416, Oct 2002.
- [151] J. Hahm and C. Lieber, “Direct Ultrasensitive Electrical Detection of DNA and DNA Sequence Variations Using Nanowire Nanosensors,” *Nano Letters*, vol. 4, no. 1, pp. 51–54, 2004.
- [152] G. Zheng, F. Patolsky, Y. Cui, W. U. Wang, and C. M. Lieber, “Multiplexed Electrical Detection of Cancer Markers with Nanowire Sensor Arrays,” *Nature Biotechnology*, vol. 23, no. 10, pp. 1294–1301, 2005.
- [153] H. Im, X. . Huang, B. Gu, and Y. . Choi, “A Dielectric-Modulated Field-Effect Transistor for Biosensing,” *Nature Nanotechnology*, vol. 2, no. 7, pp. 430–434, 2007.
- [154] Y. Cui, Q. Wei, H. Park, and C. M. Lieber, “Nanowire Nanosensors for Highly Sensitive and Selective Detection of Biological and Chemical Species,” *Science*, vol. 293, no. 5533, pp. 1289–1292, Aug 2001.
- [155] S. Gupta, M. Elias, X. Wen, J. Shapiro, and L. Brillson, “Detection of Clinical Relevant Levels of Protein Analyte Under Physiologic Buffer Using Planar Field Effect Transistors,” *Biosensors and Bioelectronics*, vol. 24, pp. 505–511, 2008.
- [156] E. Stern, J. Klemic, D. Routenberg, P. Wyrembak, D. Turner-Evans, A. Hamilton, D. Lavan, T. Fahmy, and M. Reed, “Label-Free Immunodetection with CMOS-Compatible Semiconducting Nanowires,” *Nature Letters*, vol. 445, no. 1, pp. 519–522, Feb 2007.
- [157] K. Park, S. Lee, Y. Sohn, and S. Choi, “BioFET Sensor for Detection of Albumin in Urine,” *Electronic Letters*, vol. 44, no. 3, Jan 2008.

## BIBLIOGRAPHY

---

- [158] A. Girard, F. Bendria, O. D. Sagazan, M. Harnois, F. L. Bihan, A. Salaün, T. Mohammed-Brahim, P. Brissot, and O. Loréal, “Transferrin Electronic Detector for Iron Disease Diagnostics,” *IEEE Sensors*, pp. 474–477, Oct 2006.
- [159] K. Park, Y. Sohn, C. Kim, H. Kim, Y. Bae, and S. Choi, “Development of FET-Type Albumin Sensor for Diagnosing Nephritis,” *Biosensors and Bioelectronics*, vol. 23, no. 12, pp. 1904–1907, 2008.
- [160] M. J. Deen, M. W. Shinwari, J. C. Ranuárez, and D. Landheer, “Noise Considerations in Field-Effect Biosensors,” *J.Appl.Phys.*, vol. 100, no. 7, pp. 074703–1 –074703–8, 2006.
- [161] G. Bir and G. Pikus, *Symmetry and Strain-Induced Effects in Semiconductors*. New York - Toronto: J.Wiley & Sons, 1974.
- [162] C. Kittel, *Introduction to Solid State Physics. 7th Edition*. John Wiley & Sons, 1996.
- [163] J. Singh, *Physics of Semiconductors and their Heterostructures*. McGraw-Hill, 1993.
- [164] N. Ashcroft and N. Mermin, *Solid State Physics*. Fort Worth: Harcourt College Publishers, 1976.
- [165] J. Bardeen and W. Shockley, “Deformation Potentials and Mobilities in Non-Polar Crystals,” *Physical Review*, vol. 80, no. 1, pp. 72–80, Oct 1950.
- [166] C. Herring and E. Vogt, “Transport and Deformation-Potential Theory for Many-Valley Semiconductors with Anisotropic Scattering,” *Physical Review*, vol. 101, no. 3, pp. 944–961, 1956.
- [167] J. M. Hinckley and J. Singh, “Influence of Substrate Composition and Crystallographic Orientation on the Band Structure of Pseudomorphic Si-Ge Alloy Films,” *Physical Review B*, vol. 42, no. 6, pp. 3546–3566, Aug 1990.
- [168] M. Fischetti and S. Laux, “Band Structure, Deformation Potentials, and Carrier Mobility in Si, Ge, and SiGe Alloys,” *J.Appl.Phys.*, vol. 80, no. 4, pp. 2234–2252, 1996.
- [169] I. Balslev, “Influence of Uniaxial Stress on the Indirect Absorption Edge in Silicon and Germanium,” *Physical Review*, vol. 143, pp. 636–647, 1966.
- [170] J. C. Hensel, H. Hasegawa, and M. Nakayama, “Cyclotron Resonance in Uniaxially Stressed Silicon. II. Nature of the Covalent Bond,” *Physical Review*, vol. 138, no. 1A, pp. A225–A238, April 1965.
- [171] L. D. Laude, F. H. Pollak, and M. Cardona, “Effects of Uniaxial Stress on the Indirect Exciton Spectrum of Silicon,” *Physical Review B*, vol. 3, no. 8, pp. 2623–2636, April 1971.
- [172] M. Cardona and F. H. Pollak, “Energy-Band Structure of Germanium and Silicon: The  $\mathbf{k}\cdot\mathbf{p}$  Method,” *Physical Review*, vol. 142, no. 2, pp. 530–543, 1966.
- [173] J. M. Luttinger and W. Kohn, “Motion of Electrons and Holes in Perturbed Periodic Fields,” *Physical Review*, vol. 97, no. 4, pp. 869–883, 1955.
- [174] F. Seitz, “The Theoretical Constitution of Metallic Lithium,” *Physical Review*, vol. 47, no. 5, pp. 400–412, March 1935.

## BIBLIOGRAPHY

---

- [175] E. Kane, “Energy Band Structure in p-Type Germanium and Silicon,” *J.Phys.Chem.Solids*, vol. 1, no. 1-2, pp. 82–99, 1956.
- [176] M. Tinkham, *Group Theory and Quantum Mechanics*. Dover Publications, Dec 1964.
- [177] S. E. Ungersböck, *Advanced Modeling of Strained CMOS Technology*. Dissertation, Technische Universität Wien, 2007.
- [178] K. Uchida, A. Kinoshita, and M. Saitoh, “Carrier Transport in (110) nMOSFETs: Subband Structure, Non-Parabolicity, Mobility Characteristics, and Uniaxial Stress Engineering,” in *IEEE Proc. Intl. Electron Devices Meeting*, pp. 1019–1021, Dec 2006.
- [179] V. Sverdlov, E. Ungersboeck, H. Kosina, and S. Selberherr, “Effects of Shear Strain on the Conduction Band in Silicon: An Efficient Two-Band  $\mathbf{k}\cdot\mathbf{p}$  Theory,” in *European Solid-State Device Research Conference*, pp. 386–389, 2007.
- [180] E. Ungersboeck, S. Dhar, G. Karlowatz, V. Sverdlov, H. Kosina, and S. Selberherr, “The Effect of General Strain on the Band Structure and Electron Mobility of Silicon,” *IEEE Trans.Electron Devices*, vol. 54, no. 9, pp. 2183–2190, 2007.
- [181] V. Sverdlov and S. Selberherr, “Electron Subband Structure and Controlled Valley Splitting in Silicon Thin-Body SOI FETs: Two-Band  $\mathbf{k}\cdot\mathbf{p}$  Theory and Beyond,” *Solid-State Electron.*, vol. 52, no. 12, pp. 1861–1866, 2008.
- [182] T. Ando, A. Fowler, and F. Stern, “Electronic Properties of Two-Dimensional Systems,” *Rev. Mod. Phys.*, vol. 54, no. 2, pp. 437–672, April 1982.
- [183] T. Boykin, G. Klimeck, M. Friesen, S. Coppersmith, P. von Allmen, F. Oyafuso, and S. Lee, “Valley Splitting in Low-Density Quantum-Confined Heterostructures Studied Using Tight-Binding Models,” *Physical Review B*, vol. 70, no. 16, p. 165325, Oct 2004.
- [184] T. Boykin, G. Klimeck, M. Eriksson, M. Friesen, S. Coppersmith, P. von Allmen, F. Oyafuso, and S. Lee, “Valley Splitting in Strained Si Quantum Wells,” *Appl.Phys.Lett.*, vol. 84, no. 1, pp. 115–117, 2004.
- [185] D. Esseni and P. Palestri, “Linear Combination of Bulk Bands Method for Investigating the Low-Dimensional Electron Gas in Nanostructured Devices,” *Physical Review B*, vol. 72, no. 16, p. 165342, Oct 2005.
- [186] D. Rideau, M. Feraille, M. Michailat, Y. Niquet, C. Tavernier, and H. Jaouen, “On the Validity of the Effective Mass Approximation and the Luttinger  $\mathbf{k}\cdot\mathbf{p}$  Model in Fully Depleted SOI MOSFETs,” *Solid-State Electron.*, vol. 53, no. 4, pp. 452–461, April 2009. Special Issue with papers selected from the Ultimate Integration on Silicon Conference, ULIS 2008.
- [187] V. Sverdlov, O. Baumgartner, T. Windbacher, and S. Selberherr, “Modeling of Modern MOSFETs with Strain,” *J.Comp.Electronics*, 2009.
- [188] P. Bergveld, “Development of an Ion-Sensitive Solid-State Device for Neurophysiological Measurements,” *IEEE Trans. on Biomedical Engineering*, vol. 17, no. 1, pp. 70–71, Jan 1970.

## BIBLIOGRAPHY

---

- [189] I. Willner and E. Katz, *Bioelectronics: From Theory to Applications*. Wiley-VCH, 1 ed., May 2005.
- [190] P. Delahay, *Double Layer and Electrode Kinetics*. New York: Interscience Publishers, 1965.
- [191] F. Walsh, *A First Course in Electrochemical Engineering*. Electrochemical Consultancy, 1993.
- [192] E. Gileadi, E. Kirowa-Eisner, and J. Penciner, *Interfacial Electrochemistry: An Experimental Approach*. Addison-Wesley Publishing Company, 1975.
- [193] D. Pletcher, *A First course in Electrode Processes*. Alresford Press Limited, 1991.
- [194] I. Levine, *Physical Chemistry*. New York: McGraw-Hill, 1995.
- [195] W. Coffey and B. Scaife, "On the Theory of Dielectric Saturation of Polar Fluids," in *Proc. Royal Irish Academy*, vol. 76, pp. 195–216, 1976.
- [196] D. Landheer, G. Aers, W. McKinnon, M. Deen, and J. Ranuárez, "Model for the Field Effect from Layers of Biological Macromolecules on the Gates of Meta-Oxide-Semiconductor Transistors," *J.Appl.Phys.*, vol. 98, no. 4, pp. 044701–1 – 044701–15, 2005.
- [197] L. Bousse, "Single Electrode Potentials Related to Flat-Band Voltage Measurements on EOS and MOS Structures," *J.Chem.Phys.*, vol. 76, no. 10, pp. 5128–5133, 1982.
- [198] D. E. Yates, S. Levine, and T. W. Healy, "Site-Binding Model of the Electrical Double Layer at the Oxide/Water Interface," *Journal of the Chemical Society*, vol. Faraday Transactions 1: Physical Chemistry in Condensed Phases, no. 70, pp. 1807 – 1818, 1974.
- [199] J. Xu, X. Luo, and H. Chen, "Analytical Aspects of FET-Based Biosensors," *Frontiers in Bioscience*, vol. 10, pp. 420–430, Jan 2005.
- [200] L. Bousse, S. Mostarshed, B. Van Der Shoot, N. F. De Rooij, P. Gimmel, and W. Gopel, "Zeta Potential Measurements of Ta<sub>2</sub>O<sub>5</sub> and SiO<sub>2</sub> Thin Films," *Journal of Colloid and Interface Science*, vol. 147, no. 1, pp. 22–32, 1991.
- [201] M. Giesbers, J. M. Kleijn, and M. A. C. Stuart, "The Electrical Double Layer on Gold Probed by Electrokinetic and Surface Force Measurements," *Journal of Colloid and Interface Science*, vol. 248, no. 1, pp. 88 – 95, 2002.
- [202] A. Morgenshtein, *Design and Methodology for ISFET (Ion Sensitive Field-Effect Transistors) Microsystems for Biotelemetry*. M.Sc. Thesis, Israel Institute of Technology, Haifa, 2003.
- [203] P. Bergveld, "The Development and Application of FET-Based Biosensors," *Biosensors*, vol. 2, no. 1, pp. 15–34, 1986.
- [204] L. Bousse, N. De Rooij, and P. Bergveld, "Operation of Chemically Sensitive Field-Effect Sensors as a Function of the Insulator-Electrolyte Interface," *IEEE Trans.Electron Devices*, vol. 30, no. 10, pp. 1263–1270, Oct 1983.

## BIBLIOGRAPHY

---

- [205] Y. Tsvividis, *Operation and Modeling of the MOS Transistor*. New York: McGraw-Hill Book Company, 1995.
- [206] C. Fung, P. Cheung, and W. Ko, “A Generalized Theory of an Electrolyte-Insulator-Semiconductor Field-Effect Transistor,” *IEEE Trans. Electron Devices*, vol. 33, no. 1, pp. 8–18, Jan 1986.
- [207] “<http://kerouac.pharm.uky.edu/asrg/hplc/detectors.html>.” University of Kentucky, Analytical Spectroscopy Research Group, Lecture.
- [208] M. J. Schöning, ““Playing Around” with Field-Effect Sensors on the Basis of EIS Structures, LAPS and ISFETs,” *Sensors*, vol. 5, no. 3, pp. 126–138, 2005.
- [209] S. Mohri, J. Shimizu, N. Goda, T. Miyasaka, A. Fujita, M. Nakamura, and F. Kajiya, “Measurements of  $CO_2$ , Lactic Acid and Sodium Bicarbonate Secreted by Cultured Cells Using a Flow-Through Type pH/ $CO_2$  Sensor System Based on ISFET,” *Sensors and Actuators B: Chemical*, vol. 115, no. 1, pp. 519–525, 2006.
- [210] B. Palán, F. V. Santos, J. M. Karam, B. Courtois, and M. Husák, “New ISFET Sensor Interface Circuit for Biomedical Applications,” *Sensors and Actuators B: Chemical*, vol. 57, no. 1-3, pp. 63–68, 1999.
- [211] M. Yuqing, G. Jianguo, and C. Jianrong, “Ion Sensitive Field Effect Transducer-Based Biosensors,” *Biotechnology Advances*, vol. 21, no. 6, pp. 527–534, 2003.
- [212] A. Kharitonov, M. Zayats, L. Alfonta, E. Katz, and I. Willner, “A Novel ISFET-Based  $NAD^+$ -Dependent Enzyme Sensor for Lactate,” *Sensors and Actuators B: Chemical*, vol. 76, no. 1-3, pp. 203–210, 2001.
- [213] F. Patolsky, G. Zheng, and C. M. Lieber, “Fabrication of Silicon Nanowire Devices for Ultrasensitive, Label-Free, Real-Time Detection of Biological and Chemical Species,” *Nat. Protocols*, vol. 1, no. 4, pp. 1711–1724, Nov 2006.
- [214] J. S. Liu, *Monte Carlo Strategies in Scientific Computing*. New York Berlin Heidelberg: Springer, 2001.
- [215] J. Zhou, L. Zhang, Y. Leng, H.-K. Tsao, Y.-J. Sheng, and S. Jiang, “Unbinding of the Streptavidin-Biotin Complex by Atomic Force Microscopy: A Hybrid Simulation Study,” *J. Chem. Phys.*, vol. 125, no. 10, p. 104905, 2006.
- [216] H. Grubmüller, “Force Probe Molecular Dynamics Simulations,” *Springer Protocols*, vol. 305, March 2005.
- [217] S. Selberherr, *Analysis and Simulation of Semiconductor Devices*. Springer, 1984.
- [218] T.-W. Tang and M.-K. Jeong, “Discretization of Flux Densities in Device Simulations Using Optimum Artificial Diffusivity,” *IEEE Trans. Computer-Aided Design of Integrated Circuits and Systems*, vol. 14, no. 11, pp. 1309–1315, Nov 1995.
- [219] C. Heitzinger, R. Kennell, G. Klimeck, N. Mauser, M. McLennan, and C. Ringhofer, “Modeling and Simulation of Field-Effect Biosensors (BioFETs) and Their Deployment on the nanoHUB,” *J. Phys.: Conf. Ser.*, vol. 107, pp. 012004/1–12, 2008.

## BIBLIOGRAPHY

---

- [220] C. Ringhofer and C. Heitzinger, “Multi-Scale Modeling and Simulation of Field-Effect Biosensors,” *ECS Transactions*, vol. 14, no. 1, pp. 11–19, 2008.
- [221] C. Heitzinger and G. Klimeck, “Computational Aspects of the Three-Dimensional Feature-Scale Simulation of Silicon-Nanowire Field-Effect Sensors for DNA Detection,” *J. Comput. Electron.*, vol. 6, no. 1-3, pp. 387–390, 2007.
- [222] N. A. Baker, D. Sept, S. J., M. J. Holst, and J. A. McCammon, “Electrostatics of Nanosystems: Application to Microtubules and the Ribosome,” in *Proceedings of the National Academy of Sciences of the United States of America*, vol. 98, pp. 10037–10041, Aug 2001.
- [223] M. J. Holst and F. Saied, “Multigrid Solution of the Poisson-Boltzmann Equation,” *J. Comput. Chem.*, vol. 14, pp. 105–113, 1993.
- [224] M. J. Holst and F. Saied, “Numerical Solution of the Nonlinear Poisson-Boltzmann Equation: Developing More Robust and Efficient Methods,” *J. Comput. Chem.*, vol. 16, pp. 337–364, 1995.
- [225] T. Windbacher, V. Sverdlov, and S. Selberherr, “Modeling of Low Concentrated Buffer DNA Detection with Suspend Gate Field-Effect Transistors (SGFET),” in *Proc. Intl. Workshop on Computational Electronics*, pp. 169–172, 2009.
- [226] P. Debye and E. Hückel, “Zur Theorie der Elektrolyte: I. Gefrierpunktserniedrigung und verwandte Erscheinungen.,” *Physikalische Zeitschrift*, vol. 24, no. 9, pp. 185–206, May 1923.
- [227] L. Landau and B. Deryagin), “Theory of Stability Strongly Charged Lyophobic Soles and Coalescence of Strongly Charged Particles in Solutions of Electrolytes,” *Acta Phys.-Chim.*, vol. 14, p. 633, 1941.
- [228] L. Stryer, *Biochemistry 4th Edition*. New York: W.H. Freeman and Company, 1995.
- [229] S. W. Oh, J. D. Moon, H. J. Lim, S. Y. Park, T. Kim, J. Park, M. H. Han, M. Snyder, and E. Y. Choi, “Calixarene Derivative as a Tool for Highly Sensitive Detection and Oriented Immobilization of Proteins in a Microarray Format Through Noncovalent Molecular Interaction,” *FASEB Journal*, vol. 19, no. 10, pp. 1335–1337, 2005.
- [230] R. Wacker, H. Schroder, and C. M. Niemeyer, “Performance of Antibody Microarrays Fabricated by Either DNA-Directed Immobilization, Direct Spotting, or Streptavidin-Biotin Attachment: A Comparative Study,” *Analytical Biochemistry*, vol. 330, no. 2, pp. 281–287, 2004.
- [231] W. Kusnezow, A. Jacob, A. Walijew, F. Diehl, and J. D. Hoheisel, “Antibody Microarrays: An Evaluation of Production Parameters,” *Proteomics*, vol. 3, no. 3, pp. 254–264, 2003.
- [232] P. Peluso, D. S. Wilson, D. Do, H. Tran, M. Venkatasubbaiah, D. Quincy, B. Heidecker, K. Poindexter, N. Tolani, M. Phelan, K. Witte, L. S. Jung, P. Wagner, and S. Nock, “Optimizing Antibody Immobilization Strategies for the Construction of Protein Microarrays,” *Analytical Biochemistry*, vol. 312, no. 2, pp. 113–124, 2003.

## BIBLIOGRAPHY

---

- [233] J. Turkova, “Oriented Immobilization of Biologically Active Proteins as a Tool for Revealing Protein Interactions and Function,” *Journal of Chromatography B: Biomedical Sciences and Applications*, vol. 722, no. 1-2, pp. 11–31, 1999.
- [234] M. Harnois, O. Sagazan, A. Girard, A.-C. Salaün, and T. Mohammed-Brahim, “Low Concentrated DNA Detection by SGFET,” in *Transducers & Eurosensors*, (Lyon, France), pp. 1983–1986, June 2007.
- [235] A. Poghossian, A. Cherstvy, S. Ingebrandt, A. Offenhäusser, and M. Schöning, “Possibilities and Limitations of Label-Free Detection of DNA Hybridization with Field-Effect-Based Devices,” *Sensors and Actuators, B: Chemical*, vol. 111-112, pp. 470–480, 2005.
- [236] T. Windbacher, V. Sverdlov, S. Selberherr, C. Heitzinger, N. Mauser, and C. Ringhofer, “Simulation of Field-Effect Biosensors (BioFETs),” in *Proc. Simulation of Semiconductor Processes and Devices*, pp. P18/1–4, Sep 2008.
- [237] M. J. Deen, “Highly Sensitive, Low-Cost Integrated Biosensors,” in *SBCCI 2007: 20th Symposium on Integrated Circuits and System Design*, p. 1, 2007.

---

## Own Publications

---

- [1] V. Sverdlov, T. Windbacher, H. Kosina, and S. Selberherr. Stress-Induced Valley Splitting in Silicon Thin Films. in *Proc. Intl. Conf. on Ultimate Integration on Silicon*, pp. 93–96, 2008.
- [2] T. Windbacher, V. Sverdlov, S. Selberherr, C. Heitzinger, N. Mauser, and C. Ringhofer. Simulation of Field-Effect Biosensors (BioFETs) for Biotin-Streptavidin Complexes. in *Proc. Intl. Conf. on the Physics of Semiconductors*, volume 1199, pp. 507–508, AIP, 2010.
- [3] T. Windbacher, V. Sverdlov, S. Selberherr, C. Heitzinger, N. Mauser, and C. Ringhofer. Simulation of Field-Effect Biosensors (BioFETs). in *Proc. Intl. Conf. on Simulation of Semiconductor Processes and Devices*, pp. 193–196, 2008.
- [4] V. Sverdlov, T. Windbacher, and S. Selberherr. Mobility Enhancement in Thin Silicon Films: Strain and Thickness Dependences of the Effective Masses and Non-Parabolicity Parameter. in *Intl. Conf. on Simulation of Semiconductor Processes and Devices*, pp. 145–148, 2008.
- [5] T. Windbacher, V. Sverdlov, S. Selberherr, and C. Heitzinger. A General Bottom-Up Modeling Approach for BioFETs. in *Abstracts Conf. on Nanosensors for Industrial Applications (NANOSENS)*, p. 37, 2008.
- [6] T. Windbacher, V. Sverdlov, S. Selberherr, C. Heitzinger, N. Mausern, and C. Ringhofer. Study of the Properties of Biotin-Streptavidin Sensitive Biofets. in *Final Program and Book of Abstracts*, p. 42, *Intl. Joint Conf. on Biomedical Engineering Systems and Technologies (BIOSTEC)*, 2009.
- [7] T. Windbacher, V. Sverdlov, S. Selberherr, C. Heitzinger, N. Mauser, and C. Ringhofer. Study of the Properties of Biotin-Streptavidin Sensitive BioFETs. in *Proc. Intl. Conf. on Biomedical Electronics and Devices (BIODEVICES)*, pp. 24–30, 2009.
- [8] V. Sverdlov, T. Windbacher, O. Baumgartner, and S. Selberherr. Electron Subband Structure and Valley Splitting in Silicon Ultra-Thin Body SOI Structures from the Two-Band  $\mathbf{k}\cdot\mathbf{p}$  Model. in *Proc. EUROSOI 2009 Conf.*, pp. 81–82, 2009.

- [9] V. Sverdlov, T. Windbacher, O. Baumgartner, F. Schanovsky, and S. Selberherr. Valley Splitting in Thin Silicon Films from a Two-Band  $\mathbf{k}\cdot\mathbf{p}$  Model. in *Proc. Intl. Conf. on Ultimate Integration of Silicon*, pp. 277–280, 2009.
- [10] V. Sverdlov, O. Baumgartner, T. Windbacher, F. Schanovsky, and S. Selberherr. Impact of Confinement of Semiconductor and Band Engineering on Future Device Performance. *ECS Transactions*, pp. 15–26, 2009.
- [11] T. Windbacher, V. Sverdlov, and S. Selberherr. Modeling of Low Concentrated Buffer DNA Detection with Suspend Gate Field-Effect Transistors (SGFET). in *Proc. Intl. Workshop on Computational Electronics*, pp. 169–172, 2009.
- [12] V. Sverdlov, O. Baumgartner, T. Windbacher, and S. Selberherr. Perspectives of Silicon for Future Spintronic Applications from the Peculiarities of the Subband Structure in Ultra-Thin Films. in *Proc. Intl. Workshop on Computational Electronics*, pp. 95–96, 2009.
- [13] V. Sverdlov, O. Baumgartner, T. Windbacher, and S. Selberherr. Silicon for Spintronic Applications: Strain-Enhanced Valley Splitting. in *Abstracts Advanced Research Workshop on Future Trends in Microelectronics: Unmapped Roads*, p. 58, 2009.
- [14] V. Sverdlov, O. Baumgartner, S. Tygainov, T. Windbacher, and S. Selberherr. Subband Structure in Ultra-Thin Silicon Films. in *Proc. Intl. Symposium NANOSTRUCTURES: Physics and Technology*, pp. 62–63, 2009.
- [15] V. Sverdlov, O. Baumgartner, T. Windbacher, F. Schanovsky, and S. Selberherr. Mobility Enhanced by Shear Strain Splitting of Unprimed Subbands in  $\langle 001 \rangle$  Silicon Films and Point Contacts. in *Abstracts Intl. Conf. on Spintronics and Quantum Information Technology*, p. 301, 2009.
- [16] V. Sverdlov, O. Baumgartner, T. Windbacher, F. Schanovsky, and S. Selberherr. Impact of Confinement and Stress on the Subband Parameters in Ultra-Thin Silicon Films. *ECS Transactions*, 23(1):389–396, 2009.
- [17] V. Sverdlov, O. Baumgartner, T. Windbacher, F. Schanovsky, and S. Selberherr. Thickness Dependence of Effective Masses in a Strained Thin Silicon Film. in *Proc. Intl. Conf. on Simulation of Semiconductor Processes and Devices*, pp. 51–54, 2009.
- [18] V. Sverdlov, O. Baumgartner, T. Windbacher, and S. Selberherr. Modeling Techniques for Strained CMOS Technology. *ECS Transactions*, 25(7):3–18, 2009.
- [19] V. Sverdlov, T. Windbacher, F. Schanovsky, and S. Selberherr. Mobility Modeling in Advanced MOSFETs with Ultra-Thin Silicon Body under Stress. *J. Integrated Circuits and Systems*, 4(2):55–60, 2009.
- [20] V. Sverdlov, O. Baumgartner, T. Windbacher, and S. Selberherr. Modeling of Modern MOSFETs with Strain. *J. Comp. Electronics*, 8(3):192–208, 2009.
- [21] T. Windbacher, V. Sverdlov, O. Baumgartner, and S. Selberherr. Electron Subband Structure in Strained Silicon UTB Films from the Hensel-Hasegawa-Nakayama Model - Part1 Analytical Consideration and Strain-Induced Valley Splitting. *Solid-State Electron.*, 54(2):137–142, 2010.

## OWN PUBLICATIONS

---

- [22] T. Windbacher, V. Sverdlov, and S. Selberherr. *Biomedical Engineering Systems and Technologies*, Chapter Biotin-Streptavidin Sensitive BioFETs and Their Properties, pp. 85–95. Springer, 2010.

	Author	Co-Author	Total
Journals	1	2	3
Book contributions	1	0	1
Conferences	6	12	18
Total	8	14	22

Publication Statistics.

---

# Curriculum Vitae

---

**November 24<sup>th</sup>, 1979**

Born in Mödling, Austria.

**June 1999**

High school graduation (*Matura*) at the HTBLuVA Wiener Neustadt, specializing in Energy Engineering and Power Electronics (with honors).

**October 1999**

Enrolled in Technical Physics at Vienna University of Technology, Austria.

**October 2006**

Received degree of *Diplom-Ingenieur* (M.Sc.) in Technical Physics, specializing in Methods and Technology from the Vienna University of Technology.

**October 2006**

Entered doctoral program at the Institute for Microelectronics, Vienna University of Technology, under the supervision of Prof. *Siegfried Selberherr*.

**October 17<sup>th</sup>, 2007**

Birth of daughter Lea.

**January 4<sup>th</sup>, 2010**

Birth of daughter Yana.

